Title	Synthesis of Homosumanene and its Derivatives
Author(s)	西本, 真生
Citation	大阪大学, 2023, 博士論文
Version Type	VoR
URL	https://doi.org/10.18910/91913
rights	
Note	

Doctoral Dissertation

Synthesis of Homosumanene and its Derivatives
(ホモスマネン及びその誘導体の合成)

Mikey Nishimoto

January 2023

Department of Applied Chemistry

Graduate School of Engineering

Osaka University

Table of contents

Chapter 1 **Introduction**

Chapter 2 **Synthesis of the C70 Fragment Buckybowl, Homosumanene, and Heterahomosumanenes via Ring-Expansion Reactions from Sumanenone**

Chapter 3 **Acid-mediated carbon-carbon bond cleavage on a bowl-shaped sumanenone**

Chapter 4 **Thermodynamic Differentiation of the Two Sides of Azabuckybowl through Complexation with Square Planar Platinum(II)**

Chapter 5 **Acceleration Effect of Bowl-shaped Structure in Aerobic Oxidation Reaction: Synthesis of Homosumanene *ortho*-Quinone and Azaacene-Fused Homosumanenes**

Chapter 1. Introduction

Section 1. C60 fragment buckybowls

Buckybowls are bowl-shaped π-conjugated molecules corresponding to the substructure of fullerenes or end-cap structure of carbon nanotubes. The first multi-step synthesis of corannulene, the smallest substructure of C60 with C_5 symmetry, was achieved by Lawton and Barth in 1966.[1] In the 1990s, a Flash Vacuum Pyrolysis (FVP) synthesis of corannulene was reported.[2] In 2012, Siegel et al. reported a kilogram-scale liquid-phase synthesis of corannulene.[3] In contrast, in 1993, Mehta et al. reported that sumanene, which has the smallest substructure of C60 with C_{3v} symmetry, could not be synthesized by the FVP method. So, they only named this molecule in the paper.[4] This is because sumanene has a deeper bowl structure than corannulene, making it difficult to synthesize from planar molecules. Based on this report, Sakurai and Hirao et al. reported the synthesis of sumanene in 2003 by using a norbornadiene as a starting material with a three-dimensional structure and constructing a bowl structure with sp^3 carbons by cyclotrimerization and ring-opening/ring-closing tandem metathesis reaction and finally converting the sp^3 carbons to sp^2 carbons by oxidation (Scheme 1).[5] With the development of these synthetic methods, corannulene and sumanene are now available from chemical supply companies.[6] Research on buckybowls has been conducted mainly on these compounds.[7]

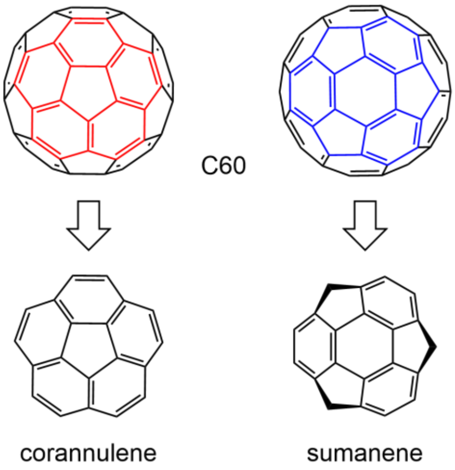

Figure 1. Pristine C60 fragment buckybowls, corannulene and sumanene.

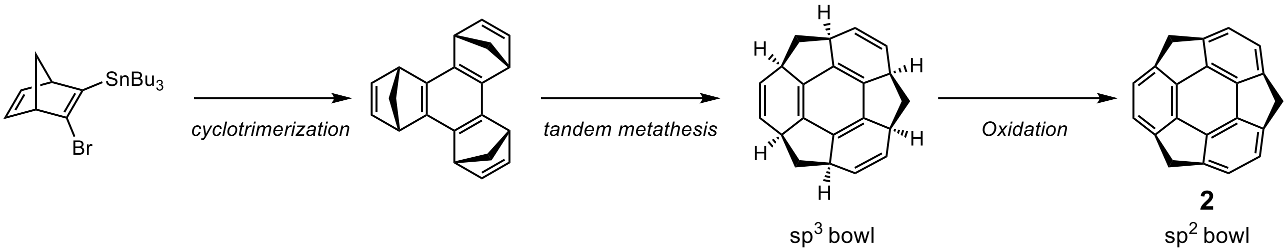

Scheme 1. Synthesis of sumanene.

One of the main reasons why buckybowls have been intensively studied is because they promise to start materials in the bottom-up synthesis of curved nanocarbon materials such as fullerenes and carbon nanotubes. The drawback of fullerenes and carbon nanotubes as materials is that it takes more work to synthesize them selectively. Due to this problem, many of their properties still need to be discovered at the molecular level. One solution to this problem is the selective bottom-up synthesis of curved nanocarbons with synthetic organic chemistry. Using synthetic organic chemistry techniques to assemble their structures, it is possible to isolate pure fullerene/carbon nanotubes, understand their properties, and synthesize curved nanocarbons with new properties. Therefore, it is crucial to develop synthetic methods and chemical modification of their substructure, buckybowls. As starting materials, many syntheses of curved nanocarbon molecules using the C60 fragment buckybowls, corannulene, and sumanene have already been reported (Figure 2). For example, end-cap molecules of [5,5]carbon nanotubes,[8] trinaphthosumanene,[9] and hemiazafullerene[10] were synthesized as precursors of carbon nanotubes and fullerenes. Unique curved nanocarbon molecules such as warped nanographene,[11] a saddle-shaped molecule with negative curvature, and quintuple [6]helicene,[12] have been synthesized utilizing corannulene as a starting material. These molecules could only have been synthesized with synthetic methods for the C60 fragment buckybowls, demonstrating that developing novel buckybowls is also essential to access novel curved nanocarbons from them.

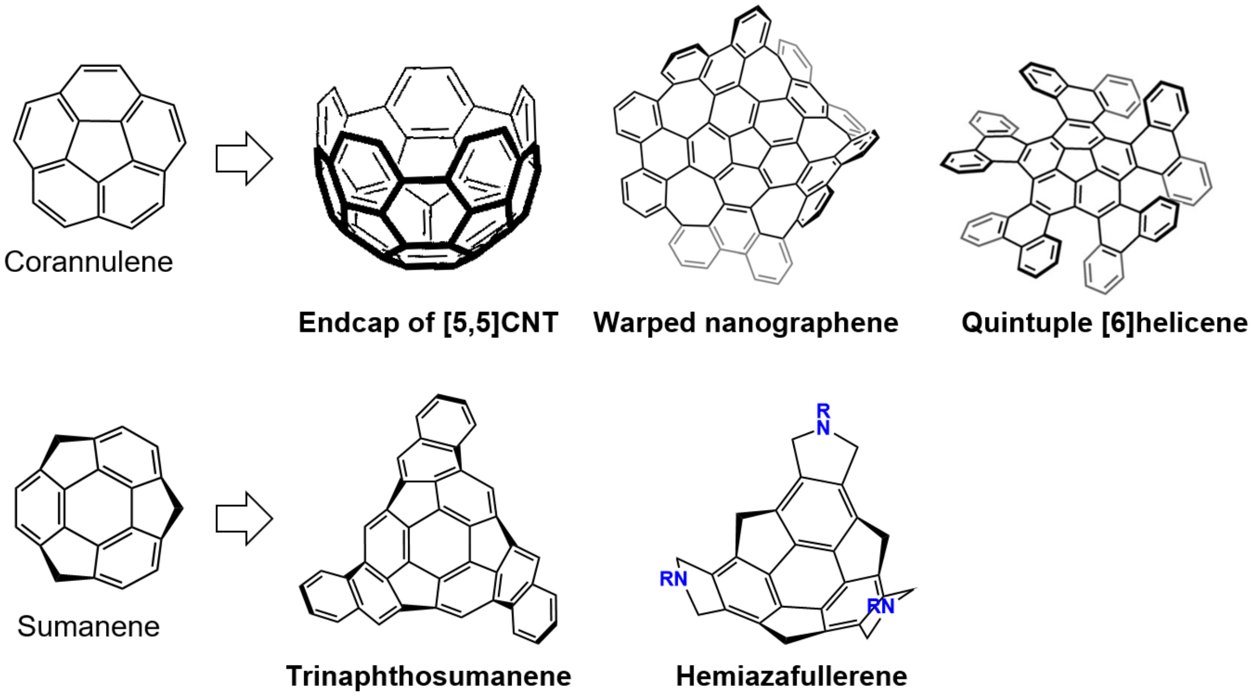

Figure 2. Examples of curved π-conjugated molecules prepared from corannulene or sumanene.

Section 2. Curved effect derived from curved π-systems

It is essential to understand the changes in properties of π-conjugated systems due to curvature to exploit the unique properties of buckybowls. In this section, the author describes the property changes caused by the curved structure.

1. Electronic perturbation

The sp^2 carbons in planar π-conjugated systems are in the same plane. In contrast, in curved π-conjugated molecules such as fullerenes and buckybowls, the sp^2 carbons are pyramided by their curved skeletons (Figure 3). This change in the structure of the sp^2 carbon results in a variety of changes.[13]

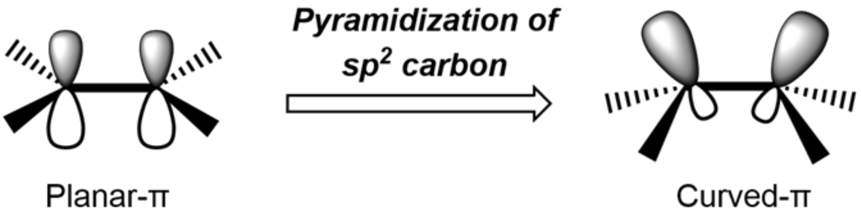

Figure 3. sp^2 carbons and their orbital in planar and curved-π systems.

First, the p-orbital overlaps become smaller, and the π bond weakens; as the π bond weakens, the energies of the bonding orbitals, including the HOMO, increase and their reactivity for addition reactions is enhanced. Therefore, it is known that electrophilic substitution reactions tend to proceed in planar π-conjugated molecules, whereas addition reactions often also proceed in curved π-conjugated molecules. Indeed, chemical modification of fullerenes has been carried out by addition reactions, such as Bingel reaction,[14] and Plato reaction[15] as typical examples (Figure 4).

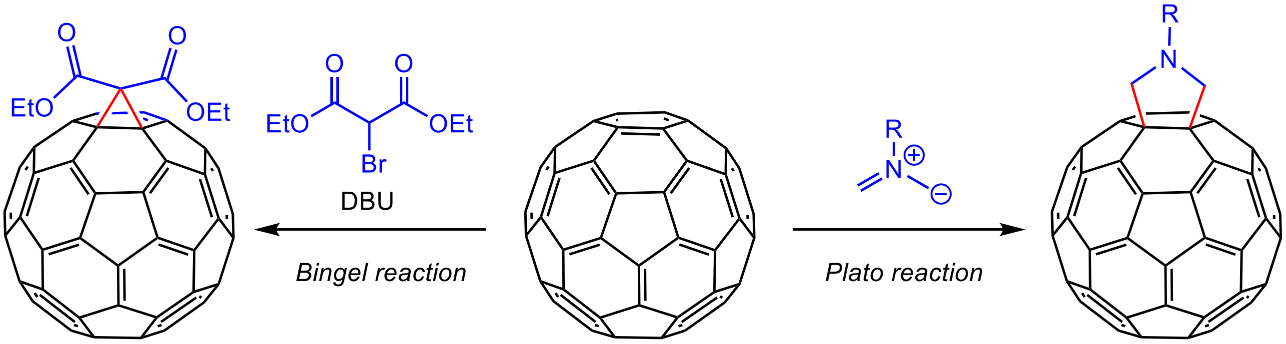

Figure 4. Chemical functionalization of C60.

Another pyramidizing effect of sp^2 carbon is an increase in the *s*-character of the orbitals. The increase in the *s*-character of the orbitals leads to their stabilization, thus lowering the energy levels of all orbitals, including the HOMO and LUMO. As for the decrease in HOMO level, this is almost canceled out by the effect of the increase in HOMO level due to the decrease in *p*-orbital overlap described above. Therefore, the decrease in the LUMO level is more significant than that of the HOMO. The apparent effect of the curvature is that the HOMO energy level remains almost unchanged while the LUMO energy level decreases. Therefore, in contrast to polycyclic aromatic hydrocarbons, which are usually electron-rich and used as p-type organic semiconductors, curved π-conjugated molecules such as fullerenes are known to be used in n-type organic semiconductors and organic photovoltaics due to their excellent electron-accepting properties.[16]

2. Concave and convex faces

Buckybowls have two distinct faces: concave and convex faces. The orbital shapes and electron densities also differ greatly depending on the concave and convex faces of the bowls, which means that the buckybowls intrinsically have a Janus character. For example, the electronic repulsion caused by the closeness of *p*-orbitals on the concave face causes the orbitals to overhang on the convex face (Figure 5). This causes the concave face to be electron-deficient and the convex face to be electron-rich, and addition reactions often proceed mainly on the convex side in a stereoselective manner (Figure 6).[17]

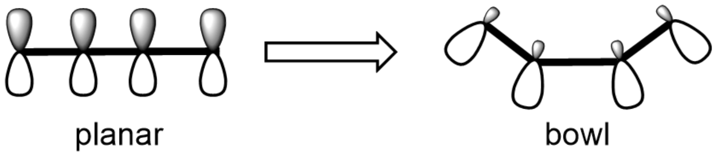

Figure 5. *p*-orbitals in planar and bowl-π systems.

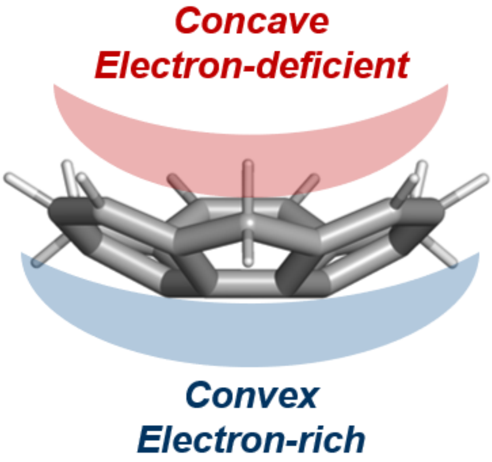

Figure 6. Schematic picture of electron density at concave/convex face in sumanene.

Due to such a difference between the two faces, buckybowls have a dipole moment in the perpendicular direction to the plane containing the bowl without introducing any polar functional group. For example, sumanene has a dipole moment of 2.51 Debye even though it is a simple hydrocarbon.[18] Buckybowls are often soluble in common organic solvents, possibly due to the existence of dipole moments derived from this bowl structure and the fact that their curvature makes them less susceptible to aggregation due to smaller $\pi\cdots\pi$ interactions compared to planar molecules. These two faces also affect their alignment in the solid state. Planar molecules usually adopt a herringbone packing structure to maximize the $\pi\cdots\pi$ and CH$\cdots\pi$ interactions (Figure 7a). In the case of bowl molecules, in addition to these contributions, the polarization due to the difference in electron density on concave/convex faces affects the packing structure. For example, Sumanene forms one-dimensional columnar stacking structure (Figure 7b).[19] This stacking structure allows sumanene to have anisotropic charge career mobility in the stacking direction.[20]

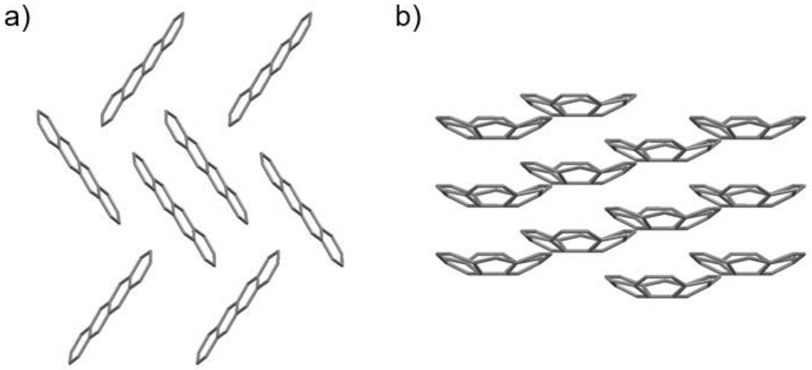

Figure 7. Crystal packing structures of a) tetracene and b) sumanene.

3. Bowl-to-bowl inversion behavior

Buckybowls exhibit a unique dynamic interconversion between concave and convex faces, so-called bowl-to-bowl inversion (Figure 8). Bowl inversion occurs only when the depth or size of the bowl is small enough to overcome the transition state. There are many studies on the bowl inversion behavior of corannulene, sumanene, and their derivatives. In most cases, the bowl inversion proceeds via planar transition states.[21] Since bowl inversion can be regarded as switching between two identical faces, it is expected to be applied to molecular memory. For this purpose, precise control of bowl inversion of sumanene supported on a metal substrate has been reported.[22] The inversion of the concave/convex faces can also be regarded as an inversion of the dipole moment originating from the bowl structure. Therefore, buckybowls have been investigated as a new organic ferroelectric material that can induce a bowl inversion by applying an electric field.[23]

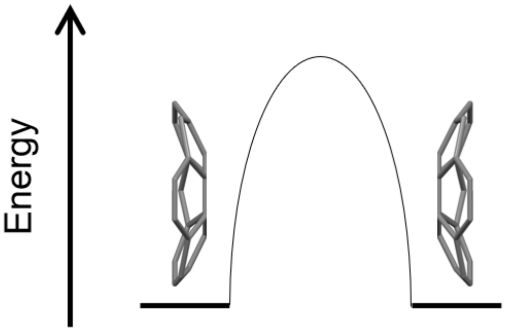

Figure 8. Schematic diagram of bowl-to-bowl inversion behavior of sumanene.

Section 3. C70 fragment buckybowls

While C60 fragment buckybowls have been well studied, there are still limited reports on C70[24] fragment buckybowls. Unlike C60, C70 has an acene or pyrene structure, which shows beneficial photophysical properties. Therefore, C70 fragment buckybowls are an attractive class of molecules that exhibit different photophysical properties than C60 fragment buckybowls and have potential applications as starting materials for synthesizing novel curved nanocarbons (Figure 9). It has been reported that compared to C60 fullerene derivatives, C70 derivatives show stronger optical absorption in the visible light region, which tends to improve the conversion efficiency of OPVs. Such changes can be expected for C70 fragment buckybowls.[25]

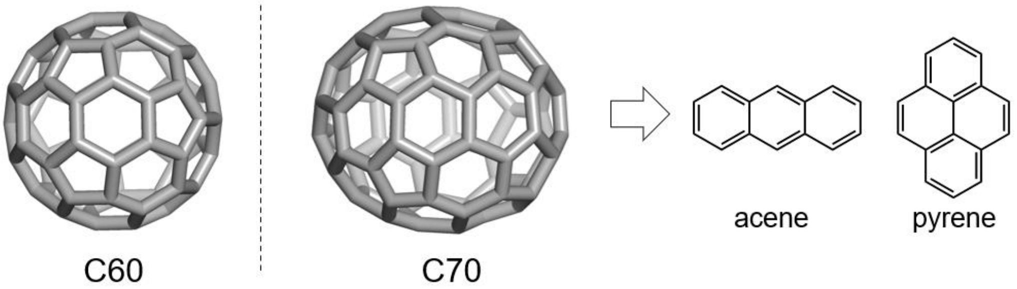

Figure 9. Structures of C60, C70, and substructures of C70.

Reported C70 substructure buckyballs are summarized in Figure 10.[26] Some of these molecules exhibit interesting properties. For example, the molecule synthesized in 2019 by Wu et al. is a stable anti-aromatic molecule, with the total number of π electrons in the periphery satisfying $16\pi = 4n\pi$.[26g] The molecule reported by Zhang et al. selectively co-crystallizes with C70, and this co-crystal exhibits high carrier mobility[26h]. Shinokubo et al. synthesized C70 fragment buckybowls containing both an indacenopyrene and a terylene subunits, exhibiting broad near-infrared absorption up to 1300 nm, even though they are stable closed-shell molecules composed of carbon and hydrogen.[26i] All these examples demonstrate that the C70 fragment buckybowls can be a fascinating molecule with unique electronic properties.

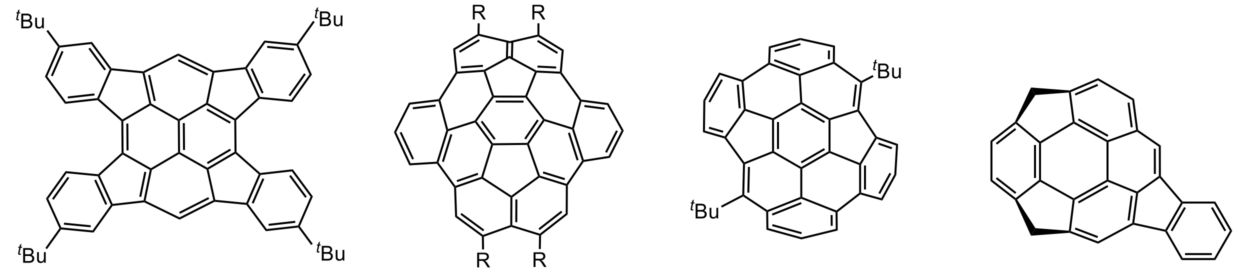

Scott et al. (2006) Wu et al. (2013) Müllen et al. (2016) Sakurai et al. (2017)

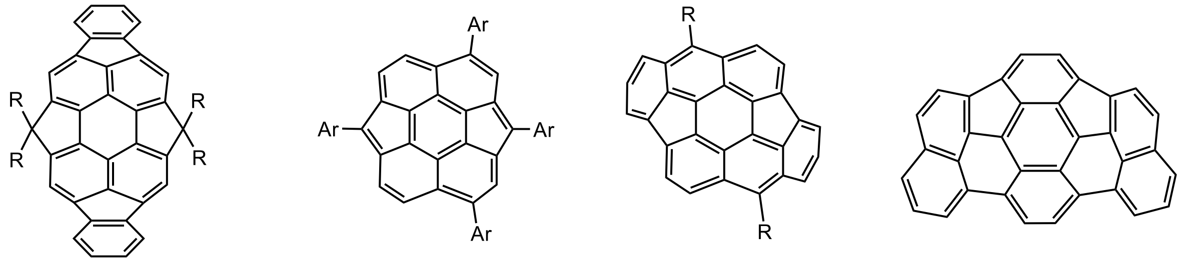

Lin et al. (2019) Wu et al. (2019) Zhang et al. (2020) Shinokubo et al. (2020)

Figure 10. Reported C70 fragment buckybowls.

Section 4. This work: Synthesis of Homosumanene and its Derivatives

The Author focused on one of the smallest the C70 fragment buckybowl, which includes a benzo[e]pyrene structure, and named it homosumanene as a buckybowl in which the five-membered ring of the sumanene skeleton has been homologated (Figure 11).

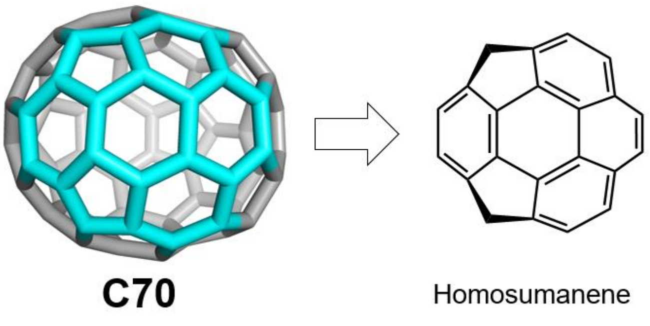

Figure 11. Structure of homosumanene.

Homosumanene is expected to have small bowl inversion energy due to its shallow bowl structure and optical properties derived from the benzopyrene backbone. It is also expected to develop stimulus responsiveness due to small bowl inversion energy derived from the shallow bowl structure and further chemical modification utilizing both aromatic and benzyl positions. Therefore, this doctoral dissertation was conducted to synthesize and characterize various C70 fragment buckybowls with homosumanene structures.

In Chapter 2, the author described the synthesis and properties of homosumanene and heterahomosumanenes using ring expansion reactions from sumanenone, and monocarbonylated sumanene derivatives.

In Chapter 3, the author described the acid-mediated ring-opening reaction of sumanenone involving C-C bond cleavage specific to the bowl molecule.

In Chapter 4, the author described the thermodynamic effects of the geometry of the platinum complexes on the concave and convex faces of the buckybowl ligand azahomosumanene.

In Chapter 5, the author described the unique reactivity of the homosumanene derivative toward oxidation reactions and the derivatization of the product, homosumanene *ortho*-quinone.

References

1. W. E. Barth, R. G. Lawton, *J. Am. Chem. Soc.*, **1966**, *88*, 380–381.

2. a) L. T. Scott, M. M. Hashemi, M. S. Bratcher, *J. Am. Chem. Soc.* **1992**, *114*, 1920–1921. b) A. Borchardt, A. Fuchicello, K. V. Kilway, K. K. Baldridge, J. S. Siegel, *J. Am. Chem. Soc.* **1992**, *114*, 1921–1923.

3. A. M. Butterfield, B. Gilomen and J. S. Siegel, *Org. Process Res. Dev.* **2012**, *16*, 664–676.

4. G. Mehta, S. R. Shah, K. Ravikumar, *J. Chem. Soc., Chem. Commun.* **1993**, 1006–1008.

5. H. Sakurai, T. Daiko, T. Hirao, *Science* **2003**, *301*, 1878.

6. a) https://www.tcichemicals.com/JP/ja/p/C2572 b) https://www.tcichemicals.com/JP/ja/p/S0888

7. a) Y.-T. Wu, J. S. Siegel, *Chem. Rev.* **2006**, *106*, 4843−4867. b) V. M. Tsefrikas, L. T. Scott, *Chem. Rev.* **2006**, *106*, 4868−4884. c) M. Saito, H. Shinokubo, H. Sakurai, *Mater. Chem. Front.* **2018**, *2*, 635−661.

8. L. T. Scott, E. A. Jackson, Q. Zhang, B. D. Steinberg, M. Bancu, B. Li, *J. Am. Chem. Soc.* **2012**, *134*, 107−110.

9. T. Amaya, T. Nakata, T. Hirao, *J. Am. Chem. Soc.* **2009**, *131*, 10810−10811.

10. H. Nakazawa, Y, Uetake, Y. Yakiyama, H. Sakurai, *Synlett* **2022**, *in press.*

11. K. Kawasumi, Q. Zhang, Y. Segawa, L. T. Scott, K. Itami, *Nat. Chem.* **2013**, *5*, 739−744.

12. K. Kato, Y. Segawa, L. T. Scott, K. Itami, *Angew. Chem. Int. Ed.* **2018**, *57*, 1337−1341.

13. L. T. Scott, H. E. Bronstein, D. V. Preda, R. B. M. Ansems, M. S. Bratcher, S. Hagen, *Pure Appl. Chem.* **1999**, *71*, 209−219.

14. C. Bingel, *Chem. Ber.* **1993**, *126*, 1957−1959.

15. M. Maggini, G. Scorrano, M. Plato, *J. Am. Chem. Soc.* **1993**, *115*, 9798–9799.

16. J. C. Hummelen, B. W. Knight, F. LePeq, F. Wudl, J. Yao, C. L. Wilkins, *J. Org. Chem.* **1995**, *60*, 532–538.

17. S. Mebs, M. Weber, P. Luger, B. M. Schmidt, H. Sakurai, S. Higashibayashi, S. Onogi, D. Lentz, *Org. Biomol. Chem.* **2012**, *10*, 2218–2222.

18. Q. Tan, P. Kaewmati, S. Higashibayashi, M. Kawano, Y. Yakiyama, H. Sakurai. *Bull. Chem. Soc. Jpn.* **2018**, *91*, 531–537.

19. H. Sakurai, T. Daiko, H. Sakane, T. Amaya, T. Hirao, *J. Am. Chem. Soc.* **2005**, *127*, 11580–11581.

20. T. Amaya, S. Seki, T. Moriuchi, K. Nakamoto, T. Nakata, H. Sakane, A. Saeki, S. Tagawa, T. Hirao, *J. Am. Chem. Soc.* **2009**, *131*, 408−409.

21. a) L. T. Scott, M. M. Hashemi, M. S. Bratcher, *J. Am. Chem. Soc.* **1992**, *114*, 1920–1921. b) T. J. Seiders, K. K. Baldridge, G. H. Grube, J. S. Siegel, *J. Am. Chem. Soc.* **2001**, *123*, 517–525. c) T. Hayama, K. K. Baldridge, Y.-T. Wu, A. Linden, J. S. Siegel, *J. Am. Chem. Soc.* **2008**, *130*, 1583–1591. d) T. Amaya, H. Sakane, T. Muneishi, T. Hirao, *Chem. Commun.* **2008**, 765–767. e) B. B. Shrestha, S. Karanjit, S. Higashibayashi, H. Sakurai, *Pure Appl. Chem.* **2014**, *86*, 747–753.

22. a) R. Jaafar, C. A. Pignedoli, G. Bussi, K. Ait-Mansour, O. Groening, T. Amaya, T. Hirao, R. Fasel, P. Ruffieux, *J. Am. Chem. Soc.* **2014**, *136*, 13666–13671. b) S. Fujii, M. Ziatdinov, S. Higashibayashi, H. Sakurai, M. Kiguchi, *J. Am. Chem. Soc.* **2016**, *138*, 12142–12149.

23. S. Furukawa, J. Wu, M. Koyama, K. Hayashi, N. Hoshino, T. Takeda, Y. Suzuki, J. Kawamata, M. Saito, T. Akutagawa, *Nat. Commun.* **2021**, *12*, 768.

24. R. Taylor, J. P. Hare, A. K. Abdul-Sada, H. W. Kroto, *J. Chem. Soc. Chem. Commun.* **1990**, *20*, 1423–1425.

25. M. M. Wienk, J. M. Kroon, W. J. H. Verhees, J. Knol, J. C. Hummelen, P. A. van Hal, R. A. J. Janssen, *Angew. Chem. Int. Ed.* **2003**, 42, 3371–3375.

26. a) H. A. Wegner, H. Reisch, K. Rauch, A. Demeter, K. A. Zachariasse, A. de Meijere, L. T. Scott, *J. Org. Chem.* **2006**, *71*, 9080−9087. b) T.-C. Wu, M.-K. Chen, Y.-W. Lee, M.-Y. Kuo, Y.-T. Wu, *Angew. Chem. Int. Ed.* **2013**, *52*, 1289−1293. c) M.-K. Chen, H.-J. Hsin, T.-C. Wu, B.-Y. Kang, Y.-W. Lee, M.-Y. Kuo, Y.-T. Wu, *Chem. Eur. J.* **2014**, *20*, 598−608. d) J. Liu, S. Osella, J. Ma, R. Berger, D. Beljonne, D. Scollmeyer, X. Feng, K. Müllen, *J. Am. Chem. Soc.* **2016**, *138*, 8364−8367. e) S. Hishikawa, Y. Okabe, R. Tsuruoka, S. Higashibayashi, H. Ohtsu, M. Kawano, Y. Yakiyama, H. Sakurai, *Chem. Lett.* **2017**, *46*, 1556–1559. f) J.-L. Huang, B. Rao, M. P. Kumar, H.-F. Lu, I. Chao, C.-H. Lin, *Org. Lett.* **2019**, *21*, 2504−2508. g) Y. Zou, W. Zeng, T. Y. Gopalakrishna, Y. Han, Q. Jiang, J. Wu, *J. Am. Chem. Soc.* **2019**, *141*, 7266−7270. h) G. Gao, M. Chen, J. Roberts, M. Feng, C. Xiao, G. Zhang, S. Parkin, C. Risko, L. Zhang, *J. Am. Chem. Soc.* **2020**, *142*, 2460−2470. i) Y. Tanaka, N. Fukui, H. Shinokubo, *Nat. Commun.* **2020**, *11*, 3873.

Chapter 2. Synthesis of the C70 Fragment Buckybowl, Homosumanene, and Heterahomosumanenes via Ring-Expansion Reactions from Sumanenone

Section 1. Introduction

As demonstrated in the synthetic chemistry of pharmaceutical and natural compounds, ring expansion reactions are widely accepted as a useful synthetic strategy for building unique ring structures.[1] Similarly, this strategy has been used to synthesize polycyclic aromatic hydrocarbons and curved π-conjugated molecules. For example, Miao et al. reported the synthesis of negatively curved saddle-shaped nanographene molecules by ring expansion strategy from bisanthraquinone (Figure 12).[2] Shao et al. also reported the synthesis of donor-acceptor macrocyclic molecules by ring-opening and re-cyclization of tricalcogenasumanenes.[3]

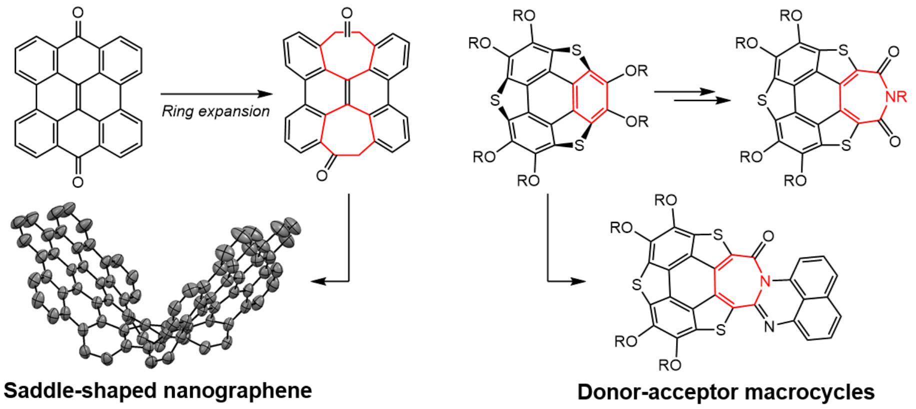

Saddle-shaped nanographene

Donor-acceptor macrocycles

Figure 12. Synthesis of unique π-conjugated molecules via ring expansion reactions.

Sakurai et al. constructed a C70 fragment buckybowl skeleton from sumanene **1** by Wagner-Meerwein rearrangement and Pd-catalyzed cyclization (Scheme 2a), demonstrating the utility of a ring expansion strategy.[4] In general, constructing distorted curved aromatic frameworks from planar molecules is difficult. In contrast, the author conceived that once a highly distorted buckybowl is prepared and used as a starting material, a moderately distorted structure can be constructed energetically favorably using reactions that can reduce the curved strain. In this point of view, **1** and its derivatives are attractive starting materials because their synthetic methods have already been established. Since these compounds have reactive benzylic sp^3 carbons, a wide range of derivatization is possible.[5] For this reason, the author considered sumanene to be one of the ideal building blocks for realizing a ring expansion strategy. In other words, several ring expansion reactions, such as the Büchner-Curtius-Schlotterbeck reaction, Baeyer-Villiger oxidation, and Beckmann rearrangement from **1**, could yield novel buckybowls, including heterobuckybbowls with carbon, oxygen, and nitrogen atoms introduced. In this chapter, three buckybowls, homosumanene, lactone, and lactam forms, were synthesized via ring expansion reactions using sumanenone **2** as a common starting material. Their crystal structures were investigated (Scheme 2b). The nitrogen-doped analogue of homosumanene, azahomosumanene, was also synthesized to investigate the change in electronic perturbation due to the introduction of nitrogen. Furthermore, the author attempted to synthesize transition metal complexes using azahomosumanene as a ligand.

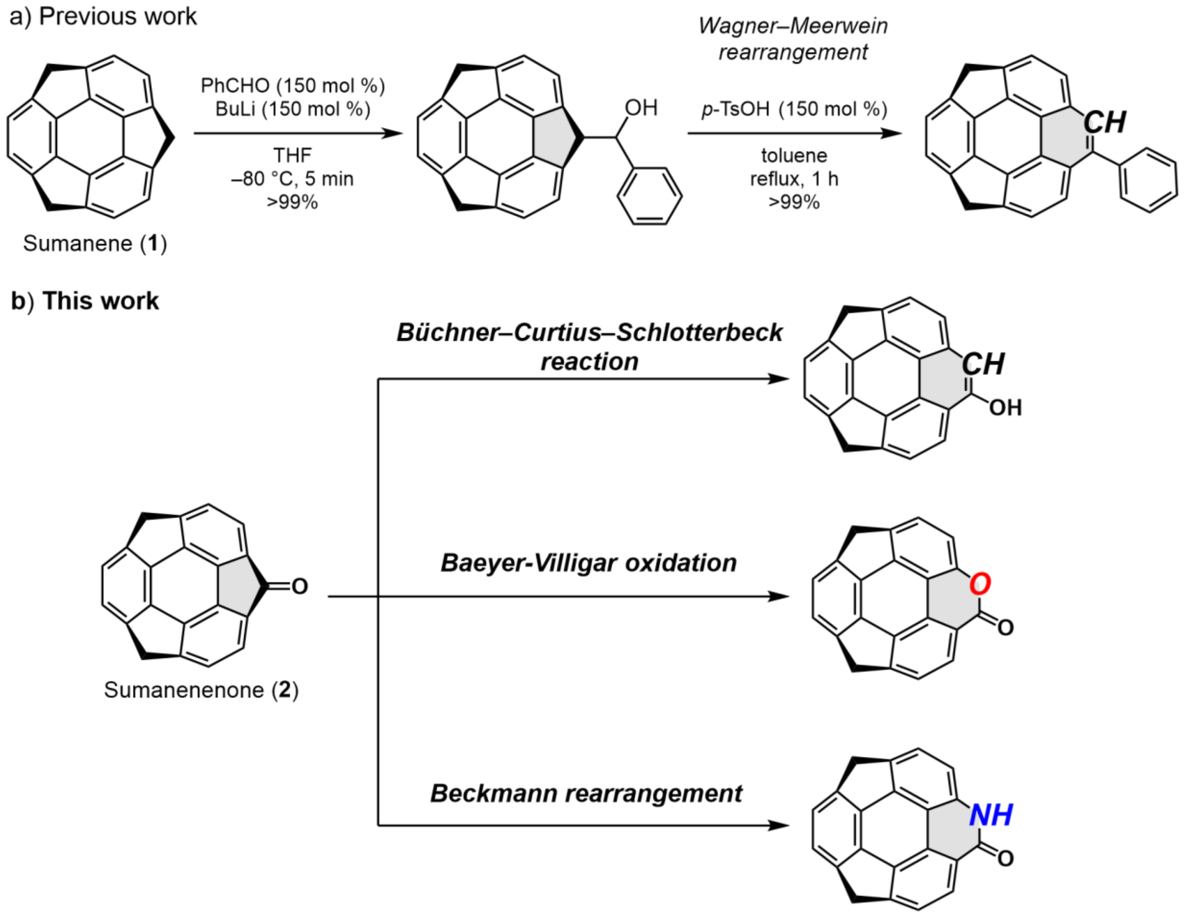

Scheme 2. Schematics of a) the previous work and b) this work.

Section 2. Synthesis and crystal structures of homosumanene and heterahomosumanenes

First, sumanenone **2** was selected as a highly distorted starting material for various ring-expansion reactions. Amaya and Hirao et al. reported the synthesis of **2**. In this approach, benzylic oxidation of **1** with excess amounts of *t*-BuOOH and phosphotungstic acid (200 wt%) affords the **2** in 51% yield, as a mixture with unreacted starting material, di, and tri-ketone (Scheme 3).[6]

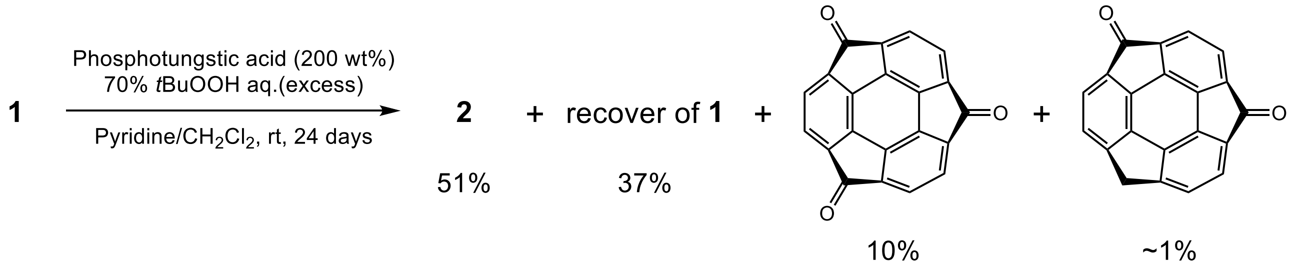

Scheme 3. The previous approach to synthesize sumanenone **2**.

To improve the selectivity and yield of **2** and to make the purification process easier, I first attempted to develop a selective mono-oxidation of the benzyl position of **1**. For selective benzylic mono-oxidation, sumanenyl monoanion was generated by adding 120 mol% *n*-butyl lithium to **1** at −80 °C, and monohydroxysumanene **1’** was synthesized by adding Davis oxaziridine (150 mol%). Subsequent oxidation with manganese oxide gave **2** in 89% yield from **1** (Scheme 4).

The synthesis of pristine homosumanene **4** was investigated via the Büchner–Curtius–Schlotterbeck reaction of **2**. By treating **2** with trimethylsilyl diazomethane in the presence of BF_3·Et_2O, the ring-expanded phenolic intermediate **3**’ was obtained. However **3**’ was found to be unstable under air and difficult to isolate; the crude mixture containing **3**’ was directly treated with trifluoromethanesulfonic anhydride (Tf_2O) to yield the corresponding triflate **3** in 58% yield. Pd-catalyzed reductive hydrogenation of **3** provided **4** in 92% yield (Scheme 4).

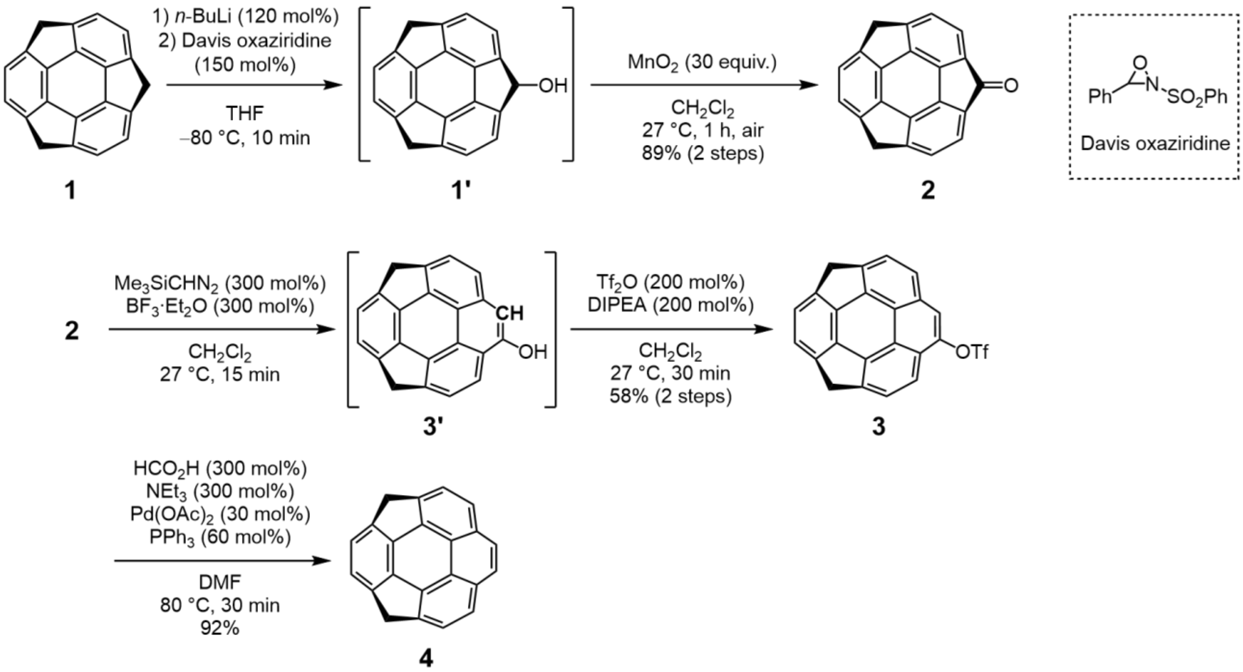

Scheme 4. Synthesis of sumanenone **2** and pristine homosumanene **4**.

The Baeyer-Villiger oxidation of **2** was then examined (Table 1). The reaction was carried out using *m*-chloroperoxybenzoic acid, and the corresponding lactone **5** was obtained in 25% yield, and the starting material was also recovered (entry 1). Next, the author attempted to improve the yield by activating the carbonyl group with various Brønsted acids. As a result, the yield was improved by about 10%, but the highest yield was only 39% (entries 2-4). The reaction conditions using Sc(OTf)$_3$ or TfOH reported by Kozuki et al. were applied, and **5** was obtained in moderate yields of 44% and 58%, respectively (entries 5 and 6).[7] Under these conditions, a small amount of starting material was recovered. The reaction time was extended in entry 7. However, the yield was not improved due to the decomposition of both starting material and **5**. Considering these results, entry 6 was selected as the optimized condition. The long reaction time may induce the decomposition due to oxidation of the internal carbon and the two reactive benzyl positions.

Table 1. Optimization of reaction conditions for Baeyer–Villiger oxidation of **2**.

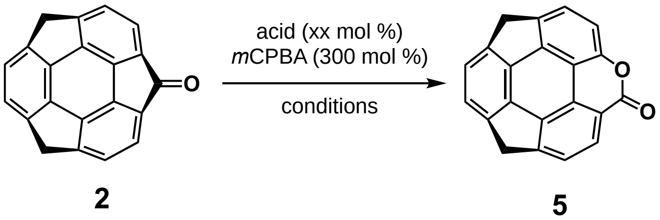

entry	acid	solvent	temperature (°C)	time (h)	yield (%)
1	none	CH_2Cl_2	40	46	25
2	$TsOH{\cdot}H_2O$ (300 mol %)	$CHCl_3$	50	37	34
3	H_2SO_4 (300 mol %)	CH_2Cl_2	27	1	0
4	CF_3CO_2H	$(CH_2Cl)_2$	70	24	39
5	$Sc(OTf)_3$ (10 mol %)	CH_2Cl_2	27	28	44
6	TfOH (300 mol %)	CH_2Cl_2	27	0.25	58
7	TfOH (300 mol %)	CH_2Cl_2	27	3.5	11

Next, the Beckmann rearrangement reaction was studied (Scheme 5). The oxime **6’** was obtained quantitatively by the reaction with $NH_2OH{\cdot}HCl$ (200 mol %) on **2** in a MeOH/pyridine mixture. The desired lactam **6** was obtained in 64% yield by heating **6’** in polyphosphoric acid. The nitrogen atom doped **6** was considered a promising precursor for azahomosumanene, a nitrogen-doped analogue of homosumanene **4**. Chlorination of **6** by heating in a solvent amount of $POCl_3$ afforded the corresponding chloroazahomosumanene **7** in 82% yield. **7** is highly reactive despite the highly reactive imidoyl chloride structure, **7** could be purified by silica gel chromatography due to stabilization by aromaticity at the pyridine moiety. Subsequent Suzuki coupling reaction with phenylboronic acid catalyzed by $PdCl_2(amphos)_2$ afforded phenylazahomosumanene **8** in 90% yield. Palladium-catalyzed dehydrogenation gave pristine azahomosumanene **9** in 90% yield. **9** was found to be more unstable than **7** and **8**, probably because **9** does not have any substituent at the α-position of the nitrogen atom. For example, **9** gradually decomposes in the air or deuterated chloroform.

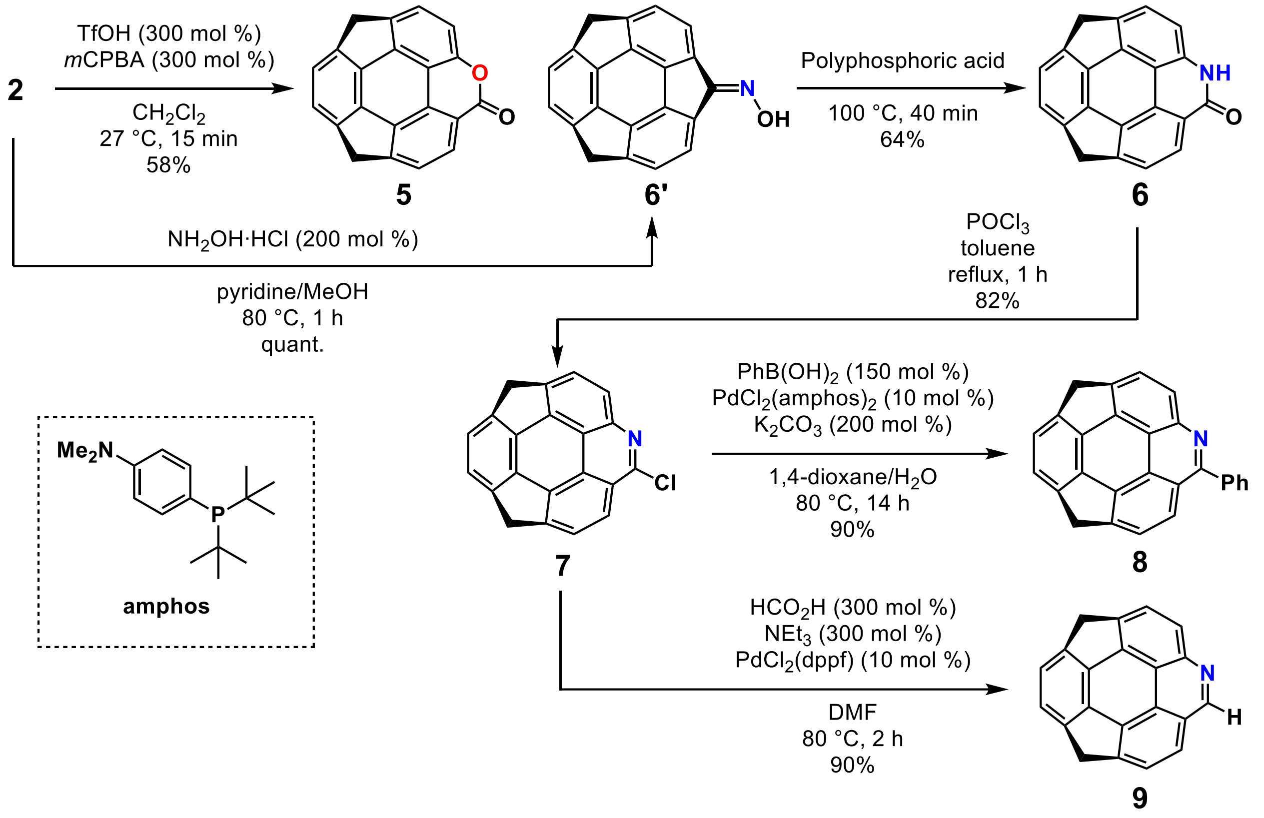

Scheme 5. Synthesis of lactone **5**, lactam **6**, and azahomosumanene **7** and its derivatives **8–9**.

Single crystals of **5** and **6** were obtained by slow evaporation from CH_2Cl_2 and the vapor diffusion method under PhCl/*n*-hexane conditions, respectively. The bowl structure was evaluated using the POAV angle (*p*-orbital axis vector pyriamidalization angle) φ^8 and the bowl depth calculated from the distance between peripheral carbon atoms and the plane containing the central six-membered ring (Figure 13).

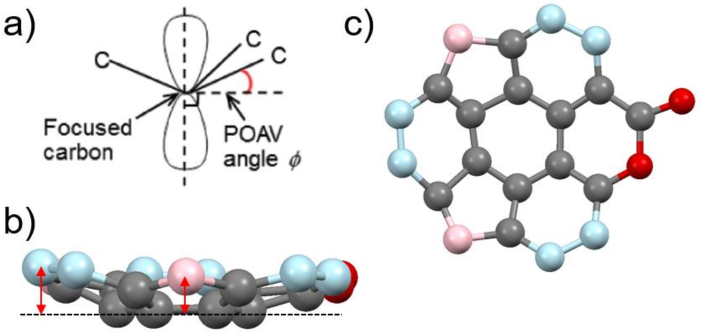

Figure 13. Definition (a) POAV angles (φ), and (b) bowl depth. The double-headed arrow shows the perpendicular line from the from the peripheral carbons to the bottom hexagonal ring. In b) and c), pink-colored atoms are benzylic, and blue-colored ones are aromatic carbons.

Single crystal X-ray structures of **5** and **6** revealed that the cyclopentanone ring with the carbonyl group of **2** was expanded to a six-membered ring with a lactone or lactam structure (Figures 14 and 15). Some buckybowls, due to their steric bowl structure, lose their planar symmetry and have a chirality called bowl chirality.[9] For example, the C_3-symmetric molecule, trimethylsumanene[10] and triazasumanene[11] have bowl chirality (Figure 16). Single crystals of **5** were obtained as a mixture of two stereoisomers due to bowl chirality because there was a disorder between the isomers due to the orientation of the concave and convex faces. The occupancy of those atoms assigned to them was 58:42 (Figure 14b); in the case of **6**, there were two crystallographically independent units, in which the two conformational isomers were found to exist in 55:45 and 38:62 occupancies (Figures 15b).

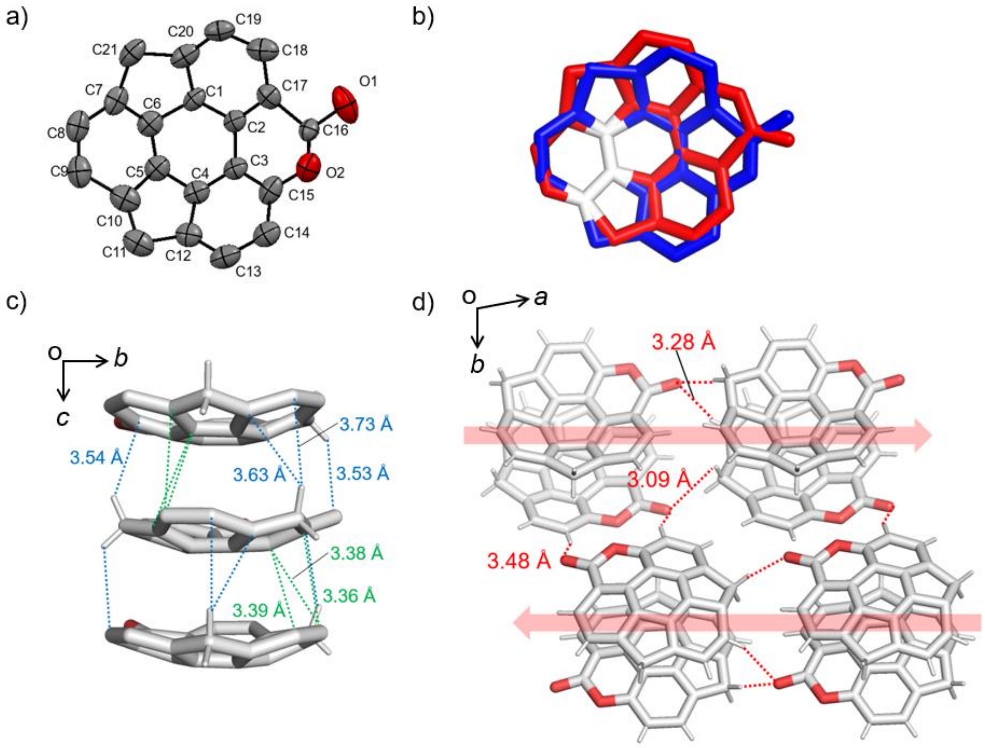

Figure 14. Crystal structure of **5**. a) Thermal displacement ellipsoid plot of **5** in the crystal structure at 50% probability. b) Colorized structure by chemical occupancy; red part: blue part = 0.58:0.42, white part = 1.0. c) CH···π (blue dotted line) and π···π (green dotted line) interactions in a stacking column. d) Intercolumnar CH···O (red dotted line) interaction in each column. Red arrows show the dipole direction. Only one stereoisomer (occ. 42%) is shown in a), c) and d). Hydrogen atoms that are not engaged in any interactions are omitted for clarity.

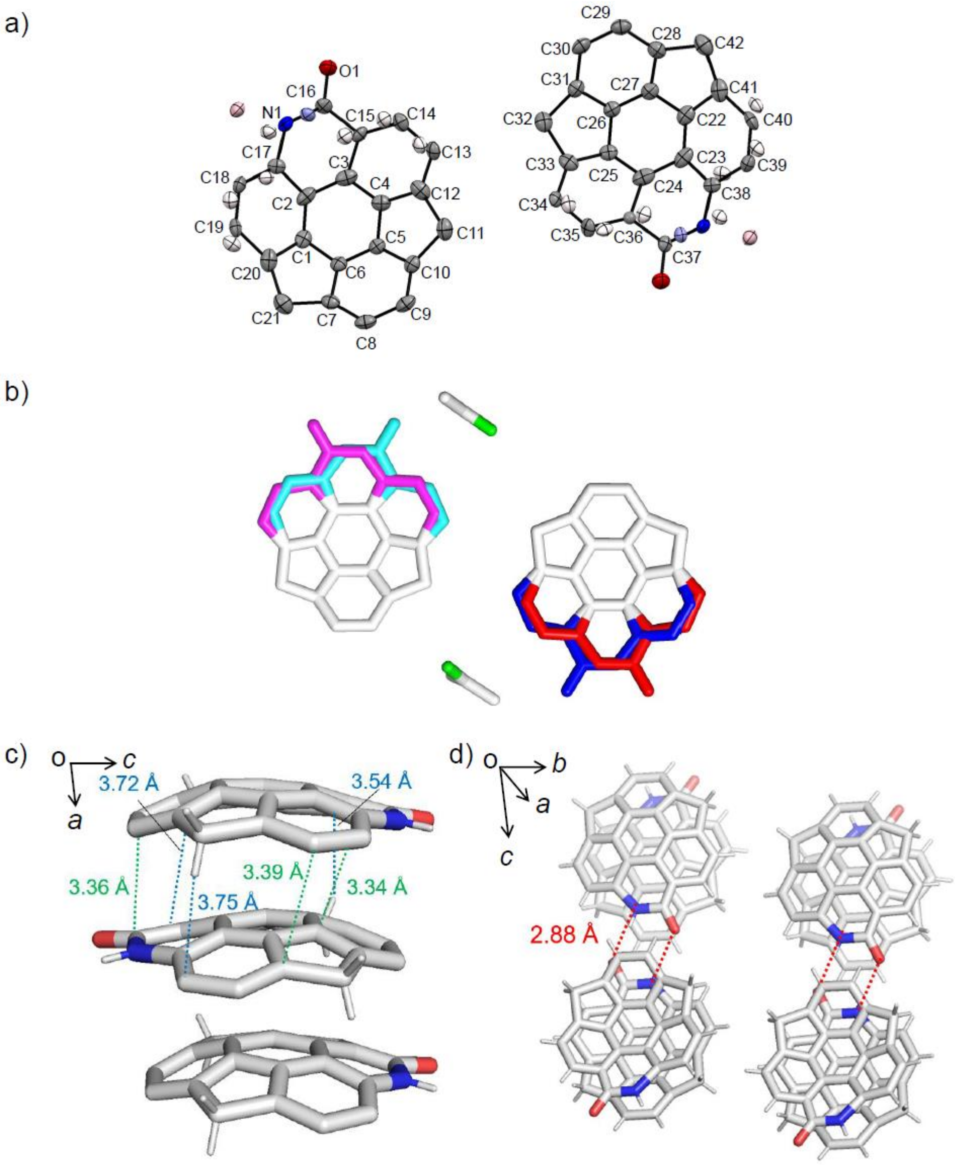

Figure 15. Crystal structure of **6**. a) Thermal displacement ellipsoid plot of **6** in the crystal structure at 50% probability. b) Colorized structure by chemical occupancy; red part: blue part = 0.55:0.45, magenta part: cyan part = 0.38:0.62 and white part = 1.0. c) CH⋯π (blue dotted line) and π⋯π (green dotted line) interactions in a stacking column. d) NH⋯O hydrogen bonds (red dotted line) in each column. Only one stereoisomer is shown in c) and d). Solvent and hydrogen atoms that are not engaged in any interactions are omitted for clarity.

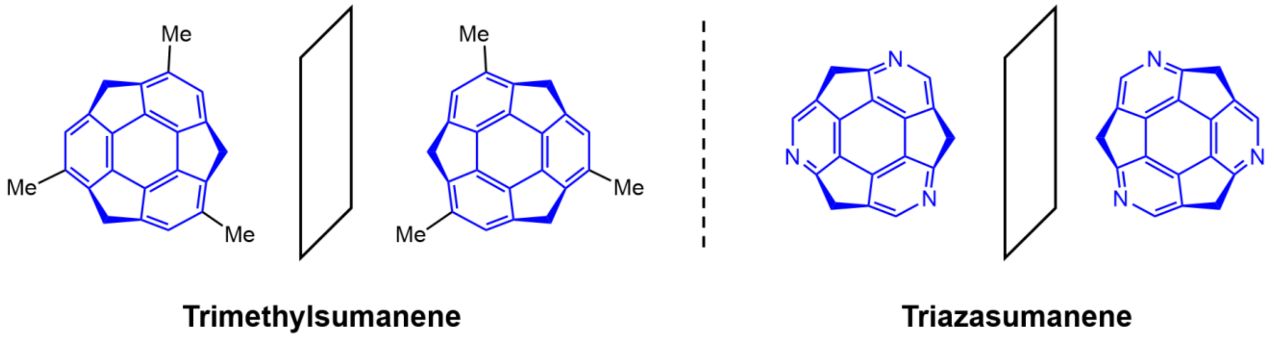

Figure 16. Examples of buckybowls with bowl charity.

The minimum and maximum POAV angles for **5** were 5.1° and 8.9°, respectively, whereas for **6** the minimum and maximum values were 4.6° and 7.0°, respectively. These are smaller than the 8.9° of sumanene **1**[12], indicating shallower bowl structures of them. Comparing **5** and **6**, **5** has a slightly deeper bowl structure than **6**, because the C=O bond lengths of lactone (C15–O2: 1.36 Å and C16–O2: 1.42 Å) are larger than those of lactam (C17–N1: 1.40 Å and C16–N1: 1.36 Å). Each packing structure well reflected the features of the curved molecular skeleton of **5** and **6**. **5** formed a one-dimensional columnar structure stacked along the *c*-axis despite the shallow bowl depth (Figure 14c). These stacking structures were formed by CH···π (Figure 14c, blue dotted line) and π···π interactions (green dotted line) with respective distances of 3.54–3.73 Å and 3.36–3.39 Å, respectively. Within the column, each lactone moiety was oriented in the same direction and aligned with the dipole moment along the *a*-axis (Figure 14d, red arrow). Furthermore, each column alignment was inverted along the *b*-axis to cancel the dipole moment in the whole crystal packing. Each of these columns was formed by three types of CH···O interactions, with C···O distances ranging from 3.09–3.48 Å (Figure 14d, red dotted line). **6** also formed a one-dimensional columnar structure stacked along the *a*-axis (Figure 15c). The packing structure of **6** is similar to that of **5**, forming π···π (Figure 15c, green dotted line) and CH···π interactions (Figure 15c blue dotted line) with distances of 3.34–3.39 Å and 3.54–3.75 Å, respectively. Intercolumnar interactions were also observed in the case of **6**, with NH···O distance of 2.88 Å (Fig. 15d, red dotted line). This is shorter than the sum of the van der Waals radii of the hydrogen and oxygen atoms, which may be due to the formation of hydrogen bonds.

Section 3. NMR, IR, UV−Vis Absorption, and fluorescence spectroscopy

The ^{1}H NMR signals for the *endo* and *exo* benzylic protons of **1** are observed as two doublet signals with coupling constants of 18.3 Hz at 3.42 ppm and 4.71 ppm at 23 °C (Figure 17). This is because the rate of bowl inversion is slower than the NMR time scale.[13] On the other hand, two singlet signals are observed as benzylic proton's peaks at 4.26 and 4.33 ppm for **5** and 4.40 and 4.33 ppm for **6**, respectively. This suggests that the bowl inversion of these two molecules occurs quite fast.

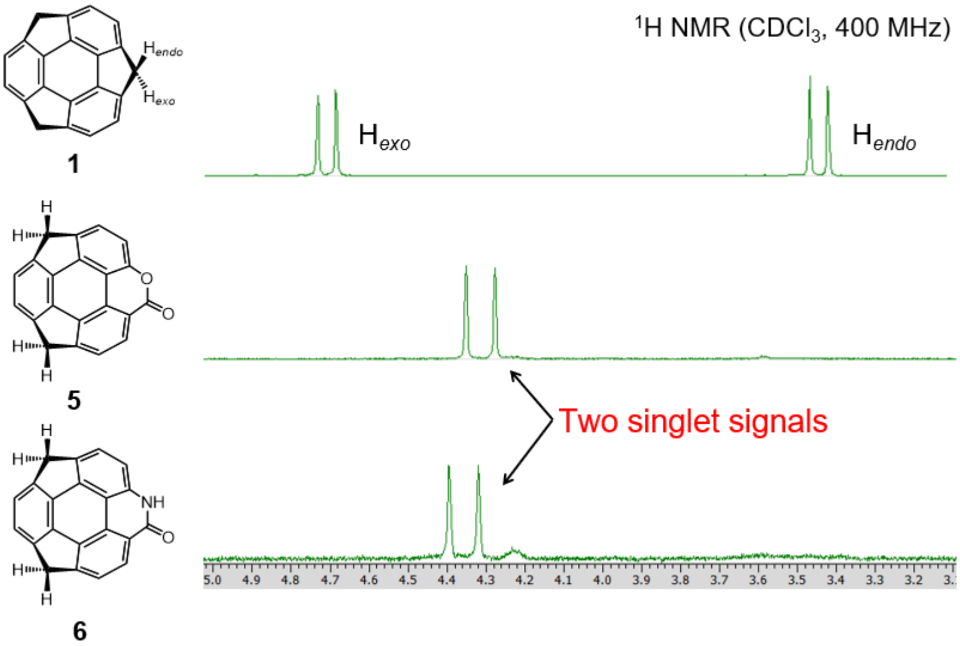

Figure 17. Magnification of ^{1}H NMR spectra of **1**, **5**, and **6** in $CDCl_3$ at 25 °C.

To evaluate these bowl inversion energies, variable-temperature NMR (VT-NMR) experiments were conducted. In the case of **5**, no doublet peaks or peak broadening due to the geminal coupling of the benzyl protons were observed at −90 °C in CD_2Cl_2 (Figure 18). This indicates that the bowl inversion energy of **5** is too small to be evaluated on the NMR time scale even at low temperatures. A similar experiment was attempted for **6**, but its low solubility in organic solvents at low temperatures prevented measurement, and it was difficult to observe the substrate peaks at temperatures lower than −70 °C. Therefore, experimental evaluation of the bowl inversion behavior by VT-NMR could not be performed (Figure 19). Instead, the bowl inversion energies were evaluated by DFT calculations at the B3LYP/cc-PVTZ level and were calculated to be 3.9 kcal/mol for **5** and 2.8 kcal/mol for **6** (Table 2). These values are smaller than the experimental values of 20.3 kcal/mol[14] of **1** and those of corannulene[15]. These results are consistent with the VT-NMR results.

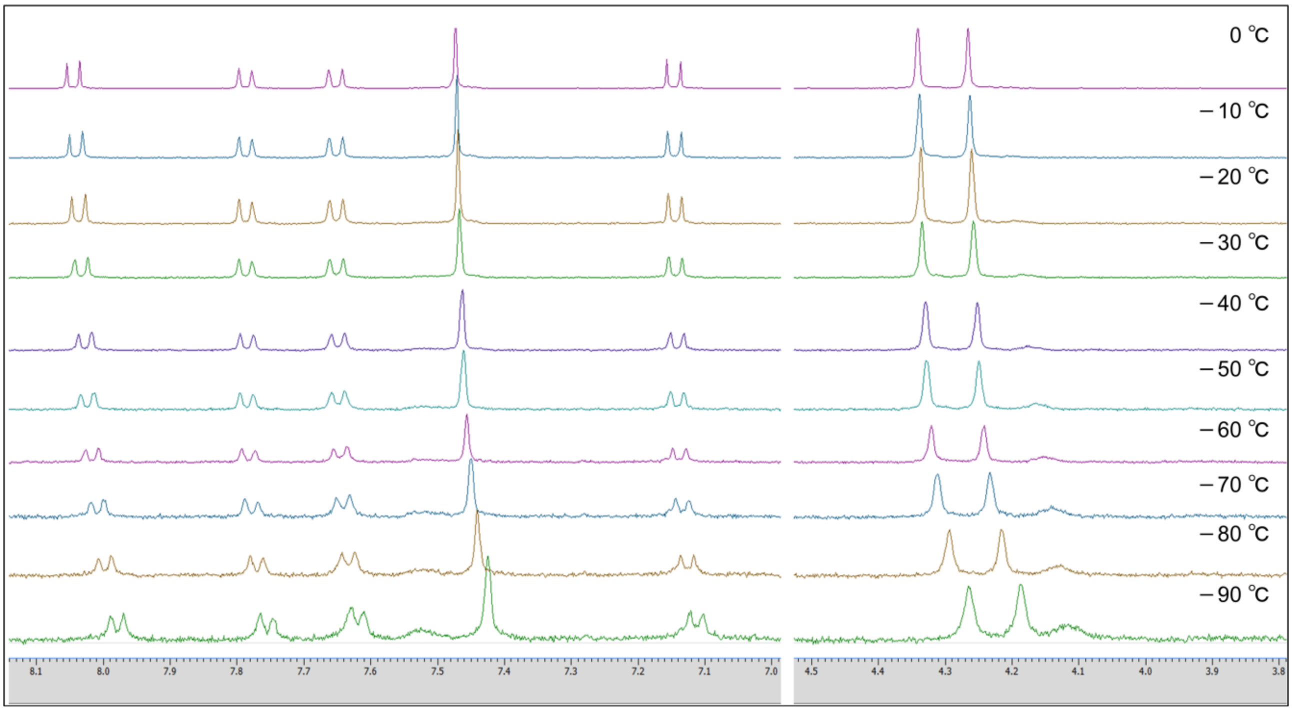

Figure 18. VT-NMR experiment of **5** in CD_2Cl_2.

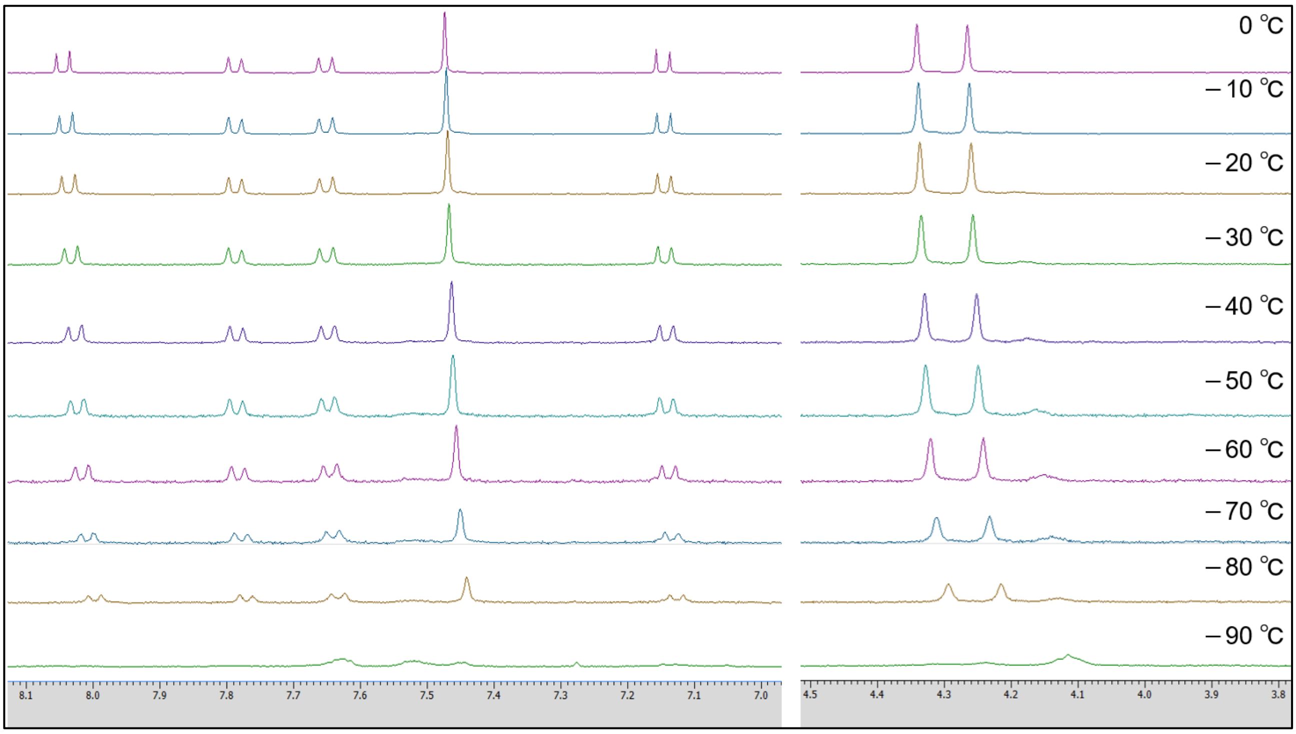

Figure 19. VT-NMR experiment of **6** in CD_2Cl_2.

Table 2. Comparison of bowl inversion energy.

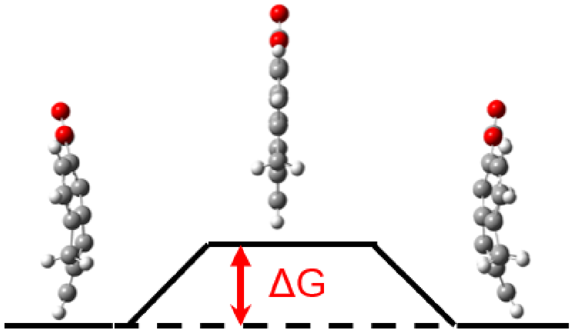

	ΔG_{calc} (kcal/mol)	ΔG_{exp} (kcal/mol)
1	18.8	20.3
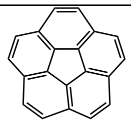 corannulene	10.4	10-11
5	3.9	-
6	2.8	-

To obtain more information into the contribution of the bowl structure on the heterocycles, the IR spectra of **5** and **6** were compared with their planer substructures, 3,4-benzocoumarin **5a**[16] and 6-phenanthridone **6a**[17] (Table 3). The absorption bands for the C=O stretching vibrations of **5** and **6** were shifted from their planar analogues to the lower frequency side by 12 $\mathrm{cm^{-1}}$ and 10 $\mathrm{cm^{-1}}$, respectively. These results reflect the delocalization of π-electrons on the carbonyl group, resulting in lower bond orders. Because no synthesis of triphenylene derivatives with ester **5b** or lactam **6b** moieties has been reported so far, the difference of electronic states between planar and bowl-shaped π-conjugated systems was compared by using optimized structures obtained by DFT calculations at the B3LYP/cc-PVTZ level. The dihedral angles of **5** and **6**, including the O1-C1-C2 plane, were larger than the corresponding planar substructures **5a**[18] and **6a**[19]. This suggests that the *p*-orbital overlap of the carbonyl group and the aromatic carbon is insufficient due to the bowl structure. On the other hand, the calculated value of **6** is almost the same as that of **6b**. This may be due to the shallow bowl structure of **6**, as shown by X-ray crystallographic analysis.

Table 3. Experimental and calculated values of C=O stretching band in FT-IR measurement and dihedral angle.[a] Calculated values are shown in parentheses.

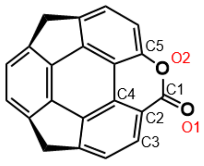

5

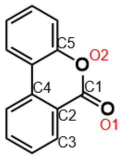

5a

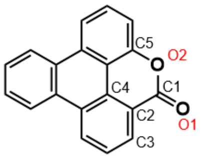

5b

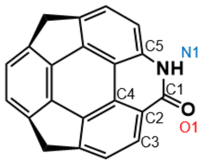

6

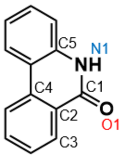

6a

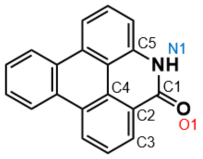

6b

Compound	**C=O stretching (cm^{-1})** ^{a}	**dihedral angle (°)** ^{a}
5	1724 (1816)	6.0 (7.9) (O1C1C2C4) 15.0 (14.9) (O1C1C2C3) 4.9 (2.2) (O1C1O2C5)
5a	1736	1.1 (O1C1C2C4) 0.2 (O1C1C2C3) 0.4 (O1C1O2C5)
5b	(1805)	(0) (O1C1C2C4) (0) (O1C1C2C3) (0) (O1C1O2C5)
6	1650 (1744)	6.9 (4.9) (O1C1C2C4) 12.8 (12.1) (O1C1C2C3) 1.0 (4.0) (O1C1N1C5)
6a	1660	0.1 (O1C1C2C4) 3.1 (O1C1C2C3) 1.8 (O1C1N1C5)
6b	(1745)	(0) (O1C1C2C4) (0) (O1C1C2C3) (0) (O1C1N1C5)

To understand the effect of the bowl structure and heterocyclic ring on the photophysical properties, UV-vis absorption and emission spectra were evaluated. First, **5** and **6** were compared with **1** (Figure 20). In the absorption spectra, the longest absorption bands were observed almost the same region, 273 nm for **5** and **6** and 278 nm for **1**, respectively. This indicates that there is almost no change in the π-conjugated system associated with the ring expansion reaction from a 5-membered ring to a 6-membered ring. In the emission spectrum, **5** shows almost no emission, while **6** shows slightly longer wavelength-shifted fluorescence compared to **1**. This is because the n-π* transition is forbidden in **5**, whereas the contribution of the enol structure, in which the lone pair on the nitrogen is conjugated with the carbonyl group, is larger in **6** than in **5**, and the n-π* transition is slightly allowed.

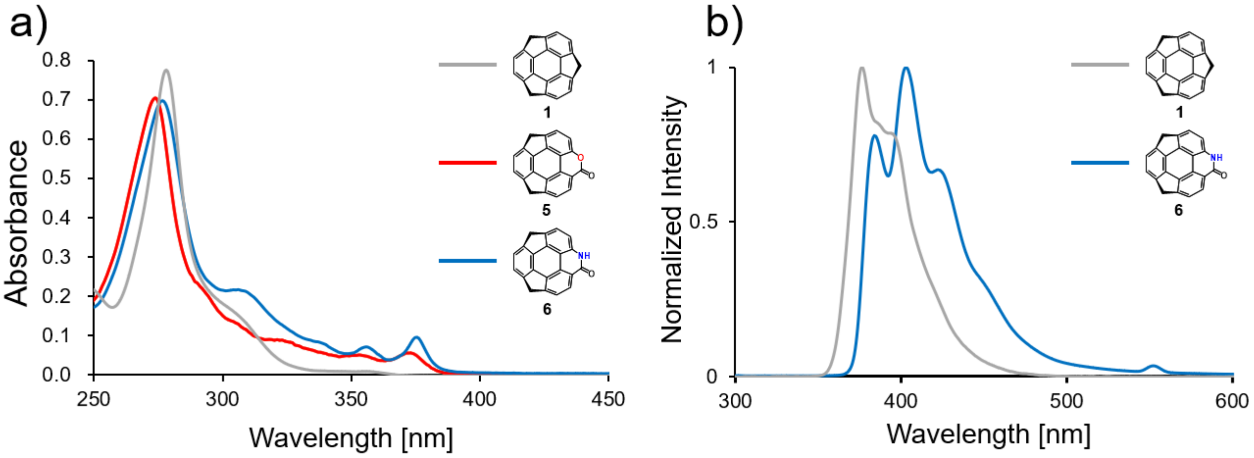

Figure 20. a) Absorption, and b) emission spectra of **1**, **5**, and **6** in CH_2Cl_2 (1.0×10^{-5} mol/L). Excitation wavelength: 273 nm for **1**; 278 nm for **6** (optical path length; 10 mm, quartz cell).

Next, the absorption and emission spectra of homosumanene **4** and its nitrogen-doped analogue azahomosumanene **9**, as well as benzo[e]pyrene **10** as a reference planar molecule to investigate the contribution of the bowl structure (Figure 21). Compared to **10**, the spectrum of **4** was observed to be slightly broadening. This may reflect the dynamic behavior in solution (i.e. bowl inversion behavior) and is because the absorption spectrum corresponds to the average of the electronic states of the various conformations. The nitrogen-doped **8** exhibits a broad absorption band up to 400 nm due to the stabilization of the LUMO level by electron-withdrawing sp^2 hybridized nitrogen atom, and narrowing of the HOMO-LUMO gap. The HOMO-LUMO gaps of **4** and **9** estimated from the absorption maxima are ΔE_{UV} = 3.60 eV (λ = 344 nm) and $\Delta \mathrm{E}_{\mathrm{UV}}$ = 3.35 eV (λ = 370 nm), respectively. The emission spectrum of **4** showed almost the same characteristics as the emission spectrum of **10** due to the similar π-conjugated system. A bathochromic shift of the emission band from 388 to 415 nm was also observed in the emission spectrum due to the doping of a nitrogen atom.

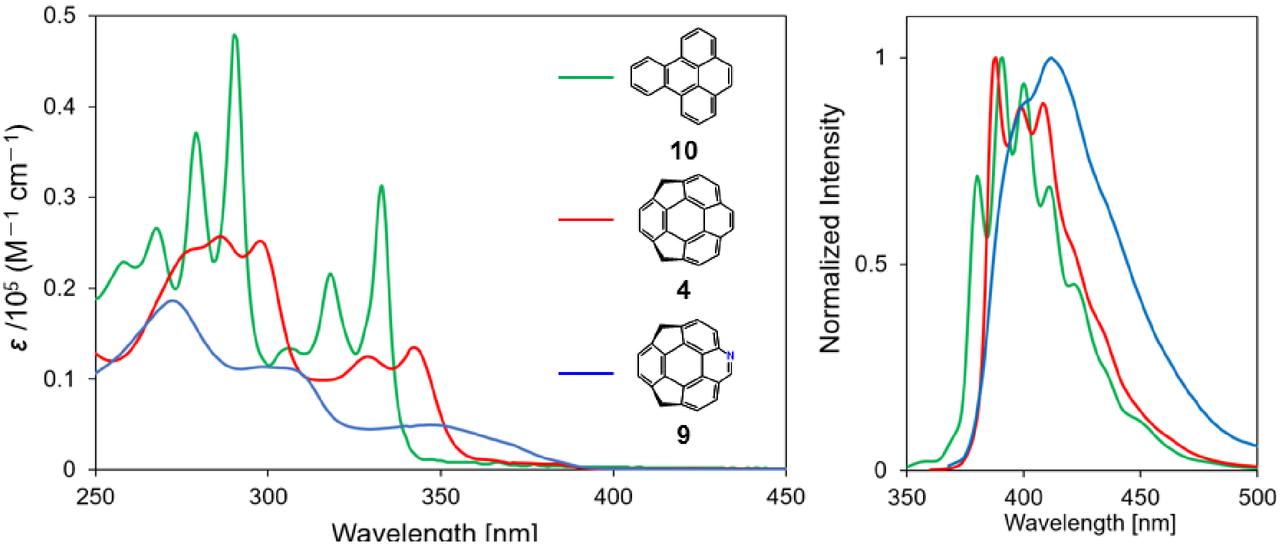

Figure 21. UV-vis absorption and emission spectra of **4**, **9**, and **10**. a) absorption spectra. b) emission spectra. All the samples were prepared as 1.0×10^{-5} mol/L in CH_2Cl_2. Excitation wavelength: 344 nm for **4**; 352 nm for **9**; 333 nm for **10**.

Cyclic voltammetry (CV) measurements were performed in MeCN with [^{n}Bu$_4$N][ClO$_4$] as the supporting electrolyte to learn about the HOMO and LUMO levels and redox behavior (Figure 22 and 23). On the reduction side, **4** exhibited a reversible redox wave ($E_p^{red} = -2.55$ V) and **9** exhibited an irreversible wave ($E_p^{red} = -2.05$ V). The lower value of the E_p^{red} for **9** than for **4** reflects the lower LUMO level due to the introduction of nitrogen atoms. On the other hand, both **4** and **9** exhibited irreversible redox waves on the oxidation side (**4**: $E_p^{ox} = 1.03$ V, **9**: $E_p^{ox} = 1.15$ V). The irreversible peaks hampered to determine the accurate information on the HOMO-LUMO gap from electrochemical measurements, the HOMO-LUMO energy difference was estimated from the onset potentials of the oxidation and reduction peaks. The HOMO-LUMO energy gaps were estimated to be $\Delta E_{CV} = 3.40$ eV for **4** and 3.05 eV for **9**, which is mostly consistent with the HOMO-LUMO energy gaps estimated from UV-vis measurements (Table 4).

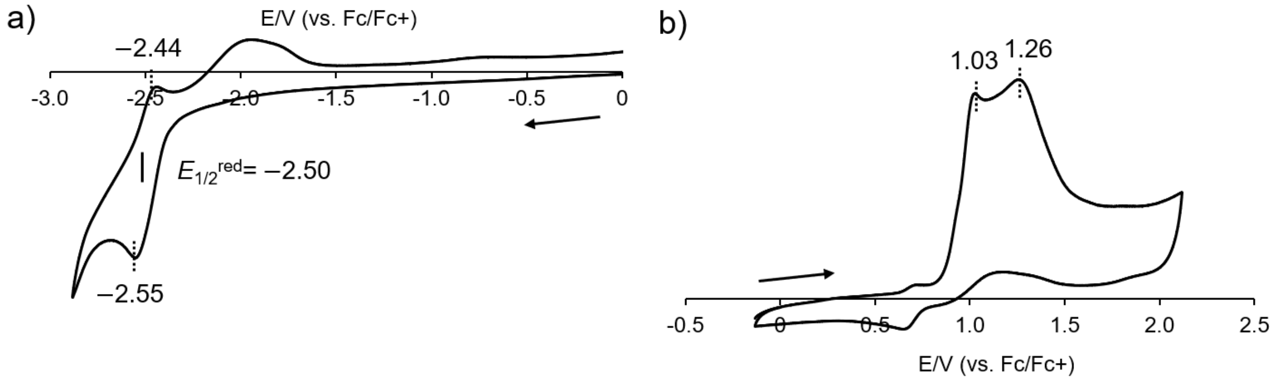

Figure 22. Cyclic voltammogram of **4**. a) reduction side. b) oxidation side.

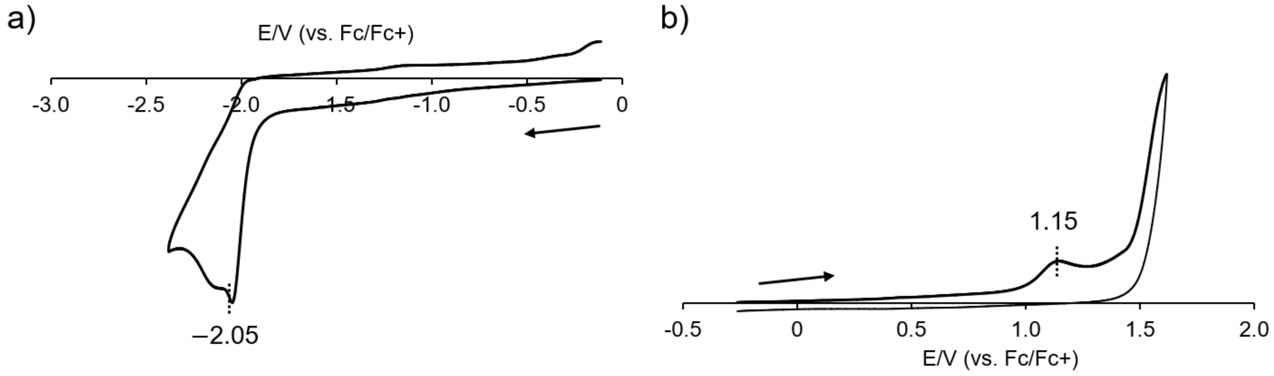

Figure 23. Cyclic voltammogram of **9**. a) reduction side. b) oxidation side.

Table 4. Electrochemical and photochemical analyses for HOMO–LUMO gap of **4** and **9**.

Compound	**ΔE_{UV} / eV**	**$E_{\mathrm{p}}^{\mathrm{red}}$ / V [a,b]**	**$E_{\mathrm{p}}^{\mathrm{ox}}$ / V [a,b]**	**ΔE_{CV} / eV [c]**
4	3.60	−2.55 (−2.44)	1.03 (0.96)	3.40
9	3.35	−2.05 (−2.00)	1.15 (1.05)	3.05

[a]The peak potential. [b]The onset potential in parentheses. [c]Calculated from the onset potential.

Section 4. Synthesis and properties of platinum complexes bearing azahomosumanene as a ligand

Azahomosumanene has a coordinative nitrogen atom and the potential to be a buckybowl ligand. Azabuckybowl complex would be a unique molecule with both bowl- and transition metal-derived properties.[20] Phenylazahomosumanene **8** was chosen as a buckybowl ligand because of its stability due to the presence of a phenyl group at imine carbon. **8** and K_2PtCl_4 were refluxed in acetic acid and ligand exchange with acetylacetone to afford the mononuclear Pt(II) complex **11** (Scheme 6).

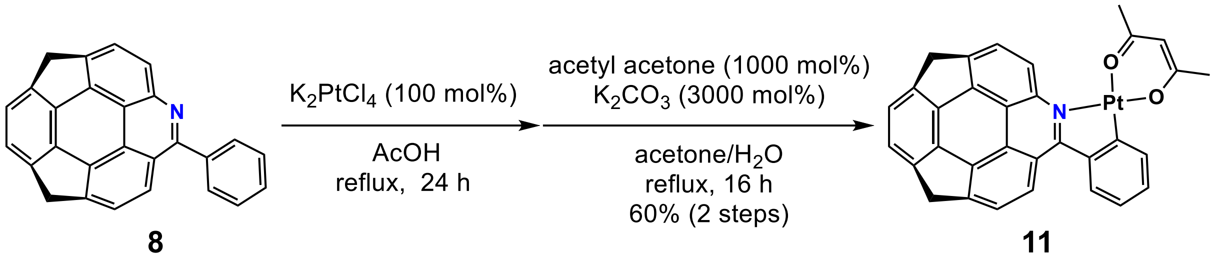

Scheme 6. Synthesis of platinum complex **11**.

Single crystals of **11** were obtained by the vapor diffusion method from $CHCl_3$/*n*-pentane. The single crystal X-ray diffraction analysis showed that **11** has a tetracoordinate square-planar structure. The minimum POAV angle of **11** is 4.0° (C3) and the maximum is 7.2° (C5), indicating that the bowl structure is retained (Table 5). The bond length between the ligand and the platinum atom are Pt-C1 = 1.961 Å, Pt-N1 = 2.048, Pt-O1 = 2.138 Å, and Pt-O2 = 2.085 Å, respectively. These value are similar to reported Pt(II)(2-phenylpyridyl)(acac) complex.[21]

Table 5. Thermal displacement plots of **11** at 50% probability, POAV angle, and bowl depth. Hydrogen atoms are omitted for clarity.

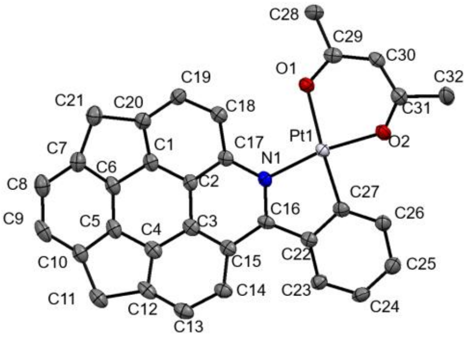

Molecule	POAV angle φ (°)		Bowl depth (Å)			
			Benzylic		Aromatic	
11	C1	5.3			C8	0.84
	C2	5.1	C11	0.63	C9	0.85
	C3	4.0	C22	0.66	C13	0.85
	C4	6.4			C14	0.77
	C5	7.2			C16	0.29
	C6	6.7			C18	0.60
					C19	0.70
					N1	0.33

As for the packing structure, the **11** formed a dimer-like unit structure with the concave/convex faces of the bowls facing each other due to the CH···π (blue dotted lines) and π···π interactions (green dotted lines), and these were stacked in a stair-like manner (Figure 24a). To obtain more quantitative information on the non-covalent interactions, electron density analysis was performed by the quantum theory of atoms-in-molecules (QTAIM) method[22] using a dimer unit of **11** as a model structure (Figure 24b). The coordinates for C, N, O, and Pt were obtained from the X-ray structural analysis, and the coordinates of hydrogens were optimized by fixing the coordinates of the other elements by DFT calculations at the B3LYP/Def2-SVP level. In addition, considering long-range corrections, the electron density was calculated by performing SCF calculations at the CAM-B3LYP-D3/def2-SVP level on the optimized coordinates. As a result, a bond path and the corresponding bond critical point (BCP) were observed between the benzylic hydrogen atom and the peripheral aromatic carbon. The electron density [$\rho_{\mathrm{BCP}}(\mathrm{r})$] at this BCP is 1.849 e Å^{-3}, which corresponds to the CH···π interaction (Figure 8b). Bond paths and BCPs were observed between the internal sp^2 carbon to the homosumanene moiety corresponding to the π···π interaction and the aromatic carbon of the phenyl group, but the ρ_{BCP}(r) at these points were two orders of magnitude lower than the CH···π interaction (0.045 and 0.036 e Å^{-3}). These calculations indicate that the packing structure is mainly controlled by the CH···π interaction. The Laplacian [$\nabla^2\rho_{\mathrm{BCP}}(r)$] of the electron density in each BCP was positive. The bond paths and BCPs between the Pt center and the internal aromatic carbon of the azahomosumanene moiety suggest the presence of an intermolecular Pt···π interaction (0.058 e Å^{-3}).

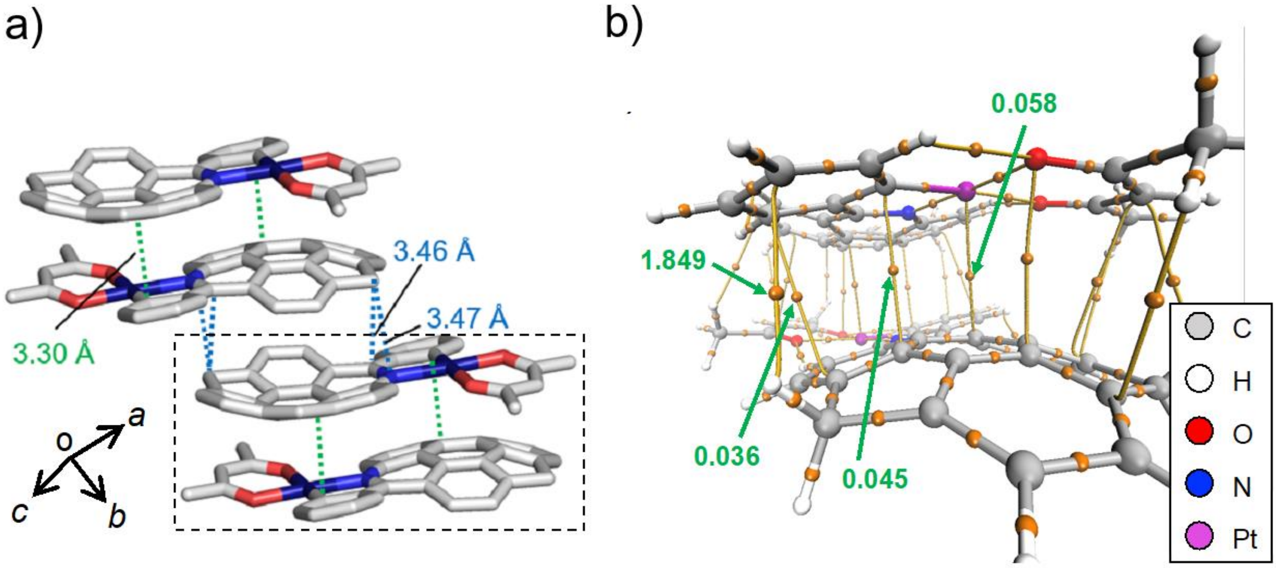

Figure 24. a) Crystal packing structures of **11**. Hydrogen atoms are omitted for clarity. b) QTAIM analysis of **11**. The bond paths (yellow line) and bond critical points (orange), and electron density (e Å^{-3}) at the bond critical points were shown.

Absorption and emission spectra measurements were performed to understand the photochemical properties (Figure 25a). In the absorption spectrum, the absorption bands around 440 nm and 482 nm were attributed mainly to the π-π* transition of the azahomosumanene moiety by TD-DFT calculations (Figure 25b). For the emission spectrum at room temperature (298 K), **11** exhibits a broad emission (absolute quantum yield Φ_{PL} = 0.8%) in the red to near-infrared region (620-850 nm), with a relatively large Stokes shift of 366 nm. Emission spectroscopy at 77 K showed that **11** exhibits red emission in a low-temperature matrix (diethyl ether/ethanol/toluene = 2:1:1), and the emission spectrum of **11** shows a distinct vibrational structure. Further time-resolved emission spectroscopic analysis revealed that the emission lifetime of **11** at 77 K is 3.9 μs, indicating that this emission component is mainly due to phosphorescence (Figures 26a and b). In addition, the emission spectra before and after bubbling oxygen gas at 298 K showed that quick quenching, suggesting that this luminescence is due to room temperature phosphorescence from the T_1 state, typical of platinum(II) complexes (Fig. 26d).[23]

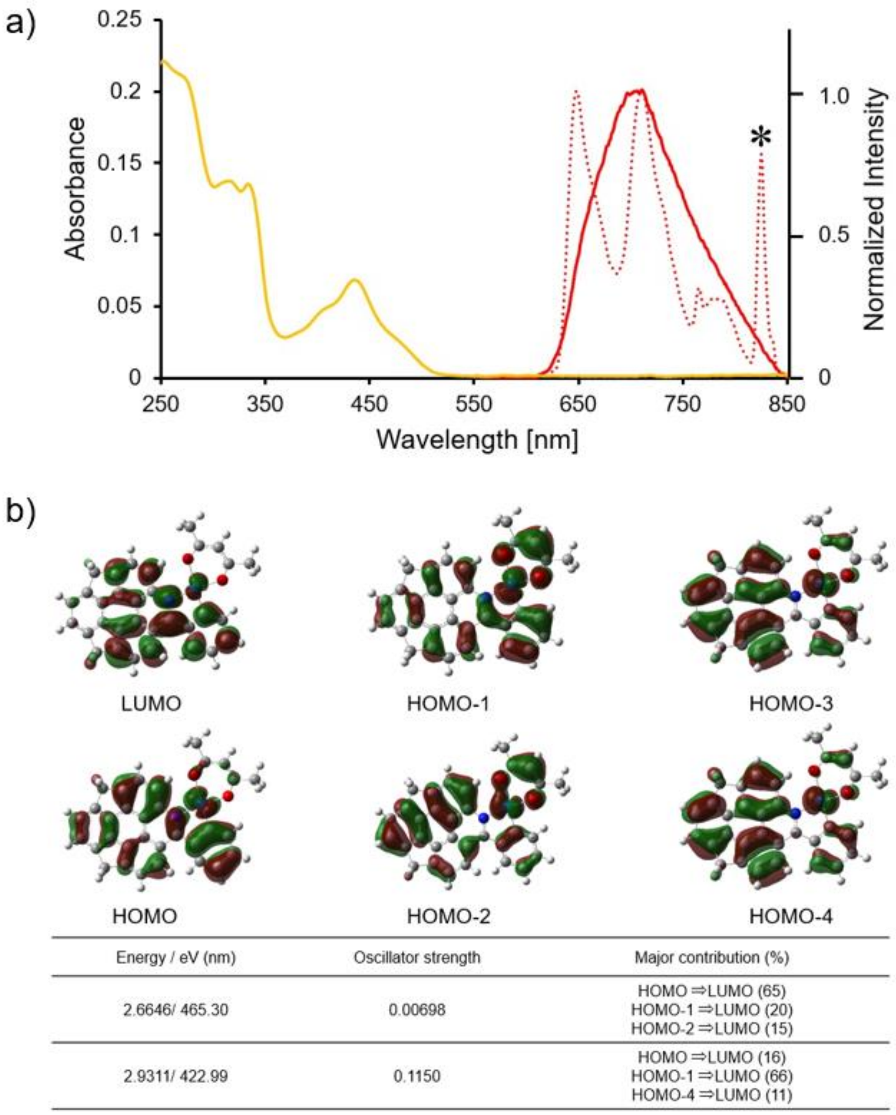

Energy / eV (nm)	Oscillator strength	Major contribution (%)
2.6646/ 465.30	0.00698	HOMO ⇒LUMO (65) HOMO-1 ⇒LUMO (20) HOMO-2 ⇒LUMO (15)
2.9311/ 422.99	0.1150	HOMO ⇒LUMO (16) HOMO-1 ⇒LUMO (66) HOMO-4 ⇒LUMO (11)

Figure 25. a) Spectroscopic data of **11**. UV-vis absorption spectrum at 298 K (yellow solid line, 1.0 × 10^{-5} mol/L in CH_2Cl_2), normalized emission spectra at 298 K (red solid line, 1.0 × 10^{-5} mol/L in CH_2Cl_2) and 77 K (red dotted line, 5.0 × 10^{-4} mol/L in diethyl ether/ethanol/toluene = 2:1:1) of **11**. Excitation wavelength: 438 nm. *A peak derived from stray light of the second order diffraction of the excitation light. b) Calculated orbital surface, energy, oscillator strength, and the major contribution of calculated transition for **11**.

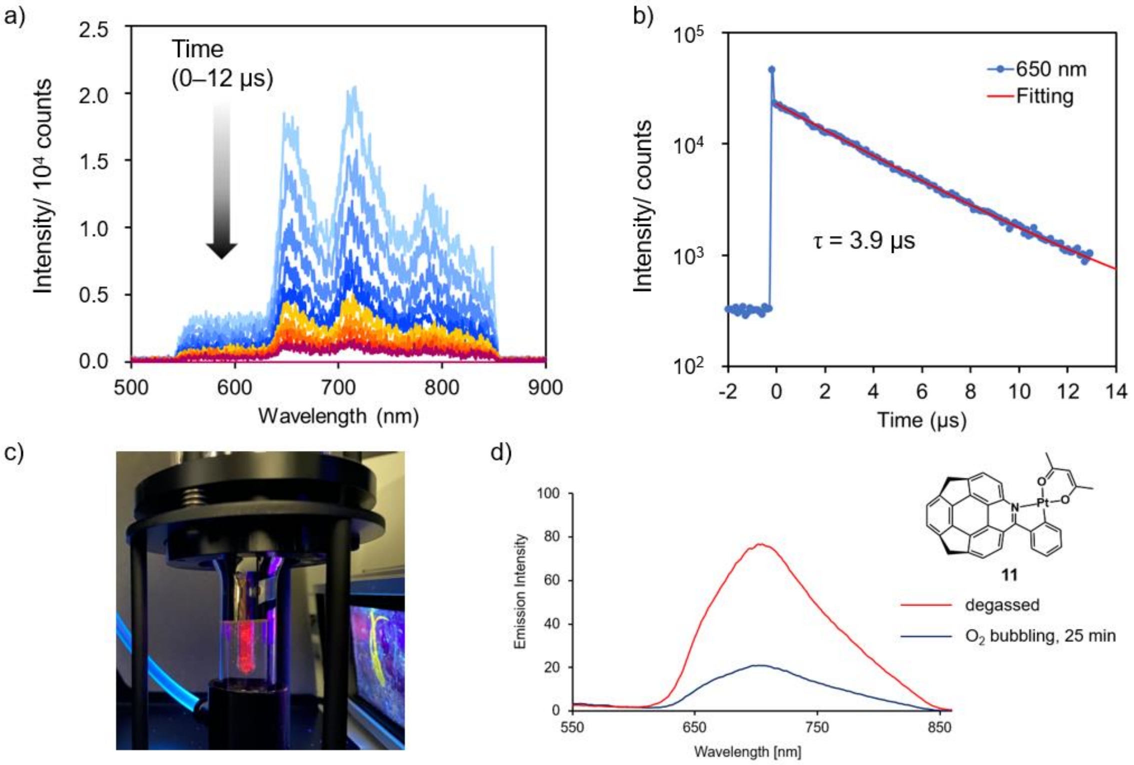

Figure 26. Time-resolved emission spectroscopy of **11** in a cold matrix (λ_{ex} = 355 nm, 77 K) (a, b, and c). a) Variation with time of the emission spectrum. b) A time course plot of the decay of the phosphorescence intensity at 650 nm. The red solid line is the least-means-square fitting with two exponential functions. The lifetime was shown in the inset. c) A picture of luminescence of **11** in a cold matrix (λ_{ex} = 365 nm, 77 K). d) Emission spectra of **11** before (red line) and after O_2 bubbling (blue line) in CH_2Cl_2 at 298 K.

Section 5. Summary

The smallest C70 fragment buckybowl, homosumanene **4** and heterahomosumanenes **5**, **6** were synthesized from a common starting material, sumanenone **2**, by three different ring-opening reactions (Büchner-Curtius-Schlotterbeck reaction, Baeyer-Villiger oxidation, and Beckmann rearrangement). These results demonstrate the usefulness of the synthetic strategy of synthesizing novel buckybowls by ring expansion reactions from a highly distorted buckybowl. Single crystal X-ray analysis revealed that lactone **5** and lactam **6** have a shallower bowl depth than **1** and form stacking structures in the crystalline state. **4**, **5**, and **6** have two more reactive benzyl positions, and thus are versatile precursors for further functionalization. Furthermore, azahomosumanene **9**, a nitrogen-doped analogue of **4**, and its derivatives **7** and **8** have reduced LUMO levels and HOMO-LUMO gaps compared to homosumanene. Focusing on the coordinative nitrogen atom of azahomosumanene, a cyclometalated platinum complex **11** with an azabuckybowl that exhibits room temperature phosphorescence was synthesized, indicating that azahomosumanene is also applicable as a ligand.

Experimental section

Instruments

All manipulations of moisture or air-sensitive compounds were performed by standard Schlenk techniques in anhydrous solvents under nitrogen atmosphere using flame-dried glasswares. Reactions were conducted in an EYELA PPS-2511 personal organic synthesizer with an aluminum heat brock as a heat source or an EYELA PSL-181low-temperaturere bath. Analytical thin-layer chromatography (TLC) was performed on pre-coated silica-gel aluminum sheets (Merck silica gel 60 F254, Cat. No. 1.05554.0001). Column chromatography was conducted on a YAMAZEN automated flash chromatography system that consists of an AI-580S and a Parallel Frac FR-360 using silica-gel (Kanto Chemical Co., Inc. Silica Gel 60 N (spherical, neutral)). Preparative thin-layer chromatography (PTLC) was prepared using Wako Wakogel B-5F. Recycling preparative high-performance liquid chromatography (HPLC) was performed by a LC-908W (Japan Analytical Industry Co., Ltd.) with high-resolution gel permeation chromatography (GPC) column (Japan Analytical Industry Co., Ltd., JAIGEL-1H and 2H) with $CHCl_3$ as an eluent. ^{1}H NMR (400 MHz), ^{13}C NMR (100 MHz), and ^{19}F NMR (373 MHz) spectra were measured on a JEOL JNM-ECZS400 spectrometer at room temperature. Chloroform-d_1 ($CDCl_3$), dichloromethane-d_2 (CD_2Cl_2), and dimethylsulfoxide-d_6 (DMSO-d_6) were used as a solvent for NMR measurements. Chemical shifts (δ) for ^{1}H NMR were given in parts per million (ppm) with coupling constants (J) in hertz (Hz) after correction by setting those of residual solvent to 7.24 ppm ($CHCl_3$), 5.32 ppm (CH_2Cl_2), and 2.50 ppm (DMSO-d_6). Chemical shifts (δ) for ^{13}C{^{1}H} NMR were given in parts per million (ppm) with coupling constants (J) in hertz (Hz) after correction by setting those of solvent to 77.0 ppm ($CDCl_3$), 53.8 ppm (CD_2Cl_2), and 39.51 ppm (DMSO-d_6). Chemical shifts (δ) for ^{19}F NMR were given in parts per million (ppm) after correction by setting that of hexafluorobenzene to –162.9 ppm. Melting points were determined on an Optimelt MPA100 automated melting point apparatus (Stanford Research Systems, Inc.), and expressed without correction. High-resolution mass spectroscopy (HRMS) measurements were conducted on a JEOL JMS-700 double-focusing mass spectrometer using electron impact (EI) or fast atom bombardment (FAB) ionization mode. Elemental analysis was performed on JM10 (J-SCIENCE LAB Co, Ltd.) organic elemental analyzer. Infrared (IR) absorption spectra were measured by KBr pellet method or attenuated total reflection (ATR) method on a JASCO FT/IR-4100 Fourier transform IR spectrometer equipped with a JASCO ATR PRO ONE single reflection ATR optical attachment and a diamond crystal plate. The absorption bands were given in wavenumber (cm^{-1}). Ultraviolet-visible (UV-vis) absorption spectroscopy was performed on a JASCO V-670 spectrophotometer by transmission mode. The absorption bands were given in wavelength (nm). Emission spectroscopy was performed on a JASCO FP6500 or FP-8300 spectrometer and expressed after normalization. The fluorescence bands were given in wavelength (nm). Absolute emission quantum yields were measured on a Quantaurus-QY Plus UV-NIR absolute PL quantum yield spectrometer (Hamamatsu Photonics K.K., C13534-21). The electrochemical analyses were performed on a BAS ALS Model 650DKMP electrochemical analyzer.

Chemicals

Unless otherwise noted, all reagents purchased from commercial suppliers were used without further purification.

Manganese(IV) oxide (MnO_2), [1,1′-Bis(diphenylphosphino)ferrocene]dichloropalladium(II) ($PdCl_2$(dppf)), bis[di-*tert*-butyl(*p*-dimethylaminophenyl)phosphino] dichloropalladium(II) ($PdCl_2(amphos)_2$), hydroxylamine hydrochloride ($NH_2OH \cdot HCl$), *n*-hexane, dichloromethane (CH_2Cl_2), ethyl acetate (EtOAc), methanol (MeOH), chloroform ($CHCl_3$), 1,2-dichloroethane ($(CH_2Cl)_2$), palladium acetate (($Pd(OAc)_2$), triphenylphosphine (PPh_3), N,N-diisopropylethylamine (DIPEA), potassium tetrachloroplatinate(II) (K_2PtCl_4), sulfuric acid (H_2SO_4) acetonitrile (MeCN, Infinity pure), and acetone were purchased from FUJIFILM Wako Pure Chemical Corporation.

Polyphosphoric acid, phosphorus(V) oxychloride ($POCl_3$) and *m*-chloroperoxybenzoic acid (*m*CPBA), and trifluoroacetic acid (CF_3CO_2H) were purchased from KISHIDA CHEMICAL Co., Ltd.

Triethylamine (NEt_3), pyridine, formic acid (HCO_2H), potassium carbonate (K_2CO_3), boron trifluoride diethyl etherate ($BF_3 \cdot Et_2O$), *n*-pentane, acetic acid (AcOH), ethanol (EtOH), and diethyl ether (Et_2O) were purchased from Nacalai Tesque, Inc.

Dichloromethane (CH_2Cl_2, dehydrated Super^2), toluene (dehydrated Super^2 Plus), tetrahydrofuran (THF, dehydrated (stabilized free) Super Plus), and 1,4-dioxane (dehydrated) were purchased from Kanto Chemical Co., Inc., and purified by passing through a Glass Contour Ultimate Solvent System (Nikko Hansen & Co. Ltd.) under nitrogen atmosphere.

Acetyl acetone was purchased from Kanto Chemical Co., Inc.

N,*N*-Dimethylformamide (DMF, super dehydrated), *p*-toluenesulfonic acid monohydrate ($TsOH \cdot H_2O$), trifluoromethanesulfonic acid (TfOH), trimethylsilyl diazomethane (Me_3SiCHN_2) scandium(III) triflate ($Sc(OTf)_3$), and tetrabutylammonium perchlorate ($[^nBu_4N][ClO_4]$) were purchased from Tokyo Chemical Industry Co., Ltd.

Phenylboronic acid ($PhB(OH)_2$) trifluoromethanesulfonic anhydride (Tf_2O), benzo[*e*]pyrene **10**, and chlorobenzene (PhCl) were purchased from Sigma–Aldrich Japan Inc.

Sumanene **1**[13] and 3-phenyl-2-(phenylsulfonyl)oxaziridine[24] were prepared according to the literature.

Synthetic Procedure and Characterization Data.

***Sumanenone* 2**. To a solution of sumanene (100 mg, 0.379 mmol, 100 mol%) in dry THF (25 mL) was slowly added *n*-BuLi (2.60 mol/L in *n*-hexane, 0.175 mL, 0.455 mmol, 120mol%) at −80 °C. After stirring for 30 min at the same temperature, to the reaction mixture was added a solution of 3-phenyl-2-(phenylsulfonyl)oxaziridine (148 mg, 0.568 mmol, 150 mol%) in THF (3 mL) at −80 °C. After stirring for 5 min at the same temperature, to the reaction mixture was added saturated aqueous NH_4Cl solution (ca. 25 mL), and then the mixture was warmed up to room temperature. The resulting mixture was extracted with ethyl acetate (ca. 30 mL × 3). The organic extract was washed with brine (ca. 30 mL), and dried over Na_2SO_4. After filtration, the filtrate was concentrated under reduced pressure. The residue was dissolved in CH_2Cl_2 (50 mL), and to this was added MnO_2 (2.00 g, 23.0 mmol, 3030 mol%) at 27 °C. After the stirring for 3 h at the same temperature, the reaction mixture was filtered through a short pad of Celite®, and eluted with CH_2Cl_2 (ca. 200 mL). The filtrate was concentrated under reduced pressure. The residue was purified by silica gel chromatography (*n*-hexane/CH_2Cl_2 = 1:1 to 1:3) to give **2** (93.5 mg, 0.336 mmol, 89%) as a yellow solid; ^{1}H NMR ($CDCl_3$, 400 MHz) δ 7.25 (d, *J* = 7.3 Hz, 2H), 7.18 (s, 2H), 7.14 (d, *J* = 7.3 Hz, 2H), 4.71 (d, *J* = 19.7 Hz, 2H), 3.51 (d, *J* = 19.7 Hz, 2H); ^{13}C{^{1}H}NMR ($CDCl_3$, 100 MHz) δ 190.0 (1C), 156.1 (2C), 149.4 (2C), 148.9 (2C), 148.7 (2C), 148.1 (2C), 139.0 (2C), 124.9 (2C), 124.4 (2C), 124.1 (2C), 42.0 (2C). The chemical shifts were consistent with those reported in the literature.[6]

***Triflate* 3**. To a solution of **2** (13.0 mg, 46.8 µmol, 100 mol%) in dry CH_2Cl_2 (10 mL) was added $BF_3 \cdot Et_2O$ (36 µL, 0.14 mmol, 300 mol%) and Me_3SiCHN_2 (0.6 mol/L in *n*-hexane, 0.23 mL, 0.14 mmol, 300 mol%) at 0 °C, and then the mixture was warmed up to 27 °C. After the stirring for 1 h at the same temperature, the reaction mixture was filtered through a short pad of Celite®, and washed with CH_2Cl_2 (ca. 30 mL). After filtration, the filtrate was concentrated under reduced pressure. The residue was dissolved in CH_2Cl_2 (5 mL), and to this was added DIPEA (16 µL, 94 µmol, 200 mol%) and Tf_2O (16 µL, 94 µmol, 200 mol%) at 27 °C. After the stirring for 30 minutes at the same temperature, to the reaction mixture was added water (ca. 10 mL). The mixture was extracted with CH_2Cl_2 (ca. 10 mL × 3). The combined organic extract was washed with brine (ca. 10 mL), dried over Na_2SO_4. After filtration, the filtrate was concentrated under reduced pressure. The residue was purified by PTLC (*n*-hexane/CH_2Cl_2 = 2:1) to give **3** (11.5 mg, 27.1 µmol, 57.9%) as a pale yellow solid; R_f: 0.45 (*n*-hexane/CH_2Cl_2 = 2:1); Mp: 139 °C (dec.); ^{1}H NMR ($CDCl_3$, 400 MHz) δ 8.00 (d, *J* = 8.2 Hz, 1H), 7.97 (d, *J* = 8.2 Hz, 1H), 7.91 (d, *J* = 7.8 Hz, 1H), 7.86 (d, *J* = 7.8 Hz, 1H), 7.82 (s, 1H), 7.52 (s, 1H + 1H, two signals overlapped), 4.42 (s, 2H), 4.38 (s, 2H); ^{13}C{^{1}H}NMR ($CDCl_3$, 100 MHz) δ 146.1 (1C), 145.2 (1C), 144.7 (1C), 143.7 (1C), 143.6 (1C), 140.6 (1C), 140.4 (1C), 140.2 (1C), 129.5 (1C), 126.4 (1C), 124.88 (1C), 124.85 (1C), 124.6 (1C), 124.5 (1C), 124.39 (1C), 124.36 (1C), 124.30 (1C), 120.5 (1C), 118.8 (1C), 118.6 (1C), 117.3 (1C), 42.1 (1C + 1C, two signals overlapped); ^{19}F NMR ($CDCl_3$, 373 MHz) δ –162.9 (3F); HRMS (EI$^+$) *m*/*z*: [M]$^+$ Calcd for $C_{23}H_{11}F_3O_3S^+$ 424.3810; Found 424.0378; IR (diamond, cm^{-1}): 3038, 2914, 1421, 1398, 1215, 1143, 1039, 960, 882, 833, 787, 739, 612.

Homosumanene **4**. To the solution of **3** (10 mg, 24 µmol, 100 mol%), $Pd(OAc)_2$ (1.6 mg, 7.1 µmol, 30 mol%) and PPh_3 (3.7 mg, 14 µmol, 60 mol%) in dry DMF (1.0 mL) was added HCO_2H (2.7 µL, 71 µmol, 300 mol%) and NEt_3 (10.0 µL, 70.8 µmol, 300 mol%) at room temperature stirred for 30 min at 80 °C. After cooling to room temperature, to the reaction mixture was added water (ca. 5 mL). The mixture was extracted with CH_2Cl_2 (ca. 10 mL × 3). The combined organic extract was washed with water (ca. 10 mL) and brine (ca. 10 mL), dried over Na_2SO_4. After filtration, the filtrate was concentrated under reduced pressure. The residue was purified by PTLC (*n*-hexane/CH_2Cl_2 = 3:1) to give **4** (6.0 mg, 22 µmol, 92%) as a colorless solid; R_f: 0.34 (*n*-hexane/CH_2Cl_2 = 4:1); Mp: 245 °C (dec.); ^{1}H NMR ($CDCl_3$, 400 MHz) δ 7.90 (s, 2H), 7.87 (d, *J* = 7.8 Hz, 2H), 7.85 (d, *J* = 7.8 Hz, 2H), 7.52 (s, 2H), 4.41 (s, 4H); ^{13}C{^{1}H}NMR ($CDCl_3$, 100 MHz) δ 143.8 (2C), 143.4 (2C), 141.1 (2C), 140.4 (2C), 130.8 (2C), 126.8(2C), 125.9 (2C), 124.0 (2C), 123.82 (2C), 123.76 (2C), 41.9 (4C); IR (diamond, cm^{-1}): 2920, 2851, 1462, 1382, 1266, 1074, 1014, 822, 788; HRMS (FAB$^+$) *m*/*z*: [M]$^+$ Calcd for $C_{22}H_{12}^+$ 277.0939; Found 277.0944; Elemental Analysis: C, 95.32; H, 4.15 (calcd for $C_{22}H_{12}$: C, 95.62; H, 4.38).

Lactone **5**. To a solution of **2** (15 mg, 36 µmol, 100 mol%) in dry CH_2Cl_2 was added TfOH (15 µL, 180 µmol, 500 mol%) and *m*CPBA (ca. 75 wt% purity, 24.9 mg, 180 µmol, 300 mol%) at 0 °C, and then the mixture was warmed up to 27 °C. After stirring for 15 min at the same temperature, to this was added excess amount of Me_2S (ca. 0.1 mL). After stirring for 10 min, the mixture was filtered through a short pad of silica-gel, and washed with CH_2Cl_2 (ca. 50 mL). The filtrate was concentrated under reduced pressure. The residue was purified by PTLC (*n*-hexane/CH_2Cl_2 = 1:4) to give **5** (9.2 mg, 31 µmol, 58%) as a white solid; R_f: 0.45 (*n*-hexane/CH_2Cl_2 = 1:4); Mp: 327 °C; ^{1}H NMR ($CDCl_3$, 400 MHz) δ 8.11 (d, *J* = 8.0 Hz, 1H), 7.78 (d, *J* = 8.0 Hz, 1H), 7.64 (d, *J* = 7.8 Hz, 1H), 7.48 (d, *J* = 8.0 Hz, 1H), 7.46 (d, *J* = 8.0 Hz, 1H), 7.17 (d, *J* = 7.8 Hz, 1H), 4.34 (s, 2H), 4.27 (s, 2H); ^{13}C{^{1}H}NMR ($CDCl_3$, 100 MHz) δ 162.6 (1C), 153.4 (1C), 151.9 (1C), 145.9 (1C), 144.5 (1C), 143.2 (1C), 142.1 (1C), 141.9 (1C), 141.7 (1C), 141.2 (1C), 131.1 (1C), 127.4 (1C), 126.9 (1C), 125.5 (1C), 124.9 (1C), 124.6 (1C), 118.9 (1C), 116.1 (1C), 112.9 (1C), 42.1 (1C), 41.2 (1C); IR (diamond, cm^{-1}): 2954, 2921, 2857, 1724, 1398, 1014, 796, 754; HRMS (FAB$^+$) *m*/*z*: [M]$^+$ Calcd for $C_{21}H_{10}O_2^+$ 294.0678; Found 294.0683.

Oxime **6**’. To a solution of **2** (20.0 mg, 71.9 µmol, 100 mol%) in MeOH/pyridine (2 mL, 1:1 (v/v)) was added $NH_2OH \cdot H_2O$ (10.0 mg, 0.144 mmol, 200 mol%) at room temperature, and the mixture was stirred for

1 h at 80 °C. After cooling to room temperature, the organic volatiles were removed under reduced pressure. The residue was dissolved in ethyl acetate (ca. 30 mL), and this mixture was filtered through a short pad of silica-gel, and eluted with $CHCl_3$ (ca. 50 mL). The filtrate was concentrated under reduced pressure. The residue was purified by PTLC (CH_2Cl_2/MeOH = 95:5) to give **6′** (21.0 mg, 71.9 μmol, 99.6%) as a pale yellow solid; R_f: 0.35 (CH_2Cl_2/MeOH=95:5); Mp: 236 °C (dec.); ^{1}H NMR (DMSO-d_6, 400 MHz) δ 12.28 (s, 1H), 7.75 (d, J = 7.8 Hz, 1H), 7.30 (d, J = 7.8 Hz, 1H), 7.28 (s, 2H, two signals overlapped), 7.24 (s, 2H, two signals overlapped), 4.71 (d, J = 20.1 Hz, 2H, two signals overlapped), 3.59 (d, J = 20.1 Hz, 1H), 3.57 (d, J = 20.1 Hz, 1H); ^{13}C{^{1}H}NMR (DMSO-d_6, 100 MHz) δ 153.7 (1C), 152.9 (1C), 151.2 (1C), 148.7 (1C), 148.5 (1C), 148.0 (1C + 1C, two signals overlapped), 147.9 (1C), 147.4 (1C), 145.6 (1C), 145.3 (1C), 139.1 (1C), 134.3 (1C), 126.7 (1C), 125.6 (1C), 125.4 (1C), 124.3 (2C, two signals overlapped), 122.1 (1C), 41.6 (1C), 41.5 (1C); IR (diamond, cm^{-1}): 3166, 3066, 2852, 1466, 1390, 1260, 1022, 968, 785; HRMS (FAB$^+$) m/z: $[M]^+$ Calcd for $C_{21}H_{11}NO^+$ 293.0838; Found 293.0845.

***Lactam* 6**. The mixture of **6′** (16.5 mg, 56.0 μmol, 100 mol%) and polyphospholic acid (2 mL) was stirred at 100 °C for 40 min. After cooling to room temperature, the mixture was carefully poured into saturated aqueous $NaHCO_3$ solution (ca. 30 mL). The mixture was extracted with CH_2Cl_2 (ca. 25 mL × 3). The combined organic extract was washed with brine (ca. 50 mL) and dried over Na_2SO_4. After filtration, the filtrate was concentrated under reduced pressure. The residue was purified by silica-gel chromatography (CH_2Cl_2/MeOH = 9:1) to give **6** (10.5 mg, 35.8 μmol, 63.9%) as a white solid; R_f = 0.14 (CH_2Cl_2/MeOH=9:1); Mp: 235 °C (dec.); ^{1}H NMR (DMSO-d_6, 400 MHz) δ 11.47 (s, 1H), 8.02 (d, J = 7.8 Hz, 1H), 7.86 (d, J = 7.8 Hz, 1H), 7.70 (d, J = 7.8 Hz, 1H), 7.50 (s, 2H, two signals overlapped), 7.15 (d, J = 7.8 Hz, 1H), 4.37 (s, 2H), 4.26 (s, 2H); ^{13}C{^{1}H}NMR (DMSO-d_6, 100 MHz) δ 163.2 (1C), 150.3 (1C), 144.6 (1C), 143.8 (1C), 140.7 (1C), 140.2 (1C), 140.1 (1C), 139.6 (1C), 138.7 (1C), 136.6 (1C), 129.1 (1C), 126.4 (1C), 124.9 (1C), 124.6 (1C + 1C, two signals overlapped), 124.5 (1C), 123.7 (1C), 114.1 (1C), 111.7 (1C), 41.6 (1C), 40.8 (1C); IR (diamond, cm^{-1}): 2923, 2852, 1650, 1450, 1259, 796, 748, 694; HRMS (FAB$^+$) m/z: $[M+H]^+$ Calcd for $C_{21}H_{12}NO^+$ 294.0916; Found 294.0976.

***Imidoyl chloride* 7**. To a solution of **6** (5.0 mg, 20 μmol, 100 mol%) in toluene (0.2 mL) was added $POCl_3$ (0.1 mL) at room temperature, and the mixture was stirred at 100 °C for 2 h. After cooling to room temperature, the mixture was carefully poured into 10% aqueous NH_3 solution (ca. 20 mL). The mixture was extracted with CH_2Cl_2 (ca. 10 mL × 3). The combined organic extract was washed with brine (ca. 20 mL) and dried over Na_2SO_4. After filtration, the filtrate was concentrated under reduced pressure. The residue was purified by PTLC (CH_2Cl_2) to give **7** (5.2 mg, 17 μmol, 82%) as a pale yellow solid; R_f: 0.50 (CH_2Cl_2); Mp: 247 °C (dec.); ^{1}H NMR ($CDCl_3$, 400 MHz) δ 8.10 (d, J = 8.2 Hz, 1H), 7.88 (d, J = 8.2 Hz, 1H), 7.86 (d, *J* = 7.8 Hz, 1H), 7.83 (d, *J* = 7.8 Hz, 1H), 7.44 (d, *J* = 7.8 Hz, 1H), 7.41 (d, *J* = 7.8 Hz, 1H), 4.29 (s, 2H), 4.27 (s, 2H); $^{13}C\{^1H\}$NMR ($CDCl_3$, 100 MHz) δ 150.9 (1C), 149.9 (1C), 145.5 (1C), 145.3 (1C), 144.9 (1C), 142.9 (1C), 142.2 (1C), 141.7 (1C), 141.5 (1C), 141.0 (1C), 129.8 (1C), 126.5 (1C), 125.4 (1C), 124.6 (1C), 124.5 (1C), 124.3 (1C), 123.7 (1C), 123.6 (1C), 120.9 (1C), 42.3 (1C), 42.0 (1C); IR (diamond, cm^{-1}): 2923, 1728, 1392, 1263, 1027, 789; HRMS (FAB^+) *m*/*z*: $[M+H]^+$ Calcd for $C_{21}H_{11}{}^{35}ClN^+$ 312.0578; Found 312.0588.

***Phenyl azahomosumanene* 8**. The solution of **7** (7.0 mg, 22 µmol, 100 mol%), $PhB(OH)_2$ (4.1 mg, 34 µmol, 150 mol%), $PdCl_2(amphos)_2$ (1.6 mg, 2.2 µmol, 10 mol%) and K_2CO_3 (6.1 mg, 44 µmol, 200 mol%) in 1,4-dioxane/water (1 mL, 4:1 (v/v)) was stirred at 80 °C for 14 h. After cooling to room temperature, to the reaction mixture was added water (ca. 5 mL). The mixture was extracted with CH_2Cl_2 (ca. 10 mL × 3). The combined organic extract was washed with water (ca. 10 mL) and brine (ca. 10 mL), and then dried over Na_2SO_4. After filtration, the filtrate was concentrated under reduced pressure. The residue was purified by PTLC (CH_2Cl_2) to give **8** (7.0 mg, 20 µmol, 90%) as a pale yellow solid; R_f: 0.33 (CH_2Cl_2); Mp: 243 °C (dec.); ^1H NMR ($CDCl_3$, 400 MHz) δ 8.13–8.07 (AA′BB′C, 2H), 8.02 (d, *J* = 8.2 Hz, 1H), 8.01 (d, *J* = 8.2 Hz, 1H), 7.95 (d, *J* = 8.2 Hz, 1H), 7.83 (d, *J* = 8.2 Hz, 1H), 7.64–7.52 (m, 3H), 7.48 (d, *J* = 7.9 Hz, 1H), 7.46 (d, *J* = 7.9 Hz, 1H), 4.37 (s, 2H + 2H, two signals overlapped); $^{13}C\{^1H\}$NMR ($CDCl_3$, 100 MHz) δ 161.9 (1C), 149.1 (1C), 145.7 (1C), 145.0 (1C), 144.6 (1C), 143.4 (1C), 142.7 (1C), 142.1 (1C), 141.7 (1C), 141.3 (1C), 139.4 (1C), 130.2 (1C), 130.0 (2C), 129.4 (1C), 128.6 (2C), 126.2 (1C), 125.3 (1C), 124.9 (1C), 124.6 (1C), 124.5 (1C), 124.3 (1C), 124.0 (1C), 120.9 (1C), 42.2 (1C), 41.9 (1C). IR (diamond, cm^{-1}): 2975, 2856, 1725, 1463, 1396, 1276, 1136, 1074, 1024, 792, 740, 702; HRMS (FAB^+) *m*/*z*: $[M+H]^+$ Calcd for $C_{27}H_{16}N^+$ 354.1279; Found 354.1281.

***Azahomosumanene* 9**. To a solution of **7** (4.6 mg, 15 µmol, 100 mol%) and $PdCl_2(dppf)$ (1.3 mg, 15 µmol, 10 mol%) in DMF (1.0 mL) was added HCO_2H (2.5 µL, 44 µmol, 300 mol%) and NEt_3 (6.7 µL, 44 µmol, 300 mol%) at room temperature, and the mixture was stirred at 90 °C for 2 h. After cooling to room temperature, to the reaction mixture was added water (ca. 5 mL). The mixture was extracted with diethyl ether (ca. 10 mL × 3). The combined organic extract was washed with water (ca. 10 mL) and brine (ca. 10 mL), and then dried over Na_2SO_4. After filtration, the filtrate was concentrated under reduced pressure. The residue was purified by PTLC (CH_2Cl_2/MeOH=95:5) to give **9** (3.7 mg, 13 µmol, 90%) as a pale yellow solid; R_f: 0.48 (CH_2Cl_2/MeOH=95:5); Mp: 186 °C (dec.); ^1H NMR ($CDCl_3$, 400 MHz) δ 9.45 (s, 1H), 7.98 (d, *J* = 8.2 Hz, 1H), 7.92 (d, *J* = 8.2 Hz, 1H), 7.91 (d, *J* = 8.2 Hz, 1H), 7.88 (d, *J* = 8.2 Hz, 1H), 7.46 (d, *J* = 8.0 Hz, 1H), 7.44 (d, *J* = 8.0 Hz, 1H), 4.35 (s, 2H), 4.33 (s, 2H); $^{13}C\{^1H\}$NMR ($CDCl_3$, 100 MHz) δ 153.8 (1C), 148.9 (1C), 145.7 (1C), 145.13 (1C), 145.08 (1C), 143.7 (1C), 142.8 (1C), 142.1 (1C), 141.9 (1C), 141.2

(1C), 128.9 (1C), 126.1 (1C), 125.8 (1C), 124.9 (1C), 124.6 (1C), 124.4 (1C), 124.10 (1C), 124.06 (1C), 121.4 (1C), 42.4 (1C), 42.0 (1C); IR (diamond, cm^{-1}): 2921, 2854, 1724, 1396, 1279, 1126, 1071; HRMS (FAB$^+$) *m*/*z*: [M]$^+$ Calcd for $C_{21}H_{11}N^+$ 277.0889; Found 277.0890.

Pt complex **11**. To a solution of **8** (5.0 mg, 14 µmol, 100 mol%) and K_2PtCl_4 (5.9 mg, 14 µmol, 100 mol%) in AcOH (2.0 mL) was stirred at 120 °C for 24 h. The reaction mixture was cooled to room temperature, and the brown precipitate was collected by filtration and washed with EtOH (ca. 5 mL × 3) to afford the µ-chloro-bridged dimer platinum(II) complex as a brown powder. This compound was directly used in the following process. To the mixture of Pt dimer complex, K_2CO_3 (58 mg, 420 µmol, 3000 mol%) in acetone (2.0 mL) and water (0.2 mL) was added acetyl acetone (14 mg, 140 µmol, 1000 mol%) at room temperature, and the mixture was stirred at 60 °C for 18 h. After cooling to room temperature, to the reaction mixture was added water (ca. 5 mL). The mixture was extracted with CH_2Cl_2 (ca. 10 mL × 3). The combined organic extract was washed with water (ca. 10 mL) and brine (ca. 10 mL), and then dried over Na_2SO_4. After filtration, the filtrate was concentrated under reduced pressure. The residue was purified by PTLC (*n*-hexane/CH_2Cl_2=4:1) to give **11** (5.4 mg, 8.4 µmol, 60%) as a yellow solid; R_f: 0.48 (*n*-hexane/CH_2Cl_2=3:1); Mp: 255 °C (dec.); ^{1}H NMR ($CDCl_3$, 400 MHz) δ 9.17 (d, *J* = 8.7 Hz, 1H), 8.49 (d, *J* = 8.2 Hz, 1H), 8.31 (d, *J* = 7.3 Hz, 1H), 7.89 (d, *J* = 7.8 Hz, 1H), 7.80 (d, *J* = 8.2 Hz, 1H + 1H, two signals overlapped), 7.42 (d, *J* = 7.8 Hz, 1H), 7.40 (d, *J* = 7.8 Hz, 1H), 7.31–7.27 (m, 1H), 7.24–7.22 (m, 1H), 5.59 (s, 1H), 4.26 (s, 2H + 2H, two signals overlapped), 2.10 (s, 3H), 2.07 (s, 3H); ^{13}C{^{1}H}NMR spectrum could not be obtained due to its low solubility; IR (diamond, cm^{-1}): 2923, 2853, 1731, 1717, 1523, 1457, 1278, 1125, 742.; HRMS (FAB$^+$) *m*/*z*: [M]$^+$ Calcd for $C_{32}H_{21}NO_2Pt^+$ 646.1220; Found 646.1237; Elemental Analysis: C, 59.02; H, 3.33; N, 2.20 (calcd for $C_{32}H_{21}NO_2Pt$: C, 59.44; H, 3.27; N, 2.17).

Computational study

Otherwise noted, all structure optimizations, self-consistent field (SCF) energies, and thermal energy correction calculations using density functional theory (DFT) were performed using Gaussian 09 suite of programs (revision E.01)[25] at B3LYP[26] level of theory in gas phase with cc-pVTZ[27] as a basis set. Harmonic frequency calculations were conducted with the same level of theory on the optimized geometries to check all stationary points as either minima or first-order saddle points. The zero-point energy (ZPE) and thermal energy corrections were calculated using vibrational frequency. The simulation of UV-Vis absorption spectra for the optimized ground state geometries using time-dependent DFT (TD-DFT) were performed on the optimized geometries at the same level of theory. As for **11**, the structure was optimized using DFT calculation at B3LYP/6-31G[28] (for C, H, and N), LanL2DZ[29] (for Pt). The simulation of UV-Vis absorption spectra for the optimized ground state geometries using TD-DFT was performed on the optimized geometries at the same level of theory.

QTAIM analysis

The coordinates of C, N, O, and Pt were obtained from the result of SC-XRD analysis, and those of H were optimized using DFT calculation at B3LYP/def2-SPV level of theory with fixing the coordinates of other elements. The electron density was calculated at CAM-B3LYP-D3/def2-SVP[30] level of theory on the optimized coordinates as the SCF energy correction. QTAIM analysis was conducted with the corresponding formatted checkpoint (fchk) file using Multiwfn program.[31] The obtained bond paths and the bond critical points (BCPs) were visualized using VMD program.[32]

Single crystal X-ray diffraction analysis.

The diffraction data for **5** was recorded on an ADSC Q210 CCD area detector with a synchrotron radiation (λ =0.70000 Å) at 2D beamline in Pohang Accelerator Laboratory (PAL). The diffraction images were processed by using HKL3000.[33] The diffraction data for **6** was recorded on a DECTRIS EIGER X 1M Detector System (λ = 0.78263 Å) at 100 K at SPring-8 BL40XU. The diffraction images were processed by using RIGAKU RAPID AUTO and *Henkankun-R*.[34] The diffraction data for **11** was recorded on a XtaLAB Synergy with a Cu-target (λ = 1.54184 Å) equipped with a Rigaku HyPix-6000HE as the detector at 123 K in house. The diffraction images were processed by using CrysAlisPro.[35] All the structures were solved by direct methods (SHELXT-2015, 2018/2)[36] and refined by full-matrix least squares calculations on F2 (SHELXL-2018/3)[36] using the Olex2[37] program package.

Preparation of single crystals.

5: Crystallization was conducted by slow evaporation method. In a small test tube, a solution of **5** in CH_2Cl_2 (3.4 mmol/L, 0.3 mL) was added, and the test tube was stored at 5 °C. After 1 day, colorless needle crystals suitable for single crystal X-ray diffraction analysis were obtained. $C_{21}H_{10}O_2$, monoclinic, space group $P2_1/c$ (No. 14), a = 10.120(2) Å, b = 17.620(4) Å, c = 7.2976(15) Å, V = 1282.2(5) Å^3, ρ_{calcd} = 1.525 g/cm^3, Z = 4, 2539 unique reflections out of 3499 with $I>2\sigma(I)$, 389 parameters, 3.060° < θ < 30.073°, $R1$ = 0.0963, w$R2$ = 0.2540, GOF = 1.163.

6: Crystallization was conducted by vapor diffusion method. In a small test tube, a solution of **6** in chlorobenzene (3.4 mmol/L, 0.5 mL) was added. The test tube was put into a vial containing *n*-hexane, and this was stored at 5 °C. After 7 days, colorless block crystals suitable for single crystal X-ray diffraction analysis were obtained. $(C_{21}H_{11}NO)_2(C_6H_4Cl)_{0.5}$, triclinic, space group P-1 (No. 2), a = 7.2703(4) Å, b = 10.2209(6) Å, c = 21.5064(11) Å, α = 80.906(4)°, β = 84.869(4)°, γ = 81.274(4)°, V = 1556.25(15) Å^3, ρ_{calcd} = 1.490 g/cm^3, Z = 2, 3770 unique reflections out of 5354 with $I>2\sigma(I)$, 647 parameters, 1.058° < θ < 27.500°, $R1$ = 0.0563, w$R2$ = 0.1385, GOF = 1.156.

11: Crystallization was conducted by vapor diffusion method. In a small test tube, a solution of **11** in chloroform (1.5 mmol/L, 0.3 mL) was added. The test tube was put into a vial containing *n*-pentane, and this was stored at 20 °C. After 3 days, yellow needle crystals suitable for single crystal X-ray diffraction analysis were obtained. $C_{32}H_{21}NO_2Pt$, monoclinic, space group $P2_1/n$ (No. 14), a = 13.7930(2) Å, b = 9.32633(9) Å, c = 17.4424(2) Å, α = 90°, β = 94.678(1)°, γ = 90°, V = 2236.28(4) Å^3, ρ_{calcd} = 1.92 g/cm^3, Z = 4, 4193 unique reflections out of 4622 with $I>2\sigma(I)$, 327 parameters, 3.933° < θ < 76.451°, R_1 = 0.0366, wR_2 = 0.0987, GOF = 1.097.

Electrochemical analysis.

Sample preparation and measurements were performed in a glovebox filled with argon gas. $[^n\mathrm{Bu}_4\mathrm{N}][\mathrm{ClO}_4]$ was recrystallized from ethanol/water prior to CV measurements. Sample (2.0 μmol) and $[^n\mathrm{Bu}_4\mathrm{N}][\mathrm{ClO}_4]$ (68.4 mg, 0.200 mmol) were dissolved in degassed MeCN (2.0 mL) to afford a sample solution (1.0×10^{-3} mol/L). The cyclic voltammetry of **4** and **9** were performed using a standard three-hole electrochemical cell with a glassy-carbon working electrode (3.0 mm diameter), a reference electrode (Ag/$AgNO_3$), and a counter electrode (Pt wire). The scan rate was set at 100 mV·s^{-1}.

UV-vis absorption and emission spectroscopies at 298 K. To a 5 mL volumetric flask were added a sample (10 μmol) and degassed CH_2Cl_2 (5.0 mL) to afford a sample solution (2.0×10^{-3} mol/L). The solution was diluted at 1.0×10^{-5} mol/L with the same solvent and transferred to a quartz cell (optical path length; 10 mm), and UV-vis absorption and emission spectroscopy measurements were performed on a JASCO FP-6500 spectrofluorometer at 298 K.

Emission and lifetime spectroscopies of 11 at 77 K. To a 5 mL volumetric flask were added **11** (6.5 mg, 10 μmol) and solvent (5.0 mL, diethyl ether/ethanol/toluene = 2:1:1) to afford a sample solution (2.0×10^{-3} mol/L). The solution was diluted at 5.0×10^{-4} mol/L with the same solvent. After venting with Ar gas for 25 min, an aliquot of the solution (ca. 0.5 mL) was transferred to a quartz tube cell with a diameter of 5 mm, and then this was placed in a vessel containing liquid nitrogen. Emission spectra at 77 K were recorded on a JASCO FP-8300 spectrofluorometer by excitation at 438 nm. Phosphorescence lifetime spectroscopies were performed at 77 K using a nanosecond laser at 355 nm of the third harmonic generation (THG) from a Nd:YAG laser (Continuum Inc., Surelite II; 10 Hz, 5–8 ns duration). The phosphorescence spectra through an undercut filter (380 nm) at delayed times were monitored by using an Andor model iStar image-intensifier ICCD camera equipped with a Solar TII model MS2004 monochromator.

Quenching Experiment of 11. To a 5 mL volumetric flask were added **11** (6.5 mg, 10 μmol) and degassed CH_2Cl_2 (5.0 mL) to give a sample solution (2.0×10^{-3} mol/L). The solution was diluted at 1.0×10^{-4} mol/L with the same solvent. The solution was transferred to a quartz cell (optical path length; 10 mm), and the emission spectroscopy of **11** was performed on a JASCO FP-6500 spectrofluorometer with excitation wavelength of 438 nm at room temperature. After that, the solution was bubbled with oxygen gas for 25 min, then emission spectroscopy measurement was performed again under the same conditions.

^1H NMR (400 MHz), $^{13}C\{^1H\}$ NMR (100 MHz), and ^{19}F NMR (373 MHz) spectra of **3** ($CDCl_3$).

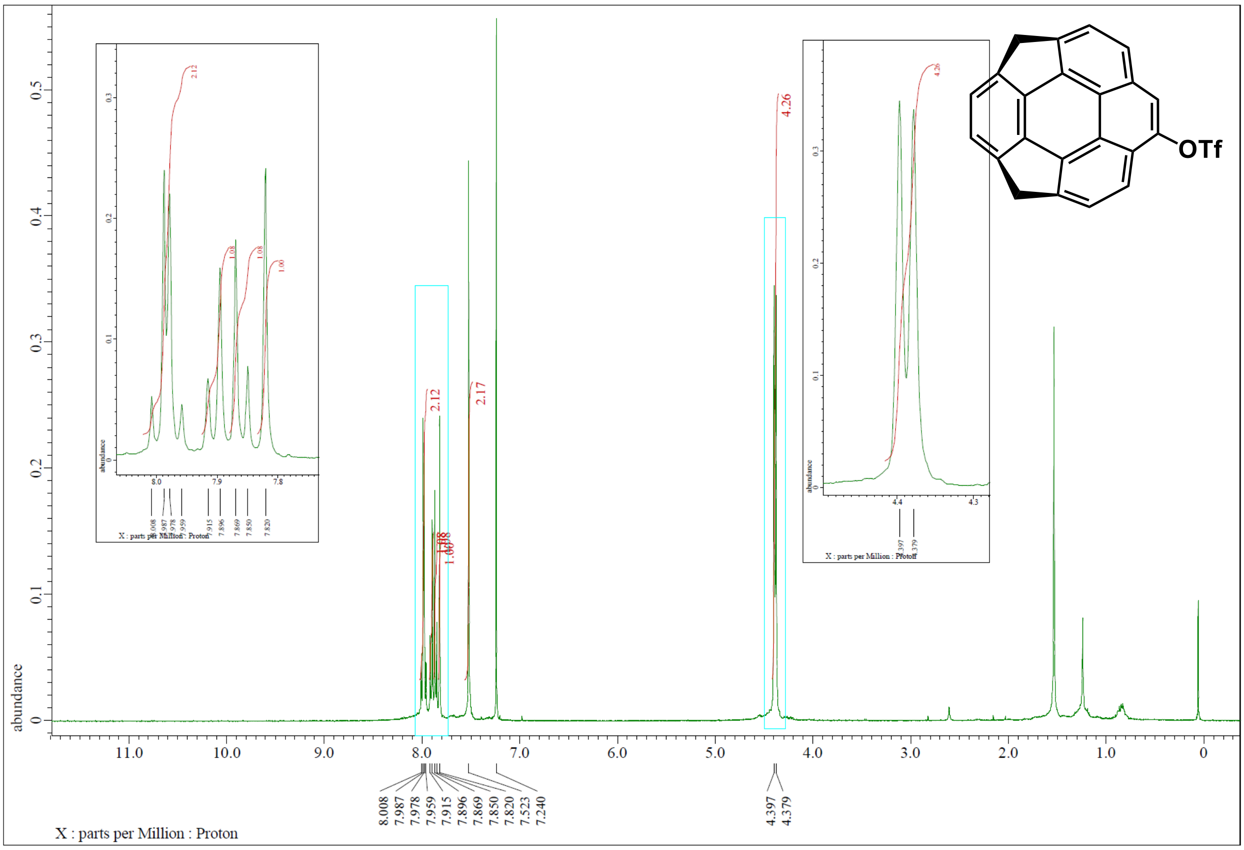

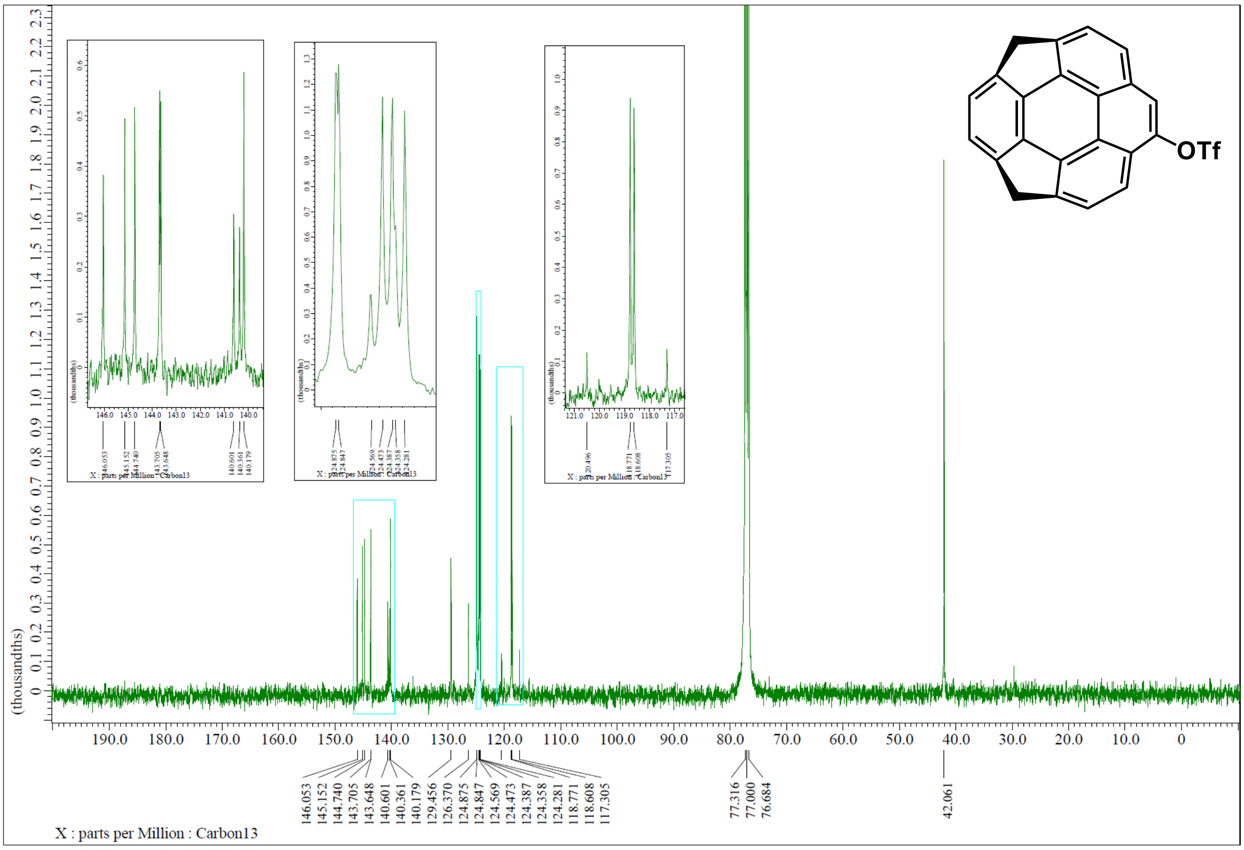

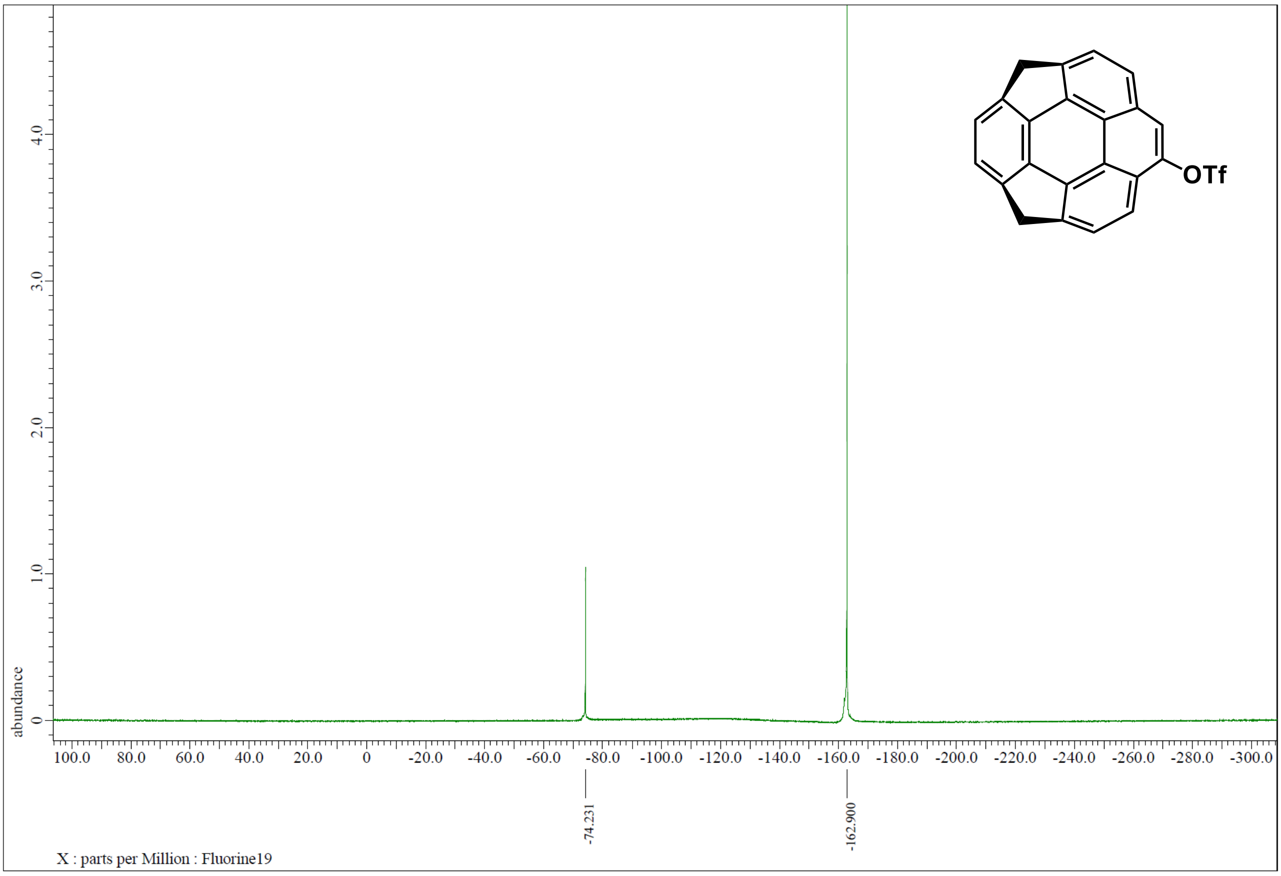
OTf
abundance
0
1.0
2.0
3.0
4.0
100.0
80.0
60.0
40.0
20.0
0
-20.0
-40.0
-60.0
-80.0
-100.0
-120.0
-140.0
-160.0
-180.0
-200.0
-220.0
-240.0
-260.0
-280.0
-300.0
-74.231
-162.900
X : parts per Million : Fluorine19

^{1}H NMR (400 MHz) and ^{13}C{^{1}H}NMR (100 MHz) spectra of **4** ($CDCl_3$).

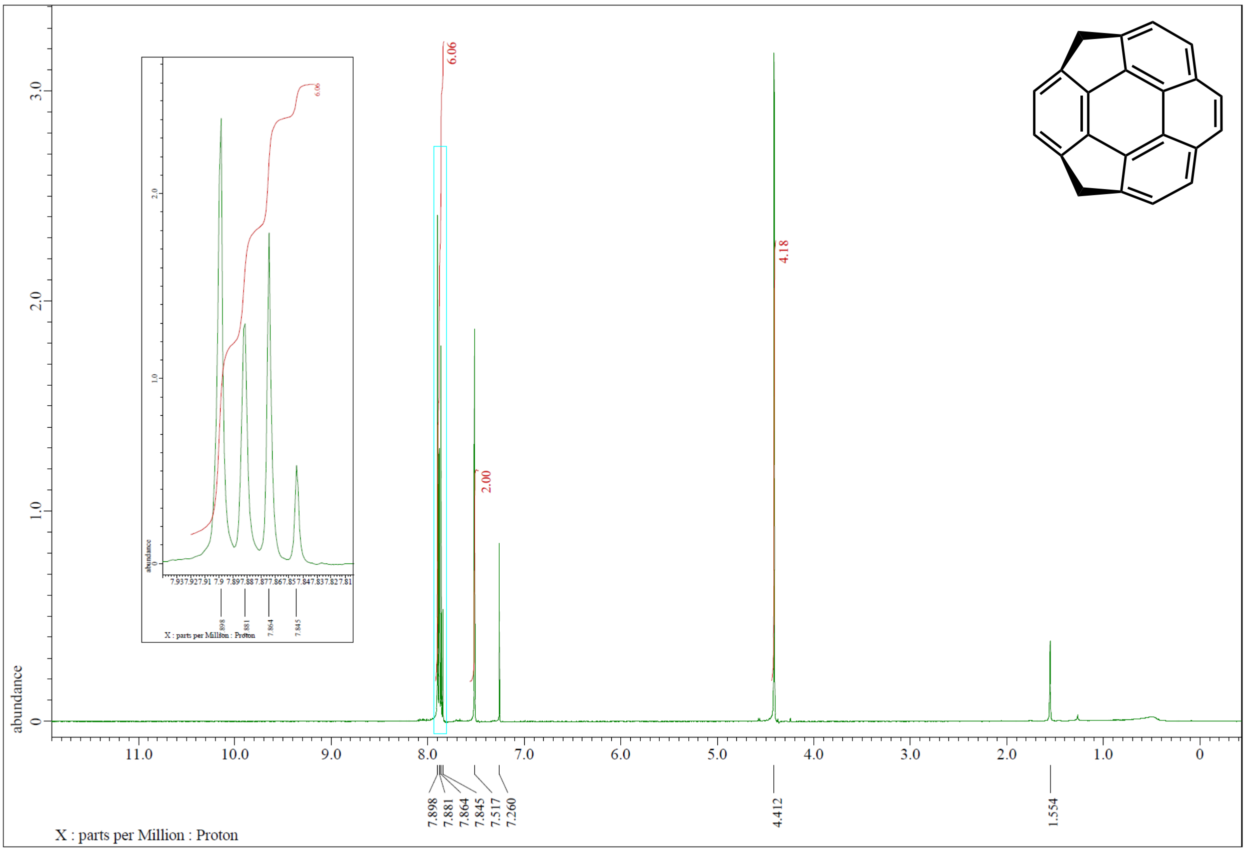

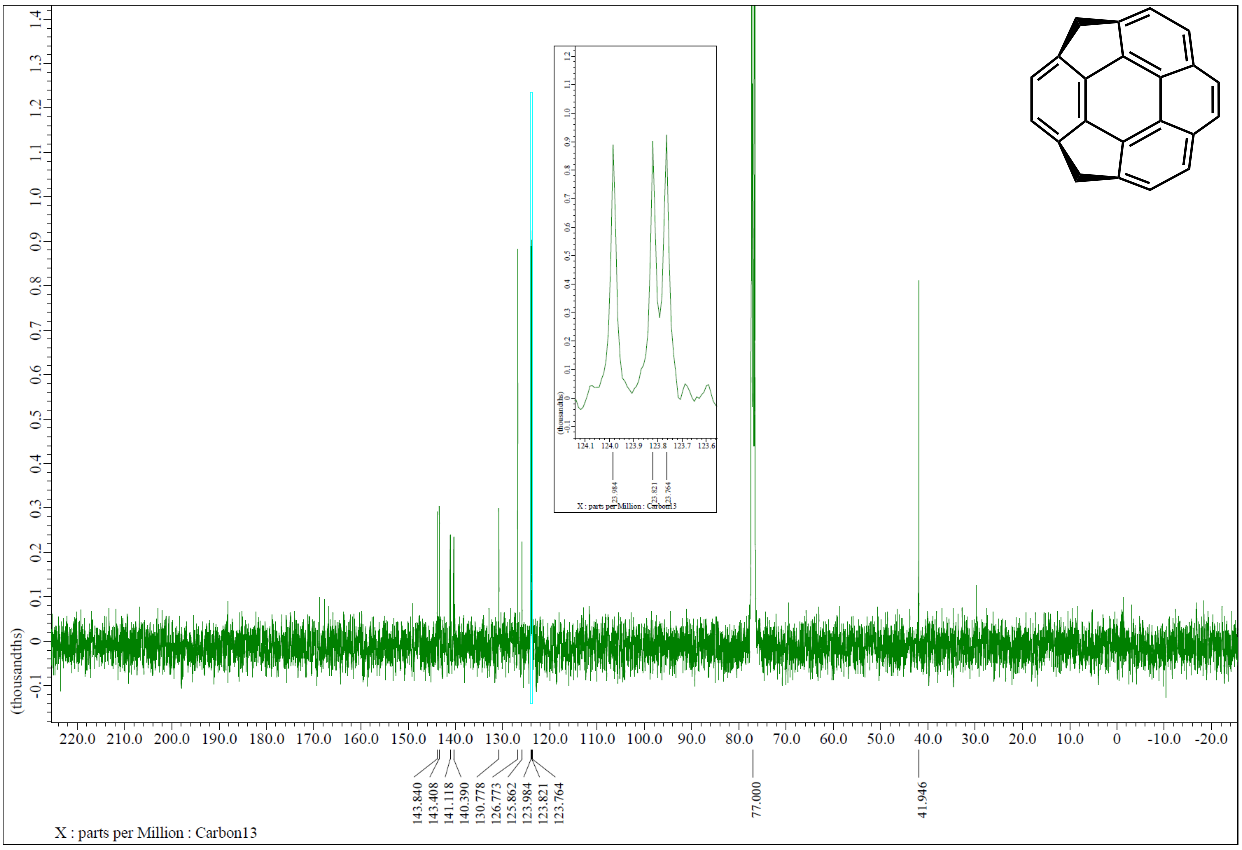

^{1}H NMR (400 MHz) and ^{13}C{^{1}H}NMR (100 MHz) spectra of **5** (CDCl$_3$).

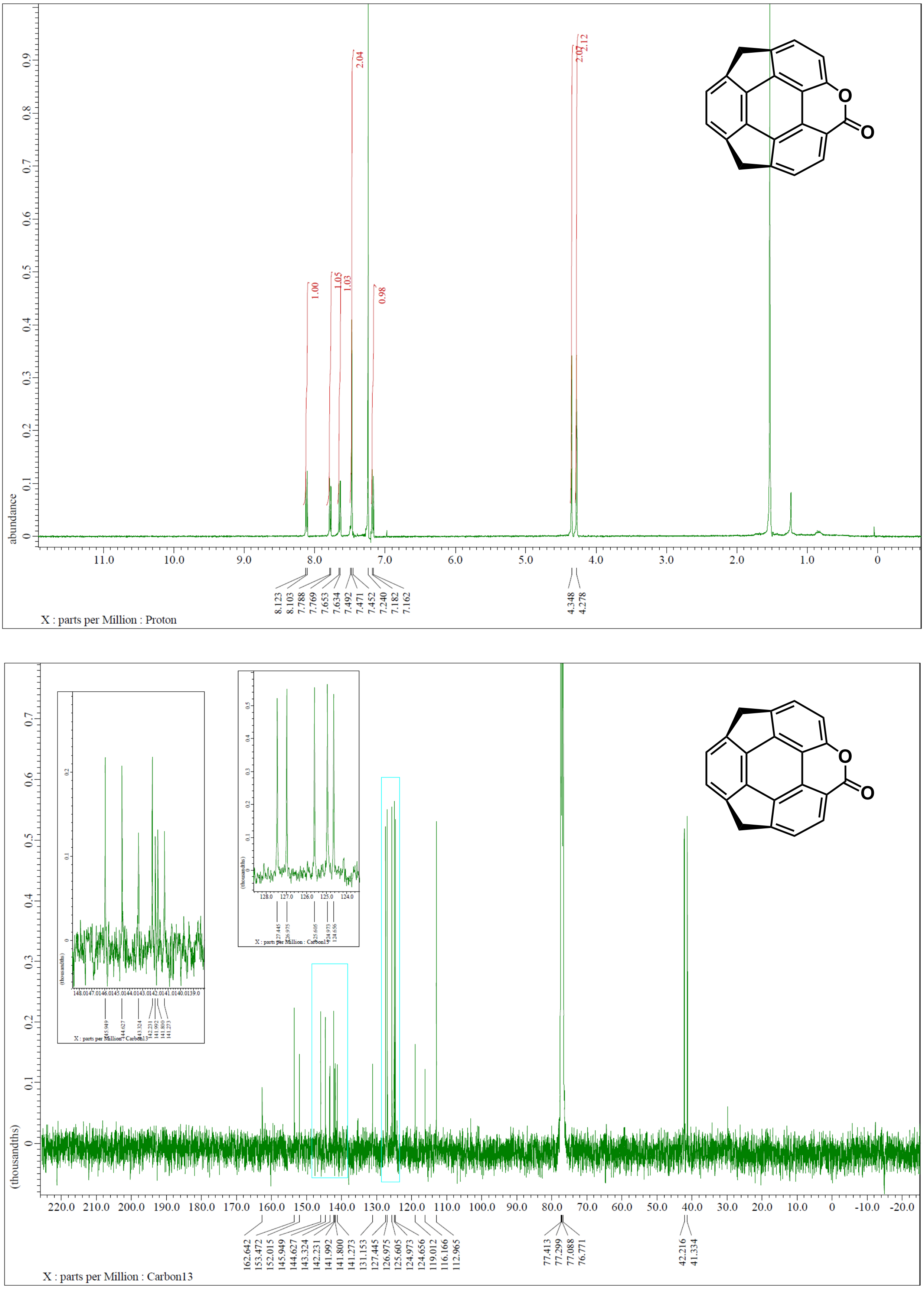

^{1}H NMR (400 MHz) and ^{13}C{^{1}H}NMR (100 MHz) spectra of **6’** (DMSO-d_6).

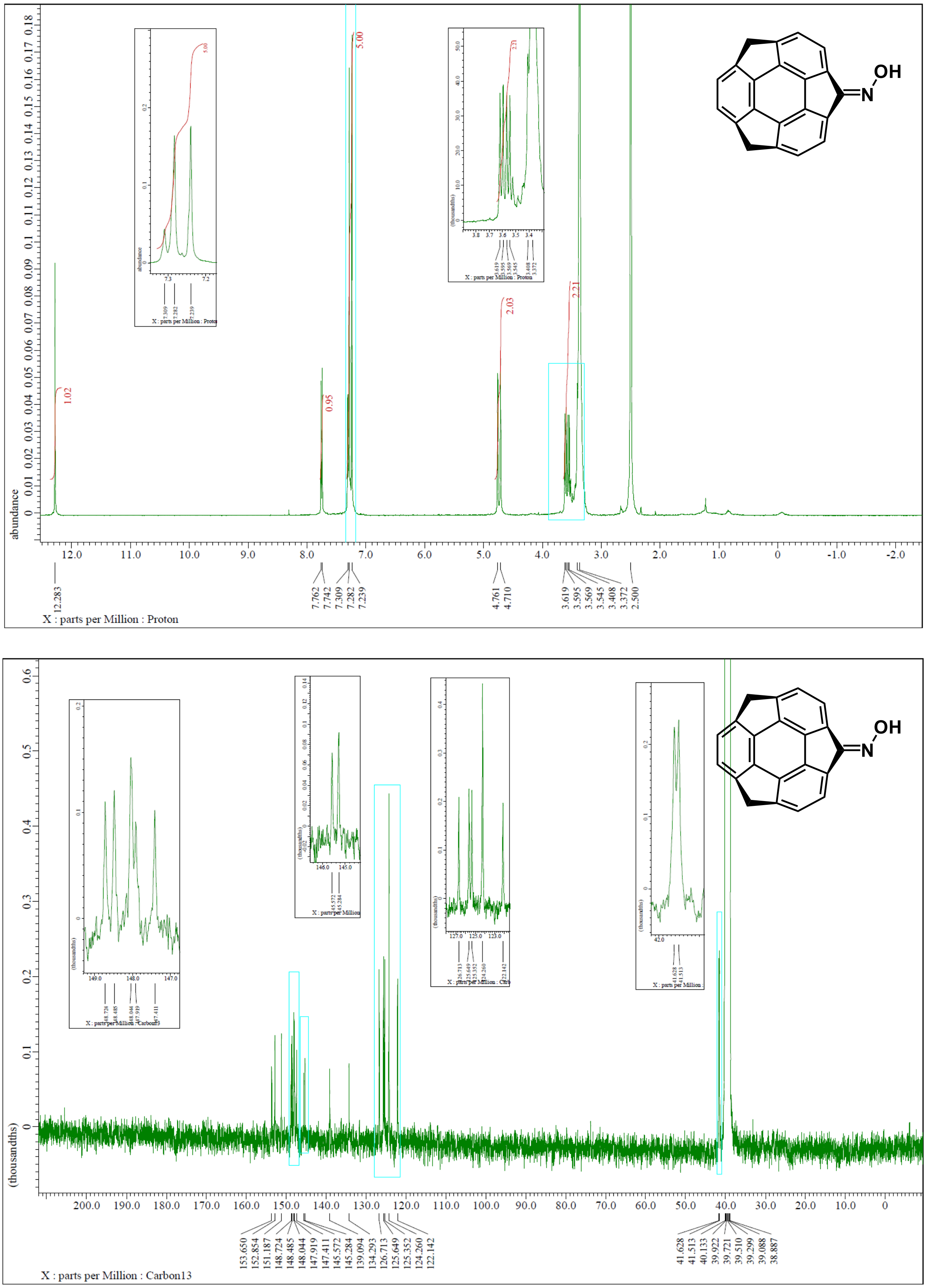

^{1}H NMR (400 MHz) and ^{13}C{^{1}H}NMR (100 MHz) spectra of **6** (DMSO-d_6).

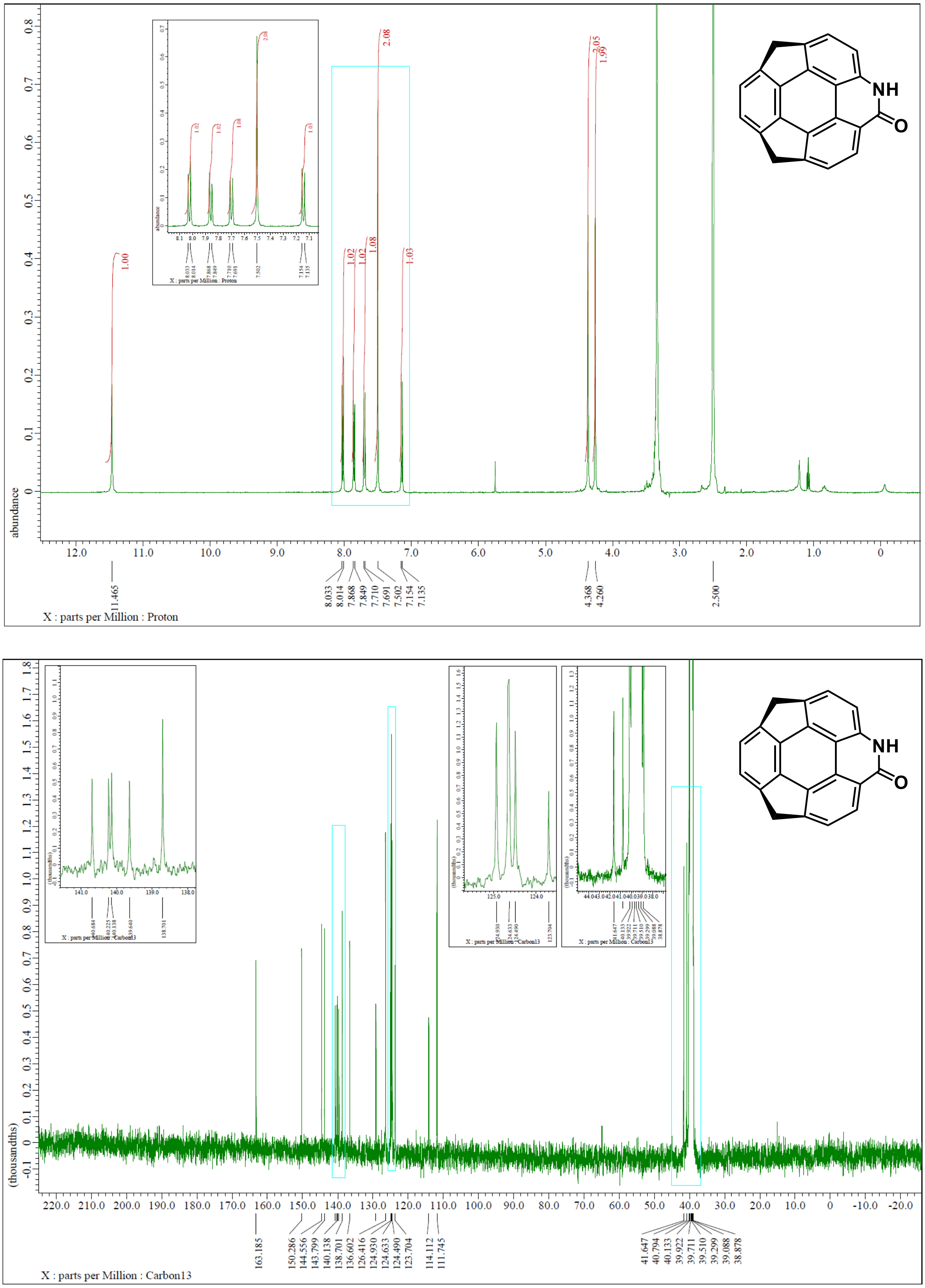

^{1}H NMR (400 MHz) and ^{13}C{^{1}H}NMR (100 MHz) spectra of **7** (CDCl$_3$).

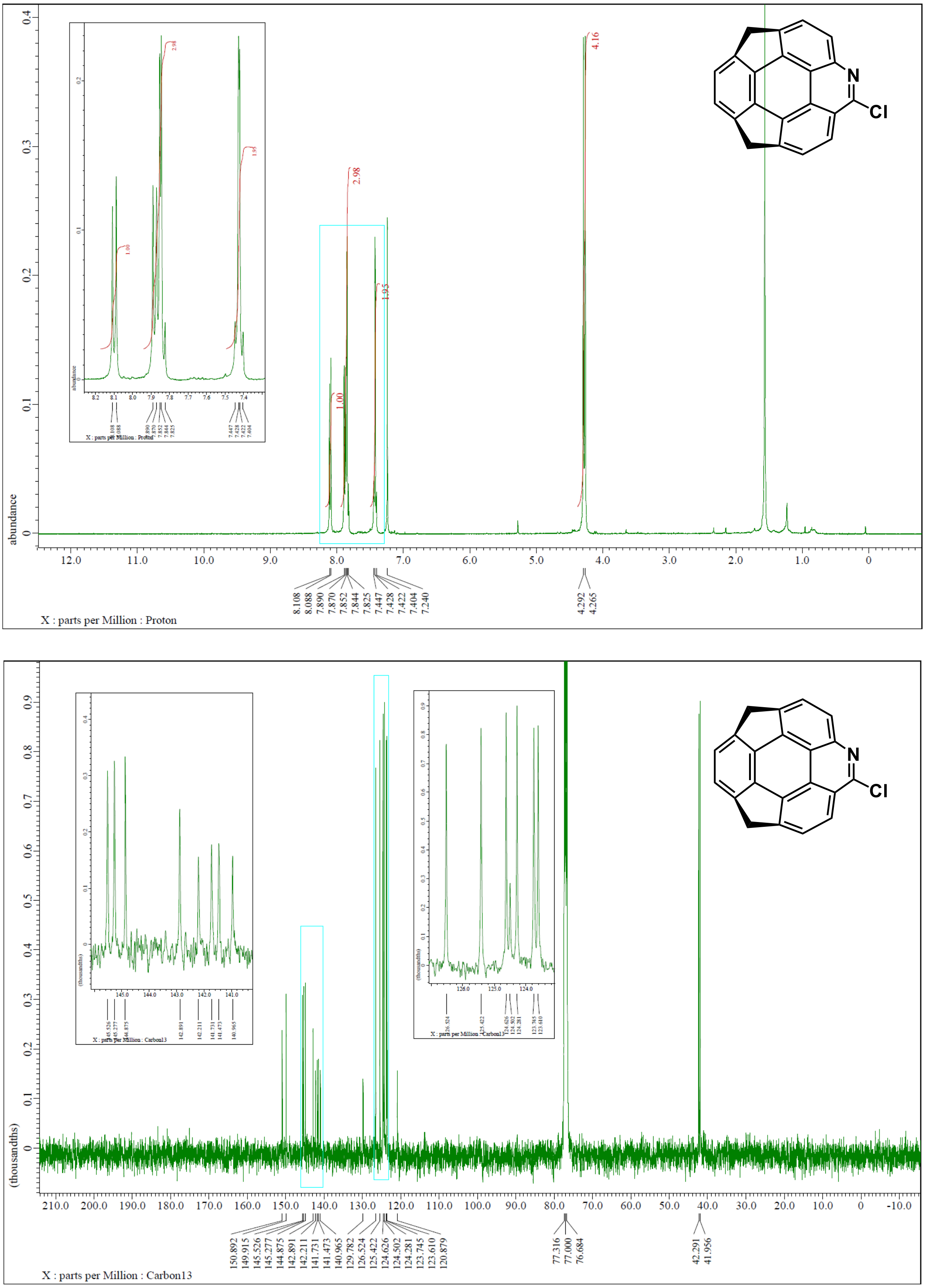

^{1}H NMR (400 MHz) and ^{13}C{^{1}H}NMR (100 MHz) spectra of **8** ($CDCl_3$).

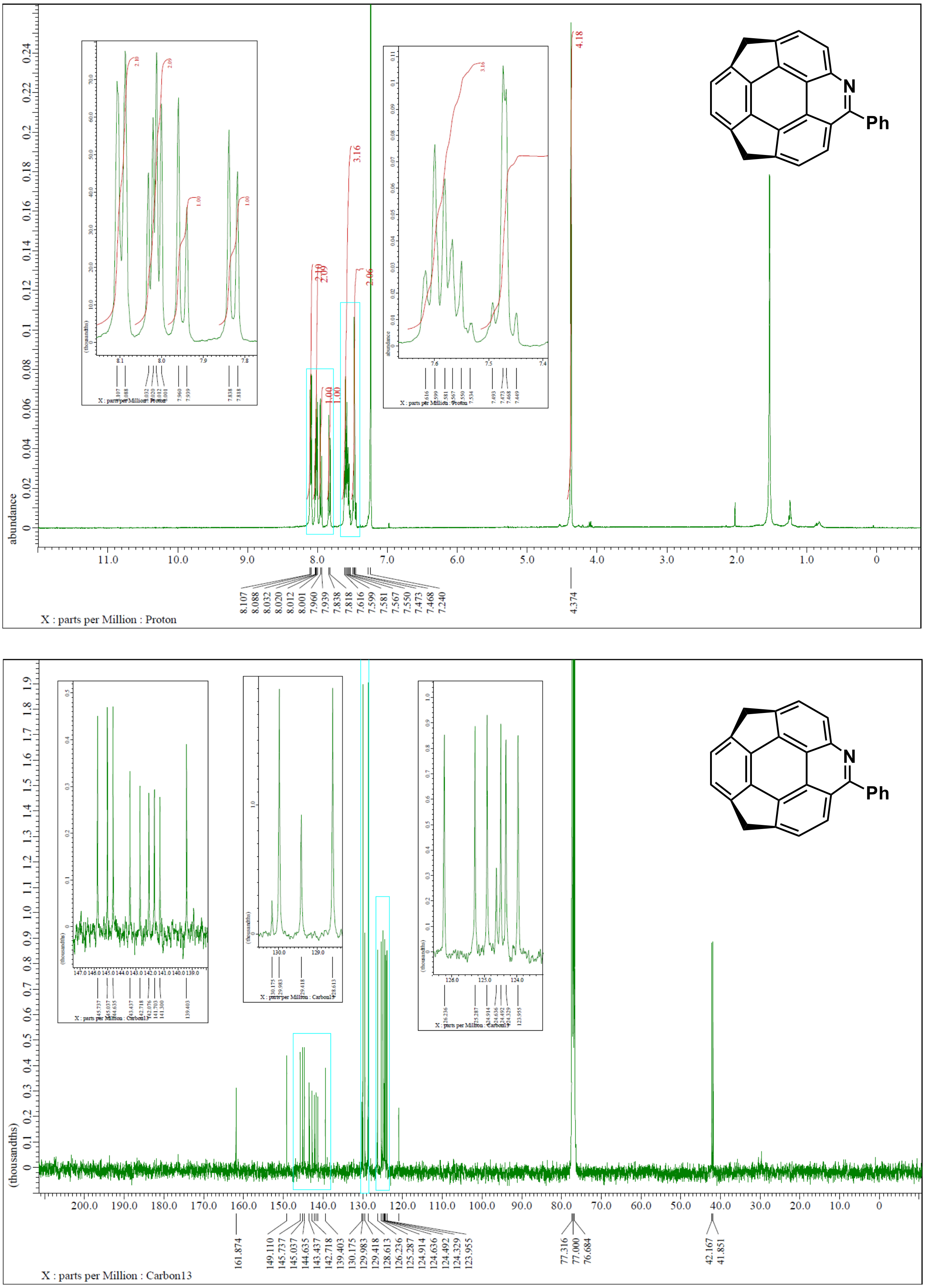

^{1}H NMR (400 MHz) and ^{13}C{^{1}H}NMR (100 MHz) spectra of **9** (CDCl$_3$).

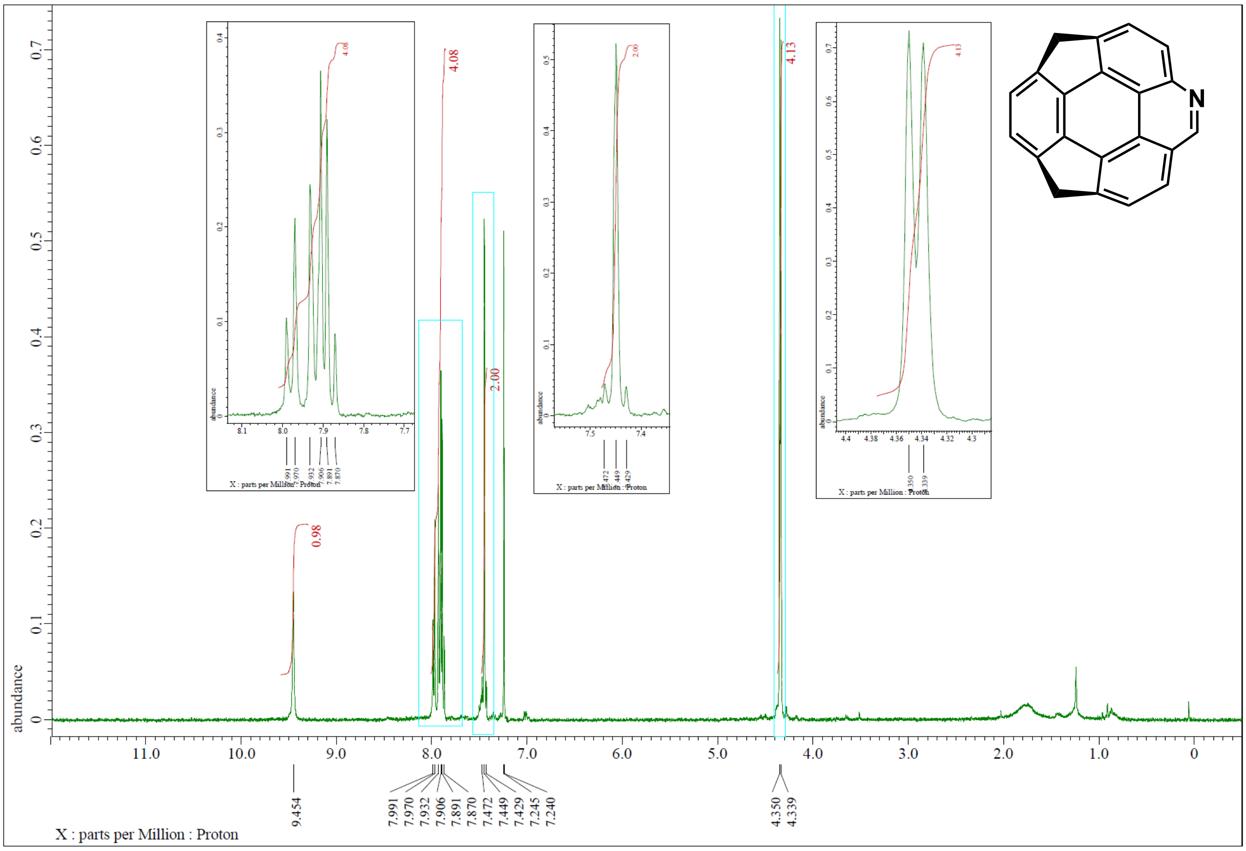

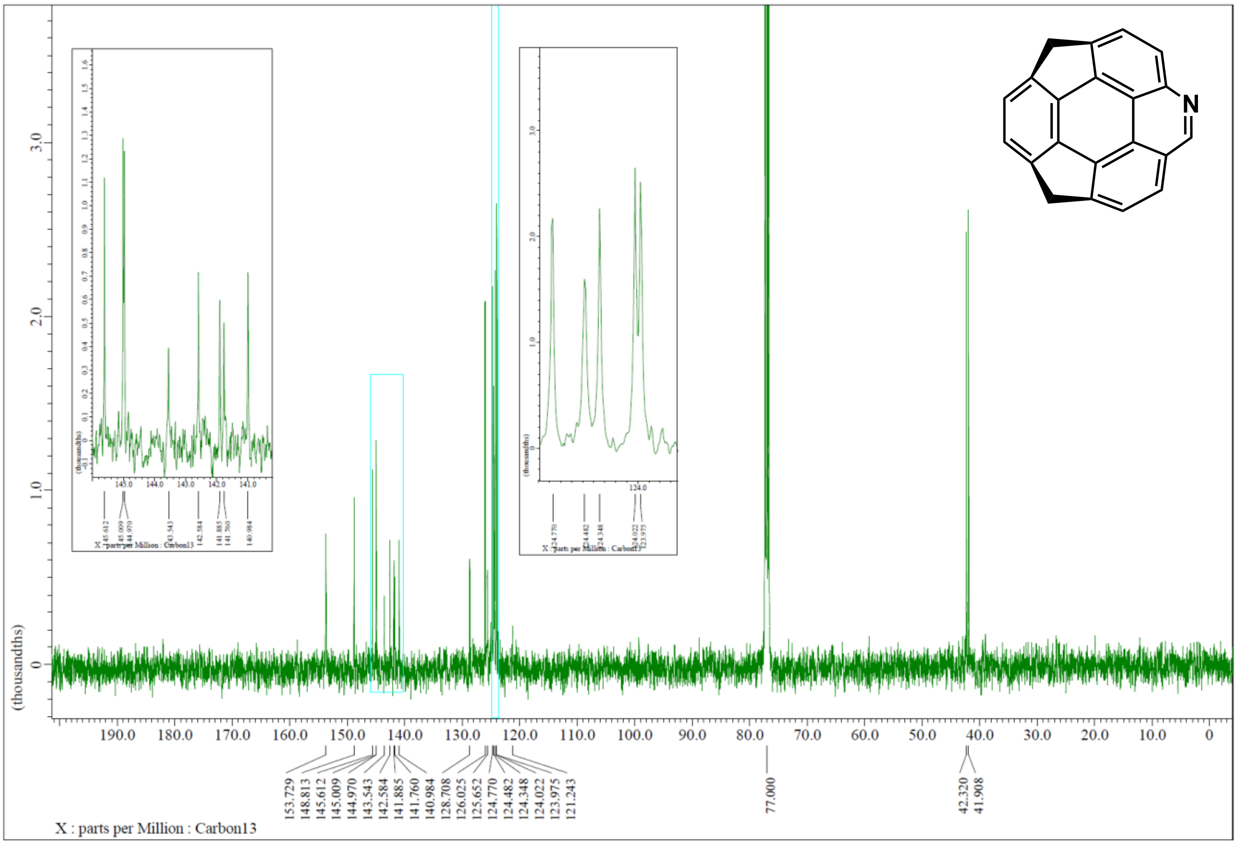

^{1}H NMR (400 MHz) spectrum of **11** ($CDCl_3$).

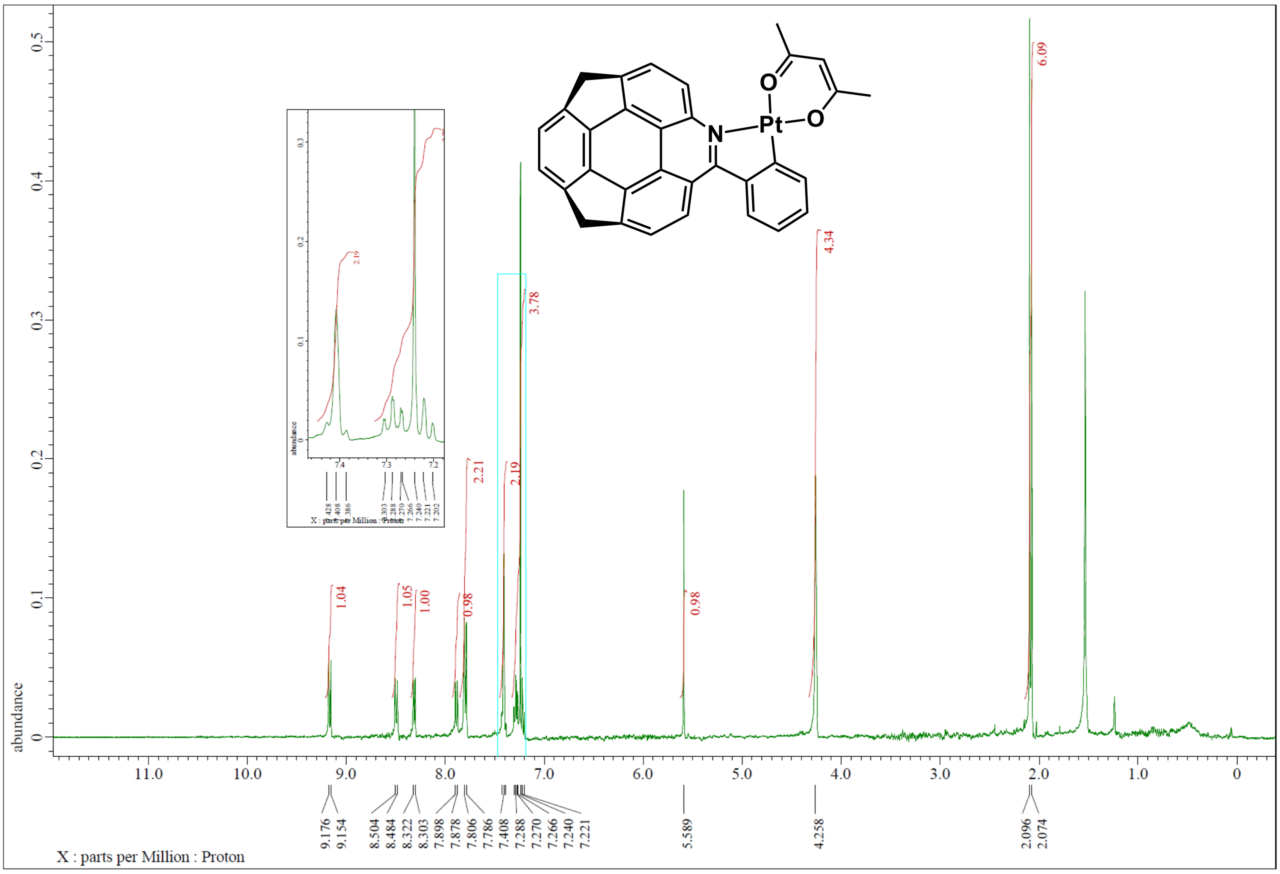

References

1. a) J. R. Donald, W. P. Unsworth, *Chem. Eur. J.* **2017**, *23*, 8780–8799. b) B. Biletskyi, P. Colonna, K. Masson, J.-L. Parrain, L. Commeiras, G. Chouraqui, *Chem. Soc. Rev.* **2021**, *50*, 7513–7538.
2. S. H. Pun, C. K. Chan, J. Luo, Z. Liu, Q. Miao, *Angew. Chem. Int. Ed.* **2018**, *57*, 1851–1856.
3. a) X. Li, Y. Zhu, J. Shao, L. Chen, S. Zhao, B. Wang, S. Zhang, Y. Shao, H.-L. Zhang, X. Shao, *Angew. Chem. Int. Ed.* **2015**, *54*, 267−271. b) Y. Sun, X. Li, C. Sun, H. Shen, X. Hou, D. Lin, H.-L. Zhang, C. Di, D. Zhu, X. Shao, *Angew. Chem. Int. Ed.* **2017**, *56*, 13470−13474. c) S. Wang, C. Yan, W. Zhao, X. Liu, C.-S. Yuan, H.-L. Zhang, X. Shao, *Chem. Sci.* **2021**, *12*, 5811−5817.
4. a) S. Hishikawa, Y. Okabe, R. Tsuruoka, S. Higashibayashi, H. Ohtsu, M. Kawano, Y. Yakiyama. H. Sakurai, *Chem. Lett.* **2017**, *46*, 1556−1559. b) Y. Yakiyama, S. Hishikawa, H. Sakurai, *Beilstein J. Org. Chem.* **2020**, *16*, 681−690.
5. S. Alvi, R. Ali, *Beilstein J. Org. Chem.* **2020**, *16*, 2212–2259.
6. T. Amaya, M. Hifumi, M. Okada, Y. Shimizu, T. Moriuchi, K. Segawa, Y. Ando, T. Hirao, *J. Org. Chem.* **2011**, *76*, 8049−8052.
7. H. Kotsuki, K. Arimura, T. Araki, T. Shinohara, *Synlett* **1999**, *4*, 462−464.
8. R. C. Haddon, *J. Am. Chem. Soc.* **1987**, *109*, 1676−1685.
9. K. Kanagaraj, K. Lin, W. Wu, G. Gao, Z. Zhong, D. Su, C. Yang, *Symmetry* **2017**, *9*, 174.
10. S. Higashibayashi, H. Sakurai, *J. Am. Chem. Soc.* **2008**, 130, 8592−8593.
11. a) Q. Tan, S. Higashibayashi, S.Karanjit, H. Sakurai, *Nat. Commun.* **2012**, *3*, 891. b) Q. Tan, P. Kaewmati, S. Higashibayashi, M. Kawano, Y. Yakiyama, H. Sakurai, *Bull. Chem. Soc. Jpn.* **2018**, *91*, 531−537.
12. H. Sakurai, T. Daiko, H. Sakane, T. Amaya, T. Hirao, *J. Am. Chem. Soc.* **2005**, 127, 11580−11581.

13. H. Sakurai, T. Daiko, T. Hirao, *Science* **2003**, *301*, 1878.
14. a) U. D. Priyakumar, G. N. Sastry, *J. Phys. Chem. A* **2001**, *105*, 4488−4494. b) T. Amaya, H. Sakane, T. Muneishi, T. Hirao, *Chem. Commun.* **2008**, 765−767. c) N. Ngamsomprasert, G. Panda, S. Higashibayashi, H. Sakurai, *J. Org. Chem.* **2016**, *81*, 11978−11981.
15. a) L. T. Scott, M. M. Hashemi, M. S. Bratcher, *J. Am. Chem. Soc.* **1992**, *114*, 1920−1921. b) T. J. Seiders, K. K. Baldridge, G. H. Grube, J. S. Siegel, *J. Am. Chem. Soc.* **2001**, *123*, 517−525. c) K. Kawasumi, Q. Zhang, Y. Segawa, L. T. Scott, K. Itami, *Nat. Chem.* **2013**, *5*, 739−744.
16. M. E. Jung, D. A. Allen, *Org. Lett.* **2009**, *11*, 757−760.
17. S.-M. Lu, H. Alper, *J. Am. Chem. Soc.* **2005**, *127*, 14776−14784.
18. A. Vriza, A. B. Canaj, R. Vismara, L. J. K. Cook, T. D. Manning, M. W. Gaultois, P. A. Wood, V. Kurlin, N. Berry, M. S. Dyer, M. J. Rosseinsky, *Chem. Sci.* **2021**, *12*, 1702−1719.
19. D. K. Sen, *Acta Crystallogr.* **1970**, *B26*, 1629−1630.

20. a) M. Yamada, S. Tashiro, R. Miyake, M. Shionoya, *Dalton Trans.* **2013**, *42*, 3300−3303. b) J. W. Facendola, M. Seifrid, J. Siegel, P. I. Djurovich, M. E. Thompson, *Dalton Trans.* **2015**, *44*, 8456−8466.
21. A. Bossi, A. F. Rausch, M. J. Leitl, R. Czerwieniec, M. T. Whited, P. I. Djurovich, H. Yersin, M. E. Thompson, *Inorg. Chem.* **2013**, *52*, 12403−12415.
22. R. F. W. Bader, *Acc. Chem. Res.* **1985**, 18, 9−15.
23. a) J. Brooks, Y. Babayan, S. Lamansky, P. I. Djurovich, I. Tsyba, R. Bau, M. E. Thompson, *Inorg. Chem.* **2002**, *41*, 3055−3066. b) R. C. Evans, P. Douglas, C. J. Winscom, *Coord. Chem. Rev.* **2006**, *250*, 2093−2126.
24. L. C. Vishwakarma, O. D. Stringer, F. A. Davis, *Org. Synth.* **1988**, *66*, 203−210.
25. Gaussian 09, Revision A.02, M. J. Frisch, G. W. Trucks, H. B. Schlegel, G. E. Scuseria, M. A. Robb, J. R. Cheeseman, G. Scalmani, V. Barone, G. A. Petersson, H. Nakatsuji, X. Li, M. Caricato, A. Marenich, J. Bloino, B. G. Janesko, R. Gomperts, B. Mennucci, H. P. Hratchian, J. V. Ortiz, A. F. Izmaylov, J. L. Sonnenberg, D. Williams-Young, F. Ding, F. Lipparini, F. Egidi, J. Goings, B. Peng, A. Petrone, T. Henderson, D. Ranasinghe, V. G. Zakrzewski, J. Gao, N. Rega, G. Zheng, W. Liang, M. Hada, M. Ehara, K. Toyota, R. Fukuda, J. Hasegawa, M. Ishida, T. Nakajima, Y. Honda, O. Kitao, H. Nakai, T. Vreven, K. Throssell, J. A. Montgomery, Jr., J. E. Peralta, F. Ogliaro, M. Bearpark, J. J. Heyd, E. Brothers, K. N. Kudin, V. N. Staroverov, T. Keith, R. Kobayashi, J. Normand, K. Raghavachari, A. Rendell, J. C. Burant, S. S. Iyengar, J. Tomasi, M. Cossi, J. M. Millam, M. Klene, C. Adamo, R. Cammi, J. W. Ochterski, R. L. Martin, K. Morokuma, O. Farkas, J. B. Foresman, and D. J. Fox, Gaussian, Inc., Wallingford CT, 2016.
26. P. J. Stephens, F. J. Devlin, C. F. Chabalowski, M. J. Frisch, *J. Phys. Chem.* **1994**, *98*, 11623–11627.
27. T. H. Dunning. Jr., *J. Chem. Phys.* **1989**, *90*, 1007–1023.
28. a) R. Ditchfield, W. J. Hehre, J. A. Pople, *J. Chem. Phys.* **1971**, *54*, 724–728. b) W. J. Hehre, R. Ditchfield, J. A. Pople, *J. Chem. Phys.* **1972**, *56*, 2257–2261. c) P. C. Hariharan, J. A. Pople, *Theor. Chim. Acta.* **1973**, *28*, 213–222. d) M. M. Francl, W. J. Pietro, W. J. Hehre, J. S. Binkley, M. S. Gordon, D. J. DeFrees, J. A. Pople, *J. Chem. Phys.* **1982**, *77*, 3654–3665. e) M. S. Gordon, J. S. Binkley, J. A. Pople, W. J. Pietro, W. J. Hehre, *J. Am. Chem. Soc.* **1982**, *104*, 2797–2803.
29. a) P. J. Hay, W. R. Wadt, *J. Chem. Phys.* **1985**, *82*, 270–283. b) W. R. Wadt, P. J. Hay, *J. Chem. Phys.* **1985**, *82*, 284–298. c) P. J. Hay, W. R. Wadt, *J. Chem. Phys.* **1985**, *82*, 299–310.
30. a) T. Yanai, D. P. Tew, N. C. Handy, *Chem. Phys. Lett.* **2004**, *393*, 51–57. b) F. Weigend, R. Ahlrichs, *Phys. Chem. Chem. Phys.* **2005**, *7*, 3297–3305.
31. T. Lu, F. Chen, *J. Comput. Chem.* **2012**, *33*, 580−592.
32. Humphrey, W.; Dalke, A.; Schulten, K. VMD: Visual Molecular Dynamics, *J. Mol. Graph.* **1996**, *14*, 33−38.
33. W. Minor, M. Cymborowski, Z. Otwinowski, M. Chruszcz, *Acta Crystallogr.* **2006**, *D62*, 859−866.

34. Henkankun-R is a software for converting Dectris-PILATUS and EIGER frames to the SFRM format written by S. Shikama, R. Nishino, M. Minoura, November, 2018, available at SPring-8.

35. CrysAlis PRO; Rigaku Oxford Diffraction: Yarnton, U.K., 2015.

36. a) G. M. Sheldrick, SHELXT − Integrated space-group and crystal-structure determination. *Acta Crystallogr., Sect. A: Found. Adv.* **2015**, 71, 3−8. b) G. M. Sheldrick, Crystal structure refinement with SHELXL. *Acta Crystallogr., Sect. C: Struct. Chem.* **2015**, *71*, 3−8.

37. O. V. Dolomanov, L. J. Bourhis, R. J. Gildea, J. A. K. Howard, H. Puschmann, *OLEX2*: a complete structure solution, refinement, and analysis program. *J. Appl. Crystallogr.* **2009**, *42*, 339−341.

Chapter 3. Acid-mediated Carbon-carbon Bond Cleavage on a Bowl-shaped Sumanenone

Section 1. Introduction

The inherent strain in a molecule has a significant impact on its reactivity. Curved π-conjugated molecules such as fullerenes and buckybowls possess unique physical properties and display distinct reactivity compared with planar π-conjugated molecule.[1] It has been observed that addition reactions take place in the distorted aromatic rings of fullerenes and buckybowls that would not normally occur in planar molecules.[2] These reactions are often driven by intrinsic molecular distortions, leading to the functionalization of curved π-conjugated molecules. Another type of chemical transformations driven by strain in curved π-conjugated molecules is C-C bond cleavage. For example, the C-C bond cleavage of fullerenes has been utilized in the synthesis of endohedral fullerenes[3] through molecular surgery, and in the synthesis of azafullerenes.[4] There have also been several reports of C-C bond cleavage reactions in buckybowls, which correspond to the partial structure of fullerenes. Shionoya et al. reported the iridium-catalyzed reductive C-C bond cleavage of 2-pyridylcorannulene.[5] Shao et al. reported a ring-opening reaction involving C-C bond cleavage of hexaalkoxytrithiasumanene with oxone under mild conditions and its application to the synthesis of unique [5-6-7] fused polyheterocyclic compounds.[6] This development of chemical transformations using C-C bond cleavage is significant for synthesizing unique π-conjugated molecules that cannot be accessed using other synthetic methods.

Sumanene, similar to corannulene, is a C60 fragment known as a buckybowl with an aromatic ring moiety and reactive benzyl positions. Chemical modifications of its peripheral and internal carbons have been intensively studied.[7] Sumanene has a more distorted bowl structure than corannulene, but its C-C bond cleavage reaction has not been reported. In this study, the author describes that ring-opening hydrolysis proceeds under acidic conditions on the curved sumanenone **2** skeleton to give the planar carboxylic acid as a product (Scheme 7). This reaction did not occur with fluorenone, the planar analogue of **2**, suggesting that the bowl structure plays a crucial role in this reaction.

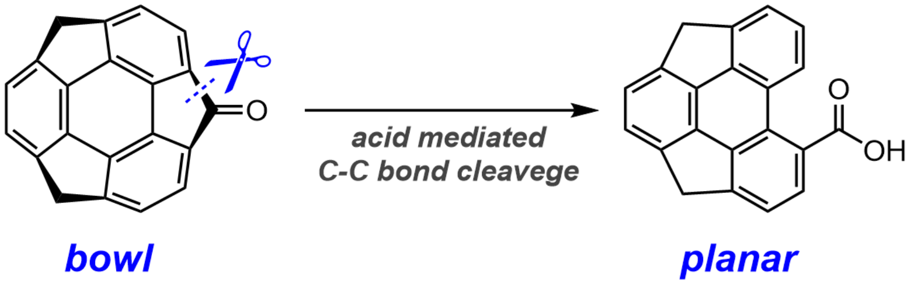

Scheme 7. Acid-mediated C-C bond cleavage of sumanenone.

Section 2. Acid-mediated ring-opening reaction of sumanenone

In Chapter 2, the author described that the carbonyl group of sumanenone **2** is activated by adding TfOH, and Baeyer-Villiger oxidation proceeds in moderate yield. During that study, the ring-opening reaction proceeded when TfOH was added to **2** in acetic acid to afford the corresponding carboxylic acid **12** (Scheme 8). ^{1}H NMR spectra of the crude mixture showed that the starting material was completely consumed, and only the product peak was observed, suggesting that **12** was produced almost quantitatively. Finally, **12** was obtained in 91% yield by only extraction and washing process. This reaction did not proceed without TfOH, implying that the addition of a strong acid is essential. The reaction did not proceed below 100 °C, and the starting material was recovered, indicating that heating was also necessary (Table 6).

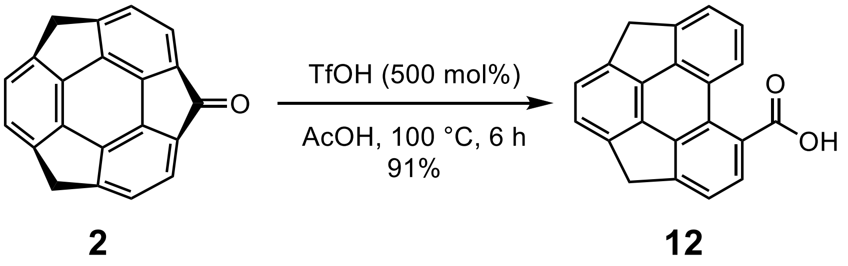

Scheme 8. Acid-mediated ring opening reaction of **12**.

Table 6. Condition screening.

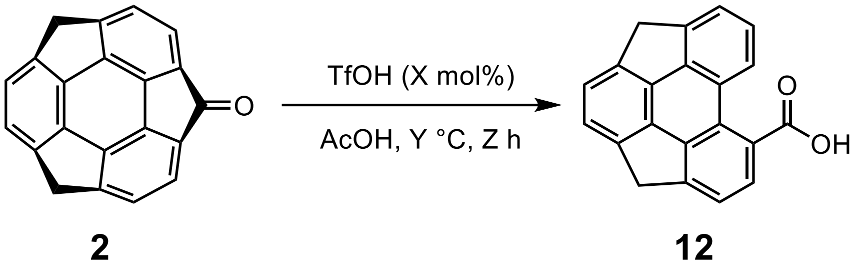

entry	TfOH (X mol%)	temperature (Y °C)	time (h)	yield of **12** (%)[a]
1	500	100	6	91
2	0	100	2	0
3	500	27	24	0

Reaction conditions: **2** (18 μmol, 100 mol%), AcOH (0.5 mL), under air. [a] Isolated yield.

12 was characterized by high-resolution mass spectroscopy and NMR measurement. High-resolution mass spectroscopy showed *m*/*z* = 296.0837 ([M$^+$]), suggesting the formation of **12**. The ^{1}H NMR spectra of **2** and **12** and their assignments are shown in Figures 27b and 27c. This assignment was also in good agreement with the ^{1}H NMR predictions from the NMR-GIAO[8] calculations at the B3LYP/6-311+G(d) level (Table 7). Comparing the ^{1}H NMR spectrum of product **12** with that of starting material (**2**), the total integration of aromatic protons increased from 6 to 7 protons (Figures 27b and 27c). The H^i signal in Figure 27c was observed at lower fields than the other aromatic protons, suggesting a deshielding effect from the adjacent carboxyl groups. In the case of **2**, due to the deep bowl structure, benzylic *endo* and *exo* protons' signals are observed as doublets with *J*-coupling constants of about 20 Hz due to the geminal coupling.[9] On the other hand, signals derived from the benzyl protons H^c and H^f in **12** are observed as singlet peaks at 4.48 ppm and 4.51 ppm, respectively. This supports that **12** has a planar structure.

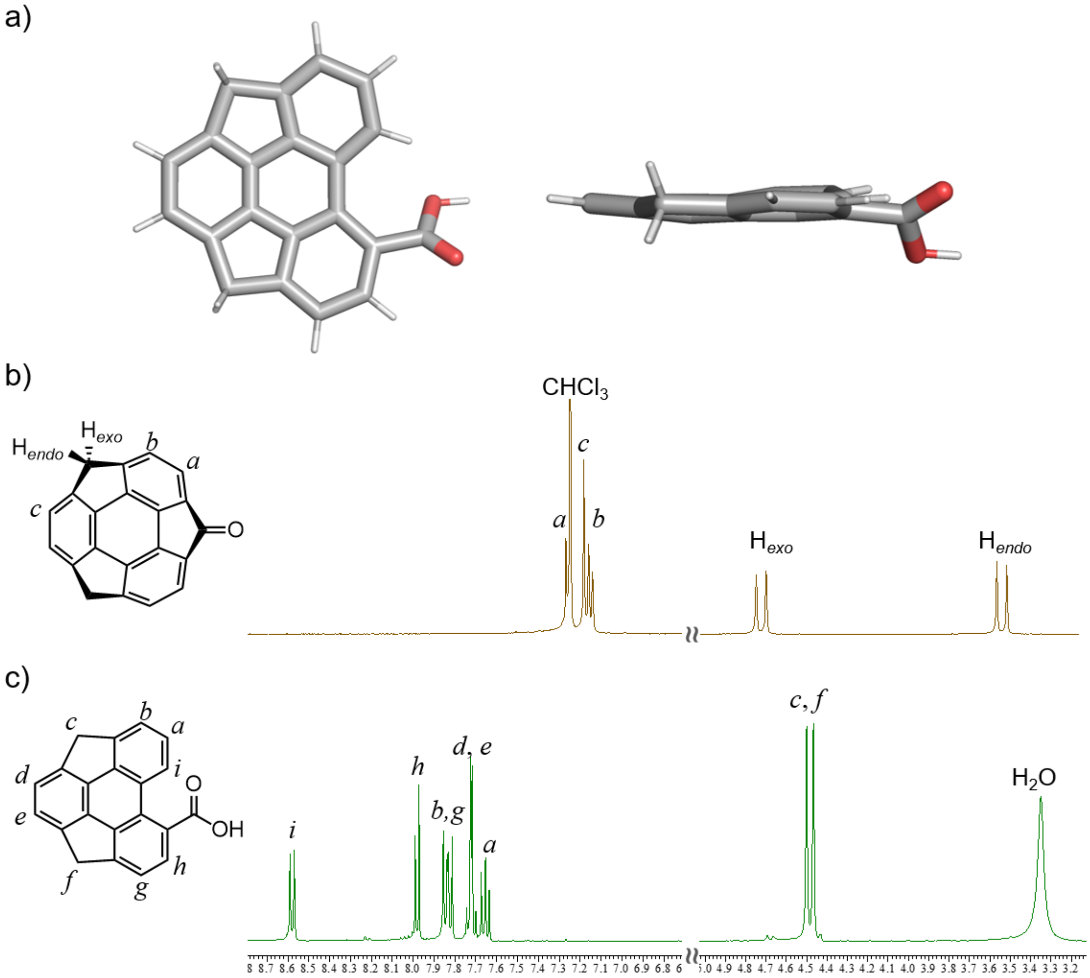

Figure 27. a) The optimized structure of **2** at the B3LYP/6-311G+G(d) level of theory, and ^{1}H NMR spectra of b) **2** in $CDCl_3$ and c) **12** in DMSO-d_6.

Table 7. Experimental and calculated ^{1}H NMR chemical shifts of **12**. The calculated chemical shift was given by TMS (B3LYP/6-311G+(2d,p)) as a reference.

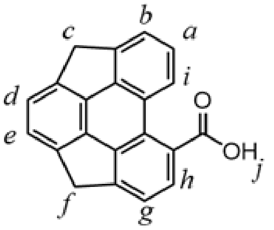

Protons	Experimental (ppm)	Calculation (ppm)
a	7.65	7.50
b	7.82	7.57
c	4.50	4.39, 4.00
d	7.74	7.51
e	7.71	7.48
f	4.47	4.24, 3.96
g	7.85	7.50
h	7.98	8.12
i	8.58	8.66
j	13.4	5.79

To elucidate the structure of **12** by single crystal X-ray diffraction analysis, recrystallization of **12** was conducted to prepare a single crystal. However, only a powdery fine crystalline solid was obtained, and a single crystal with sufficient size for measurement could not be obtained. Thus, methylation of **12** was conducted to improve crystallinity by converting the carboxy group of **12** to a methyl ester. The corresponding methyl ester **12-Me** was obtained in 92% yield by the reaction of trimethylsilyl diazomethane with **12** in a toluene/methanol mixture (Scheme 9).[10] Recrystallization of **12-Me** provided tiny needle crystals. However, they are still small to perform the X-ray measurement. To improve the crystallinity, screening of ester moieties, such as ester formation with *p*-bromophenol, would be necessary.

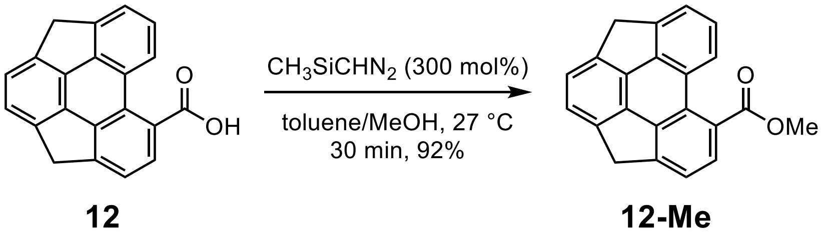

Scheme 9. Methylation of **12**.

Section 3. Comparison of the reactivity between the bowl and planar molecules

To investigate the difference in reactivity between planar and curved π-systems, the same reaction was examined in fluorenone **13**, which corresponds to the planar substructure of **12**. Ring-opening hydrolysis of **13** has been reported to proceed under high temperature in the presence of the excess base.[11] However, ring-opening hydrolysis of **13** under acidic conditions has not been reported to the best of the author's knowledge. Therefore, the ring-opening reaction of **13** was performed under the same conditions as **2**, but the reaction did not proceed, and **13** was recovered (Scheme 10). This suggests that the strained bowl structure plays a vital role in this reaction.

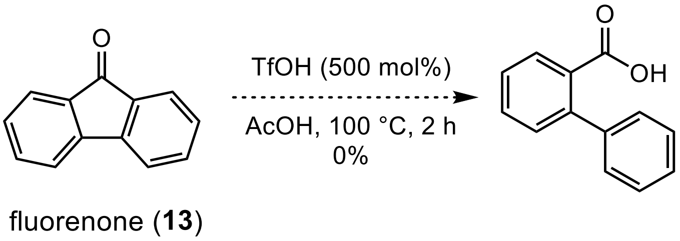

Scheme 10. Acid-mediated ring-opening reaction of fluorenone **13**.

A possible reaction mechanism is shown in figure 28. First, the carbonyl group of **2** is protonated by acid to form an oxonium ion, which reacts with acetic acid to form the corresponding tetrahedral intermediate. Subsequently, the sp^2 carbon at the α-position of the quaternary carbon center is protonated by TfOH, a superacid, to form a cationic intermediate. A similar reaction involving the electrophilic addition of bromonium ions to the sumanene skeleton has been reported.[12] The cationic intermediate undergoes ring-opening with strain-release to give the corresponding mixed acid anhydride, and the following hydrolysis affords the target compound. The driving force of this reaction is releasing the bowl strain in the ring-opening step, resulting in a planar structure.

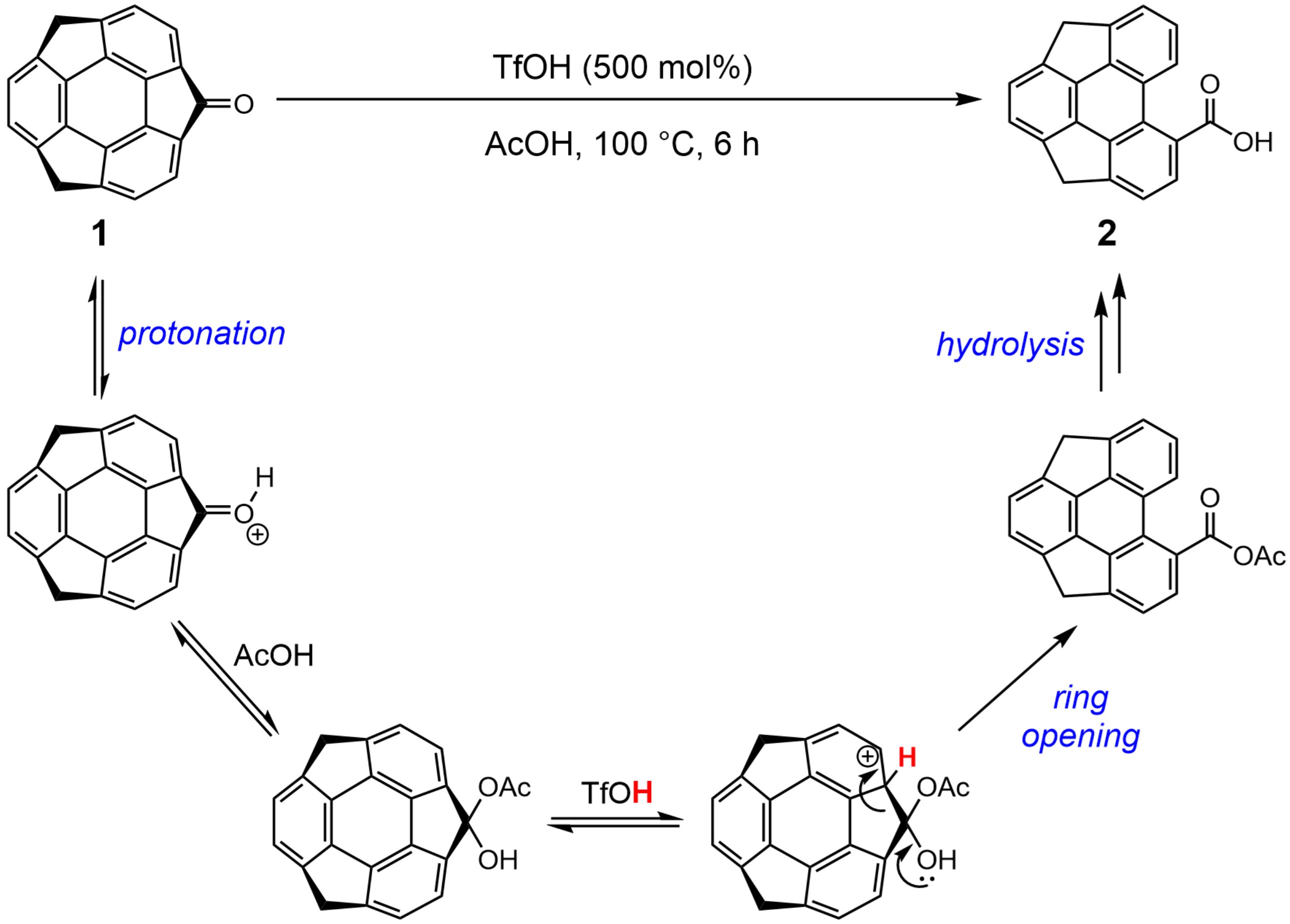

Figure 28. Possible reaction mechanism.

Section 4. Summary

In this chapter, the ring-opening reaction involving acid-mediated C-C bond cleavage of the sumanene skeleton was described. Such ring-opening reactions do not proceed in the analogous planar molecules, suggesting that the release of the curved strain is essential. To the best of the author's knowledge, this is the first example of a ring-opening C-C bond cleavage reaction in sumanene. This result indicates that the curved π-conjugated system exhibits unique reactivity due to its strained structure. The resulting carboxylic acid is expected to be a valuable precursor for reconstructing heteroatom-doped buckybowls or novel planar π-conjugated molecules with the unique polycyclic skeleton.

Experimental section

General information about instruments and measurements is provided in chapter 2, experimental section.

Chemicals

Unless otherwise noted, all reagents purchased from commercial suppliers were used without further purification.

Acetic acid (AcOH), dichloromethane (CH_2Cl_2), ethyl acetate (EtOAc), methanol (MeOH), and chloroform ($CHCl_3$), and toluene were purchased from FUJIFILM Wako Pure Chemical Corporation.

Fluorenone, Trifluoromethanesulfonic Acid (TfOH), and trimethylsilyl diazomethane (Me_3SiCHN_2) were purchased from Tokyo Chemical Industry Co., Ltd.

Anhydrous sodium sulfate (Na_2SO_4) was purchased from KISHIDA CHEMICAL Co., Ltd.

Synthetic Procedure and Characterization Data.

***Ring-opened carboxylic acid* 12**. To a test tube equipped with a magnetic stir bar were added sumanenone (**2**) (10.0 mg, 36.0 μmol, 100 mol%) and AcOH (1.0 mL). To the mixture was added trifluoromethanesulfonic acid (14.0 μL, 110 μmol, 500 mol%), and the mixture was stirred for 6 h at 100 °C under aerobic atmosphere. After stirring for 6 h, the reaction mixture was cool to room temperature. Then, the mixture was carefully poured into saturated aqueous $NaHCO_3$ solution (ca. 10 mL). The mixture was extracted with ethyl acetate (ca. 10 mL × 3). The combined organic extract was washed with brine (ca. 25 mL), dried over Na_2SO_4. After filtration, the filtrate was concentrated under reduced pressure. The residue was reprecipitated from CH_2Cl_2 and *n*-hexane, then the precipitate was collected by filtration and washed with *n*-hexane to give **6** (9.7 mg, 33 μmol, 91%) as a white solid; R_f = 0.1 (CH_2Cl_2: MeOH=9:1); Melting point: 245 °C (dec.); ^{1}H NMR (DMSO-d_6, 400 MHz) δ 13.4 (s, br, 1H), 8.58 (d, J = 8.4 Hz, 1H), 7.98 (d, J = 7.6 Hz, 1H), 7.85 (d, J = 6.9 Hz, 1H), 7.82 (d, J = 6.9 Hz, 1H), 7.74 (d, J = 7.6 Hz, 1H), 7.71 Hz (d, J = 7.6 Hz, 1H), 7.65 (dd, J = 8.4 Hz, J = 6.9 Hz, 1H), 4.50 (s, 2H), 4.47 (s, 2H); ^{13}C{^{1}H} NMR ($CDCl_3$, 100 MHz) δ 171.0 (1C), 147.6 (1C), 144.6 (1C), 138.33 (1C), 138.29 (1C), 137.24 (1C), 137.17 (1C), 134.4 (1C), 133.6 (1C), 130.0 (1C), 129.1 (1C), 127.5 (1C), 126.2 (1C), 125.0 (1C), 123.98 (1C), 123.95 (1C), 123.6 (1C), 123.15 (1C), 123.10 (1C) (two signals are overlapped to the residual solvent peak.); IR (KBr, cm^{-1}) 2906, 1671, 1396, 1284, 1255, 765; HRMS (EI$^+$) *m*/*z*: [M]$^+$ Calcd for $C_{21}H_{12}O_2$ 296.0837; Found 296.0841.

***Methyl ester* 12-Me**. To a test tube equipped with a magnetic stir bar were added **2** (10.0 mg, 33.9 μmol, 100 mol%), toluene (1.4 mL), and CH_3OH (0.4 mL). To the mixture was added Me_3SiCHN_2 solution (ca. 0.6 mol/L in *n*-hexane, 0.17 mL, 0.10 mmol, 300 mol%) at 27 °C, and the mixture was stirred for 30 min at the same temperature. After stirring for 30 min, to the mixture was added H_2O solution (ca. 10 mL). The mixture was extracted with $CHCl_3$ (ca. 10 mL × 3). The combined organic extract was washed with brine (ca. 10 mL), and dried over Na_2SO_4. After filtration, the filtrate was concentrated under reduced pressure. The residue was purified by PTLC ($CHCl_3$) to give **12-Me** (9.7 mg, 31.2 μmol, 92%) as a white solid; $R_f = 0.51$ ($CHCl_3$); Melting point: 157 °C (dec.); ^{1}H NMR ($CDCl_3$, 400 MHz) δ 8.51 (d, $J = 8.2$ Hz, 1H), 8.03 (d, $J = 7.3$ Hz, 1H), 7.76 (d, $J = 6.9$ Hz, 1H), 7.73 (d, $J = 6.9$ Hz, 1H), 7.70 (d, $J = 7.3$ Hz, 1H), 7.66 Hz (d, $J = 7.6$ Hz, 1H), 7.63 (dd, $J = 8.2$ Hz, $J = 6.9$ Hz, 1H), 4.45 (s, 2H), 4.44 (s, 2H), 4.14 (s, 3H); ^{13}C{^{1}H} NMR ($CDCl_3$, 100 MHz) δ 170.3 (1C), 148.6 (1C), 144.7 (1C), 139.4 (1C), 139.3 (1C), 137.6 (1C), 137.2 (1C), 135.4 (1C), 134.4 (1C), 129.8 (1C), 128.3 (1C), 127.4 (1C), 126.8 (1C), 125.5 (1C), 125.4 (1C), 123.7 (1C), 123.2 (1C), 122.7 (1C), 122.4 (1C), 52.5 (1C), 40.1 (1C), 40.0 (1C); IR (KBr, cm^{-1}) 2925, 1720, 1397, 1248, 1149, 766; HRMS (EI$^+$) *m*/*z*: [M]$^+$ Calcd for $C_{22}H_{14}O_2^+$ 310.0994; Found 310.0985.

Computational study

Otherwise noted, all structure optimizations, self-consistent field (SCF) energies, and thermal energy correction calculations using density functional theory (DFT) were performed using Gaussian 09 suite of programs (revision E.01)[13] at B3LYP[14] level of theory in gas phase with 6-311+G(d)[15] as a basis set. GIAO was also calculated at B3LYP level of theory in gas phase with 6-311+G(d) as a basis set.

^{1}H NMR (400 MHz) and ^{13}C{^{1}H}NMR (100 MHz) of **12** (DMSO-d_6, 25 °C).

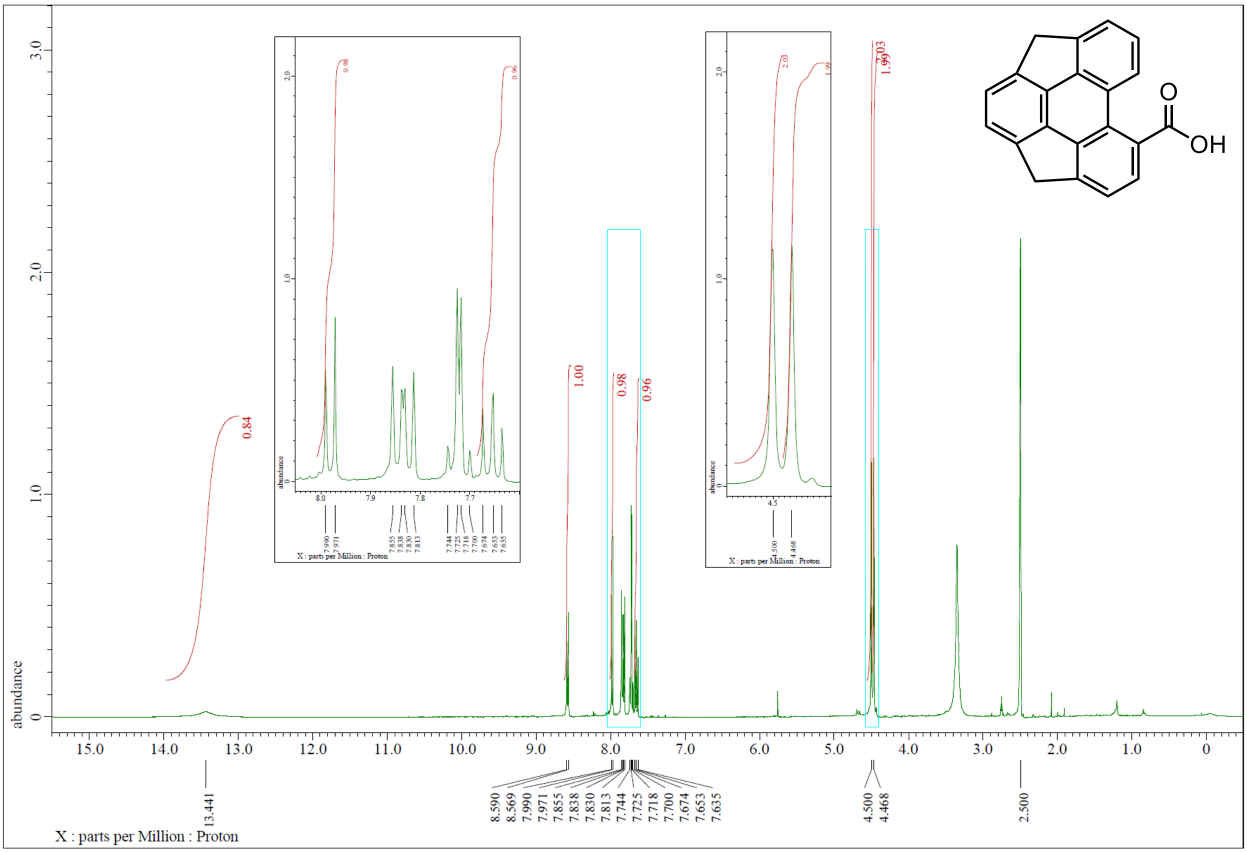

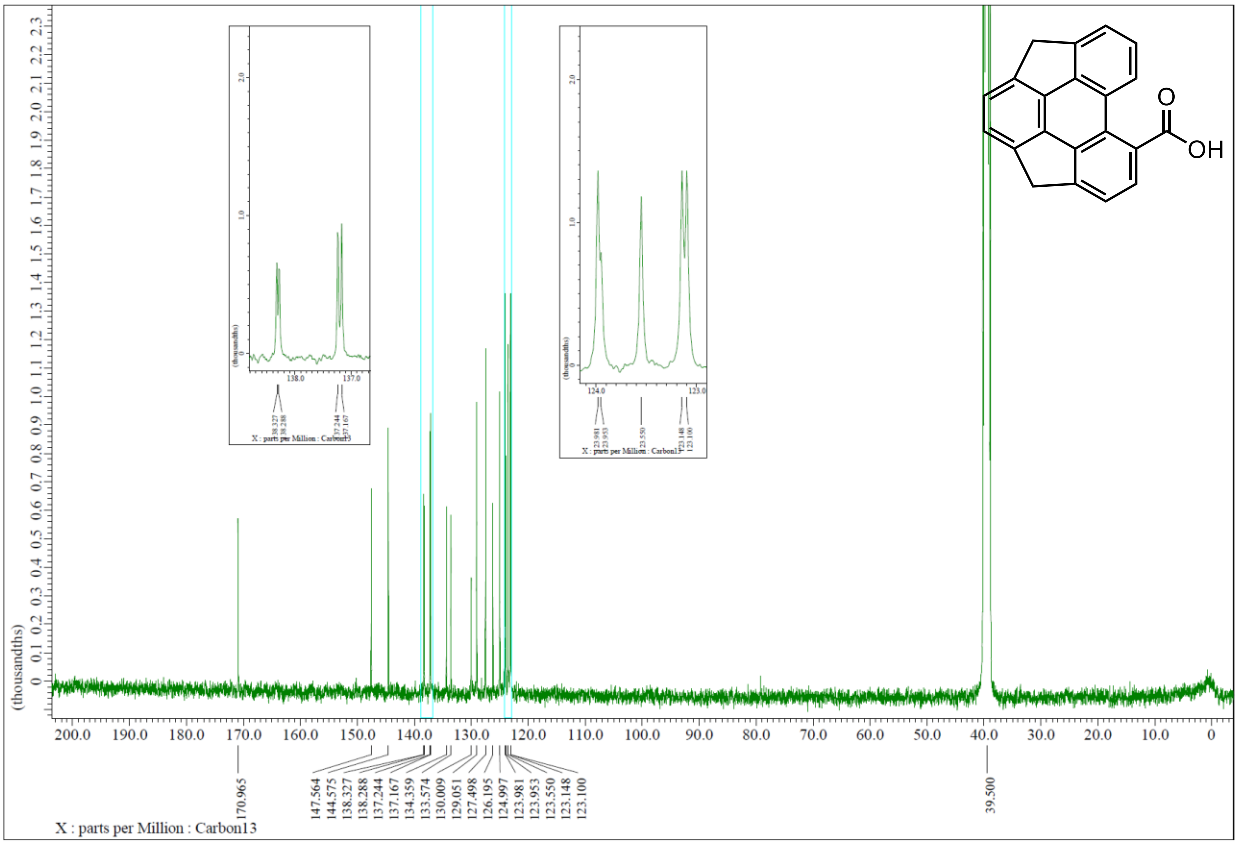

^{1}H NMR (400 MHz) and ^{13}C{^{1}H}NMR (100 MHz) spectra of **12-Me** (CDCl$_3$, 25 °C).

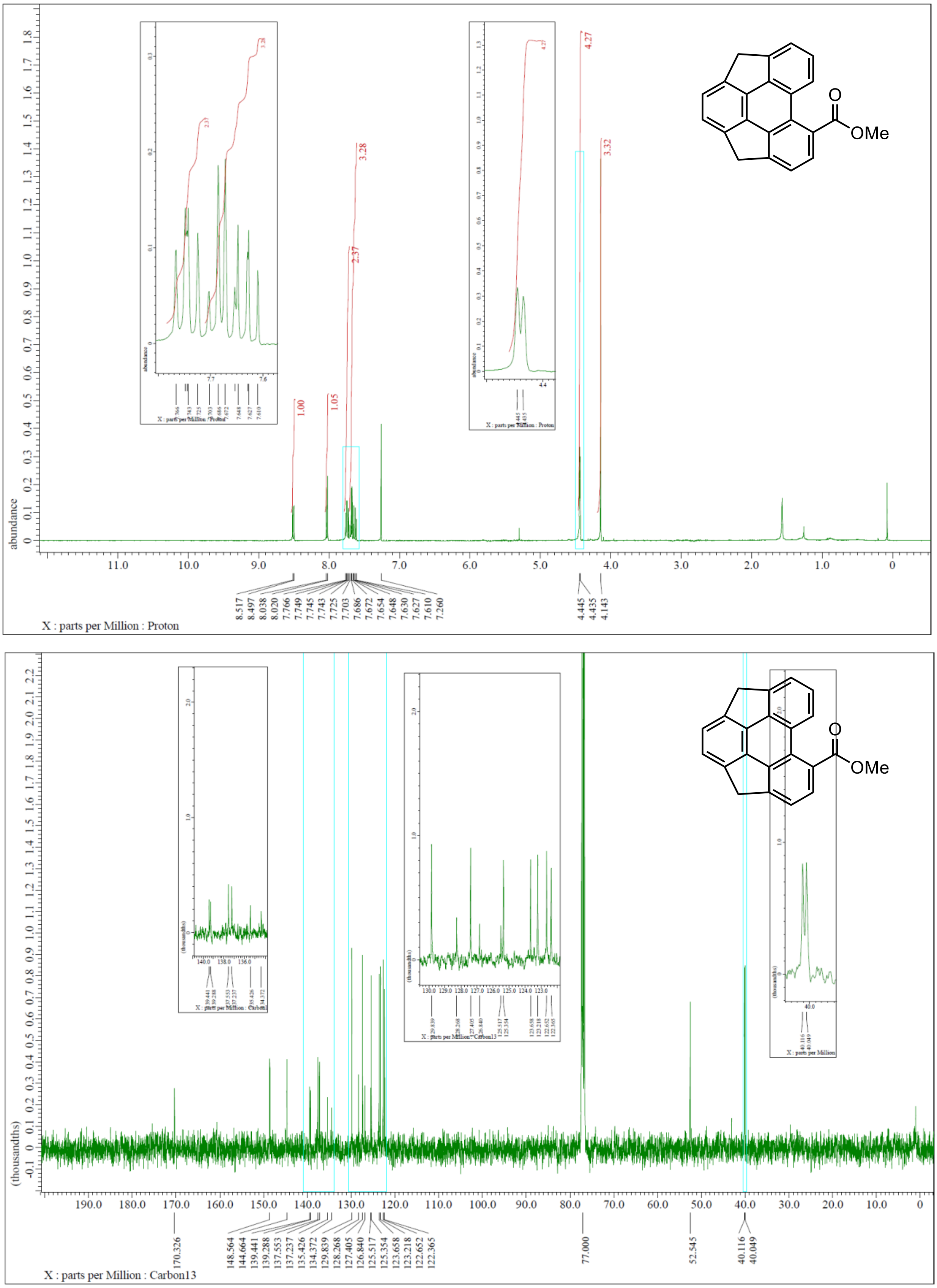

References

1. a) H. W. Kroto, J. R. Heath, S. C. O'Brien, R. F. Curl, R. D. Smalley, *Nature* **1985**, *318*, 162−163. b) R. C. Haddon, *Science* **1993**, *261*, 1545−1550. c) Y.-T. Wu, J. S. Siegel, *Chem. Rev.* **2006**, *106*, 4843−4867. d) V. M. Tsefrikas, L. T. Scott, *Chem. Rev.* **2006**, *106*, 4868−4884. e) M. Saito, H. Shinokubo, H. Sakurai, *Mater. Chem. Front.* **2018**, *2*, 635−661.
2. a) Hirsch, A. *Synthesis* **1995**, *8*, 895−913. b) M. Plato, *J. Mater. Chem.* **1997**, *7*, 1097–1109. c) F. Diederich, C. Thilgen, *Science* **1997**, *271*, 317−324. d) Y. Matsuo, E. Nakamura, *Chem. Rev.* **2008**, *108,* 3016−3028. e) D. V. Preda, L. T. Scott, *Tetrahedron Lett*. **2000**, *41*, 9633−9637. f) A. V. Zabula, S. N. Spisak, A. S. Filatov, A. Y. Rogachev, M. A. Petrukhina, *Angew. Chem. Int. Ed.* **2011**, *50*, 2971−2974. g) M. Yanney, F. R. Fronczek, A. Sygula, *Org. Lett.* **2012**, *14*, 4942−4945. h) H. E. Bronstein, L. T. Scott, *J. Org. Chem.* **2008**, 73, 88−93. i) J. A. Steckel, K. D. Jordan, *J. Phys. Chem. A*. **2002**, *106*, 2572–2579. j) H. Y. Cho, R. B. M. Ansems, L. T. Scott, *Beilstein J. Org. Chem.* **2014**, *10*, 956−968. k) N. Ikuma, Y. Yoshida, Y. Yakiyama, N. Ngamsomprasert, H. Sakurai, *Chem. Lett.* **2018**, *47*, 736−739.
3. a) K. Komatsu, M. Murata, Y. Murata, *Science* **2005**, *307*, 238–240. b) M. Murata, Y. Murata, K. Kumatsu, *Chem. Commun.* **2008**, 6083–6094; c) K. Kurotobi, Y. Murata, *Science* **2011**, *333*, 613–616.
4. J. C. Hummelen, B. Knight, J. Pavlovich, R. González, F. Wudl, *Science*, **1995**, 269, 1554–1556.
5. S. Tashiro, M. Yamada, M. Shionoya, *Angew. Chem. Int. Ed.* **2015**, *54*, 5351–5354.
6. X. Li, Y. Zhu, J. Shao, L. Chen, S. Zhao, B. Wang, S. Zhang, Y. Shao, H.-L. Zhang, X. Shao, *Angew. Chem. Int. Ed.* **2015**, *54*, 267−271.
7. S. Alvi, R. Ali, *Beilstein J. Org. Chem.* **2020**, *16,* 2212–2259.
8. K. Wolinski, J. F. Hilton, P. Pulay, *J. Am. Chem. Soc.* **1990**, *112*, 8251–8260.
9. T. Amaya, M. Hifumi, M. Okada, Y. Shimizu, T. Moriuchi, K. Segawa, Y. Ando, T. Hirao, *J. Org. Chem.* **2011**, *76*, 8049–8052.
10. T. Shioiri, T. Aoyama, S. Mori, *Org. Synth.* **1993**, *68*, 1–4.
11. R. Fittig, E. Ostermayer, *Justus Liebigs Ann. Chem.* **1873**, *166*, 361–382.
12. N. Ngamsomprasert, J.-S. Dang, S. Higashibayashi, Y. Yakiyama, H. Sakurai, *Chem. Commun.* **2017**, *53*, 697–700.
13. Gaussian 09, Revision E.01, M. J. Frisch, G. W. Trucks, H. B. Schlegel, G. E. Scuseria, M. A. Robb, J. R. Cheeseman, G. Scalmani, V. Barone, B. Mennucci, G. A. Petersson, H. Nakatsuji, M. Caricato, X. Li, H. P. Hratchian, A. F. Izmaylov, J. Bloino, G. Zheng, J. L. Sonnenberg, M. Hada, M. Ehara, K. Toyota, R. Fukuda, J. Hasegawa, M. Ishida, T. Nakajima, Y. Honda, O. Kitao, H. Nakai, T. Vreven, J. A. Montgomery, Jr., J. E. Peralta, F. Ogliaro, M. Bearpark, J. J. Heyd, E. Brothers, K. N. Kudin, V. N. Staroverov, T. Keith, R. Kobayashi, J. Normand, K. Raghavachari, A. Rendell, J. C. Burant, S. S. Iyengar, J. Tomasi, M. Cossi, N. Rega, J. M. Millam, M. Klene, J. E. Knox, J. B. Cross, V. Bakken, C. Adamo, J.

Jaramillo, R. Gomperts, R. E. Stratmann, O. Yazyev, A. J. Austin, R. Cammi, C. Pomelli, J. W. Ochterski, R. L. Martin, K. Morokuma, V. G. Zakrzewski, G. A. Voth, P. Salvador, J. J. Dannenberg, S. Dapprich, A. D. Daniels, O. Farkas, J. B. Foresman, J. V. Ortiz, J. Cioslowski, and D. J. Fox, Gaussian, Inc., Wall

14) T. Clark, J. Chandrasekhar, G. W. Spitznagel, P. v. R. Schleyer, *J. Comput. Chem.* **1983**, *4*, 294–301.

15) R. Krishnan, J. S. Binkley, R. Seeger, J. A. People, *J. Chem. Phys.* **1980**, *72*, 650–654.

Chapter 4. Thermodynamic Differentiation of the Two Sides of Azabuckybowl through Complexation with Square Planar Platinum(II)

Section 1. Introduction

As described in Chapter 1, Section 2, buckybowls have a curved molecular skeleton that results in two distinct faces: a concave face and a convex face. These faces have different orbital shapes and electronic states, leading to unique properties that are not found in planar π-conjugated molecules.[1] Examples of these properties include the dynamic interconversion of dipole moments due to bowl inversion,[2] face-selective adsorption on metal surfaces,[3] and ferroelectric properties induced by the application of an electric field[4]. Therefore, it is essential to develop a method to control the direction of the bowls in order to take advantage of these properties. To distinguish the two faces of the buckybowl, it is necessary to construct an asymmetric environment with respect to the plane containing the buckybowl (Figure 29a).

If the structures before and after bowl inversion are equivalent, they are enantiomers, and their concave/convex faces cannot be distinguished. On the other hand, if the isomers are dissymmetrized with respect to the plane containing bowl by introducing substituents, they are distinguishable diastereomers, and a difference in thermodynamic stability (ΔG) is generated between the isomers. The isomeric ratio is determined by this ΔG. Several methods for distinguishing concave/convex faces by chemical modification have been reported in previous studies. For example, since sumanene has reactive benzylic positions at its periphery, it is possible to dissymmetrize sumanenone by introducing a substituent (E) at the benzylic position (Figure 29b). Sakurai and Higashibayashi have reported that the isomeric ratio of monosubstituted sumanene derivatives changes depending on the substituent introduced at the benzyl position. Theoretical calculations revealed that this is due to the strength of the stereoelectronic effect between the π-conjugated system and the σ(C-E) bond of sumanene moiety.[5] For example, when substituent E is a hydroxyl group, the isomeric ratio between *endo*-E and *exo*-E is 90:10, whereas when the substituent E is a trimethylsilyl group, the ratio is 0:100. This result suggests that the choice of substituent can control the face of the bowl moiety. Buckybowl coordination with transition metals is another way to dissymmetrize the concave/convex faces.[6] Amaya and Hirao et al. synthesized η6-ruthenium complexes by the reaction of ruthenocenes and sumanene. The obtained ruthenium complex exists as a mixture of two isomers, *concave*-m and *convex*-m depending on the plane to which the ruthenium coordinates. The isomeric ratio of *concave*-m and *convex*-m is 75:25 in the solution state. The C-Ru bond length is long enough to induce bowl inversion behavior between the isomers while maintaining the π-coordination (Figure 29b).[7]

Compared to these previous studies, the author hypothesized that a transition metal complex using buckybowl as a monodentate ligand could be used to control the concave/convex isomers. In this case, not only the various structural features of transition metals are available but also various structures can be realized by combining with other ligands, and the isomer ratio can be flexibly controlled. Furthermore, the pyridine structure has been reported to form complexes with a variety of metals, making the preparation of complexes easier compared with the chemical modification of buckybowls. Also, the monodentate coordination manner is less likely to inhibit bowl inversion. Therefore, this dissymetrization method can combine the various structural features of transition metals with the features of buckybowls.

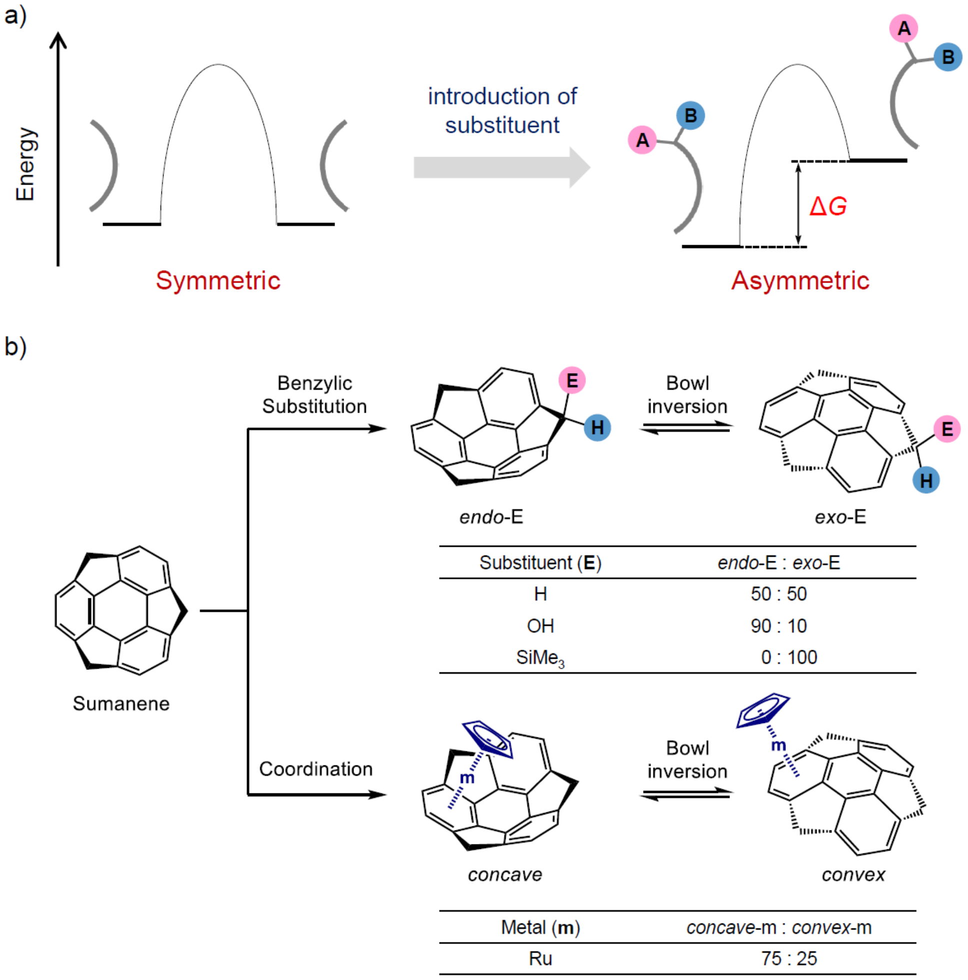

Substituent (**E**)	*endo*-E : *exo*-E
H	50 : 50
OH	90 : 10
$SiMe_3$	0 : 100

Metal (**m**)	*concave*-m : *convex*-m
Ru	75 : 25

Figure 29. a) Comparison of energy diagrams of bowl-inversion of buckybowls before and after dissymmetrization. b) Previous dissymmetrizations of sumanene by chemical modifications and the isomeric ratio between the two conformers.

In Chapter 2, the synthesis of *α*-phenylazahomosumanene **8** with a nitrogen atom at the periphery of the framework is described. **8** can form a square planar platinum(II) complex as a C,N-ligand. When **8** is coordinated to a transition metal with a square planar ligand field at the nitrogen atom, the plane formed by the transition metal center and the plane formed by the azahomosumanene are expected to be orthogonal to each other due to the steric hindrance of the phenyl group (Figure 30). In such a configuration, the concave/convex faces are differentiated by the ligands located in the *cis*-position (L1 and L2) of the azahomosumanene. In this chapter, the synthesis of a platinum(II) complex with **8** as a monodentate ligand and the investigation of the effect of the ligand-field structure on the bowl direction of the azahomosumanene is described.

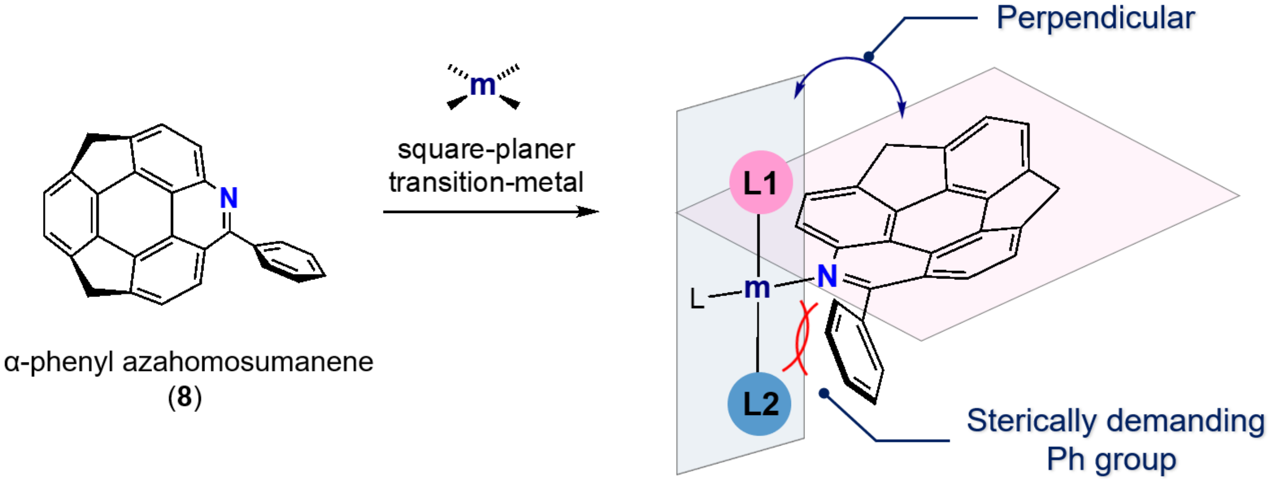

Figure 30. Dissymmetrization of two faces by coordination with azabuckybowl (This work).

Section 2. Synthesis and crystal structure of the platinum complex

In Chapter 2, **8** was synthesized via four steps: oxime formation from sumanenone **2**, Beckmann rearrangement, chlorination, and Suzuki-Miyaura cross-coupling. To reduce the synthetic steps, the synthetic route of **8** was reconsidered, and a simpler route using the acid-mediated ring expansion reaction reported by Gu et al.[8] The reaction of **2** with PhMgBr afforded the corresponding tertiary alcohol **14** in 86% yield. Following Gu's report, the ring expansion reaction of **14** proceeded by heating in the presence of sodium azide in hexafluoro-2-propanol/trifluoroacetic acid to afford **8** in 52% yield. **8** and $PtCl_2(DMSO)_2$ were mixed in methanol to give the complex **15** in 30% yield. The Pt(II) complex **15** was obtained in 30% yield (Scheme 11).

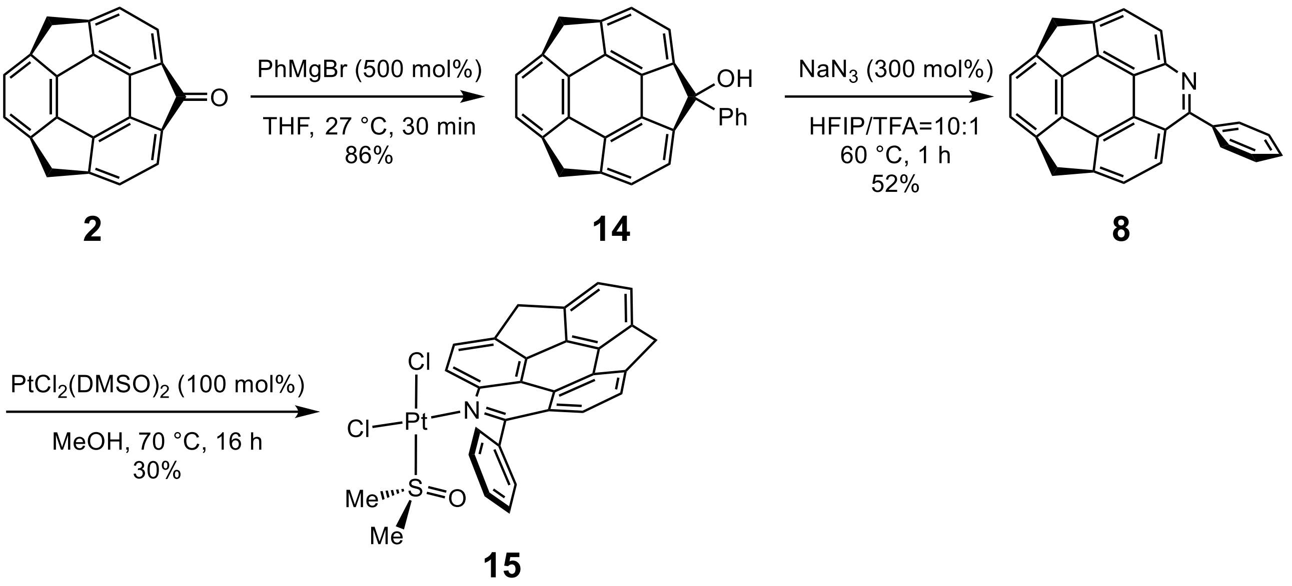

Scheme 11. Synthesis of platinum complex **15**.

The structure of **15** was determined by single crystal X-ray diffraction analysis (Figure 31). Recrystallization of **15** was conducted by vaper diffusion method using chloroform as a good solvent and *n*-pentane as a poor solvent. The platinum atoms had a tetracoordinate square planar structure, typical of platinum(II) complexes with a d^8 electron configuration. The Pt-N bond length was 2.03 Å, within the range of ordinary Pt(II)/pyridine complexes (Figure 31a). The plane containing azahomosumanene moiety was perpendicular to the plane containing the Pt center with other ligands due to steric repulsion with the phenyl group. The bowl structure of **8** was retained in the crystal structure of **15**, with the convex face of the bowl facing the DMSO side. In no disorder was observed in the crystal structure (Figure 31b). The bowl depth of the azahomosumanene moiety, defined by the distance between the bottom six-membered ring and the peripheral carbons, was 0.53–0.91 Å, comparable to the previously reported C70 fragment buckybowls.[9] In the packing structure, **15** forms a stacking structure along the *b*-axis, with CH···π interactions between the hydrogen atoms of the phenyl groups and the azahomosumanene skeleton (3.56–3.63 Å, red dotted lines, Figure 31c), and π···π interactions between each convex face (3.36–3.38 Å, green dotted lines, Figure 31c) between the convex faces. Each bowl moiety overlaps with an alternating arrangement of convex-convex and concave-concave manner. These one-dimensional columnar structures are composed of the CH···π interaction between one methyl group of DMSO and the azahomosumanene skeleton (3.56–3.64 Å, red dotted line, Figure 31d) and the CH···O interaction between each DMSO moiety (3.34 Å, blue dotted line, Figure 31d). These results suggest that interactions derived from the azahomosumanene moiety play an essential role in determining the packing structure, and no significant Pt···Pt interactions were observed.

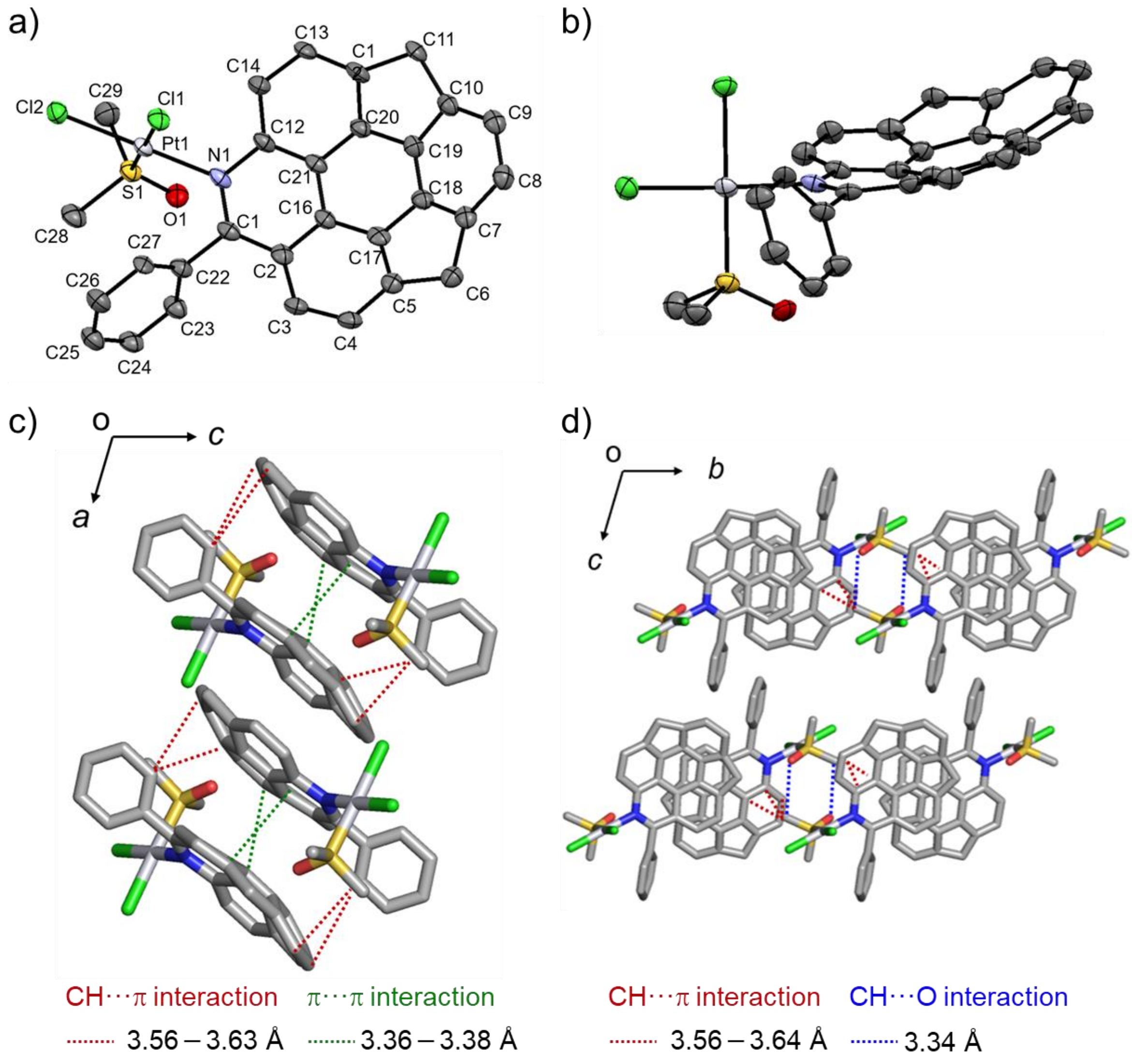

Figure 31. Crystal structure of **15**. a) and b): Thermal displacement ellipsoid plots in the crystal structures for the top and side view. c) and d) Packing structures and intermolecular interactions from the b and a-axis, respectively; CH···π (red dotted line), π···π (green dotted line), and CH···O (blue dotted line) interactions. Hydrogen atoms and solvents were omitted for clarity.

Section 3. Observation of bowl inversion behavior by one- and two-dimensional NMR measurements

^{1}H NMR spectra of **8** and **15** are shown in Figure 32. For example, if the interconversion of the concave and convex faces due to bowl inversion behavior is sufficiently slower than the NMR time scale, such as sumanene, the benzylic *endo* and *exo* protons are observed as two different doublet signals at 20 Hz of *J*-coupling due to geminal coupling.[10] In contrast, in the case of **8**, the bowl inversion is extremely fast due to the shallow bowl structure, and benzylic protons are observed as singlet peaks (H^a and H^b, 4.37 ppm). On the other hand, the proton signal at the benzyl position of **15** was observed as two pairs of doublet peaks with different chemical shifts at 25 °C (4.74 ppm, d, J = 20.6 Hz, H^{b}_{exo}; 4.15 ppm, d, J = 20.6 Hz, H^{b}_{endo}; 4.73 ppm, d, J = 21.0 Hz, H^{a}_{exo}; 4.12 ppm, d, J = 21.0 Hz, H^{a}_{endo}). These doublet signals may be due to the magnetic inequivalence of H_{endo} and H_{exo} due to the presence of two different ligands (Cl and DMSO) located perpendicular to the plane containing the bowl. However, these bowl inversion energies and rate constants could not be determined because **8** has a very shallow bowl structure and bowl inversion occur much faster than the NMR time scale.

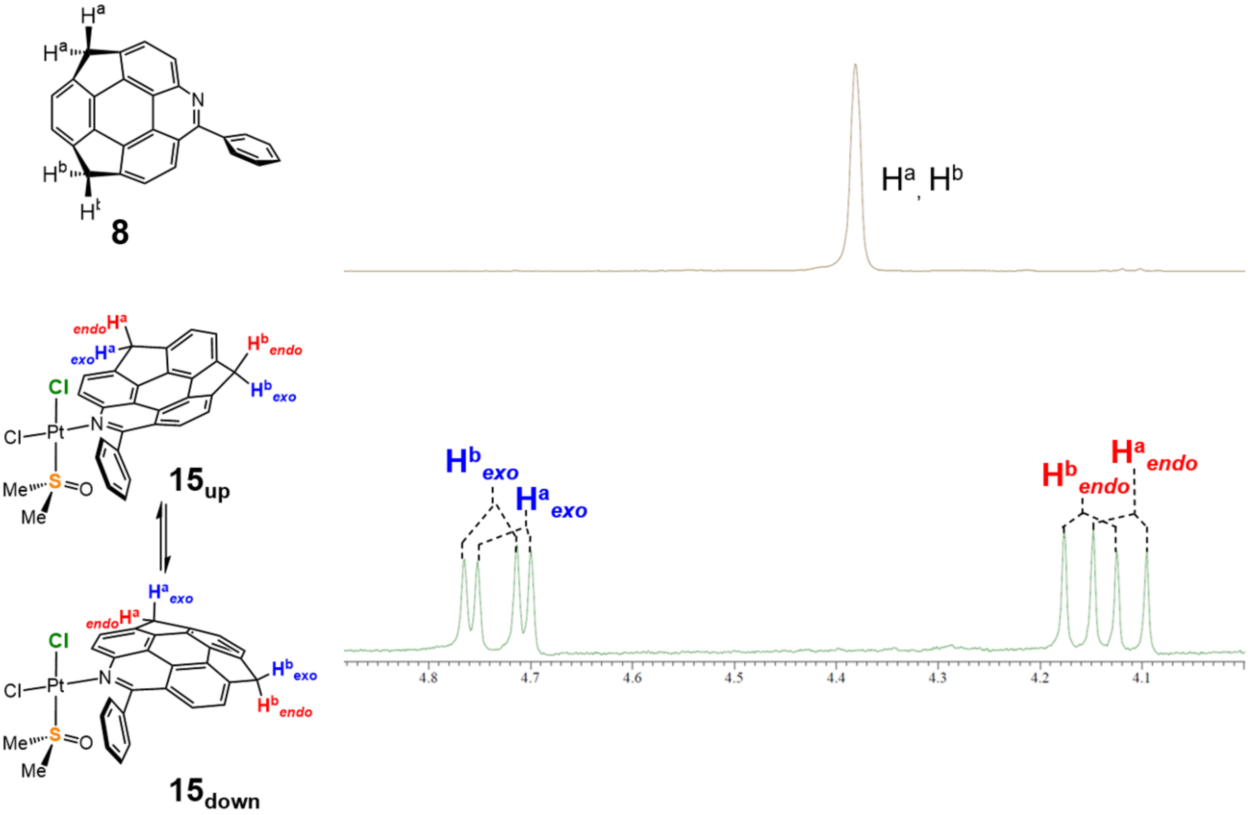

Figure 32. ^{1}H NMR spectra of **8** and **15** in $CDCl_3$ at 25 °C.

2D 1H Exchange Spectroscopy (EXSY) NMR experiments were performed to obtain more detailed information on the bowl inversion behavior. This method has often been used to determine the bowl inversion energies experimentally.[2e] Bowl inversion corresponds to isomerization between two diastereomers, and the exchange of these two species can be observed as a cross peak in the EXSY NMR spectrum.[11] This method requires the deuteration of one of the benzyl protons to prevent overlap of the NOE-derived signals between benzylic protons. Therefore, **15**-d_2, in which the benzyl position of **15** is stereoselectively deuterated, was synthesized from the previously reported deuterated sumanene (Sumanene-d_3) (Scheme 12).[2f] As in the synthesis of **2** in Chapter 2, 120 mol% n-butyllithium was added to sumanene-d_3 to form the mono-anion and the subsequent oxidation by Davis oxaziridine and MnO_2 provided deuterated sumanenone **2**-d_2. The reaction of **2-**d_2 with PhMgBr gave the tertiary alcohol **14**-d_2, followed by acid-mediated ring expansion reaction and subsequent complexation to give **15**-d_2. However, the hydrogen and deuterium at the benzyl position are expected to have high acidity. However, no scrambling of the deuterium was observed during the synthesis.

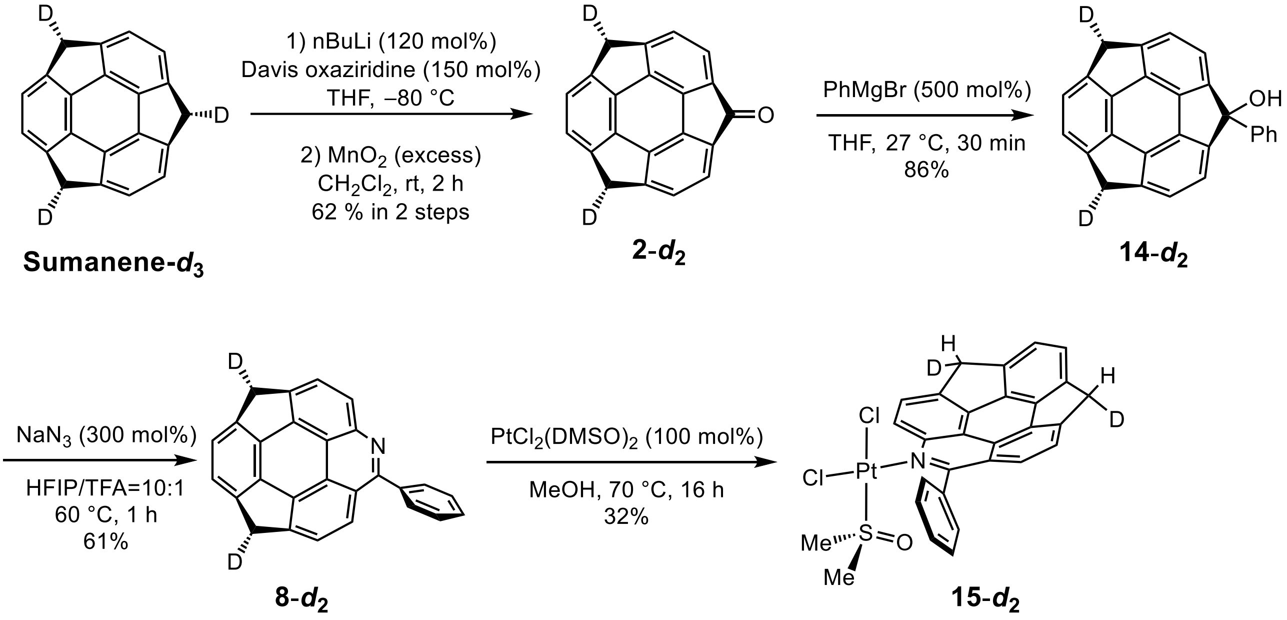

Scheme 12. Synthesis of dideuterio-Pt(Ph-azahomosumanene)(DMSO)Cl_2 **15-*d*₂**.

EXSY measurements of **15**-d_2 were performed (Figure 33). In the EXSY spectrum, two cross-peaks were observed that are derived from the exchange of benzyl protons, indicating that the two isomers (**15$_{up}$** and **15$_{down}$**) are interconverted by bowl inversion, depending on the direction of the concave/convex faces. It was also shown that the spectra observed in 1D ^{1}H NMR were averaged by a very fast bowl inversion process and were regarded as if they were a single isomer. However, the integral values of the cross-peaks were too small to determine the rate constant of the bowl inversion, the inversion energy, or the isomer ratio. This result indicates that the ratio of one isomer is much larger than that of the other.

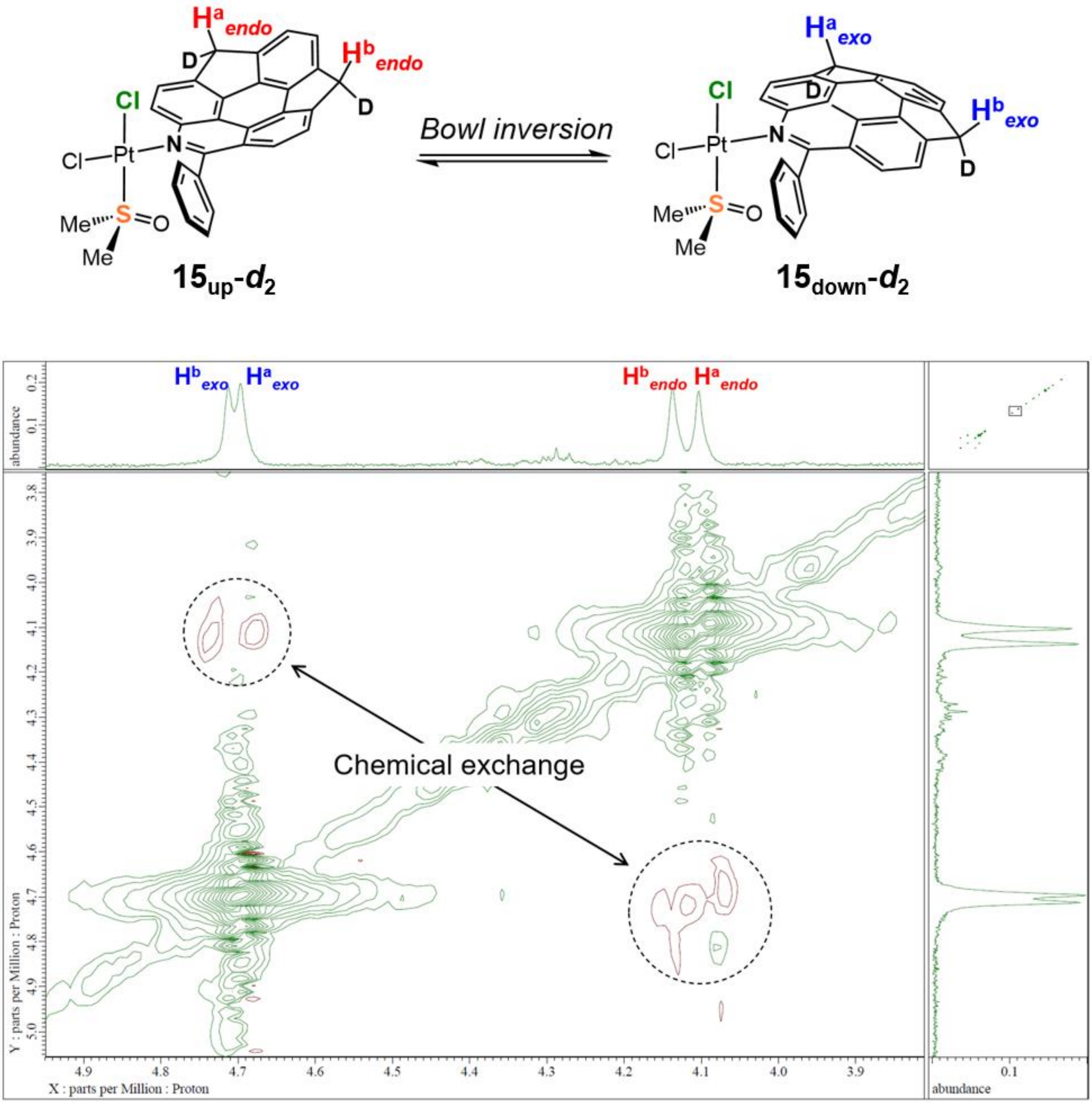

Figure 33. A 2D-EXSY experiment of **15-*d*$_2$**.

Section 4. Considerations on the isomeric ratio based on theoretical calculations

To obtain information about the isomeric ratio of **15$_{up}$** and **15$_{down}$** and their energy differences, quantum chemical calculations at the B3LYP/Def2-TZVP level were performed (Figure 34). The results show that **15$_{up}$** is thermodynamically more stable than **15$_{down}$** by 7.4 kJ mol^{-1}. The isomeric ratio of **15$_{up}$:15$_{down}$** was estimated to be 95:5 at 25 °C from Boltzmann's equation ($k_B = 1.3806 \times 10^{-23}$ J K^{-1}, T = 298.15 K).

$$\frac{N_i}{N_0} = \exp\left(-\Delta G / k_B T\right)$$

These results are almost consistent with the very small cross-peaks observed in the EXSY NMR experiments. The calculated bowl inversion energies were 19.4 kJ mol^{-1} ($\Delta G_1^{\ddagger}$) and 12.1 kJ mol^{-1} ($\Delta G_2^{\ddagger}$), respectively. These calculated results are small enough to induce bowl inversion behavior at 25 °C, and are also in agreement with the experimental results. These results suggest that **15**$_{\mathbf{up}}$ is thermodynamically stable, so even if it is converted to **15**$_{\mathbf{down}}$ via bowl inversion process, the reverse process proceeds, and the two isomers **15**$_{\mathbf{up}}$ and **15**$_{\mathbf{down}}$ exist in a very biased existence ratio on the NMR timescale.

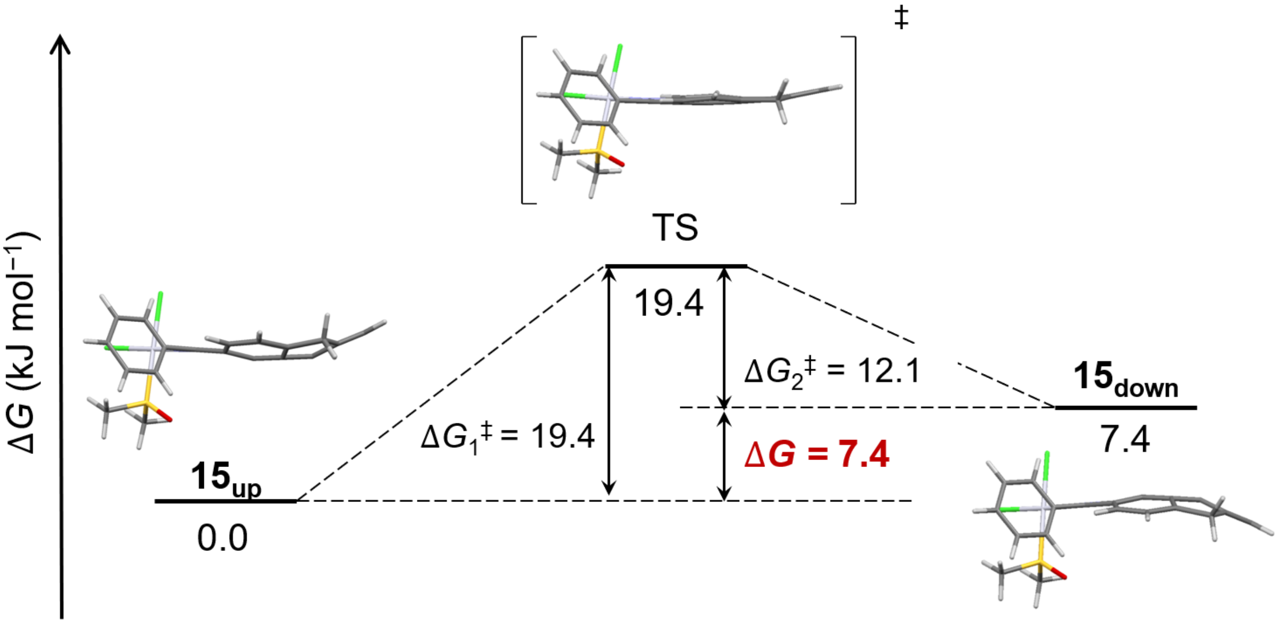

Figure 34. Bowl-to-bowl inversion energy of **15** estimated by DFT calculation (298.15 K, 1 atm).

The author first hypothesized that the energy difference between **15**$_{\mathbf{up}}$ and **15**$_{\mathbf{down}}$ is due to different intramolecular interactions depending on the bowl conformation and performed quantum theory of atoms-in-molecules (QTAIM)[12] calculations (Figure 35). The results show that there are similar bond paths and bond critical points (BCPs) both **15**$_{\mathbf{up}}$ and **15**$_{\mathbf{down}}$. For example, electron densities [$\rho_{\mathrm{BCP}}(r)$] at the BCP corresponding to the CH···Cl interaction between the chlorine atom and the hydrogen atom at 2-position of the phenyl group were observed at 0.924 e bohr^{-3} (**15**$_{\mathbf{up}}$) and 0.765 e bohr^{-3} (**15**$_{\mathbf{down}}$), respectively. BCPs (**15**$_{\mathbf{up}}$; 0.417 e bohr^{-3}, **15**$_{\mathbf{down}}$; 0.518 e bohr^{-3}) were also observed between the hydrogen of the methyl group in DMSO and the phenyl ring, corresponding to an intramolecular CH···π interaction. O···π interactions were also observed between the oxygen atom and the phenyl ring, with BCP [$\rho_{\mathrm{BCP}}(r)$] values of 0.458 e bohr^{-3} (**15**$_{\mathbf{up}}$) and 0.597 e bohr^{-3} (**15**$_{\mathbf{down}}$), respectively. The Laplacian [$\nabla^2\rho_{\mathrm{BCP}}(r)$] of these electron densities were all positive. These interactions may play an important role in inhibiting the rotation of the phenyl group, consistent with the fact that the proton of the phenyl group is observed inequivalently in the ^{1}H NMR of **15**. On the other hand, a BCP corresponding to the CH···Cl interaction between the two methyl group hydrogens and the chlorine atom in DMSO is observed, with $\rho_{\mathrm{BCP}}(r)$ of 0.987 *e* bohr^{-3} and 0.109 *e* bohr^{-3} for $\mathbf{15_{up}}$ and 0.993 *e* bohr^{-3} and 0.112 *e* bohr^{-3} for $\mathbf{15_{down}}$. These Laplacian [$\nabla^2\rho_{\mathrm{BCP}}(r)$] were also all positive. However, no significant intramolecular interaction differences between $\mathbf{15_{up}}$ and $\mathbf{15_{down}}$ were observed in the QTAIM calculations.

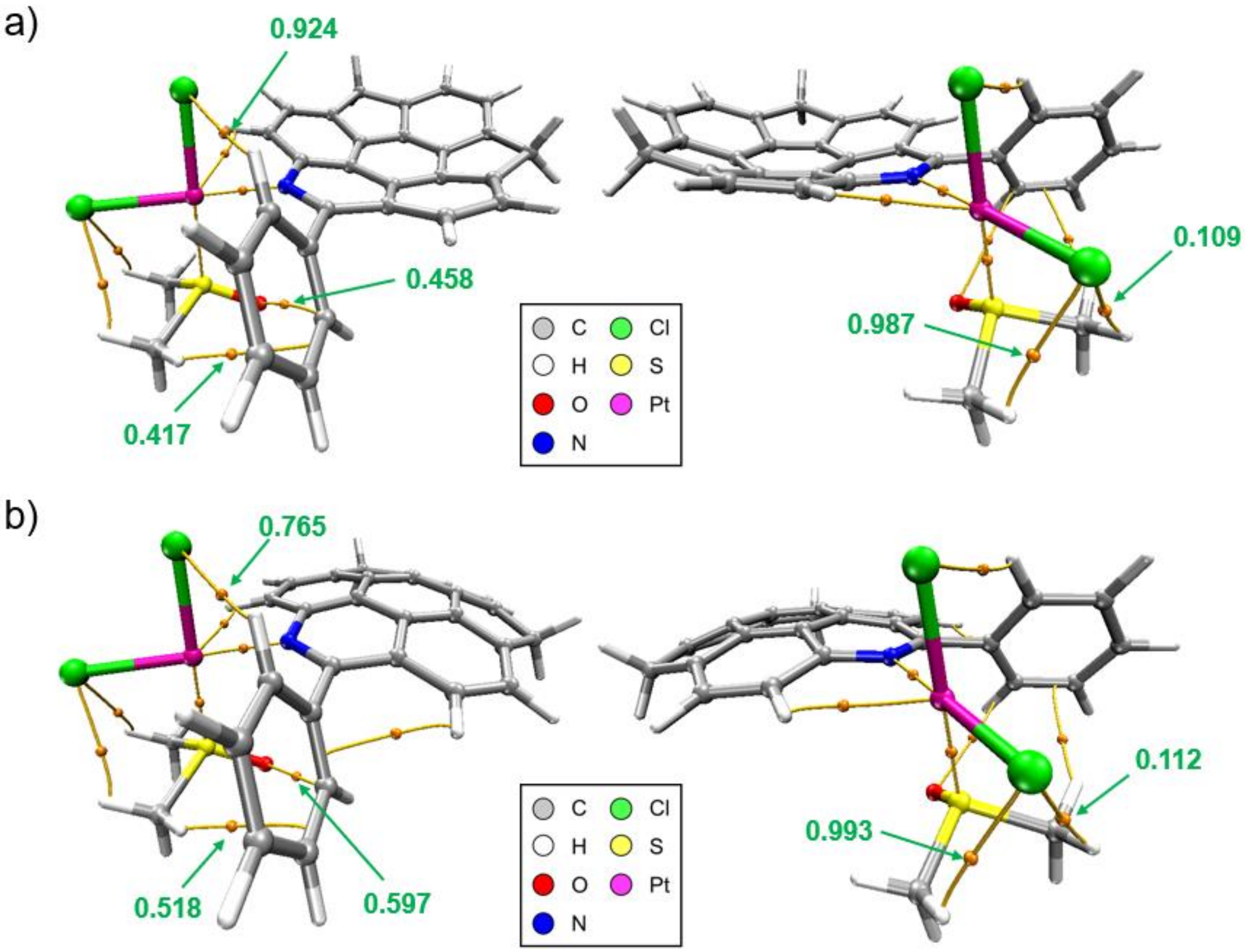

Figure 35. QTAIM analysis of a) $\mathbf{15_{up}}$ and b) $\mathbf{15_{down}}$. The bond paths (yellow line), bond critical points (orange), and electron density (*e* bohr^{-3}) at the bond critical points are shown.

Then the author hypothesized that the energy difference between the $\mathbf{15_{up}}$ and $\mathbf{15_{down}}$ might originate from the direction of the concave/convex face of azahomosumanene moiety, so their dipole moments were compared. The inversion of the concave/convex face corresponds to an inversion of the inherent dipole moment of buckybowl. The magnitudes of the *z*-axis component of dipole moments in $\mathbf{15_{up}}$ and $\mathbf{15_{down}}$ are 4.1 and 6.6 Debye, respectively. In the case of $\mathbf{15_{up}}$, the dipole moment of the azahomosumanene moiety aligned opposite to platinum and other ligands, weakening each other (Figure 36a). On the other hand, both dipole moments exist in the same direction in the case of $\mathbf{15_{down}}$, and these enhance each other (Figure 36b). Hence, the dipole moment of the whole molecule is smaller in $\mathbf{15_{up}}$ than in $\mathbf{15_{down}}$, and $\mathbf{15_{up}}$ is possibly more stable and observed as a single conformer.

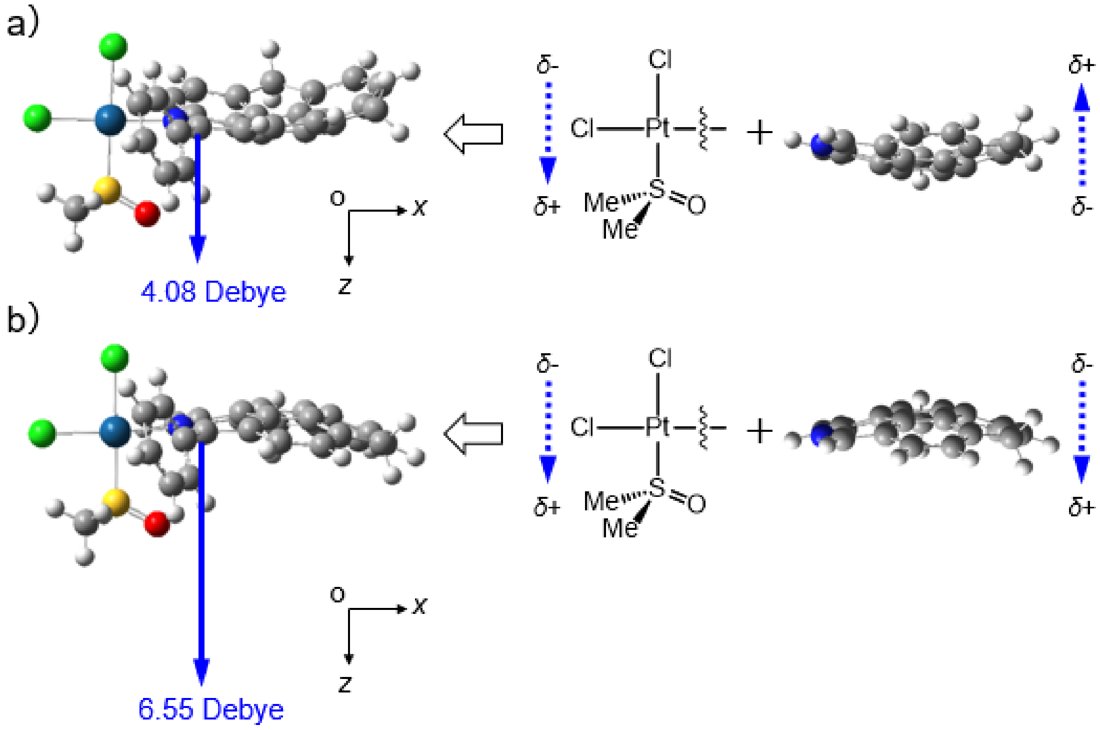

Figure 36. The z-axis component of dipole moment (solid blue arrow) and that for each element (blue dotted arrow) of a) $\mathbf{15_{up}}$ and b) $\mathbf{15_{down}}$.

Next, Energy Decomposition Analysis (EDA) was performed to obtain more quantitative information on the origin of the difference in thermodynamic stability between $\mathbf{15_{up}}$ and $\mathbf{15_{down}}$ (Tables 8, 9, and 10). The optimized structures of the platinum complexes ($\mathbf{15_{up}}$ and $\mathbf{15_{down}}$) by DFT calculations, were analyzed by cleaving between Pt-N and splitting them into two fragments (Figure 37). The complexation energy ($\Delta E_{\mathrm{total}}$) is defined as the sum of the preparation energy (ΔE_{prep}) and the interaction energy (ΔE_{int}) ($\Delta E_{\mathrm{total}} = \Delta E_{\mathrm{prep}} + \Delta E_{\mathrm{int}}$). ΔE_{prep} refers to the deformation energy resulting from the strain and orbital hybridization. The ΔE_{int} term was further decomposed by the second-generation energy decomposition analysis based on absolute localized molecular orbitals at the B3LYP-D3(BJ)/Def2-TZVP level (ALMO-EDA) method,[13] and the difference between each decomposition energy ($\Delta\Delta E = \Delta E(\mathbf{15_{up}}) - \Delta E(\mathbf{15_{down}})$) was compared. Comparing the calculated $\mathbf{15_{up}}$ and $\mathbf{15_{down}}$ decomposition energy components, the term originating from electrostatic interactions ($\Delta\Delta E_{\mathrm{elstat}} = -1.18$ kJ mol^{-1}) is the larger contribution for stabilization than the term originating from charge transfer ($\Delta\Delta E_{\mathrm{CT}} = -0.22$ kJ mol^{-1}), polarization ($\Delta\Delta E_{\mathrm{pol}} = -0.34$ kJ mol^{-1}), and dispersion

($\Delta\Delta E_{\text{disp}}$ = –0.42 kJ mol^{-1}) (Table 10). The stabilization by polarization is very small, suggesting that the hypothesis of an effect of dipole moments derived from bowl direction is not reasonable. However, the difference in interaction energy calculated by EDA ($\Delta\Delta E_{\text{int}}$ = –0.57 kJ mol^{-1}) is much smaller than the difference in electrostatic energy $E(\mathbf{15}_{\mathbf{up}}) - E(\mathbf{15}_{\mathbf{down}})$ = –6.34 kJ mol^{-1} (Table 8). Given that the effect of thermodynamic parameters is negligible (Table 8), the difference in thermodynamic stability between $\mathbf{15}_{\mathbf{up}}$ and $\mathbf{15}_{\mathbf{down}}$ can be attributed to the effects of distortion and orbital rehybridization in the molecular structure.[14] Each preparation energy (ΔE_{prep}) for $\mathbf{15}_{\mathbf{up}}$ and $\mathbf{15}_{\mathbf{down}}$ are calculated as 36.28 kJ mol^{-1} and 40.93 kJ mol^{-1} ($\Delta\Delta E_{\text{prep}}$ = –4.65 kJ mol^{-1}), respectively (Table 9). These results clearly indicate that $\mathbf{15}_{\mathbf{up}}$ has a less distorted molecular structure than $\mathbf{15}_{\mathbf{down}}$. Furthermore, the difference in SCF energy (ΔE_{frag2}) before and after structural relaxation of the azahomosumanene moiety is estimated to be –4.69 kJ mol^{-1}, which is larger than that of the platinum moiety (ΔE_{frag1} = +0.04 kJ mol^{-1}), suggesting that the difference in strain energy of the azahomosumanene moiety is a major factor in determining the isomer ratio between $\mathbf{15}_{\mathbf{up}}$ and $\mathbf{15}_{\mathbf{down}}$.

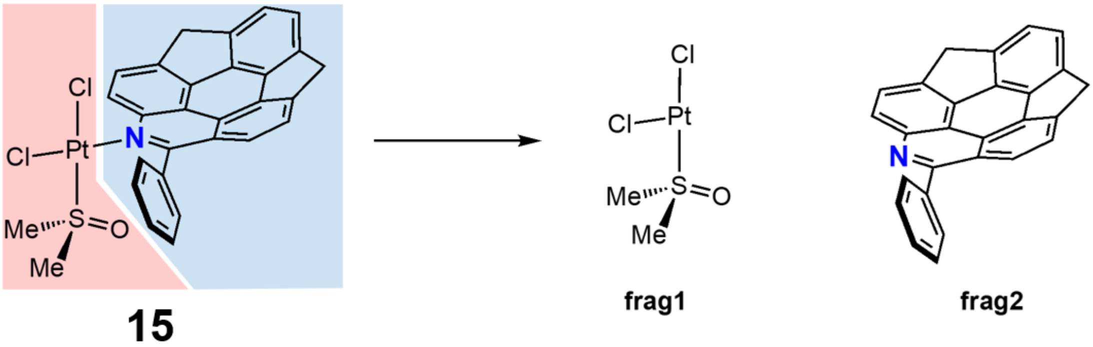

Figure 37. Fragmentation of **15** for EDA calculation.

Table 8. Calculated energies and thermochemical parameters of **15** at 298.15 K.

	E (hartree)	ZPE (hartree)	*H* (hartree)	*TS* (hartree)	*G* (hartree)
$\mathbf{15}_{\mathbf{up}}$	–2686.341978	0.421312	–2685.889711	0.092163	–2685.981872
$\mathbf{15}_{\mathbf{down}}$	–2686.339548	0.421403	–2685.887230	0.091884	–2685.979114
	ΔE (kJ/mol)	ΔZPE (kJ/mol)	ΔH (kJ/mol)	$T\Delta S$ (kJ/mol)	ΔG (kJ/mol)
$\mathbf{15}_{\mathbf{up}} - \mathbf{15}_{\mathbf{down}}$	–6.34	–0.24	–6.51	+0.73	–7.24

Table 9. Evaluation of the preparation energies of $\mathbf{15_{up}}$ and $\mathbf{15_{down}}$.

	$\mathbf{15_{up}}$	$\mathbf{15_{down}}$	$\Delta\Delta E$
E_{fix}^{frag1} (hartree)	–1593.228096	–1593.228112	-
E_{fix}^{frag2} (hartree)	–1093.044907	–1093.043122	-
E_{relax}^{frag1} (hartree)	–1593.237999		-
E_{relax}^{frag2} (hartree)	–1093.048822		-
$\left(E_{fix}^{frag1} - E_{relax}^{frag1}\right)$ (kJ mol^{-1})	26.00	25.96	+0.04
$\left(E_{fix}^{frag2} - E_{relax}^{frag2}\right)$ (kJ mol^{-1})	10.28	14.97	–4.69
ΔE_{prep} (kJ mol^{-1})	36.28	40.93	–4.65

Table 10. Decomposed energy components of $\mathbf{15_{up}}$ and $\mathbf{15_{down}}$ (kJ mol^{-1}).

	$\Delta E_{\mathrm{elstat}}$	$\Delta E_{\mathrm{Pauli}}$	ΔE_{disp}	ΔE_{pol}	ΔE_{CT}	ΔE_{int}
$\mathbf{15_{up}}$	–471.00	599.44	–21.51	–133.88	–233.95	–260.90
$\mathbf{15_{down}}$	–469.82	597.85	–21.09	–133.54	–233.73	–260.33
$\Delta\Delta E$	–1.18	+1.59	–0.42	–0.34	–0.22	–0.57

Section 5. UV-vis absorption spectroscopy

To investigate the change in electronic structure due to complexation, absorption spectra of **8** and **15** in CH_2Cl_2 were measured (Figure 38a). Absorption bands at 313 nm, 329 nm, and 404 nm of **15** showed a bathochromic shift compared to those of **8**, which is attributed to the delocalization of electrons to the platinum center. DFT calculations also suggest that the HOMO of **15** is delocalized to the phenylazahomosumanene moiety and the Pt atom (Figure 38b). TD-DFT calculations at the B3LYP/Def2-TZVP level also suggest that the absorption bands around 404 nm are derived from [HOMO]-[LUMO] (65%), [HOMO–1]-[LUMO] (13%), and [HOMO–3]-[LUMO] (13%) transitions. These are corresponding to metal-ligand charge transfer (MLCT) and π-π* transitions originating from the phenylazahomosumanene moiety (Figures 39 and 40). **15** showed almost no luminescence at room temperature. In Chapter 1, a Pt(II) complex with **8** as a bidentate ligand exhibits weak room temperature phosphorescence (Φ_{PL} = 0.8%, 298 K). In the case of **15**, **8** coordinates to Pt in monodentate manner and can rotate on the Pt-N bond. Therefore, the no emission of **8** may be due to the large contribution of thermal deactivation caused by dynamic behavior in solution.

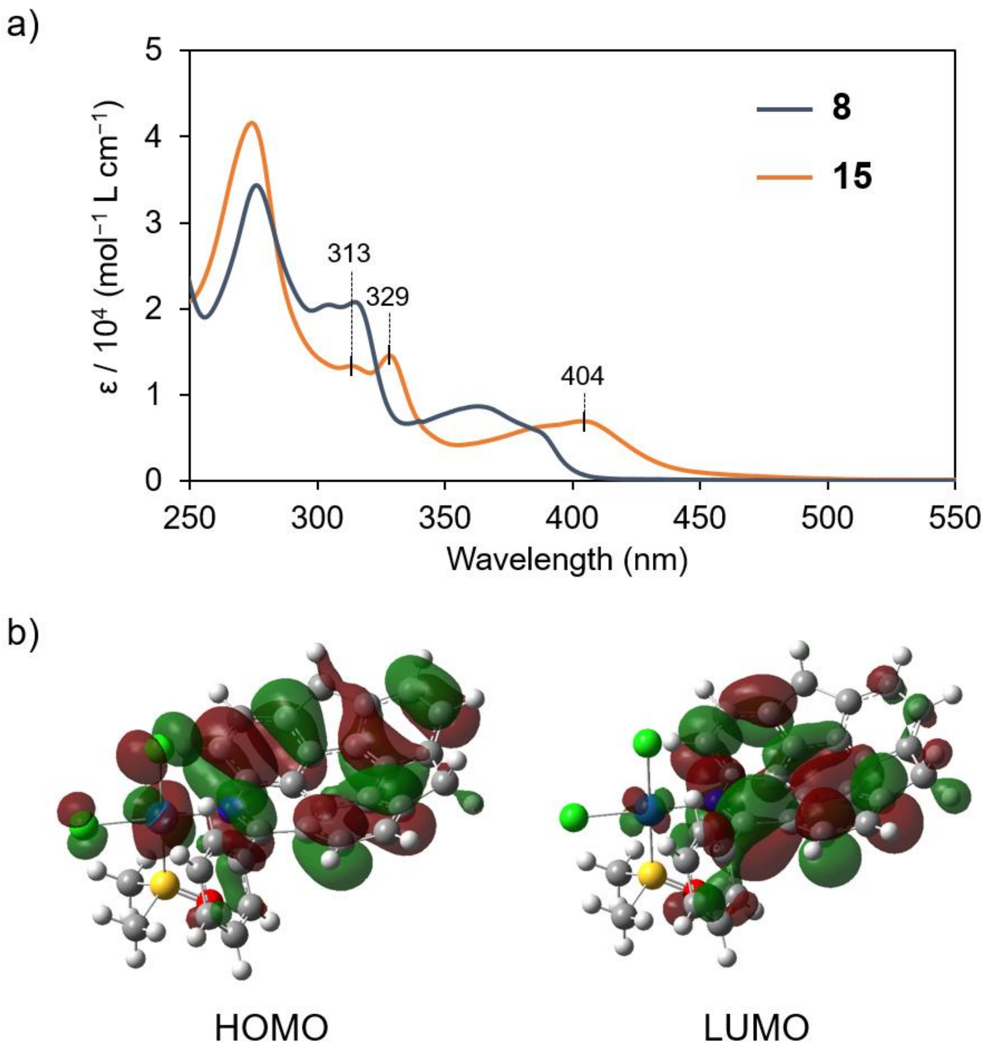

Figure 38. a) UV-vis absorption spectra of **8** and **15** in CH_2Cl_2 (1.0×10^{-5} mol/L). b) Kohn−Sham orbitals at the HOMO and LUMO level of **15** calculated at the B3LYP/Def2-TZVP level of theory.

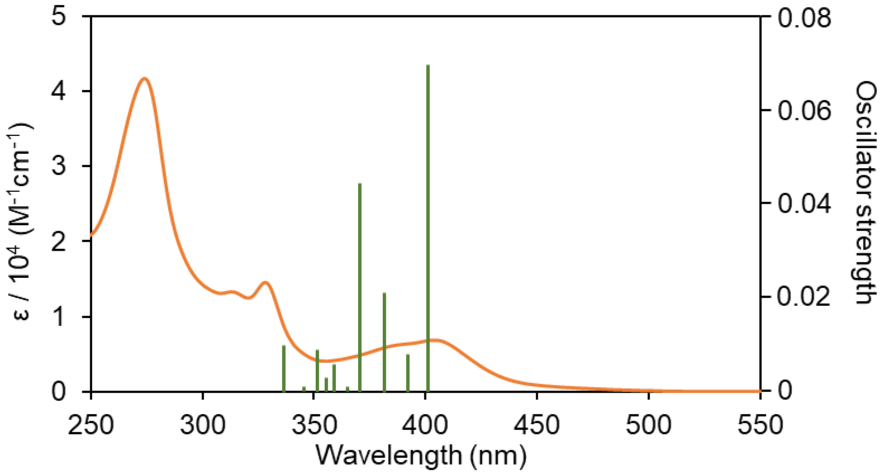

Figure 39. UV-vis absorption spectra of $\mathbf{15_{up}}$ with the simulated oscillator strengths.

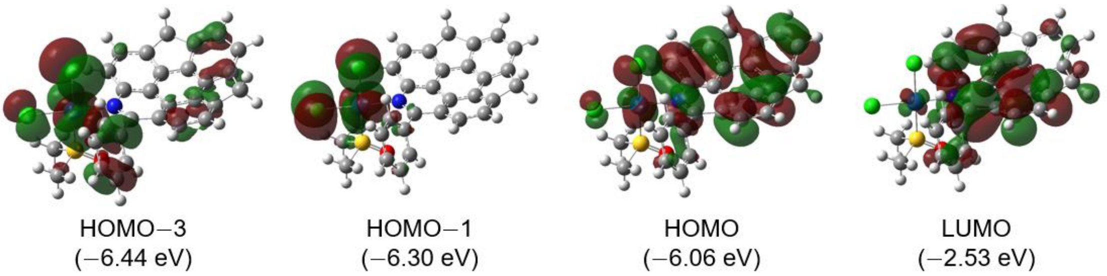

Energy / eV (nm)	Oscillator strength	Major contribution (%)
3.0942/ 400.70	0.0733	HOMO ⇒LUMO (65) HOMO-1 ⇒LUMO (13) HOMO-3 ⇒LUMO (13)

Figure 40. Kohn–Sham orbitals, energy, oscillator strength, and the major contribution of calculated transition of **15**.

Section 6. Summary

In this chapter, concave and convex faces of azabuckybowl can be thermodynamically differentiated through the complexation of platinum(II) with different ligands. The strategy to control the faces of the bowls is simple and versatile because a variety of transition metals with diverse coordination geometries can be used. The author expects the control of the isomeric ratio by changing the transition metal and ligand. The finding is also expected to realize the stereoselective introduction of a functional group to the benzylic positions of azabuckybowls.

Experimental section

General information about instruments and measurements is provided in experimental section, chapter 2.

Chemicals

Unless otherwise noted, all reagents purchased from commercial suppliers were used without further purification.

n-Hexane, dichloromethane (CH_2Cl_2), ethyl acetate (EtOAc), methanol (MeOH), chloroform ($CHCl_3$), potassium bromide (KBr), bromobenzene (PhBr), and acetone were purchased from FUJIFILM Wako Pure Chemical Corporation.

Diethyl ether (Et_2O), magnesium (turnings), and dimethyl sulfoxide (DMSO) were purchased from Nacalai Tesque, Inc.

Dichloromethane (CH_2Cl_2, dehydrated Super^2) and tetrahydrofuran (THF, dehydrated (stabilized free) Super Plus) were purchased from Kanto Chemical Co., Inc., and purified by passing through a Glass Contour Ultimate Solvent System (Nikko Hansen & Co. Ltd.) under nitrogen atmosphere.

n-Butyl lithium (*n*-BuLi) was purchased from Kanto Chemical Co., Inc.

Dibromoethane, 1,1,1,3,3,3-hexafluoro-2-propanol (HFIP), trifluoroacetic acid (TFA), *n*-pentane, and sodium azide (NaN_3) were purchased from Tokyo Chemical Industry Co., Ltd.

Manganese(IV) Oxide (MnO_2) was purchased from Sigma–Aldrich Japan Inc.

3-phenyl-2-(phenylsulfonyl)oxaziridine,[15] $PtCl_2(DMSO)_2$,[16] and trideuterio-sumanene[2f] were prepared according to the literatures.

Synthetic Procedure and Characterization Data.

***Phenylazahomosumanene* 8**. To a solution of **14** (20.0 mg, 56.6 μmol, 100 mol%) and NaN_3 (11.0 mg, 170 μmol, 300 mol%) in HFIP (1.0 mL) was added TFA (0.1 mL) at room temperature, and the mixture was stirred at 60 °C for 1 h. After cooling to room temperature, the mixture was carefully poured into saturated aqueous $NaHCO_3$ solution (ca. 20 mL). The mixture was extracted with CH_2Cl_2 (ca. 10 mL × 3). The combined organic extract was washed with brine (ca. 20 mL) and dried over Na_2SO_4. After filtration, the filtrate was concentrated under reduced pressure. The residue was purified by PTLC (CH_2Cl_2) to give **8** (10.5 mg, 29.7 μmol, 52.5%) as a pale yellow solid; ^{1}H NMR (CD_2Cl_2, 400 MHz) δ 8.12–8.09 (AA′BB′C, 2H), 7.97 (d, *J* = 8.2 Hz, 1H), 7.91 (d, *J* = 8.2 Hz, 1H), 7.88 (d, *J* = 8.2 Hz, 1H), 7.78 (d, *J* = 8.2 Hz, 1H), 7.63–7.57 (m, 3H), 7.43 (d, *J* = 7.3 Hz, 1H), 7.40 (d, *J* = 7.3 Hz, 1H), 4.26 (s, 2H + 2H, two signals overlapped);

^{13}C{^{1}H}NMR (CD_2Cl_2, 100 MHz) δ 161.7 (1C), 149.5 (1C), 146.1 (1C), 145.5 (1C), 145.1 (1C), 143.7 (1C), 142.8 (1C), 142.2 (1C), 141.9 (1C), 141.4 (1C), 139.8 (1C), 130.4 (2C), 130.3 (1C), 129.7 (1C), 128.8 (2C), 126.5 (1C), 125.4 (1C), 125.3 (1C), 124.7 (1C), 124.6 (1C), 124.5 (1C), 124.3 (1C), 121.0 (1C), 42.4 (1C), 42.1 (1C). The chemical shifts were consistent with those reported in the chapter 2.

***Phenylhydroxysumanene* 14**. To a 50 mL round bottom flask equipped with a magnetic stir bar were added magnesium tunning (122 mg, 5.02 mmol), dry THF (0.5 mL), and dibromoethane (one drop). To the mixture was slowly added PhBr (523 µL, 5.00 mmol) in THF (4.5 mL) using a dropping funnel, and the mixture was stirred for 1 h at room temperature to give ca. 1.0 mol/L PhMgBr solution. To a solution of **2** (20.0 mg, 71.9 µmol, 100 mol%) in dry THF (10 mL) was slowly added PhMgBr (1.0 mol/L in THF, 0.36 mL, 500 mol%) at 0 °C. After stirring for 30 min at the same temperature, to the reaction mixture was added saturated aqueous NH_4Cl solution (ca. 25 mL), and then the mixture was warmed up to room temperature. The mixture was extracted with diethyl ether (ca. 30 mL × 3). The organic extract was washed with brine (ca. 30 mL) and dried over Na_2SO_4. After filtration, the filtrate was concentrated under reduced pressure. The residue was purified by PTLC ($CHCl_3$) to give **14** (22.0 mg, 61.8 µmol, 86.0%) as a white solid; R_f = 0.33 ($CHCl_3$); Melting point: 183 °C (dec.);^{1}H NMR ($CDCl_3$, 400 MHz) δ 8.20 (d, J = 7.3 Hz, 2H), 7.60 (dd, J = 7.3, 7.3 Hz, 2H), 7.52 (t, J = 7.3 Hz, 1H), 7.35 (d, J = 7.8 Hz, 2 H), 7.27 (d, J = 7.8 Hz, 2 H), 7.26 (s, 2 H), 4.84 (d, J = 19.2 Hz, 2 H), 3.59 (d, J = 19.2 Hz, 2 H); ^{13}C{^{1}H} NMR ($CDCl_3$, 100 MHz) δ 156.8 (2C), 150.9 (2C), 149.4 (2C), 149.3 (2C), 149.0 (2C), 146.3 (2C), 142.0 (1C), 128.6 (2C), 128.1 (1C), 126.4 (2C), 124.2 (2C), 123.4 (2C), 121.0 (2C), 93.3 (1C), 41.7 (2C); IR (diamond, cm^{-1}) 3524, 3048, 2887,1600, 1446, 1337, 993, 793, 736, 567; HRMS (FAB^{+}) *m/z*: [M]$^{+}$ Calcd for $C_{27}H_{16}O^{+}$ 356.1197; Found 356.1205.

***$PtCl_2$[(Ph-azahomosumanene)(DMSO)]* 15**. To a mixture of **8** (10.0 mg, 28.3 µmol, 100 mol%) and $PtCl_2(DMSO)_2$ (11.9 mg, 28.3 µmol, 100 mol%) was added MeOH (1.5 mL) at room temperature, and the mixture was stirred at 70 °C for 16 h. After cooling to room temperature, and the yellow precipitate was collected by filtration and washed with MeOH (ca. 5 mL × 3) and diethyl ether (ca. 5 mL × 3). The crude was purified by PTLC (CH_2Cl_2/MeOH = 98:2) to give **15** (6.0 mg, 8.6 µmol, 30%) as a yellow solid; R_f = 0.58 (CH_2Cl_2/MeOH = 98:2); Melting point: 286 °C (dec.); ^{1}H NMR ($CDCl_3$, 400 MHz) δ 9.55 (d, J = 8.2 Hz, 1H), 8.88 (d, J = 7.8 Hz, 1H), 8.16 (d, J = 8.2 Hz, 1H), 7.90—7.86 (m, 2H), 7.81 (d, J = 7.8 Hz, 1H), 7.77 (t, J = 7.8 Hz, 1H), 7.69—7.65 (m, 2H), 7.57 (d, J = 7.8 Hz, 1H), 7.54 (d, J = 7.8 Hz, 1H), 4.74 (d, J = 20.6 Hz, 1H), 4.73 (d, J = 21.0 Hz, 1H), 4.15 (d, J = 20.6 Hz, 1H), 4.12 (d, J = 21.0 Hz, 1H), 3.39 (s, 3H), 2.74 (s, 3H); ^{13}C{^{1}H} NMR ($CDCl_3$, 100 MHz) δ 167.8 (1C), 151.8 (1C), 146.6 (1C), 145.6 (1C), 144.8 (1C), 141.8 (1C), 141.22 (1C), 141.20 (1C) 140.7 (1C), 137.9 (1C), 132.8 (1C), 131.0 (1C), 130.6 (1C), 129.2 (1C), 128.7 (1C), 127.4 (1C), 127.2 (1C), 127.0 (1C), 126.7 (1C), 125.8 (1C), 125.4 (1C), 125.2 (1C), 124.8 (1C),

121.3 (1C), 45.1 (1C), 43.1 (1C), 42.7 (1C), 42.0 (1C); IR (KBr, cm^{-1}) 2919, 2851, 1716, 1636, 1441, 1392, 1147, 1017, 792, 704, 436;
HRMS (FAB) *m*/*z*: [M+H]$^+$ Calcd for $C_{29}H_{22}Cl_2NOPtS$ 697.0447; Found 697.0420.

Sumanenone-d_2 **2-d_2**. To a solution of trideuterio-sumanene (60.0 mg, 214 µmol, 100 mol%) in dry THF (25 mL) was slowly added *n*-BuLi (2.60 mol/L in *n*-hexane, 99 µL, 0.26 mmol, 120 mol%) at −80 °C. After stirring for 30 min at the same temperature, to the reaction mixture was added a solution of 3-phenyl-2 (phenylsulfonyl)oxaziridine (83.9 mg, 321 µmol, 150 mol%) in THF (2 mL) at −80 °C. After stirring for 5 min at the same temperature, to the reaction mixture was added saturated aqueous NH_4Cl solution (ca. 25 mL), and the mixture was warmed up to room temperature. The mixture was extracted with ethyl acetate (ca. 30 mL × 3). The organic extract was washed with brine (ca. 10 mL) and dried over Na_2SO_4. After filtration, the filtrate was concentrated under reduced pressure. The residue was dissolved in CH_2Cl_2 (20 mL), and to this was added MnO_2 (1.00 g, 11.5 mmol, 5380 mol%) at 27 °C. After the stirring for 1 h at the same temperature, the reaction mixture was filtered through a short pad of Celite®and eluted with $CHCl_3$ (ca. 200 mL). The filtrate was concentrated under reduced pressure. The residue was purified by silica-gel column chromatography (*n*-hexane/$CHCl_3$ = 1:1 to 1:3) to give **2-d_2** (37.2 mg, 133 µmol , 62.1%) as a yellow solid; R_f = 0.35 (*n*-hexane/$CHCl_3$ = 1:1); Melting point: 324 °C (dec.); ^{1}H NMR ($CDCl_3$, 400 MHz) δ 7.27 (d, J = 7.3 Hz, 2H), 7.19 (s, 2H), 7.16 (d, J = 7.3 Hz, 2H), 4.72 (s, 1H), 3.50 (s, 1H); $^{13}C\{^1H\}$NMR ($CDCl_3$, 100 MHz) δ 190.0 (1C), 156.0 (2C), 149.4 (2C), 149.0 (2C), 148.8 (2C), 148.1 (2C), 139.2 (2C), 124.9 (1C), 124.8 (1C), 124.3 (2C), 124.12 (1C), 124.05 (1C), 41.8 (d, J = 21.2 Hz, 1C), 41.6 (d, J = 20.2 Hz, 1C); IR (diamond, cm^{-1}): 2958, 2923, 2852, 1695, 1255. 1085, 1017, 797, 749; HRMS (EI$^+$) m/z: [M]$^+$ Calcd for $C_{21}H_8D_2O^+$ 280.0857; Found 280.0853.

Phenylhydroxysumanene-d_2 **14-d_2**. To a 50 mL round bottom flask equipped with a magnetic stir bar were added magnesium tunning (122 mg, 5.02 mmol), dry THF (0.5 mL), and dibromoethane (one drop). To the mixture was slowly added PhBr (523 µL, 5.00 mmol) in THF (4.5 mL) using a dropping funnel, and the mixture was stirred for 1 h at room temperature to give ca. 1.0 mol/L PhMgBr solution. To a solution of **2-d_2** (40.0 mg, 143 µmol, 100 mol%) in dry THF (25 mL) was slowly added PhMgBr (1.0 M in THF, 0.714 mL, 500 mol%) at 0 °C. After stirring for 30 min at the same temperature, to the reaction mixture was added saturated aqueous NH_4Cl solution (ca. 25 mL), and then the mixture was warmed up to room temperature. The resulting mixture was extracted with diethyl ether (ca. 30 mL × 3). The organic extract was washed with brine (ca. 30 mL), and dried over Na_2SO_4. After filtration, the filtrate was concentrated under reduced pressure. The residue was purified by PTLC ($CHCl_3$) to give **14-d_2** (44.2 mg, 123 µmol, 86.3%) as a white solid; R_f = 0.31 ($CHCl_3$); Melting point: 187 °C (dec.); ^{1}H NMR ($CDCl_3$, 400 MHz) δ 8.06 (d, J = 7.3 Hz, 2H), 7.47 (dd, J = 7.3, 7.3 Hz, 2H), 7.39 (t, J = 7.3 Hz, 1H), 7.21 (d, J = 7.8 Hz, 2H), 7.16 (d, J = 7.8 Hz, 2H), 7.13 (d, J = 7.8 Hz, 2H), 7.12 (s, 2H), 4.69 (s, 1H), 3.43 (s, 2H), 1.94 (s, br, 1H); $^{13}C\{^1H\}$NMR ($CDCl_3$, 100 MHz) δ 156.8 (2C), 150.9 (2C), 149.5 (2C), 149.4 (2C), 149.0 (2C), 146.4 (2C), 142.1 (1C), 128.6 (2C), 128.1 (1C), 126.4 (2C), 124.2 (2C), 123.4 (2C), 121.0 (2C), 93.3 (1C), 41.5 (d, J = 21.2 Hz, 1C), 41.3 (d, J = 20.2 Hz, 1C); IR (diamond, cm^{-1}) 3526, 3049, 2853, 1446, 1328, 993, 780, 732, 697; HRMS (FAB^+) m/z: $[M]^+$ Calcd for $C_{27}H_{14}D_2O^+$ 358.1327; Found 358.1319.

Phenylazahomosumanene-d₂ **8-*d*₂**. To a solution of **14-*d*₂** (20.0 mg, 55.8 mmol, 100 mol%) and NaN_3 (10.9 mg, 168 μmol, 300 mol%) in HFIP (0.5 mL) was added TFA (50 μL) at room temperature, and the mixture was stirred for 1 h at 60 °C. After cooling to room temperature, the mixture was carefully poured into saturated aqueous $NaHCO_3$ solution (ca. 20 mL). The mixture was extracted with CH_2Cl_2 (ca. 10 mL × 3). The combined organic extract was washed with brine (ca. 20 mL) and dried over Na_2SO_4. After filtration, the filtrate was concentrated under reduced pressure. The residue was purified by PTLC (CH_2Cl_2) to give **8-*d*₂** (12.1 mg, 34.1 μmol, 61.1%) as a pale yellow solid; R_f = 0.33 (CH_2Cl_2);

Melting point: 245 °C (dec.); ^1H NMR (CD_2Cl_2, 400 MHz) δ 8.11–8.09 (AA′BB′C, 2H), 7.95 (d, J = 8.2 Hz, 1H), 7.89 (d, J = 8.2 Hz, 1H), 7.87 (d, J = 7.8 Hz, 1H), 7.76 (d, J = 7.8 Hz, 1H), 7.63–7.57 (m, 3H), 7.41 (d, J = 7.3 Hz, 1H), 7.38 (d, J = 7.3 Hz, 1H), 4.23 (s, 2H); $^{13}C\{^1H\}$NMR (CD_2Cl_2, 100 MHz) δ 161.6 (1C), 149.4 (1C), 145.9 (1C), 145.3 (1C), 144.9 (1C), 143.6 (1C), 142.7 (1C), 142.1 (1C), 141.8 (1C), 141.3 (1C), 139.8 (1C), 130.4 (2C), 130.2 (1C), 129.7 (1C), 128.8 (2C), 126.4 (1C), 125.3 (1C), 125.2 (1C), 124.6 (1C), 124.55 (1C), 124.45 (1C), 124.2 (1C), 120.9 (1C), 42.2 (d, J = 19.3 Hz, 0.5C), 42.0 (d, J = 21.2 Hz, 0.5C), 41.9 (d, J = 17.3 Hz, 0.5C), 41.7 (d, J = 20.3 Hz, 0.5C); IR (diamond, cm^{-1}) 2955, 2852, 1719, 1444, 1260, 1086, 1014, 803, 791, 700;

HRMS (FAB^+) m/z: $[M]^+$ Calcd for $C_{27}H_{13}D_2N^+$ 355.1330; Found 355.1331.

PtCl₂[(Ph-azahomosumanene)(DMSO)]-d₂ **15-*d*₂**. To the mixture of **8-*d*₂** (10.0 mg, 28.1 μmol, 100 mol%) and $PtCl_2(DMSO)_2$ (11.9 mg, 28.1 μmol, 100 mol%) was added MeOH (1.5 mL) at room temperature, and the mixture was stirred for 16 h at 70 °C. After cooling to room temperature, and the yellow precipitate was collected by filtration and washed with MeOH (ca. 5 mL × 3) and diethyl ether (ca. 5 mL × 3) to afford the crude. This crude was purified by PTLC (CH_2Cl_2/MeOH = 98:2) to give **15-*d*₂** (4.9 mg, 7.0 μmol, 32%) as a yellow solid; R_f = 0.59 (CH_2Cl_2/MeOH = 98:2); Melting point: 279 °C (dec.); ^1H NMR ($CDCl_3$, 600 MHz) δ 9.54 (d, J = 8.2 Hz, 1H), 8.88 (d, J = 7.3 Hz, 1H), 8.15 (d, J = 8.2 Hz, 1H), 7.86 (dd, J = 7.8, 7.3 Hz, 1H), 7.84 (d, J = 8.2 Hz, 1H), 7.81–7.74 (m, 2H), 7.67 (dd, J = 6.9, 8.2 Hz, 1H), 7.65 (d, J = 8.2 Hz, 1H), 7.52 (d, J = 7.3 Hz, 1H), 7.50 (d, J = 7.3 Hz, 1H), 4.68 (s, 0.5H), 4.65 (s, 0.5H), 4.10 (s, 0.5H), 4.05 (s, 0.5H), 3.38 (s, 3H), 2.74 (s, 3H); $^{13}C\{^1H\}$ NMR ($CDCl_3$, 151 MHz) δ 167.8 (1C), 151.7 (1C), 146.4 (1C), 145.4 (1C), 144.7

(1C), 141.84 (1C), 141.77 (1C), 141.2 (1C), 140.7 (1C), 137.9 (1C), 132.8 (1C), 131.0 (1C), 130.5 (1C), 129.2 (1C), 128.6 (1C), 127.4 (1C), 127.1 (1C), 127.0 (1C), 126.7 (1C), 125.8 (1C), 125.3 (1C), 125.1 (1C), 124.7 (1C), 121.2 (1C), 45.1 (1C), 43.2 (1C), 42.5 (d, *J* = 17.9 Hz, 0.5C), 42.4 (d, *J* = 19.7 Hz, 0.5C), 41.8 (d, *J* = 20.8 Hz, 0.5C), 41.7 (d, *J* = 20.2 Hz, 0.5C); IR (KBr, cm^{-1}) 2922, 2852, 1722, 1636, 1441, 1394, 1148, 1016, 811, 707, 438;

HRMS (FAB$^+$) *m*/*z*: [M+Na]$^+$ Calcd for $C_{29}H_{19}D_2Cl_2NOSPtNa^+$ 721.0392; Found 721.0377.

2D ^{1}H EXSY NMR Experiment

To prepare sample solution, an NMR tube were added 15-d2 (6.0 mg, 8.6 μmol) and CDCl3 (0.40 mL). This sample solution was degassed by passing nitrogen gas.

2D EXSY (2D NOESY) experiments were acquired with a spectrum width of 15 ppm, with the acquisition time of 0.276 s, using 2048 data points in the t_2 dimension and 256 in t_1, with subsequent weighting with the sinebell function with 8 scans for each t_1 increment, and the mixing time was 2.2 s.

Computational Study

Unless otherwise noted, all theoretical calculations were performed using Gaussian 16 suite of programs (revision C.01).[17] Geometry optimization and transition state (TS) calculations were carried out by the DFT method at the B3LYP[18] level of theory with Def2-SVP[19] as a basis set for all atoms in gas phase. Harmonic frequency calculations were conducted with the same level of theory on the optimized geometries to check all stationary points as either minima or first-order saddle points. The zero-point energy (ZPE) and thermal energy corrections were calculated using vibrational frequency at 298.15 K and 393.15K (1 atm). The self-consistent field energies were corrected at the B3LYP level of theory with Def2-TZVP as a basis set for all atoms in gas phase.

The simulation of UV-Vis absorption spectrum of **15$_{up}$** was performed on the optimized ground state geometries using the time-dependent DFT (TD-DFT) method at B3LYP level of theory with a Def2-TZVP as a basis set for all atoms in gas phase.

Energy decomposition analysis

The complexation energy was express as the sum of the preparation energy (ΔE_{prep}) and interaction energy (ΔE_{int}):

$$\Delta E = \Delta E_{prep} + \Delta E_{int}$$

The optimized geometries of the platinum complexes (**15_{up}** and **15_{down}**) were separated into two fragments between platinum and nitrogen as shown in Figure S5, and the single-point calculation of each fragment was performed at the geometries with B3LYP/Def2-TZVP/gas phase level of theory to afford E_{fix}^{frag}. Next, the geometry optimization of each fragments was performed at the B3LYP/Def2-SVP/gas phase level of theory, and the single-point calculation of each fragments were performed at the optimized geometries with B3LYP/Def2-TZVP/gas phase level of theory to afford E_{relax}^{frag}. The preparation energy (ΔE_{prep}), which corresponds to the deformation energy derived from the strain and orbital rehybridization, was defined by the following equation:

$$\Delta E_{prep} = \left(E_{fix}^{frag1} - E_{relax}^{frag1}\right) + \left(E_{fix}^{frag2} - E_{relax}^{frag2}\right)$$

The interaction energy (ΔE_{int}) was decomposed into the following five components; $\Delta E_{\mathrm{elstat}}$, $\Delta E_{\mathrm{Pauli}}$, ΔE_{disp}, ΔE_{pol}, and ΔE_{CT}, which signify the permanent electrostatics, Pauli repulsion, dispersion, polarization, and charge-transfer terms, respectively.

$$\Delta E_{int} = \Delta E_{Frozen} + \Delta E_{pol} + \Delta E_{ct}$$

$$\Delta E_{Frozen} = \Delta E_{elstat} + \Delta E_{Pauli} + \Delta E_{disp}$$

The energy decomposition analysis (EDA) was performed using Q-Chem 5.0.2 package[20] by the second-generation energy decomposition analysis based on the absolutely localized molecular orbitals (ALMO-EDA) method[13] at the B3LYP level of theory with Def2-TZVP as a basis set for all atoms in gas phase. The optimized geometries of the platinum complexes (**15_{up}** and **15_{down}**) calculated using Gaussian 16 were separated into two fragments as shown in Figure 26. The D3 version of Grimme's dispersion with Becke-Johnson damping (D3-BJ)[21] was applied. The results of EDA calculation were expressed in kJ mol^{-1}.

$\Delta\Delta E$ for each term was defined following equation: [$\Delta\Delta E = \Delta E(\mathbf{15_{up}}) - \Delta E(\mathbf{15_{down}})$].

QTAIM analysis

The quantum theory of atoms-in-molecule (QTAIM) analysis on the optimized geometries was performed with the electron density calculated at the B3LYP/Def2-TZVP/gas phase level of theory using Multiwfn program.[22] The wavefunction files in a formatted gaussian checkpoint (fchk) file format were generated using Gaussian 16. The obtained bond paths and the bond critical points (BCPs) were visualized using VMD program.[23]

^{1}H NMR (400 MHz) and ^{13}C{^{1}H}NMR (100 MHz) spectra of **8** (CD$_2$Cl$_2$, 25 °C).

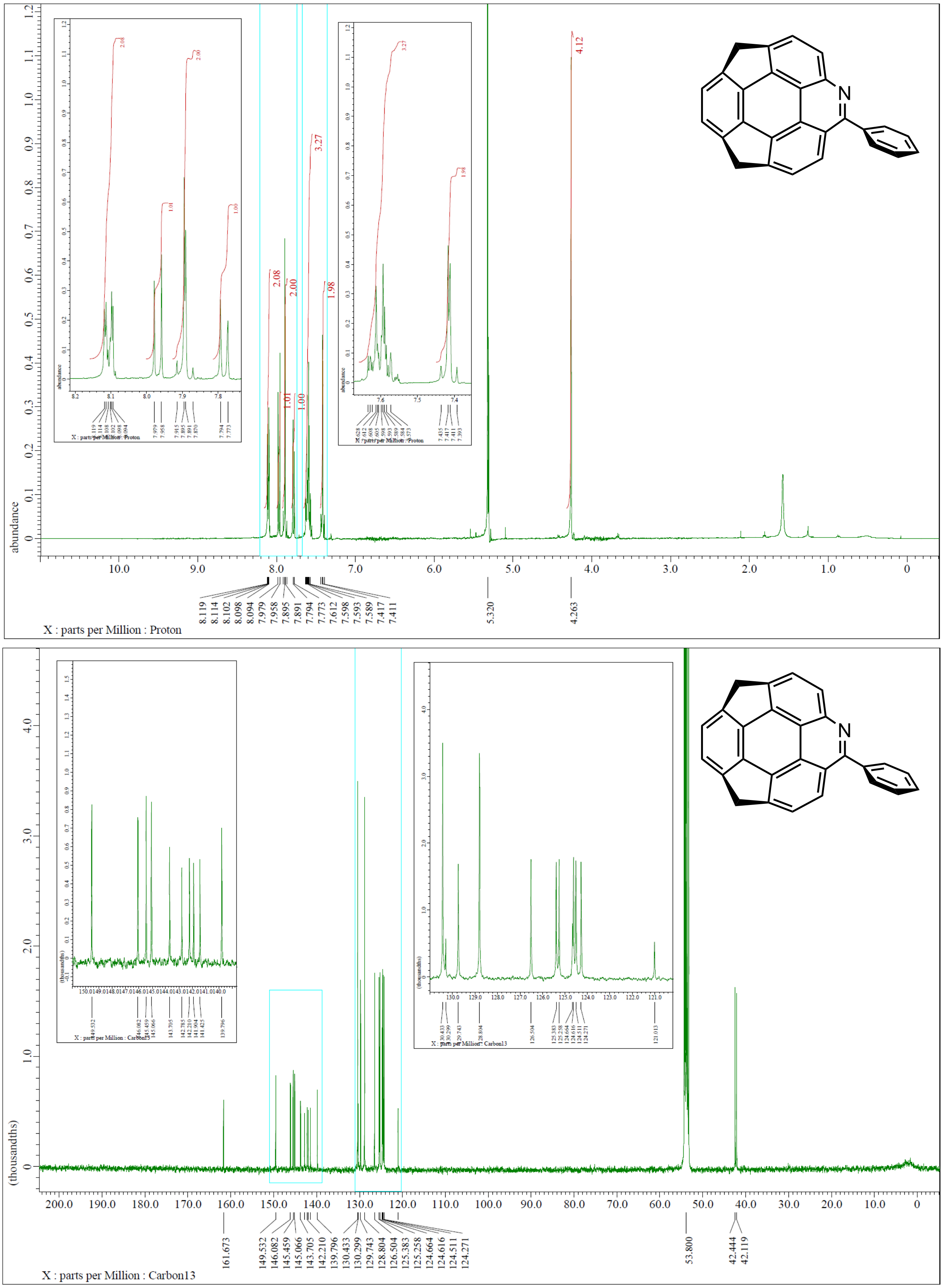

^{1}H NMR (400 MHz) and ^{13}C{^{1}H}NMR (100 MHz) spectra of **14** (CDCl$_3$, 25 °C).

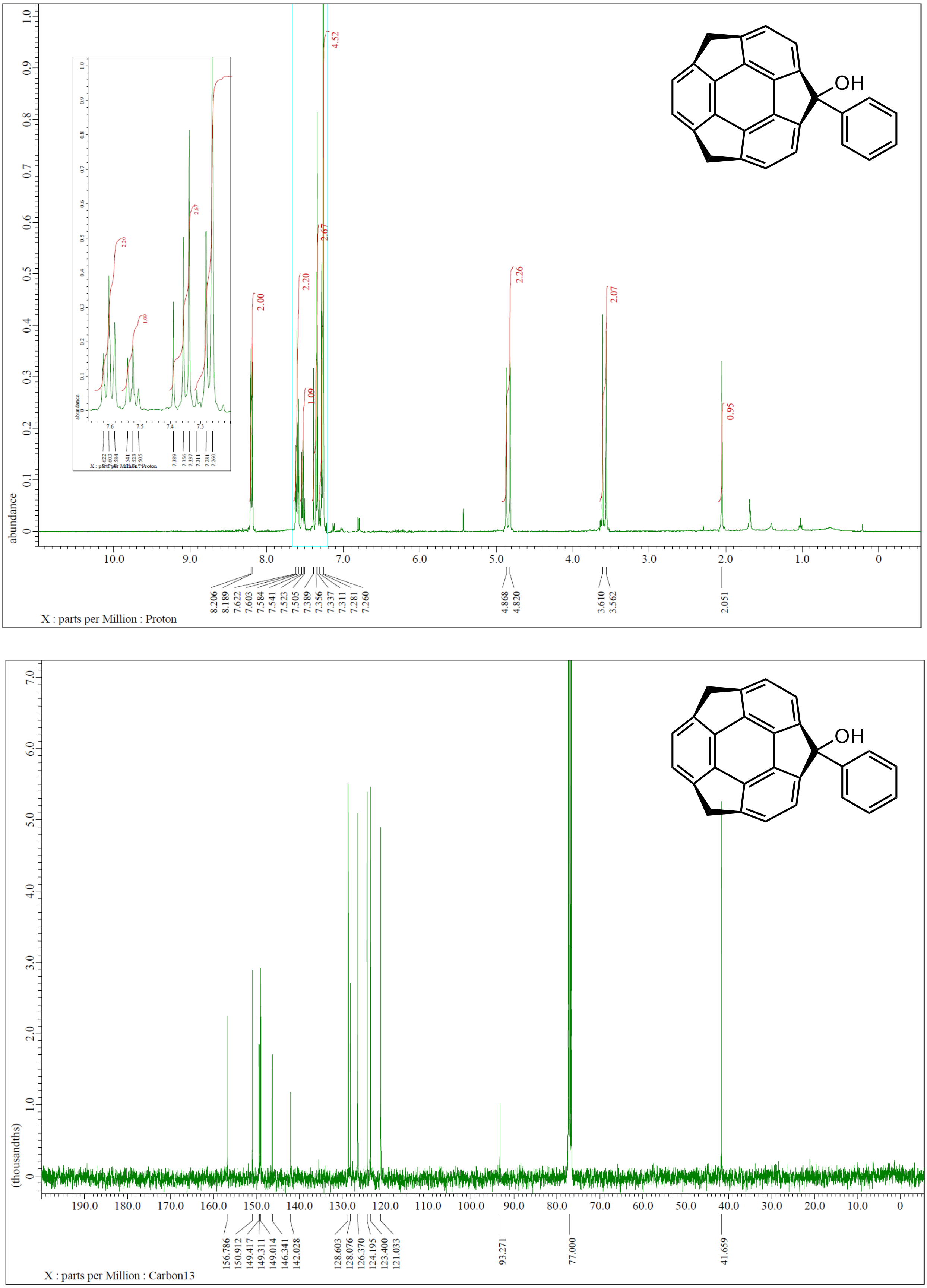

^{1}H NMR (400 MHz) and $^{13}C\{^{1}H\}$NMR (100 MHz) spectra of **15** ($CDCl_3$, 25 °C).

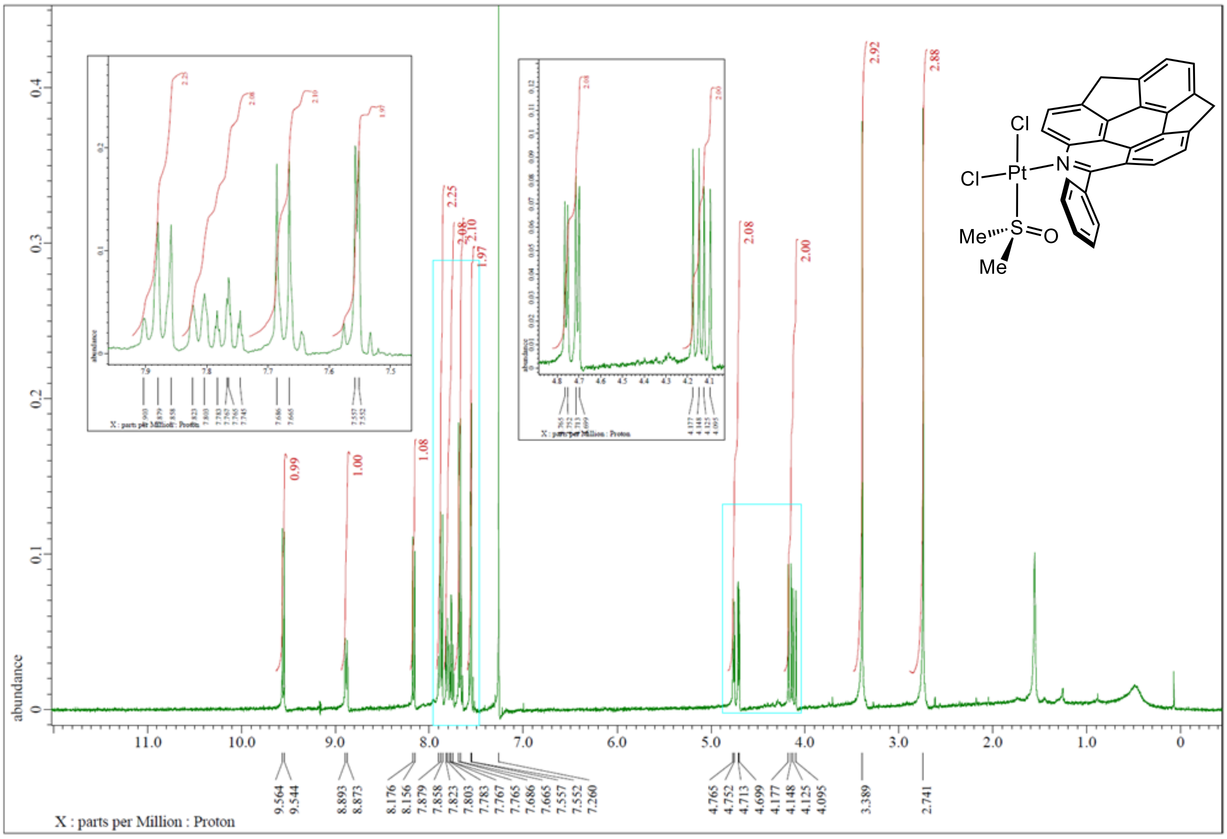

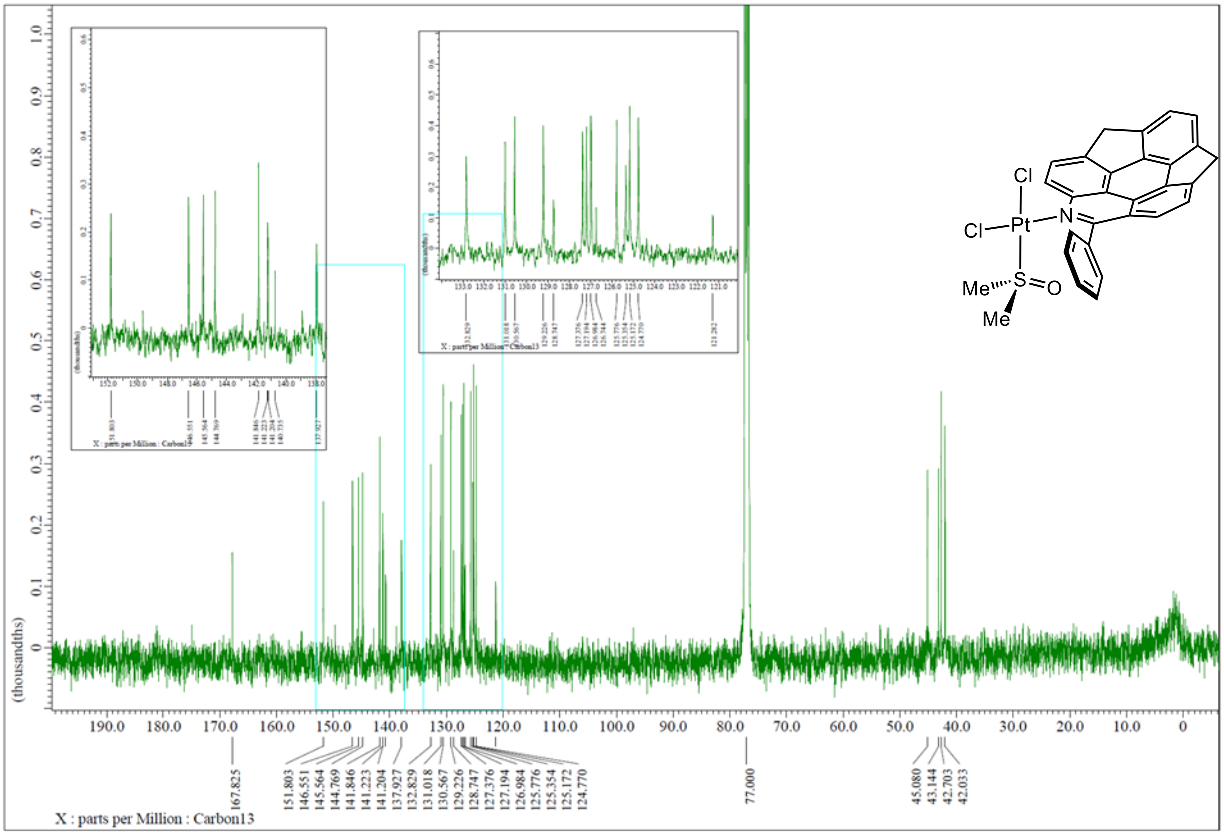

^{1}H NMR (400 MHz) and ^{13}C{^{1}H}NMR (100 MHz) spectra of **8-*d*$_2$** (CD_2Cl_2, 25 °C).

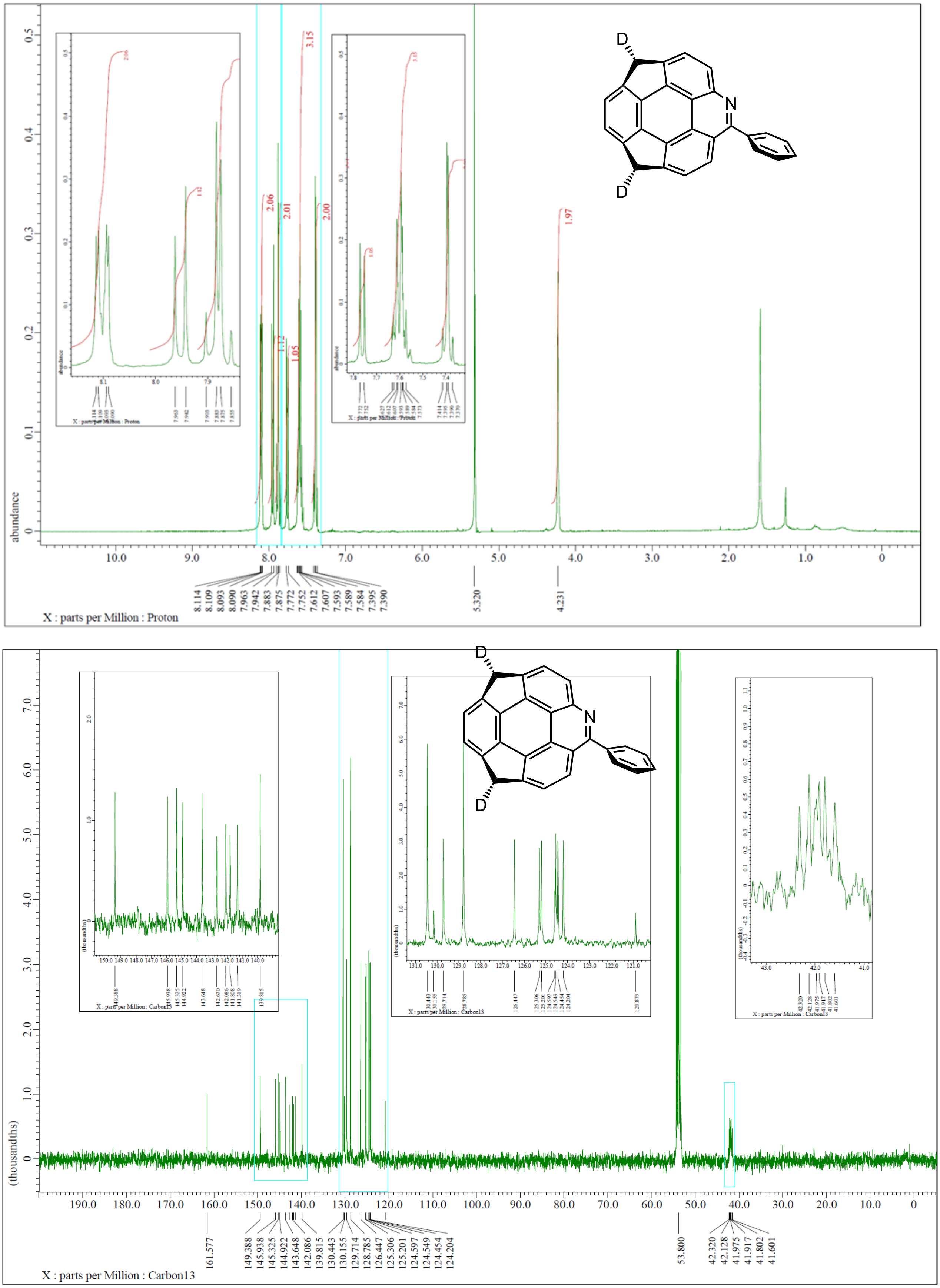

^{1}H NMR (400 MHz) and ^{13}C{^{1}H}NMR (100 MHz) spectra of **2-d_2** ($CDCl_3$, 45 °C).

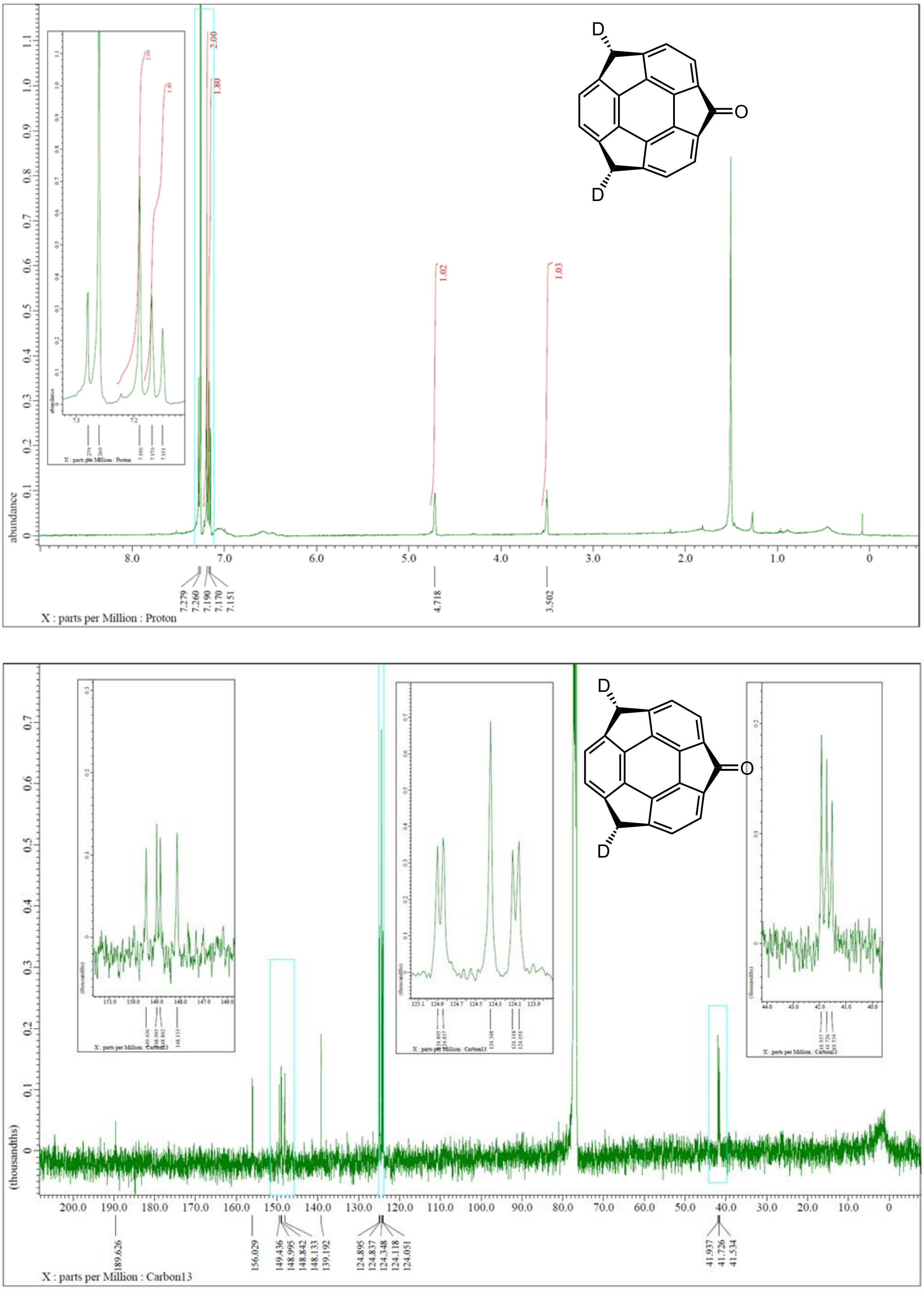

^{1}H NMR (400 MHz) and ^{13}C{^{1}H}NMR (100 MHz) spectra of **14-*d*$_2$** ($CDCl_3$, 25 °C).

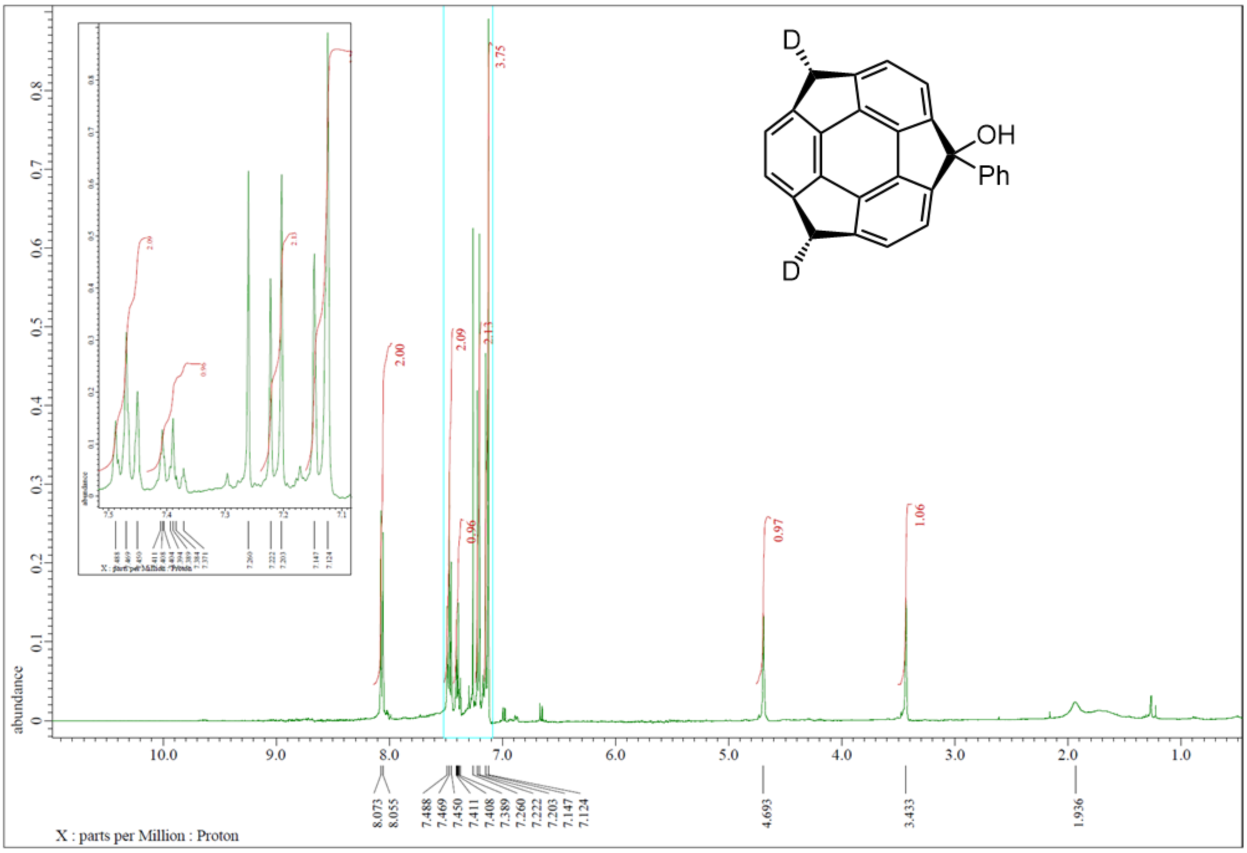

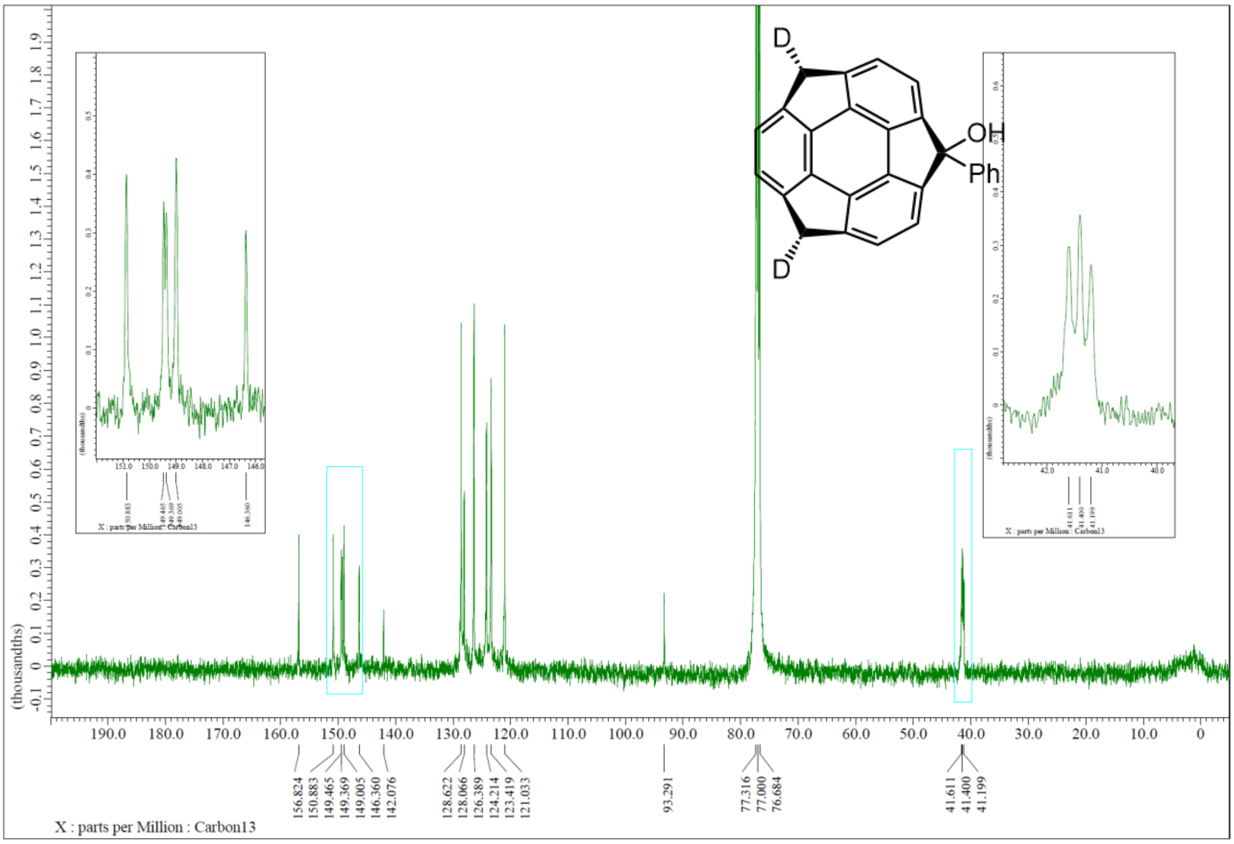

^{1}H NMR (600 MHz) and ^{13}C{^{1}H}NMR (151 MHz) spectra of **15-*d*$_2$** (CDCl$_3$, 25 °C).

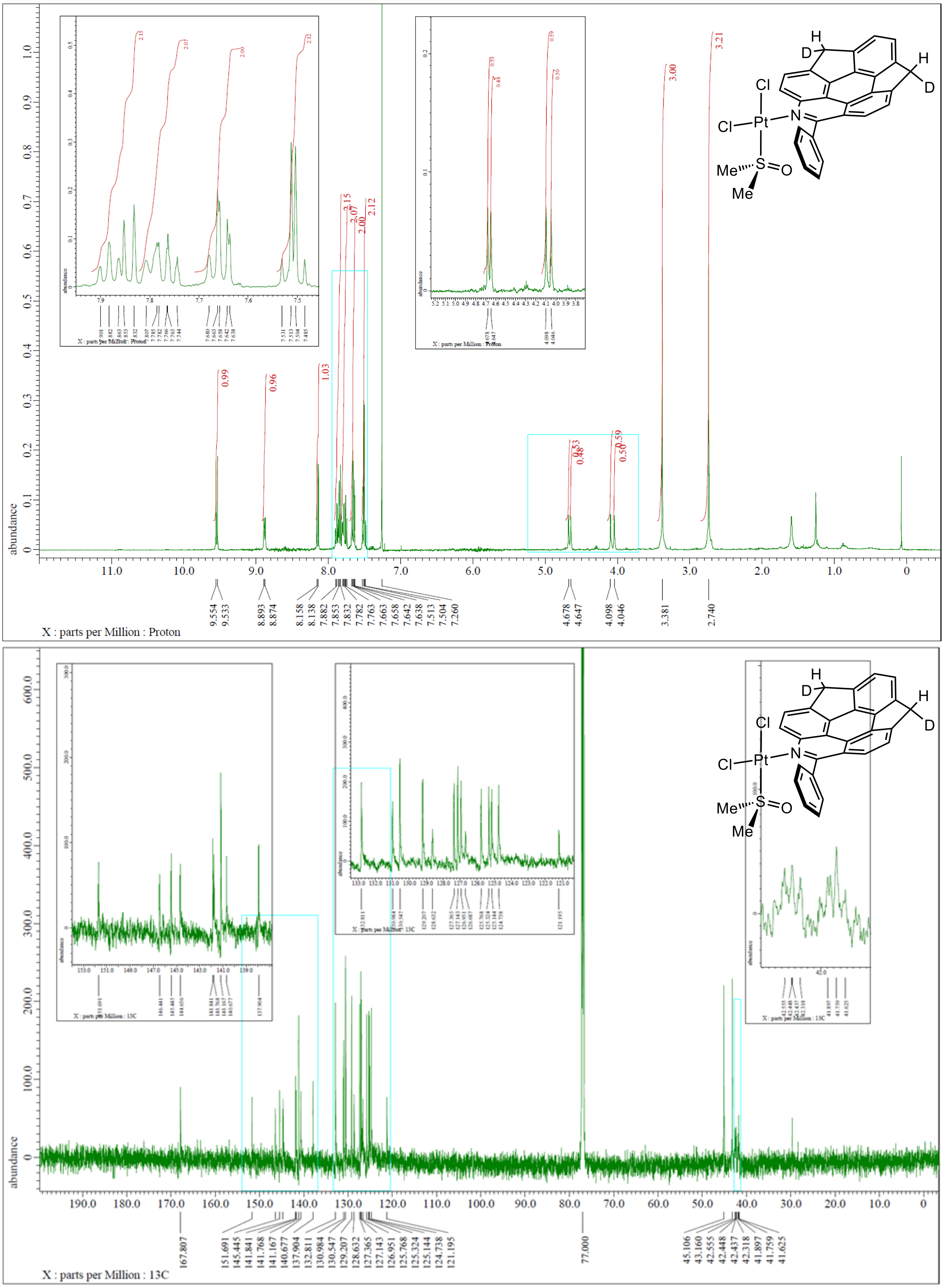

References

1. a) Y.-T. Wu, J. S. Siegel, *Chem. Rev.* **2006**, *106*, 4843−4867. b) T. Kawase, H. Kurata, *Chem. Rev.* **2006**, *106*, 5250−5273. c) M. Saito, H. Shinokubo, H. Sakurai, *Mater. Chem. Front.* **2018**, *2*, 635−661.
2. a) L. T. Scott, M. M. Hashemi, M. S. Bratcher, *J. Am. Chem. Soc.* **1992**, *114,* 1920−1921. b) T. J. Seiders, K. K. Baldridge, G. H. Grube, J. S. Siegel, *J. Am. Chem. Soc.* **2001**, *123*, 517−525. c) H. Sakurai, T. Daiko, T. Hirao. *Science* **2003**, *301*, 1878. d) T. Hayama, K. K. Baldridge, Y.-T. Wu, A. Linden, J. S. Siegel. *J. Am. Chem. Soc.* **2008**, *130*, 1583−1591. e) T. Amaya, H. Sakane, T. Muneishi, T. Hirao. *Chem. Commun.* **2008**, 765−767. f) B. B. Shrestha, S. Karanjit, S. Higashibayashi, H. Sakurai, *Pure Appl. Chem.* **2014**, *86*, 747−753.
3. a) M. Parschau, R. Fasel, K.-H. Ernst, O. Gröning, L. Brandenberger, R. Schillinger, T. Greber, A. P. Seitsonen, Y.-T. Wu, J. S. Siegel, *Angew. Chem. Int. Ed.* **2007**, *46*, 8258–8261. b) R. Jaafar, C. A. Pignedoli, G. Bussi, K. Aït-Mansour, O. Groening, T. Amaya, T. Hirao, R. Fasel, P. Ruffieux, *J. Am. Chem. Soc.* **2014**, *136*, 13666–13671. c) S. Fujii, M. Ziatdinov, S. Higashibayashi, H. Sakurai, M. Kiguchi, *J. Am. Chem. Soc.* **2016**, *138*, 12142–12149. d) S. Furukawa, Y. Suda, J. Kobayashi, T. Kawashima, T. Tada, S. Fujii, M. Kiguchi, M. Saito, *J. Am. Chem. Soc.* **2017**, *139*, 5787–5792.
4. S. Furukawa, J. Wu, M. Koyama, K. Hayashi, N. Hoshino, T. Takeda, Y. Suzuki, J. Kawamata, M. Saito, T, Akutagawa, *Nat. Commun.* **2021**, *12*, 768.
5. S. Higashibayashi, S. Onogi, H. K. Srivastava, G. N. Sastry, Y.-T. Wu, H. Sakurai, *Angew. Chem. Int. Ed.* **2013**, *52*, 7314–7316.
6. A. S. Filatov, M. A. Petrukhina, *Coord. Chem. Rev.* **2010**, *254*, 2234–2246.
7. T. Amaya, W.-Z. Wang, H. Sakane, T. Moriuchi, T. Hirao, *Angew. Chem. Int. Ed.* **2010**, *49*, 403–406.
8. J. Feng, L. Wang, X. Xue, Z. Chao, B, Hong, Z. Gu, *Org. Lett.* **2021**, *23*, 8056−8061.
9. S. Hishikawa, Y. Okabe, R. Tsuruoka, S. Higashibayashi, H. Ohtsu, M. Kawano, Y. Yakiyama, H. Sakurai, *Chem. Lett.* **2017**, *46*, 1556−1559.
10. H. Sakurai, T. Daiko, T. Hirao, *Science* **2003**, *301*, 1878.
11. C. L. Perrin, T. J. Dwyer, *Chem. Rev.* **1990**, *90*, 935−967.
12. Bader, R. F. W. *Acc. Chem. Res.* **1985**, *18*, 9−15.
13. P. R. Horn, Y. Mao, M. Head-Gordon, *Phys. Chem. Chem. Phys.* **2016**, *18*, 23067–23079.
14. L. S. Levin, M. Head-Gordon, *Nat. Commun.* **2020**, *11*, 4893.
15. L. C. Vishwakarma, O. D. Stringer, F. A. Davis, *Org. Synth.* **1988**, *66*, 203−210.
16. M. J. Woolley, G. N. Khairallah, G. Silva, P. S. Donnelly, B. F. Yates, R. A. J. O'Hair, *Organometallics* **2013**, *32*, 6931−6944.
17. Gaussian 16, Revision C.01, M. J. Frisch, G. W. Trucks, H. B. Schlegel, G. E. Scuseria, M. A. Robb, J. R. Cheeseman, G. Scalmani, V. Barone, G. A. Petersson, H. Nakatsuji, X. Li, M. Caricato, A. V. Marenich, J.

Bloino, B. G. Janesko, R. Gomperts, B. Mennucci, H. P. Hratchian, J. V. Ortiz, A. F. Izmaylov, J. L. Sonnenberg, D. Williams-Young, F. Ding, F. Lipparini, F. Egidi, J. Goings, B. Peng, A. Petrone, T. Henderson, D. Ranasinghe, V. G. Zakrzewski, J. Gao, N. Rega, G. Zheng, W. Liang, M. Hada, M. Ehara, K. Toyota, R. Fukuda, J. Hasegawa, M. Ishida, T. Nakajima, Y. Honda, O. Kitao, H. Nakai, T. Vreven, K. Throssell, J. A. Montgomery, Jr., J. E. Peralta, F. Ogliaro, M. J. Bearpark, J. J. Heyd, E. N. Brothers, K. N. Kudin, V. N. Staroverov, T. A. Keith, R. Kobayashi, J. Normand, K. Raghavachari, A. P. Rendell, J. C. Burant, S. S. Iyengar, J. Tomasi, M. Cossi, J. M. Millam, M. Klene, C. Adamo, R. Cammi, J. W. Ochterski, R. L. Martin, K. Morokuma, O. Farkas, J. B. Foresman, and D. J. Fox, Gaussian, Inc., Wallin.

18. P. J. Stephens, F. J. Devlin, C. F. Chabalowski, M. J. Frisch, *J. Phys. Chem.* **1994**, *98*, 11623–11627.
19. F. Weigend, R. Ahlrichs, *Phys. Chem. Chem. Phys.* **2005**, *7*, 3297–3305.
20. Q-Chem 5.0.2, Y. Shao, Z. Gan, E. Epifanovsky, A. T. B. Gilbert, M. Wormit, J. Kussmann, A. W. Lange, A. Behn, J. Deng, X. Feng, D. Ghosh, M. Goldey, P. R. Horn, L. D. Jacobson, I. Kaliman, R. Z. Khaliullin, T. Kuś, A. Landau, J. Liu, E. I. Proynov, Y. M. Rhee, R. M. Richard, M. A. Rohrdanz, R. P. Steele, E. J. Sundstrom, H. L. Woodcock, P. M. Zimmerman, D. Zuev, B. Albrecht, E. Alguire, B. Austin, G. J. O. Beran, Y. A. Bernard, E. Berquist, K. Brandhorst, K. B. Bravaya, S. T. Brown, D. Casanova, C.-M. Chang, Y. Chen, S. H. Chien, K. D. Closser, D. L. Crittenden, M. Diedenhofen, R. A. DiStasio, H. Do, A. D. Dutoi, R. G. Edgar, S. Fatehi, L. Fusti-Molnar, A. Ghysels, A. Golubeva-Zadorozhnaya, J. Gomes, M. W. D. Hanson-Heine, P. H. P. Harbach, A. W. Hauser, E. G. Hohenstein, Z. C. Holden, T.-C. Jagau, H. Ji, B. Kaduk, K. Khistyaev, J. Kim, J. Kim, R. A. King, P. Klunzinger, D. Kosenkov, T. Kowalczyk, C. M. Krauter, K. U. Lao, A. D. Laurent, K. V. Lawler, S. V. Levchenko, C. Y. Lin, F. Liu, E. Livshits, R. C. Lochan, A. Luenser, P. Manohar, S. F. Manzer, S.-P. Mao, N. Mardirossian, A. V. Marenich, S. A. Maurer, N. J. Mayhall, E. Neuscamman, C. M. Oana, R. Olivares-Amaya, D. P. O'Neill, J. A. Parkhill, T. M. Perrine, R. Peverati, A. Prociuk, D. R. Rehn, E. Rosta, N. J. Russ, S. M. Sharada, S. Sharma, D. W. Small, A. Sodt, T. Stein, D. Stück, Y.-C. Su, A. J. W. Thom, T. Tsuchimochi, V. Vanovschi, L. Vogt, O. Vydrov, T. Wang, M. A. Watson, J. Wenzel, A. White, C. F. Williams, J. Yang, S. Yeganeh, S. R. Yost, Z.-Q. You, I. Y. Zhang, X. Zhang, Y. Zhao, B. R. Brooks, G. K. L. Chan, D. M. Chipman, C. J. Cramer, W. A Goddard, M. S. Gordon, W. J. Hehre, A. Klamt, H. F. Schaefer, M. W. Schmidt, C. D. Sherrill, D. G. Truhlar, A. Warshel, X. Xu, A. Aspuru-Guzik, R. Baer, A. T. Bell, N. A. Besley, J.-D. Chai, A. Dreuw, B. D. Dunietz, T. R. Furlani, S. R. Gwaltney, C.-P. Hsu, Y. Jung, J. Kong, D. S. Lambrecht, W. Liang, C. Ochsenfeld, V. A. Rassolov, L. V. Slipchenko, J. E. Subotnik, T. Van Voorhis, J. M. Herbert, A. I. Krylov, P. M. W. Gill, M. Head-Gordon, *Mol. Phys.* **2015**, *113*, 184–185.
21. S. Grimme, S. Ehrlich, L. Goerigk, *J. Comput. Chem.* **2011**, *32*, 1456–1465.
22. T. Lu, F. Chen, *J. Comput. Chem.* **2012**, *33*, 580−592.
23. W. Humphrey, A. Dalke, K. Schulten, *J. Mol. Graph.* **1996**, *14*, 33−38.

Chapter 5. Acceleration Effect of Bowl-shaped Structure in Aerobic Oxidation Reaction: Synthesis of Homosumanene *ortho*-Quinone and Azaacene-Fused Homosumanenes

Section 1. Introduction

The inherent strain in a molecule affects its reactivity. As shown by the development of chemical functionalization of fullerenes[1], carbon nanobelts[2], and buckybowls[3], curved π-conjugated molecules often exhibit higher reactivity than planar π-conjugated molecules. As mentioned in Chapter 1, the curved structure reduces the overlap of *p*-orbitals, resulting in changes in electronic structure, such as a lowering of the LUMO level due to an increase in the *s*-character of the bonds. These changes increase the reactivity for nucleophilic addition reactions (Figure 41a). In addition, their aromaticity is also subject to changes in electronic perturbations. For example, the aromaticity of their six-membered rings in C60 fullerene is smaller than that of planar π-conjugated molecules such as benzene.[4] Furthermore, a variety of addition reactions can proceed on fullerenes that would be difficult to proceed on planar π-conjugated molecules.[5] Recently, Itami et al. reported a strain-promoted Diels-Alder reaction in the benzene ring of [6,6]carbon nanobelts.[6] Bodwell and Ito et al. synthesized π-extended azacorannulenophanes by a strain-promoted addition reaction using bent pyrenophanes.[7] Similarly, buckybowls with the fragmented structure of fullerenes are expected to exhibit high or unique reactivity for various reactions. Indeed, several addition reactions have been reported in buckybowls, such as corannulene[8], diindenochrysene[9], and circumtriindene[10]. In addition, Sakurai et al. reported that the osmium dihydroxylation of sumanene proceeds at the internal aromatic rings via an energetically unfavorable dearomatization step.[11] The reactions described above proceed without pre-functionalization and are potent methods for the synthesis of novel curved molecular nanocarbons.

Chapter 2 described the synthesis of C70 minimal fragment buckybowl, homosumanene, from sumanenone (2) by a ring expansion reaction. In that work, the author noticed that hydroxyhomosumanene (**3’**) was unstable and changed to an unknown compound during purification. After the product was characterized, air oxidation of **3’** proceeded on silica gel to form homosumanene *ortho*-quinone (**16**). Strunz et al. reported that irradiation of 7-hydroxycadalene adsorbed on silica gel with white light leads to the oxidation to give mansonone *ortho*-quinone. This oxidation reaction needs 5-6 days and affords the *ortho*-quinone in only 36% (Figure 41b).[12] On the other hand, the oxidation of **3’** is completed in 1 hour. In this chapter, the accelerating effect of air oxidation in **3’** due to the distorted bowl-shaped structure was experimentally and theoretically evaluated by comparing it with phenanthrenol, a planar congener. Furthermore, azaacene-fused homosumanenes and azaacenohomosumanenes were synthesized using **16** as a common intermediate, and their electronic properties were investigated (Figure 41d).

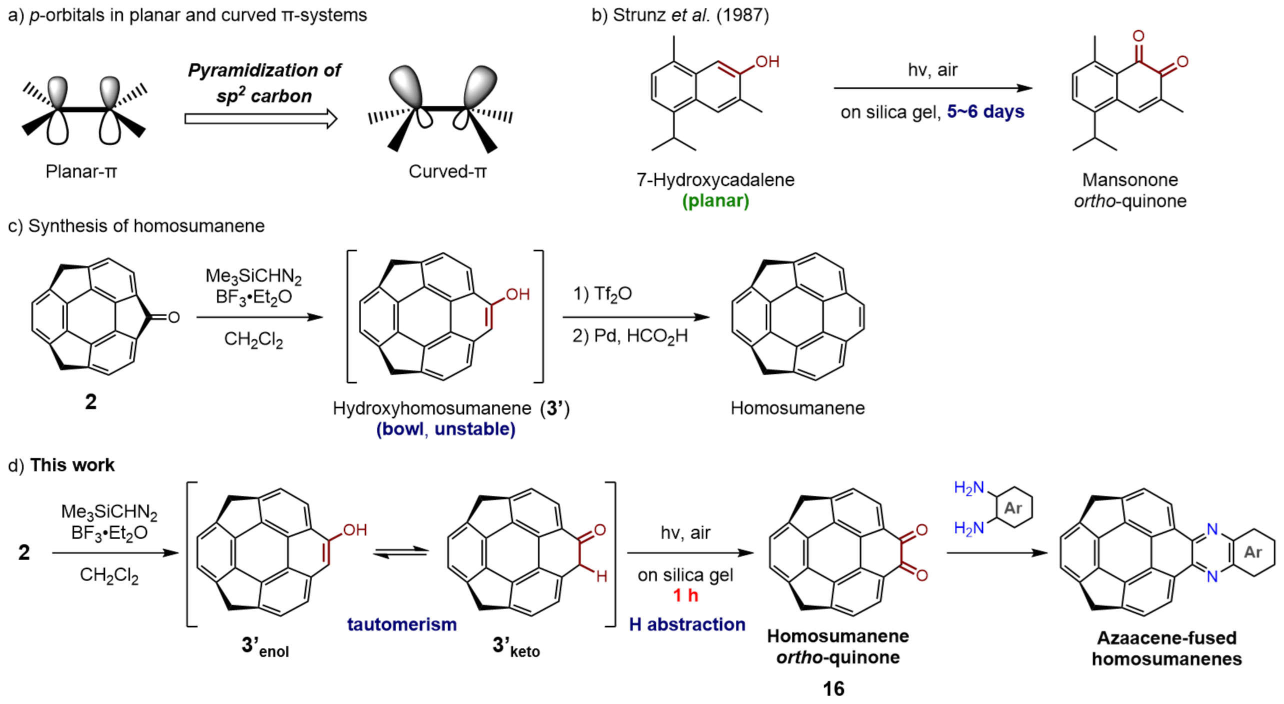

Figure 41. a) *p*-orbitals of planar and curved-π systems. b) Oxidation of 7-hydroxycadalene on silica gel. c) Synthesis of homosumanene. d) This work.

Section 2. Generation of homosumanene *o*-quinone

While investigating the synthesis of homosumanene in Chapter 2, the author noticed that the air oxidation of **3’$_{\mathbf{enol}}$** proceeded to give homosumanene *o*-quinone **16**. After the addition of trimethylsilyl diazomethane to the sumanenone (**2**), the TLC of crude mixture clearly showed the disappearance of **2** and generation of **3’$_{\mathbf{enol}}$** (Scheme 13). The color of the TLC spot of **3’$_{\mathbf{enol}}$** immediately changed from colorless to orange after UV light (λ = 254 nm) irradiation, implying the unexpected reaction proceeded on silica gel. Based on this, a two-dimensional TLC experiment of **3’$_{\mathbf{enol}}$** was conducted. After the light irradiation, the colorless spot of **3’$_{\mathbf{enol}}$** changes to an orange spot with a different R_f value from **3’$_{\mathbf{enol}}$**. This result suggests that the **3’$_{\mathbf{enol}}$** was converted to a different compound. ^{1}H NMR analysis of the crude product (without photoirradiation) showed the successive formation of **3’**, suggesting that this conversion occurred by UV irradiation of **3’** adsorbed on silica gel. To isolate this compound, purification was performed using preparative thin layer chromatography (PTLC) instead of silica gel column chromatography. In the experimental procedure, the crude product containing **3’$_{\mathbf{enol}}$** was adsorbed on silica gel of PTLC, and UV light was irradiated for 1 hour. After UV-light irradiation, the PTLC was developed, and the target fraction was collected (Figure 42). ^{1}H NMR analysis of the product showed the disappearance of the enol proton, and high-resolution mass spectroscopy showed a peak at m/z = 306.0681 ([M]+), indicating the formation of *ortho*-quinone **16**. Finally, the structure of **16** was determined by single crystal X-ray diffraction analysis and found to be afforded in 62% yield. The dimer **17** was also obtained as a byproduct in 9% yield, suggesting the involvement of a radical mechanism in this oxidation reaction.

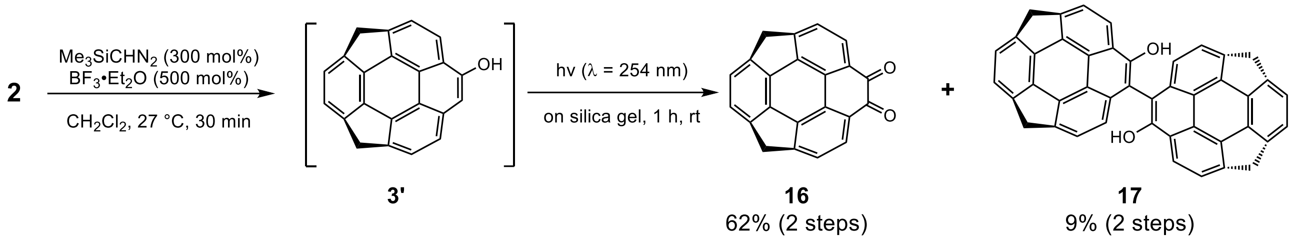

Scheme 13. Synthesis of homosumanene *o*-quinone **16**, dimer **17**.

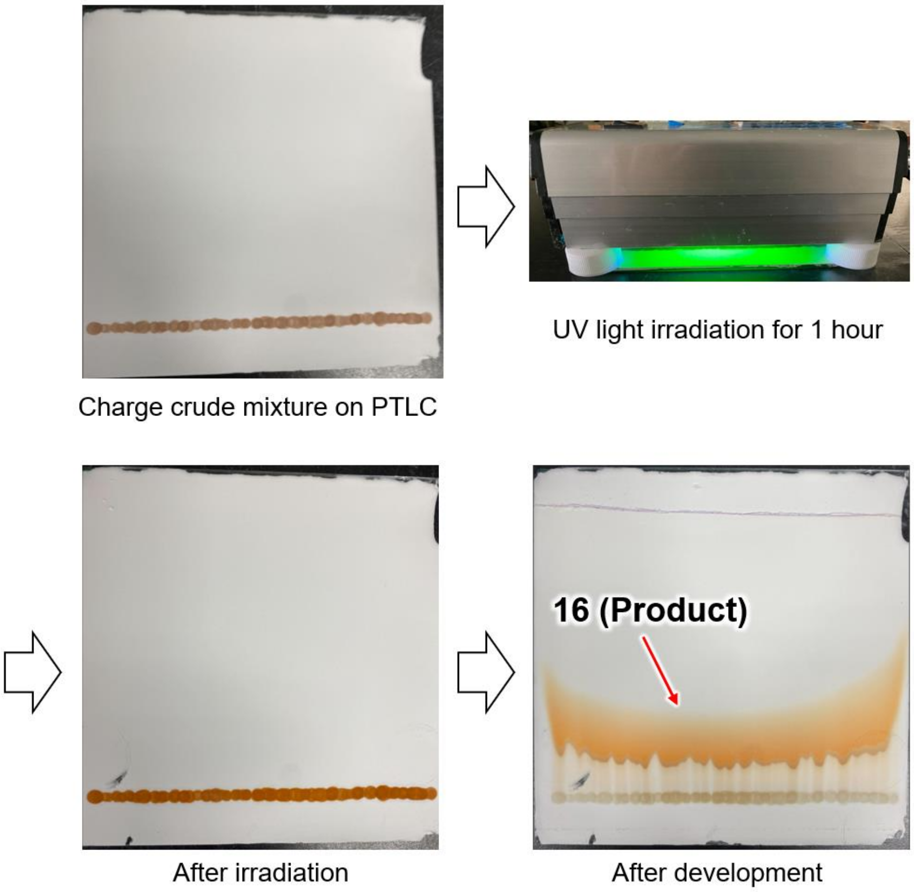
Charge crude mixture on PTLC

UV light irradiation for 1 hour

After irradiation

After development

Figure 42. Snapshots of aerobic oxidation reaction on PTLC.

Single crystal X-ray diffraction analysis revealed that **16** has a shallow bowl structure similar to other homosumanene derivatives (Bowl depth: 0.43-0.82 Å, Figure 43a). The C-C bond length between the two carbonyl carbons (C16-C17: 1.61 Å) is longer than the typical C(sp^2)-C(sp^2) bond (1.49 Å)[13] and other planar *ortho*-quinone compounds (9,10-phenanthrenequinone: 1.54 Å[14] and 4,5-pyrenedione: 1.54 Å[15]) (Figure 43a). This C-C bond elongation is considered to reduce the curved strain. Similar bond elongation has been reported in corannulene *ortho*-quinone.[16] For the packing structure of **16**, a one-dimensional columnar structure was observed along the *c*-axis despite the shallow bowl structure (Figure 43c). In this columnar structure, the *ortho*-quinone moieties of each molecule were stacked in a 180° rotated manner to cancel the in-plane dipole moments. Each column was oriented in opposite directions, and CH···O interactions (3.3–3.4 Å) between each column contributed to the stabilization of the overall packing structure.

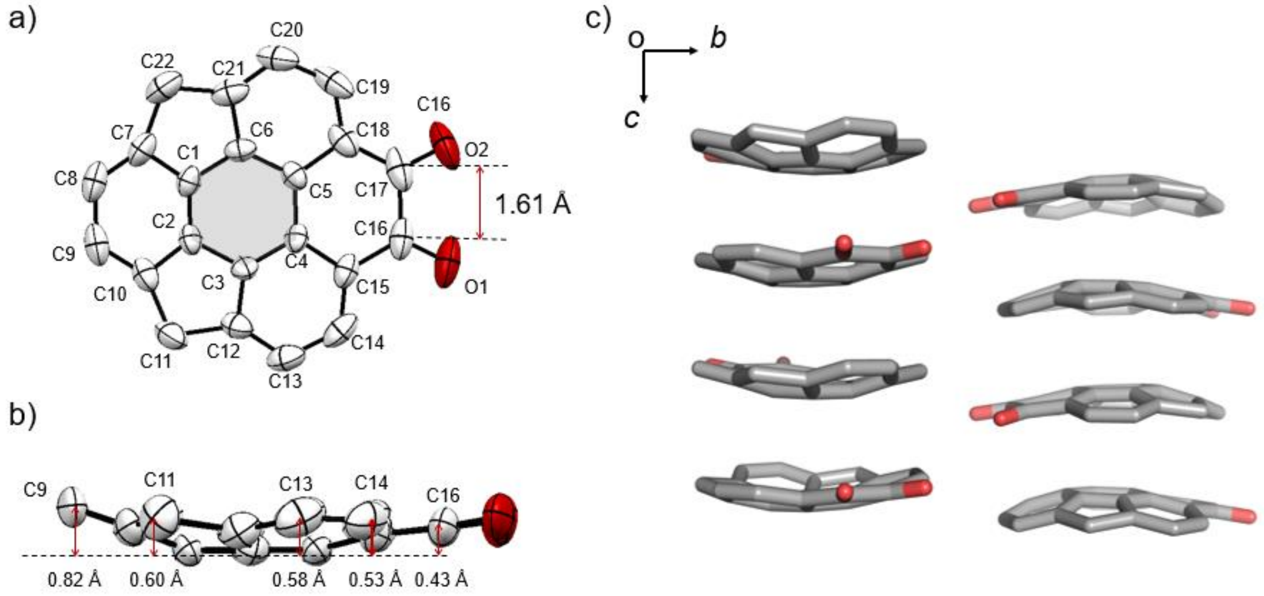

Figure 43. Crystal structure of **16**. a) Top and b) side views of thermal displacement plots of **16** at 50% probability. c) Packing structure viewed from a axis. Solvent and hydrogen atoms were omitted for clarity.

Several conversions of phenol or aniline derivatives to *o*-quinones by oxidants have been reported. Recently, Sýkora and Storch et al. reported that a photo-induced air oxidation reaction proceeds in distorted aminohelicene. They proposed that singlet oxygen ($^1O_2$) produced by energy transfer from the photo-excited substrate is involved in the reaction mechanism.[17] On the other hand, considering the formation of the dimer (**17**), triplet oxygen ($^3O_2$) may be involved in this case. Before the investigation of reaction conditions, acetyl-protected **18** was synthesized as the precursor of the unstable **3’**. Direct acylation of the crude product containing **3’** by acetic anhydride afforded **18** in 69% yield (Scheme 14).

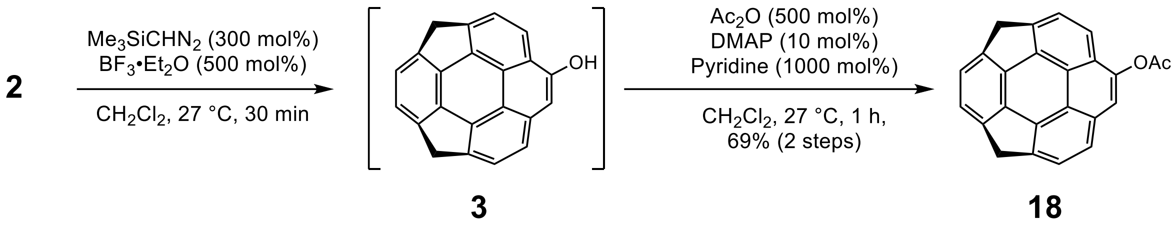

Scheme 14. Synthesis of acetyl homosumanene **18**.

In the reaction condition screening for the oxidation, **18** was deprotected by potassium carbonate/methanol prior to the reaction, and the resulting **3’** was used without purification (Table 11). When the wavelength of the light was changed to λ = 365 nm from λ = 254 nm, the yields of **16** changed to 60% from 70%. (entries 1 and 2). When the on-silica gel oxidation was attempted under a nitrogen atmosphere (in a glove box), the reaction did not proceed. This indicates that oxygen is essential for this reaction (entry 3). Without UV irradiation, **16** was formed in 29% yield (entry 4). This result suggests that UV irradiation isn’t essential but accelerates the reaction. To confirm the contribution of $^1O_2$, the reaction was then examined under solution conditions with and without the addition of rose bengal as a photosensitizer while silica gel was dispersed in chloroform. The oxidation in the solution phase afforded **16** in 38% yield; however, the yield was still lower than on silica gel condition (entry 5). On the other hand, adding rose bengal as a photosensitizer had little effect on the reaction (entry 6). These results suggest that $^3O_2$ and related radical species are involved in the reaction mechanism rather than $^1O_2$. When the reaction was performed under UV light in $CHCl_3$ without silica gel, **16** was obtained in 30% yield (entry 7). This suggested that the addition of silica gel had little effect on the reaction in the solution phase.

Table 11. Screening of reaction conditions for the oxidation of **2**.

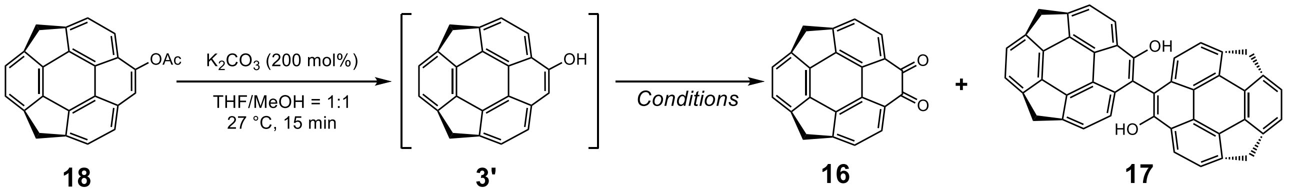

Entry	Conditions	Yield of **16** (%)	Yield of **17** (%)
1	air, on silica-gel, λ = 254 nm, 1 h	72[a]	7[a]
2	air, on silica-gel, λ = 365 nm, 1 h	60[a]	9[a]
3	N_2, on silica-gel, λ = 254 nm, 1 h	0[b]	0[b]
4	air, on silica-gel, dark, 1 h	29[b]	trace[b]
5	air, silica-gel dispersion in $CHCl_3$, λ = 254 nm, 1 h	38[b]	trace[b]
6	air, silica-gel dispersed in $CHCl_3$, Rose Bengal, λ = 254 nm, 1 h	29[b]	trace[b]
7	air, $CHCl_3$, λ = 254 nm, 1 h	30[b]	trace[b]

[a] Isolated yield. [b] Determined by ^{1}H NMR analysis using 1,1,2,2-tetrachloroethane as an internal standard.

Section 3. Comparison of the reactivity with the planar molecule

Next, the reaction rates of bowl-shaped **3’** and the planar congener, phenanthrenol **19**, were compared. As in the condition screening, in situ generated **3’** by deprotection of **18**, and air-stable **19** were adsorbed on silica gel, and irradiated with light, and the reaction rates were compared by plotting the yield of products every 10 minutes. The same experiments were performed three times (Figure 44, Tables 12 and 13) because of the large influence of experimental manipulation errors. As a result, the oxidation proceeds with the planar **19**, and the reaction rate of **3’** is greater than that of **19**. These results suggest that the curved structure plays an important role in this oxidation.

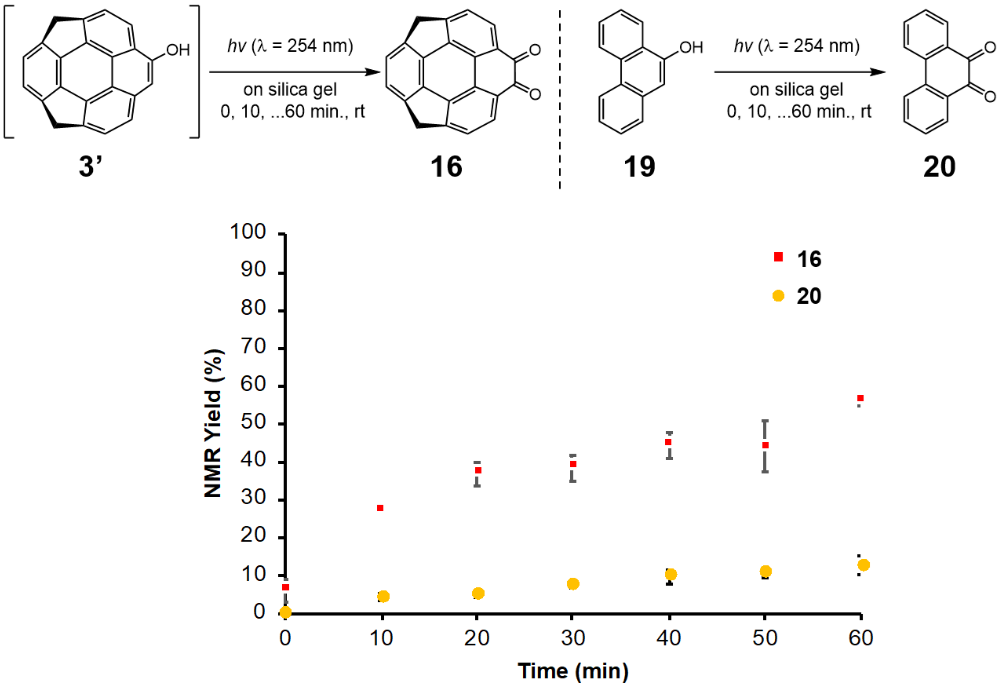

Figure 44. Time-course plots of the yield of **16** and **20** in the oxidation of **3’** and **19** on silica gel oxidation.

Table 12. Time course of the yield of **16**.

		0 min	10 min	20 min	30 min	40 min	50 min	60 min
Yield (%)	run 1	7	27	34	35	43	35	58
	run 2	9	27	41	37	41	46	54
	run 3	2	28	35	43	49	51	57

Table 13. Time course of yield of **20**.

		0 min	10 min	20 min	30 min	40 min	50 min	60 min
Yield (%)	run 1	0	3	4	7	7	9	10
	run 2	0	5	5	7	11	11	12
	run 3	0	5	6	9	11	12	16

During the above condition screening, **3’** was found to exist as an isomeric mixture of enol (**3’**$_{\mathbf{enol}}$) and keto (**3’**$_{\mathbf{keto}}$) forms in CD_2Cl_2 (**3’**$_{\mathbf{enol}}$: **3’**$_{\mathbf{keto}}$ = 77:23, 25 °C). In the case of **19**, only the enol form was observed under the same conditions. DFT calculations at the ωB97X-D/Def2-TZVP level for **3’**, **19**, and hydroxybenzopyrene **21** were performed to compare the thermodynamic stability of the keto and enol forms. In the case of bowl-shaped **3’**, the keto form is more stable than the enol form by 2.65 kcal/mol. In contrast, the **19’** and **21’** enol forms were 1.66 and 1.56 kcal/mol, more stable than the corresponding keto forms, respectively (Figure 45b). Although the DFT calculations could not fully reproduce the experimental keto/enol ratio (**3’**$_{\mathbf{enol}}$: **3’**$_{\mathbf{keto}}$ = 77: 23, 25 °C), the trend that the isomeric ratio of keto forms increases in **3’** is consistent with the trend in the experimental results. These results suggest that the keto/enol ratio is affected by the structure of the molecule and influences the reaction rate in air oxidation. In the case of planar phenol derivatives, their *p*-orbitals are in the same plane, allowing for adequate orbital overlap. On the other hand, the sp^2 carbons in **3’** is distorted into a tetrahedral shape due to its bowl structure, resulting in inefficient orbital overlaps (Figure 45a). As a result, the stabilization by aromaticity in the **3’**$_{\mathbf{enol}}$ is reduced, and thus the **3’**$_{\mathbf{keto}}$ is more observed than the keto forms of planar molecules. Indeed, the NICS(0)[4] value of the phenolic six-membered ring of **3’** at the B3LYP/6-311+G(d) level is –4.3, which is larger than that of planar molecules **19** (–6.5) and **21** (–5.0) (Figure 45b).

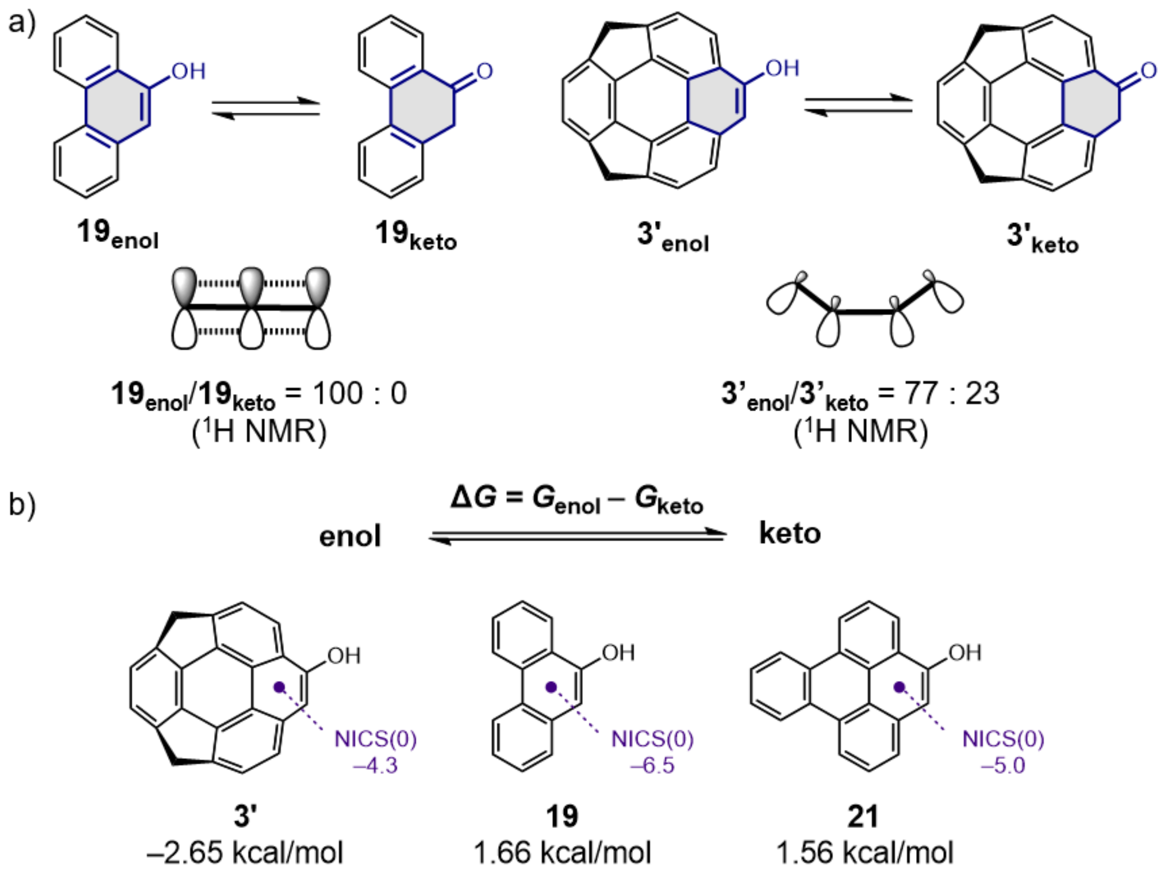

Figure 45. Evaluation of keto/enol tautomerization. a) Experimental keto/enol ratio in CD_2Cl_2 at 25 °C and *p*-orbitals of **19**$_{\mathbf{enol}}$ and **3’**$_{\mathbf{enol}}$. b) Calculated difference of Gibbs free energy between enol and keto isomers at ωB97X-D/Def2-TZVP level of theory. The enol isomer of each compound and its NICS(0) value are shown.

Based on these results, the presumed reaction mechanism of the photo-induced oxidation reaction on silica gel is shown in Figure 46. First, **3’**$_{\mathbf{keto}}$ is generated by tautomerization, and the hydrogen at the α-position of the carbonyl group in **3’**$_{\mathbf{keto}}$ is abstracted by triplet oxygen ($^3O_2$) to afford the corresponding α-keto radical.

This radical reacts with oxygen or hydroperoxy radical to form the α-ketohydroperoxide.[18] After tautomerization, elimination of H_2O proceeds to afford the *ortho*-quinone **16**. DFT calculations also support the tautomerization and elimination of H_2O (Figure 47). In this reaction mechanism, silica gel may work as a solid acid to promote the formation of the **3'$_{\mathbf{keto}}$** and the dehydration step. Although the detailed effect of UV light irradiation is still unclear, the author considered that the UV light irradiation induces the excitation of **3'** and promotes the formation of ketoradicals. Dimer **17** is a byproduct formed by the dimerization of the ketoradical. Although the possibility of radical formation by the SET (Single Electron Transfer) process from **3'$_{\mathbf{enol}}$** cannot be excluded, it is likely not to occur because both **16** and **17** were not obtained under nitrogen conditions. Based on these considerations, the oxidation is expected to proceed more efficiently in buckybowl, where keto forms are more efficiently generated than in planar molecules.

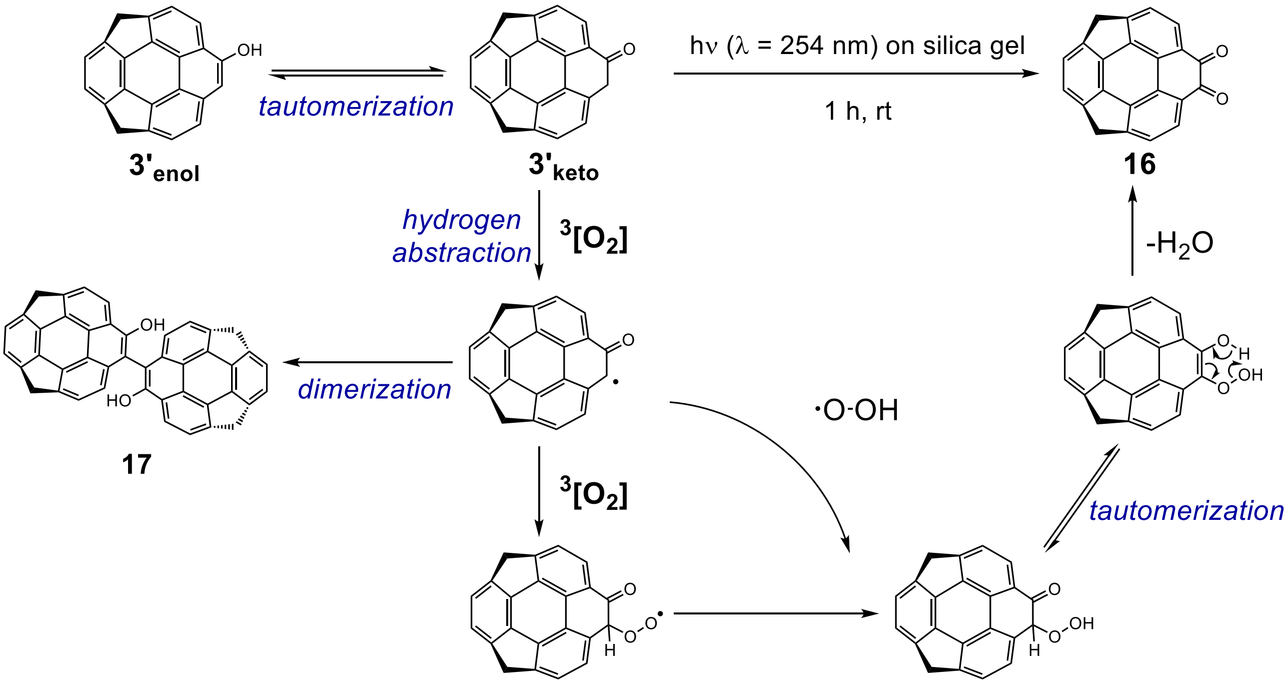

Figure 46. Possible reaction mechanism.

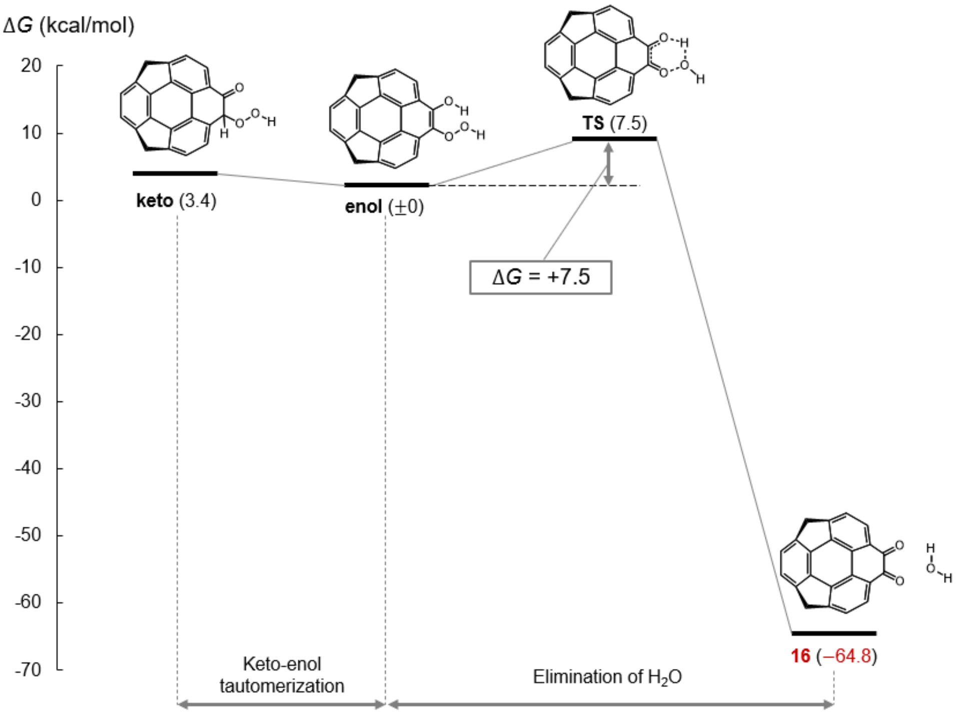

Figure 47. Energy profile of the tautomerization of intermediates and elimination of H_2O. The calculated Gibbs free energies (Δ*G*, 298.15 K, 1 atm) are shown in kcal mol^{-1}.

Section 4. Synthesis and crystal structures of azaacene-fused homosumanenes

ortho-quinone is one of the useful building blocks for constructing azaacenes[19] that are beneficial electron deficient π-conjugated molecules as n-type semiconductors. The previous studies about acene-fused buckybowls demonstrated that azaacene-fused buckybowls may exhibit attractive physical properties such as high charge carrier mobility and singlet fission efficiency.[20] Therefore, the author tried to synthesize azaacene-fused homosumanenes, azaacenohomosumanenes. The azaacenohomosumanenes (**22a-22d**) were synthesized by cyclocondensation reaction of **16** with a series of *ortho*-diamines in the presence of acetic acid and anhydrous sodium sulfate in chloroform/acetic acid (Scheme 15).[21] Cyclocondensation of **16** proceeded smoothly in moderate yields to give azaacenohomosumanenes (**22a-22c**). Only in the case of **22d**, a mixture of **22d** and its partially reduced form was obtained. This crude mixture was oxidized using MnO_2 to afford **22d** in 52% yield.

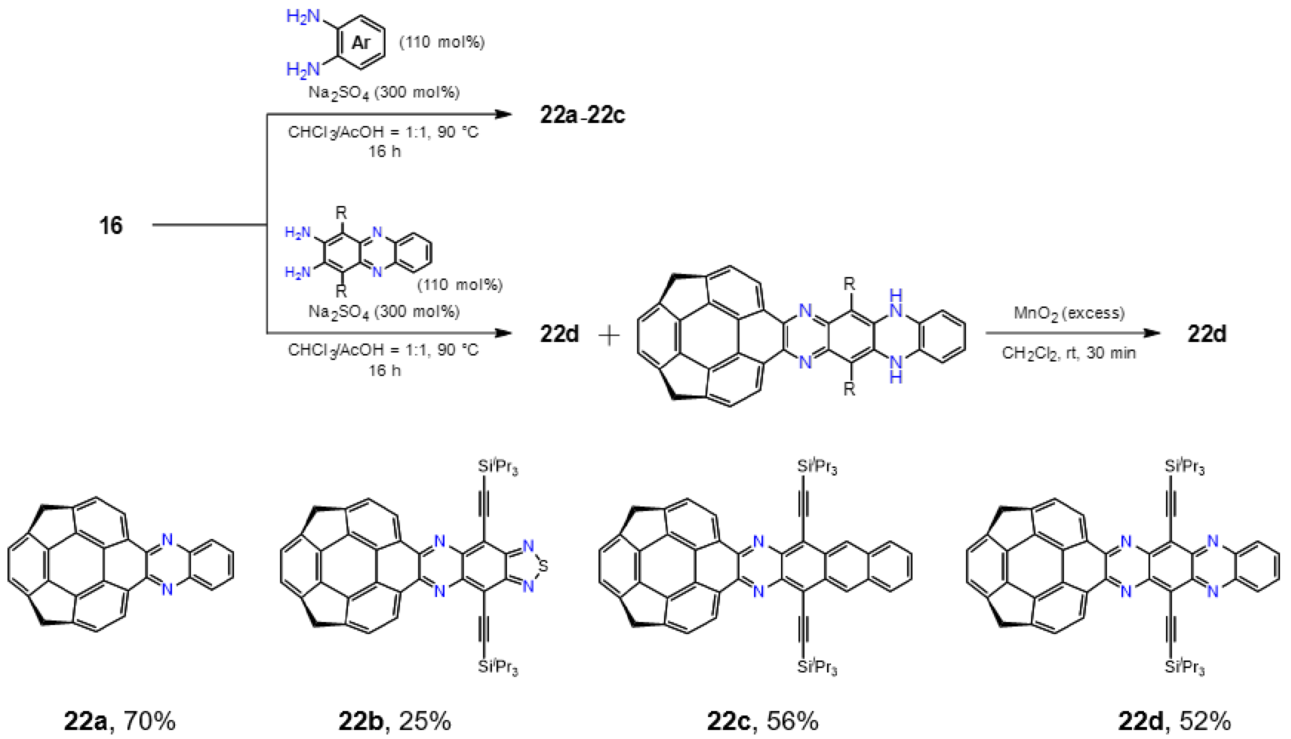

Scheme 15. Synthesis of azaacenohomosumanenes **22a**–**22d**.

The structures of **22a**, **22b**, and **22c** were determined by single crystal X-ray diffraction analysis (Figure 48). Every single crystal was obtained by vapor diffusion method using chloroform as a good solvent and *n*-hexane as a poor solvent. **22a-22c** had a spoon-like structure where the azaacene moiety fused to homosumanene skeleton (Figures 48a, 48c, 48e). The bowl depths calculated from the distance from the central six-membered ring to the peripheral carbon atoms are 0.53–0.80 Å for **22a**, 0.41–0.61 Å for **22b**, and 0.51–0.66 Å for **22c**. These values were smaller than those of corannulene (0.88 Å) and comparable to the homosumanene derivatives discussed in Chapter 2. Despite the structure similarities, the packing structures of **22a-22c** are all different (Figures 48b, 48d, and 48f). In the packing structure of **22a**, homosumanene moieties completely overlapped. A stacked-columnar structure was formed (Fig. 48b). These stacked columns are stabilized by CH···π (red dotted lines, Figure 48b) and π···π (blue dotted lines, Figure 48b) interactions within the column, with distances of 3.35–3.38 Å and 3.54–3.72 Å, respectively. On the other hand, **22b** showed a head-to-tail type stacking structure, stabilized by π···π interactions (3.33–3.40 Å) between the convex face of the bowl and the pyrazine rings in azaacene moieties (Figure 48d). This is likely due to a donor-acceptor like electrostatic interaction between the electron-rich convex face and the electron-deficient azaacene moiety containing thiadiazol rings. Such electrostatic interactions are more dominant than stabilization by stacking at the bowl site. **22c** also formed columnar stacking structures, but each azaacenohomosumanene skeleton was stacked with larger overlap than in **22a**. This may be due to the dispersion forces at the large π-conjugated surface and the bulky TIPS groups, and the electrostatic interactions between the pyrazine ring and the convex face of the bowl. The stacking results in the formation of CH···π and π···π interactions in the stacking column, with distances of 3.79 Å and 3.21–3.40 Å, respectively. These results suggest that the interactions derived from the homosumanene moiety play a crucial role in determining the final packing structure of the azaacene-fused homosumanenes.

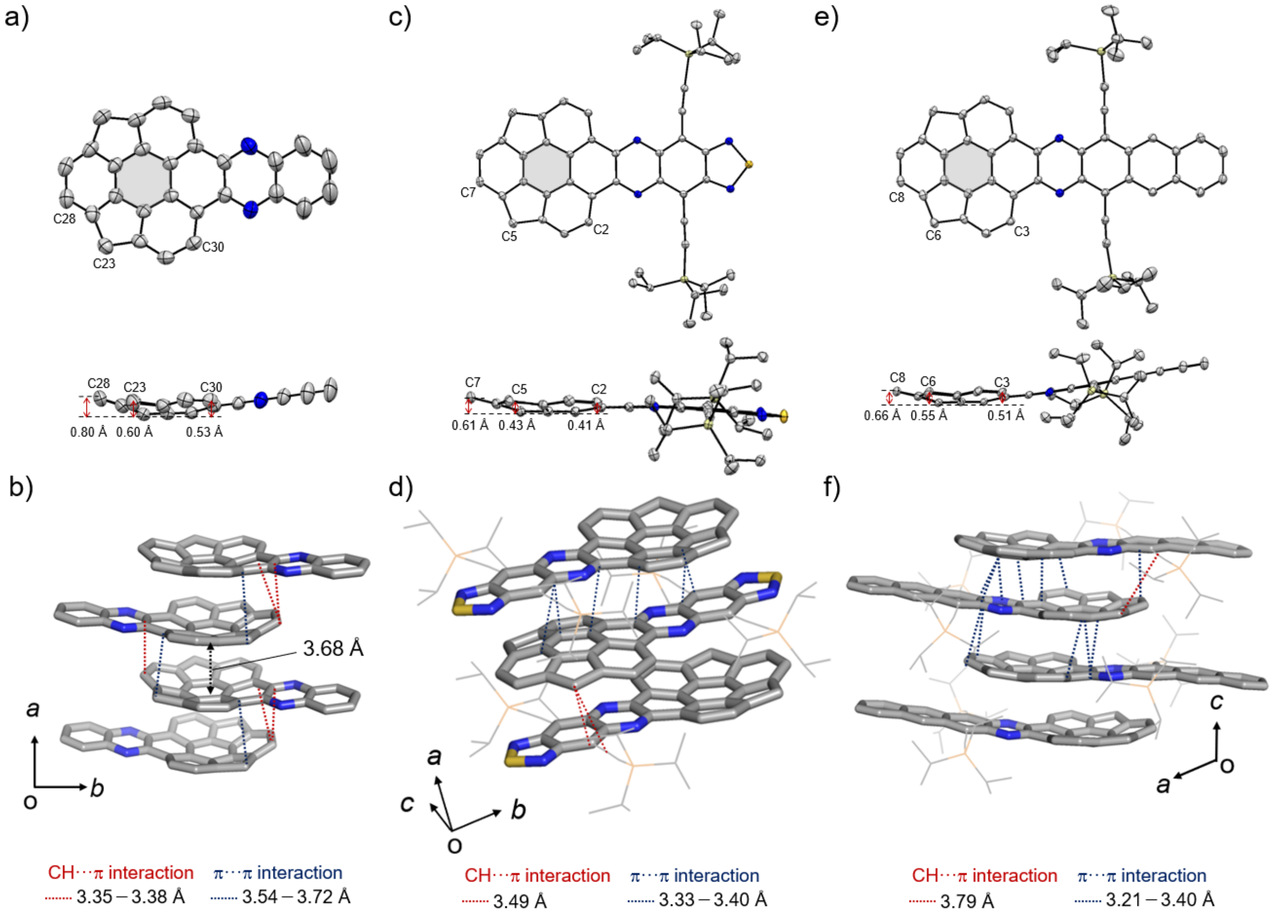

Figure 48. Crystal structures of **22a**, **22b**, and **22c**. a), c) and e): Thermal displacement ellipsoid plots in the crystal structures for the top and side view. b), d) and f): Packing structures and intermolecular interactions; CH···π (red dotted line) and π···π (blue dotted line) interactions. TIPS-ethynyl substituents were reduced in size and hydrogen atoms were omitted for clarity.

Section 5. Electronic properties of azaacene-fused homosumanenes

The electronic properties of azaacenohomosumanenes were investigated (Figure 49). **22a** shows an absorption band around 429 nm in the UV-Vis absorption spectrum, which was attributed to the π-π* transition by TD-DFT calculations (Figure 50). **22b-22d** showed absorption bands in the 450-700 nm region due to π-π* transitions originating from the π-extended azaacene moieties (**22b**: $\lambda_{\mathrm{abs,max}}$ = 590 nm; **22c**:

$\lambda_{abs,max}$ = 634 nm; **22d**: $\lambda_{abs,max}$ = 624 nm). The absorption band around 450-700 nm of **22c** well reflected the vibrionic structure of the azaacene moiety. In the emission spectra, **22b** (λ_{max} = 647 nm, Φ_{PL} = 26%), **22c** (λ_{max} = 669 nm, Φ_{PL} = 47%), and **22d** (λ_{max} = 650 nm, Φ_{PL} = 17%) show a bathochromic shift compared with **22a** (λ_{max} = 480 nm, Φ_{PL} = 19%), which is due to the extension of π-conjugation. In general, planar azaacenes show sharper emission spectra, reflecting the rigid molecular skeleton.[22] On the other hand, the absorption spectra of azaacenohomosumanenes showed a broader shape than planar azaacene's. This reflects bowl inversion behavior in solution due to the flexible bowl structure, and the absorption bands correspond to the average of the electronic states of the various conformations.

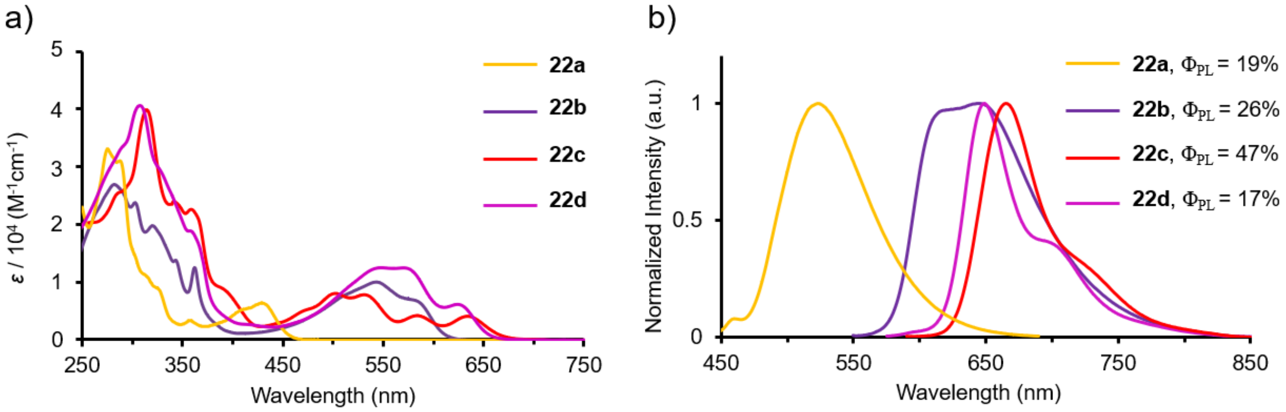

Figure 49. UV-vis absorption and fluorescence spectra of **22a**–**22d**. a) Absorption spectra. b) Emission spectra. All the samples were prepared as 1.0×10^{-5} mol/L in CH_2Cl_2. Excitation wavelength: 350 nm for **22a**; 545 nm for **22b**; 585 nm for **22c**; and 570 nm for **22d**.

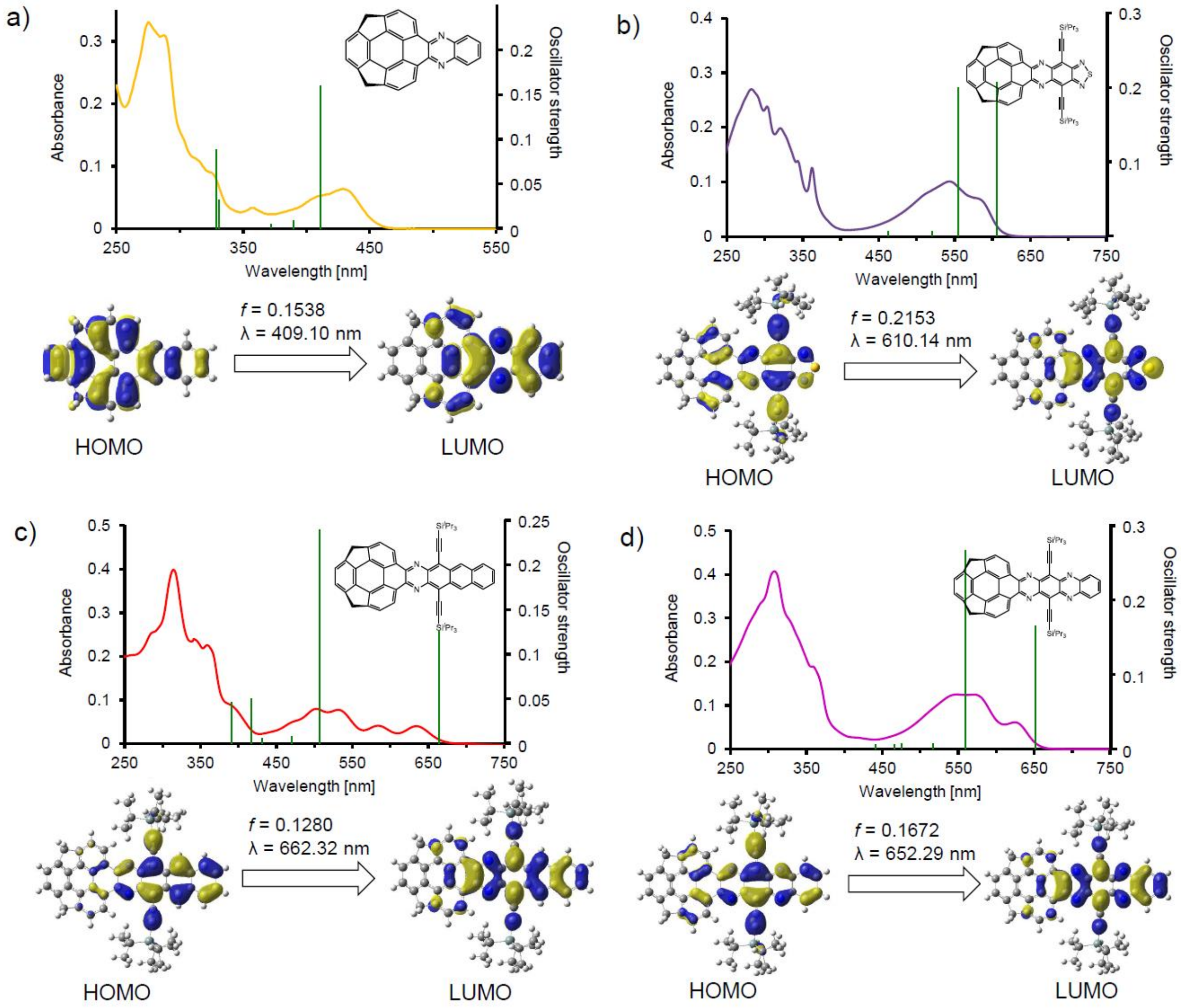

Figure 50. UV-vis absorption spectra with the simulated oscillator strengths calculated by TD-DFT, and the oscillator strength (*f*) of the S_0–S_1 transition of a) **22a**, b) **22b**, c) **22c**, and d) **22d**.

Fluorescence lifetime measurements were also performed to investigate the behavior of the excited states of **22b-22d**. These measurements were performed at 5.0×10^{-6} mol/L in degassed CH_2Cl_2, and the fluorescence lifetimes were determined from the decay curves of the fluorescence at the maximum emission wavelengths described above (Figure 51). All these decay curves can be fitted as linear functions, indicating that they have a single emission component. The fluorescence lifetimes of **22b**, **22c**, and **22d** were 5.06 ns, 5.43 ns, and 5.06 ns, respectively, in the order **22c** > **22b** ≅ **22d**. The shorter fluorescence lifetimes for **22b** and **22d** compared to **22c** may be due to the larger contribution of the n-π* transition due to the 4 nitrogen atoms, which leads to inter system crossing (ISC).

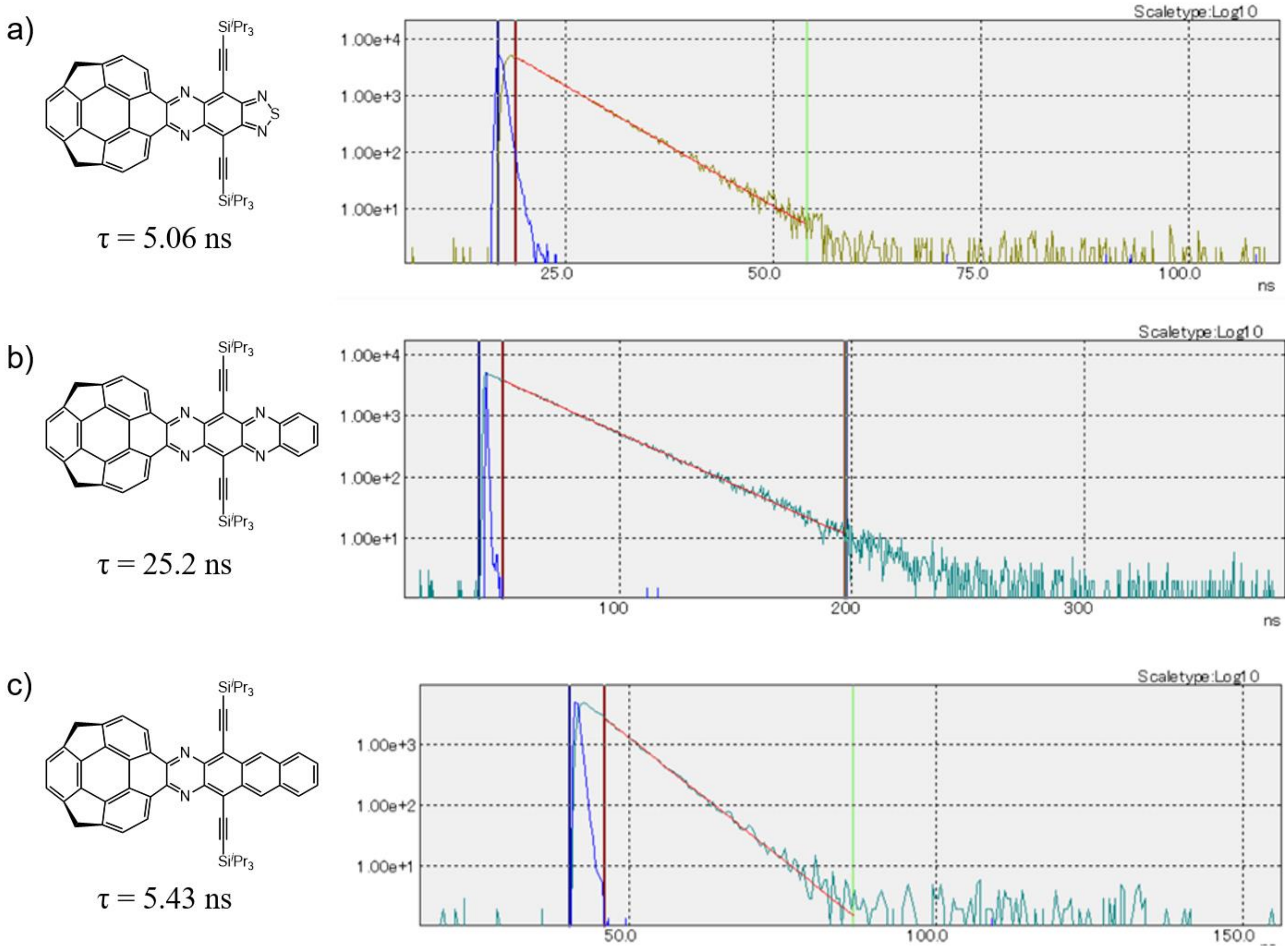

Figure 51. Emission lifetime and decay for a) **22b**, b) **22c**, and c) **22d**.

Cyclic voltammetry (CV) of **22b-22d** was performed using [^{n}Bu$_4$N][ClO$_4$] as the supporting electrolyte in THF solution to investigate their redox properties and electron-accepting ability (Figure 52, Table 14). They all showed multiple reversible peaks on the reducing side, indicating that they are stable to reduction. **22d** exhibited two reversible redox waves, with the largest first reduction potential ($E^{\mathrm{red1}}{}_{1/2} = -0.92$ V), suggesting that it is highly electron-deficient due to its four nitrogen atoms and large π-conjugated system. The first reduction potential of **22d** is 1.52 V larger than that of pristine homosumanene (−2.44 V) and is even larger than the typical electron acceptors such as fullerene (−0.97 V)[23] and perylenebisimide (−1.08 V)[24]. The LUMO level of **22d** estimated from $E^{\mathrm{red1}}{}_{1/2}$ is −3.88 eV vs. vacuum. This value is slightly higher than that of TIPS-tetraazapentacene (−4.01 eV vs. vacuum)[25]. This is because the homosumanene moiety acts as a weak electron donor unit compared with the electron-deficient azaacene moiety, resulting in a slightly higher LUMO energy level (Figure 53).

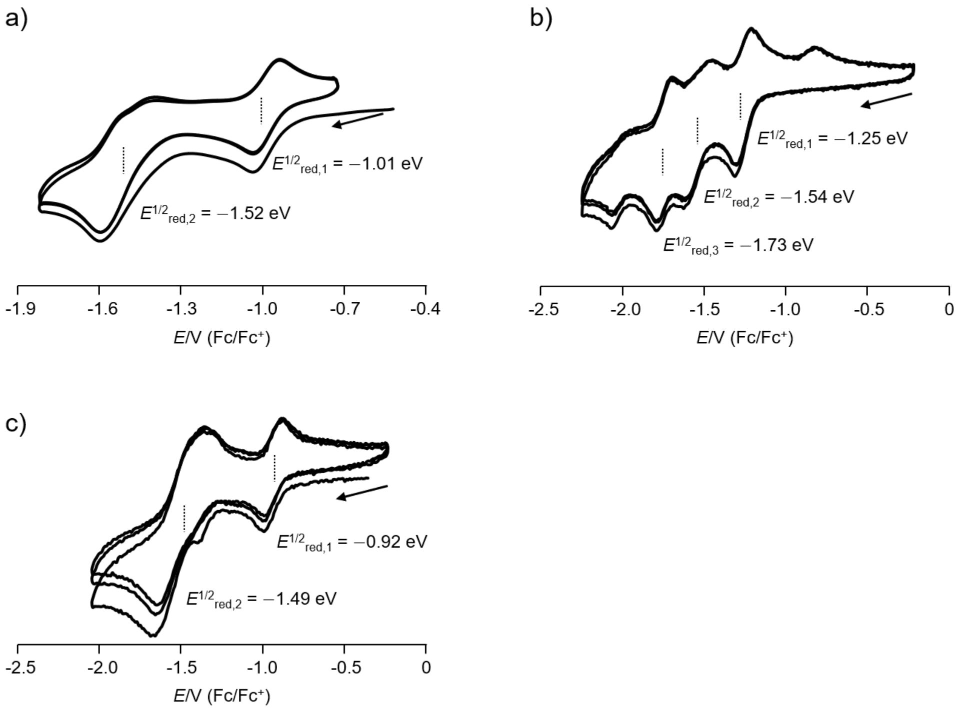

Figure 52. Cyclic voltammograms of azaacenohomosumanenes a) **22b**, b) **22c**, and c) **22d**.

Table 14. Electrochemical and photochemical analyses for energy levels.

	$E^{\mathrm{red1}}_{1/2}$ (V)[a]	E_{LUMO} (eV)[b]
22b	−1.01	−3.79
22c	−1.25	−3.55
22d	−0.92	−3.88

[a] First reduction potentials measured by cyclic voltammetry (CV) in THF using Fc/Fc$^+$ as an internal standard. [b] $E_{\mathrm{LUMO}} = -E^{\mathrm{red1}}_{1/2} - 4.80$ (Fc/Fc$^+$ vs. vacuum).[26]

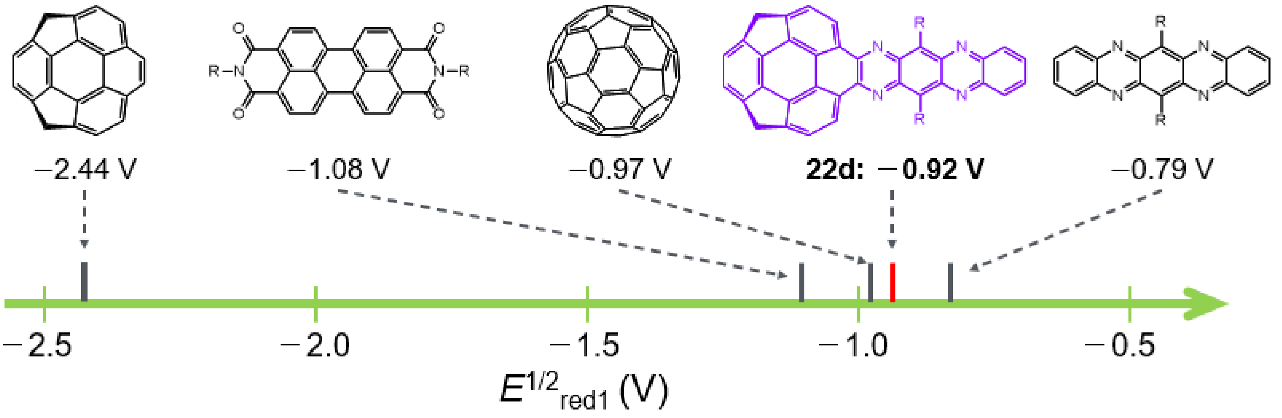

Figure 53. Comparison of first reduction potential of **22d** and typical electron acceptor molecules.

To evaluate the effect of incorporating sp^2-hybridized nitrogen atoms, DFT calculations were performed using the **22b-22d** and the acene-fused homosumanene (**23**) as a reference compound. Structural optimization was performed at the ωB97X-D/D/Def2-SVP level, and energy calculations at the ωB97X-D/6-311G(d)/IEF-PCM(THF) level was performed for the optimized structures. The HOMO and LUMO electron densities of **22b-22d** were localized mainly in the azaacene moieties. This result is consistent with absorption spectra and TD-DFT calculations, indicating that the electronic character of azaacenohomosumanene is primarily determined by azaacene moieties, not homosumanene moieties. On the other hand, the LUMO levels decrease significantly in the order **23**, **22c**, **22b**, and **22d**, which is consistent with the experimental trend obtained from CV measurements. This suggests that the electron-withdrawing imine-type sp^2 hybridized nitrogen atoms effectively stabilize the LUMO.

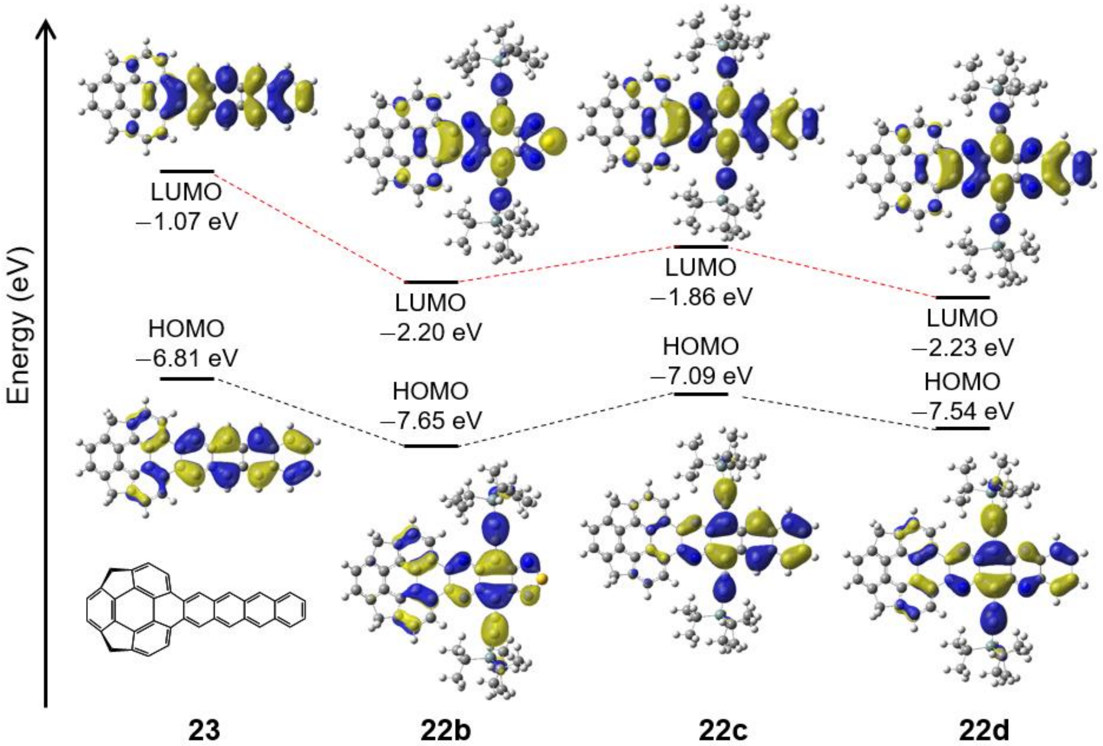

Figure 54. Calculated energy level and Kohn–Sham orbitals at the HOMO and LUMO of **22b**, **22c**, **22d**, and **23**.

Section 6. Evaluation of carrier mobility by FP-TRMC method

To investigate the charge transport properties of **22b-22d**, flash photolysis time-resolved microwave conductivity (FP-TRMC) measurements were carried out on powder samples (Figure 55).[27] This measurement evaluates the pseudo-photoconductivity ($\varphi\Sigma\mu_{\max}$), which is considered the minimum charge carrier mobility intrinsic to the material, without complicated device preparation. **22b** and **22d** exhibit almost similar $\varphi\Sigma\mu_{\max}$ values ($\varphi\Sigma\mu_{\max}$: 7.3 × 10^{-5} cm^2 V^{-1} s^{-1} for **22b**; 7.7 × 10^{-5} cm^2 V^{-1} s^{-1} for **22d**), and **22c** exhibited a slightly lower value ($\varphi\Sigma\mu_{\max}$: 6.6 × 10^{-5} cm^2 V^{-1} s^{-1}). These results are also consistent with the electron affinity trends deduced from cyclic voltammetry. These values are comparable to those reported for azaacene-fused polycyclic aromatic hydrocarbons[28] and nitrogen-doped graphene nanoribbons[29] (Figure 56).

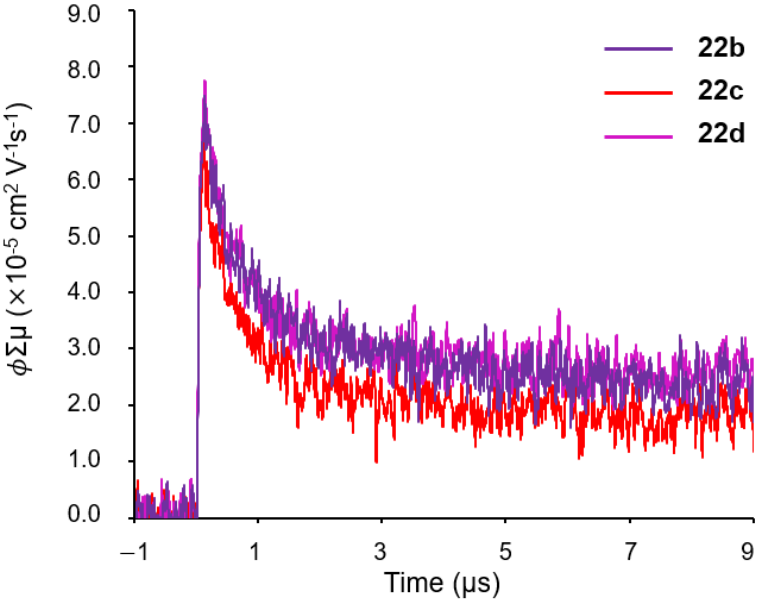

Figure 55. FP-TRMC data of **22b**, **22c**, and **22d**.

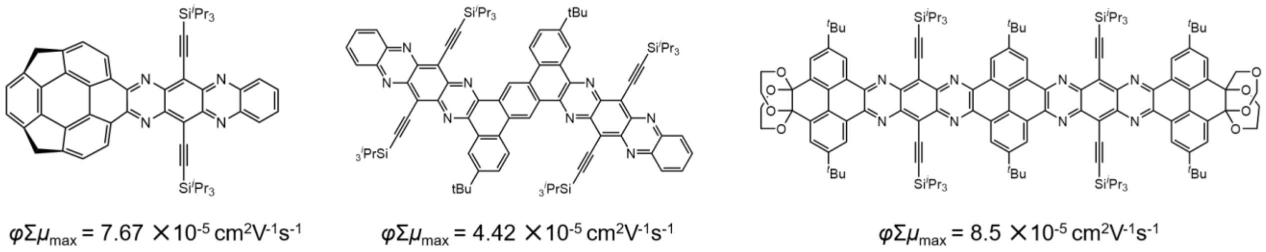

Figure 56. Comparison of charge carrier mobility measured by FP-TRMC method.

Section 7. Chemical reduction of 22d

Highly electron-deficient π-conjugated molecules sometimes provide stable radical anion species that are usually unstable by one-electron reduction.[30] This is because their high electron affinity can stabilize the resulting radical anion species. The stable radical anion species exhibits interesting properties, such as magnetic properties[31] and application as photocatalysts.[32] In addition, the radical anion corresponds to the carrier state that transports electrons when it works as an n-type semiconductor. Thus, understanding its structure is essential for improving semiconductor properties. The chemical reduction of **22d**, the most electron-deficient azaacenohomosumanene, by cobaltocene was attempted. In a nitrogen-filled glove box, one equivalent of cobaltocene was added to **22d** and stirred for 30 minutes, then the solvent was evaporated, and the violet solid was obtained. The absorption spectrum of the product was measured in THF (Scheme 16, Figure 57).

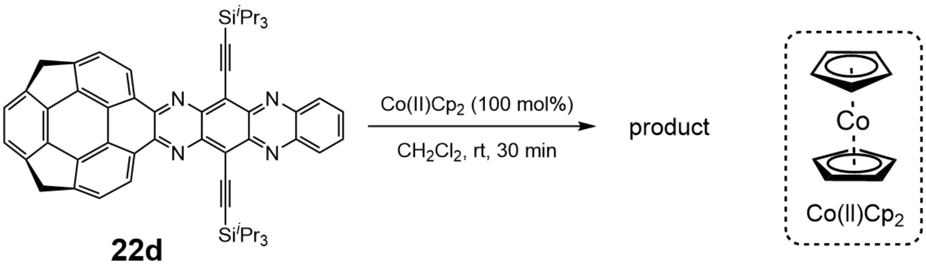

Scheme 16. Chemical reduction of **22d** by cobaltcene.

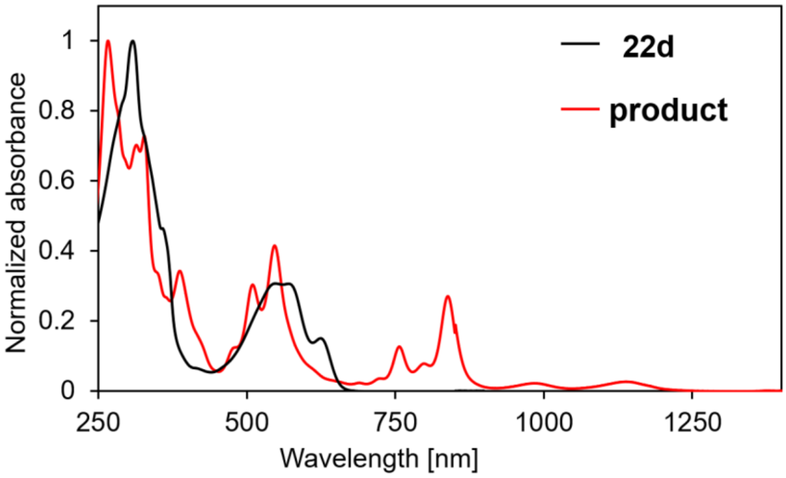

Figure 57. UV-vis absorption spectra of **22d** and the product.

The product exhibited broad near-infrared absorption up to around 1250 nm. This absorption band is considered to derive from the SOMO-LUMO transition of the radical anion with a very small energy gap. It has been reported that the absorption spectrum of the radical anion of TIPS-tetraazapentacene, which corresponds to the substructure of **22d**, shows near-infrared absorption from the SOMO-LUMO transition up to around 1500 nm.[33] Therefore, ESR measurement was conducted to observe the radical species directly. A solution of about 1.0 × 10^{-4} mol/L of the product was prepared in a glove box and used as the ESR sample. The ESR measurement at room temperature (298 K) showed no signals originating from radicals. This may be due to the decomposition of the radical anion species by the reaction with the highly acidic benzylic protons of homosumanene skeleton, and no ESR signal was observed. To indirectly confirm the progress of the reduction, the product was stirred in MeOH to check if the corresponding amine moiety could be obtained (Scheme 17). As a result, **22d** and the reduced diamine **24** were obtained, suggesting that the reduction by cobaltocene proceeds, but the product radical species are unstable and may not be observed due to side reactions such as protonation.

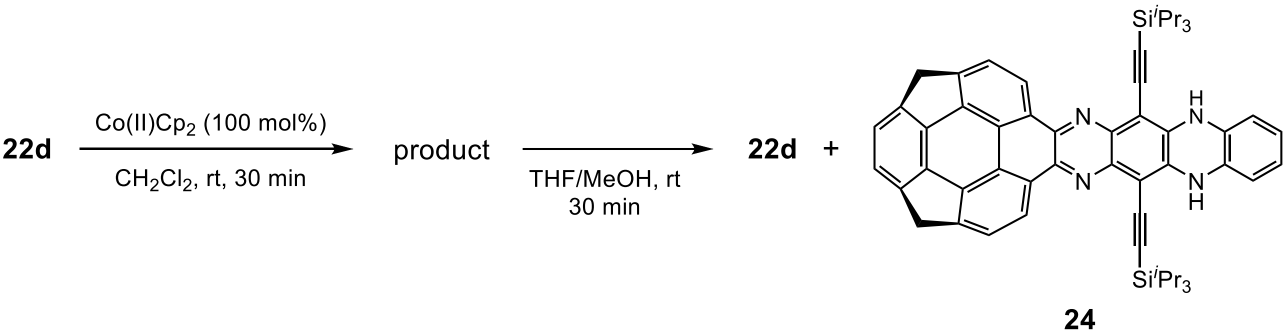

24

Scheme 17. Protonation of the product after reduction of **22d**.

The stability of the product was evaluated by tracing changes in UV spectra over time (Figure 58). The sample solutions were left in air and under room light, and UV spectra were measured at periodic intervals. In this experiment, a gradual broadening of the UV spectrum was observed, suggesting the decomposition of the product. Recrystallization of the product for X-ray analysis was also attempted. However, only tiny crystals were obtained, and single crystals of sufficient size for the measurement could not be obtained. This is probably due to the low stability of the product, and it inhibits crystallization. In conclusion, the radical anion of **22d** could not be identified and isolated. To isolate the radical anion of azaacenohomosumanene, a molecular design that can prevent side reactions at the reactive benzyl position is needed.

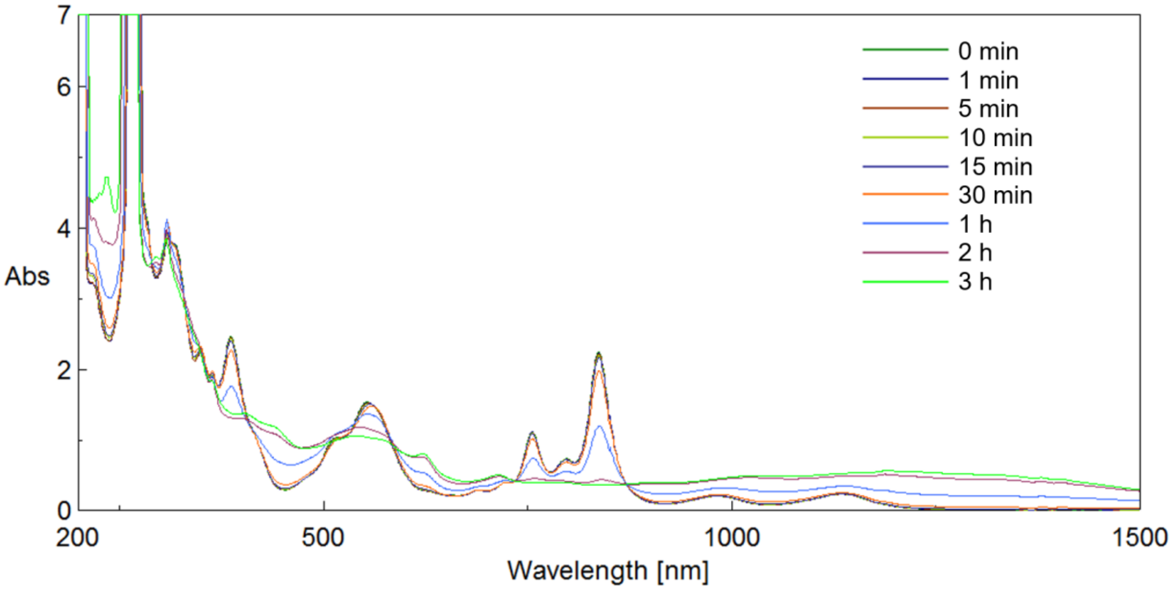

Figure 58. Time-dependent UV-vis spectra of the product.

Section 8. Summary

In this chapter, the author established the synthesis of homosumanene *ortho*-quinone by aerobic oxidation on silica gel. The oxidation reaction proceeded more smoothly with curved molecules than with planar molecules, and this reactivity was attributed to the unusual keto-enol tautomerism due to the curved skeleton. To investigate the usefulness of obtained *o*-quinone as precursors for synthesizing π-extended homosumanene derivatives, a series of azaacene-fused homosumanenes (**22a-22d**) were synthesized by condensation reactions with *ortho*-diamines. **22a**, **22b**, and **22c** formed stacked structures mainly by interaction at the bowl moiety. The spectroscopic analysis of **22a-22d** revealed that combining the homosumanene structure with the electron-deficient azaacene structure efficiently stabilizes the LUMO energy levels of azaacenohomosumanene, with **22d** exhibiting high electron affinity (−3.88 eV vs. vacuum). Screening of the charge transport properties of **22b-22d** by FP-TRMC measurements revealed that **22d** exhibited the highest $\varphi\Sigma\mu_{\mathrm{max}}$ value (7.7×10^{-5} cm^2 V^{-1} s^{-1}), suggesting that **22d** has potential as an n-type organic semiconductor.

Experimental section

General information about instruments and measurements is provided in chapter 2.

Chemicals

Unless otherwise noted, all reagents purchased from commercial suppliers were used without further purification.

Manganese(IV) oxide (MnO_2), acetic anhydride (Ac_2O), acetic acid (AcOH), *n*-hexane, dichloromethane (CH_2Cl_2), ethyl acetate (EtOAc), methanol (MeOH), carbon disulfide (CS_2) and chloroform ($CHCl_3$) were purchased from FUJIFILM Wako Pure Chemical Corporation.

Pyridine, potassium carbonate (K_2CO_3), 1,2-phenylenediamine and boron trifluoride diethyl etherate (BF_3·Et_2O) were purchased from Nacalai Tesque, Inc.

Dichloromethane (CH_2Cl_2, dehydrated Super^2) and tetrahydrofuran (THF) was purchased from Kanto Chemical Co., Inc., and purified by passing through a Glass Contour Ultimate Solvent System (Nikko Hansen & Co. Ltd.) under nitrogen atmosphere.

4-Dimethylaminopyridine (DMAP), trimethylsilyl diazomethane (Me_3SiCHN_2), Cobaltcene (Co(II)Cp_2), tetrabutylammonium perchlorate ([^{n}Bu_4N][ClO_4]), and Rose Bengal were purchased from Tokyo Chemical Industry Co., Ltd.

Anhydrous sodium sulfate (Na_2SO_4) was purchased from KISHIDA CHEMICAL Co., Ltd.

phenanthrenol,[34] 4,9-bis((triisopropylsilyl)ethynyl)-[1,2,5]thiadiazolo[3,4-*g*]quinoxaline-6,7-diamine (**S22b**),[21a] 5,12-bis((triisopropylsilyl)ethynyl)naphtho[2,3-*g*]quinoxaline-2,3-diamine (**S22c**,[21b,21c] and 5,12-bis((triisopropylsilyl)ethynyl)pyrazino[2,3-*b*]phenazine-2,3-diamine (**S22d**)[21d] were prepared according to the literatures.

Two-dimensional TLC Experiment.

To a solution of **1** (30.0 mg, 0.108 mmol, 100 mol%) in dry CH_2Cl_2 (25 mL) were added BF_3·Et_2O (55.2 μL, 0.324 mmol, 300 mol%) and Me_3SiCHN_2 solution (0.6 mol/L in *n*-hexane, 0.54 mL, 0.3 mmol, 300 mol%) at 0 °C, and then the mixture was warmed up to 27 °C. After stirring for 15 min at the same temperature, the reaction mixture was filtered through a short pad of Celite®, and washed with CH_2Cl_2 (ca. 100 mL). After concentration, a solution of **2** was spotted on a TLC plate (40 mm×40 mm) and the TLC plate was soaked in CH_2Cl_2 to develop under shading conditions. After drying, the TLC plate was irradiated with UV light (λ = 254 nm) for 30 min, and then, soaked again in CH_2Cl_2.

Synthetic Procedure and Characterization Data.

***o-quinone* 16** and ***dimer* 17**. To a solution of **2** (30.0 mg, 0.108 mmol, 100 mol%) in dry CH_2Cl_2 (25 mL) were added $BF_3{\cdot}Et_2O$ (55.2 µL, 0.324 mmol, 300 mol%) and Me_3SiCHN_2 solution (ca. 0.6 mol/L in *n*-hexane, 0.54 mL, 0.3 mmol, 300 mol%) at 0 °C, and then the mixture was warmed up to 27 °C. After stirring for 15 min at the same temperature, the reaction mixture was filtered through a short pad of Celite®, and washed with CH_2Cl_2 (ca. 100 mL). After concentration, the filtrate was charged on a PTLC plate, and the PTCL plate was irradiated with UV light (λ = 254 nm) for 1 h (Figure S2). Then, the PTLC plate was soaked in $CHCl_3$ to separate, affording **16** (20.5 mg, 66.9 µmol, 62.0%) as an orange solid and **17** (5.7 mg, 10 µmol, 9.0%) as a white solid;

***o-quinone* 16**: R_f = 0.15 ($CHCl_3$); Melting point: 327 °C (dec.); ^{1}H NMR ($CDCl_3$, 400 MHz) δ (ppm) 8.03 (d, *J* = 7.8 Hz, 2H), 7.65 (d, *J* = 7.8 Hz, 2H), 7.56 (s, 2H), 4.32 (s, 4H); $^{13}C\{^1H\}$ NMR ($CDCl_3$, 100 MHz) 180.4 (2C), 153.1 (2C), 141.8 (2C), 140.3 (2C), 138.3 (2C), 129.1 (2C), 128.9 (2C), 128.6 (2C), 125.4 (2C), 125.1 (2C), 124.9 (2C), 41.8 (2C); IR (diamond, cm^{-1}) 2919, 1668, 1390, 1338, 1250, 1076, 1020, 833, 793; HRMS (EI^+) *m*/*z* $[M]^+$ Calcd for $C_{22}H_{10}O_2^+$ 306.0680, found 306.0861.

Dimer (**17**): R_f = 0.12 (*n*-hexane/CH_2Cl_2=1:1); Melting point: 167 °C (dec.); ^{1}H NMR ($CDCl_3$, 400 MHz) δ (ppm) 8.32 (d, *J* = 7.8 Hz, 1H), 8.05 (d, *J* = 8.2 Hz, 1H), 7.70 (d, *J* = 8.2 Hz, 1H), 7.61 (d, *J* = 7.8 Hz, 1H), 7.59 (d, *J* = 7.8 Hz, 1H), 7.33 (d, *J* = 7.8 Hz, 1H), 5.92 (s, 1H), 4.56 (s, 1H), 4.43 (s, 1H); $^{13}C\{^1H\}$ NMR ($CDCl_3$, 100 MHz) 151.5 (2C), 145.1 (2C), 144.0 (2C), 143.6 (2C), 141.7 (2C), 141.0 (2C), 140.8 (2C), 140.6 (2C), 140.3 (2C), 131.3 (2C), 126.8 (2C), 124.9 (2C), 124.2 (2C), 124.14 (2C), 124.08 (2C), 124.0 (2C), 122.4 (2C), 121.7 (2C), 120.6 (2C), 107.9 (2C), 42.2 (2C), 41.8 (2C); IR (diamond, cm^{-1}) 3482, 2922, 1419, 1396, 1214, 1065, 793, 751; HRMS (FAB^+) *m*/*z* $[M]^+$ Calcd for $C_{44}H_{22}O_2^+$ 582.1620, found 582.1629.

***Acetylhomosumanene* 18**. To a solution of **2** (30.0 mg, 0.108 mmol, 300 mol%) in dry CH_2Cl_2 (25 mL) were added $BF_3{\cdot}Et_2O$ (67.0 µL, 0.540 mmol, 500 mol%) and Me_3SiCHN_2 solution (ca. 0.6 mol/L in *n*-hexane, 0.54 mL, 0.3 mmol, 300 mol%) at 0 °C, and then the mixture was warmed up to 27 °C. After stirring for 30 min at the same temperature, the mixture was filtered through a short pad of Celite®, and washed with CH_2Cl_2 (ca. 100 mL). After filtration, the filtrate was concentrated under reduced pressure under shading conditions. The residue was dissolved in CH_2Cl_2 (5 mL), and to this were added pyridine (87 µL, 1.1 mmol, 1000 mol%), DMAP (1.3 mg, 11 µmol, 10 mol%) and Ac_2O (51.0 µL, 0.540 mmol, 500 mol%) at 27 °C. After stirring for 1 h at the same temperature, to the reaction mixture was added saturated aqueous $NaHCO_3$ solution (ca. 10 mL), and extracted with $CHCl_3$ (ca. 10 mL × 3). The combined organic extract was washed with brine (ca. 10 mL), dried over Na_2SO_4. After filtration, the filtrate was concentrated under reduced pressure. The residue was purified by PTLC ($CHCl_3$) to give **18** (25.0 mg, 74.8 µmol, 69.0%) as a pale yellow solid;

R_f = 0.43 (*n*-hexane/CH_2Cl_2=1:1); Melting point: 187 °C (dec.); ^{1}H NMR ($CDCl_3$, 400 MHz) δ (ppm) 7.94 (d, *J* = 8.2 Hz, 1H), 7.91 (d, *J* = 7.8 Hz, 1H), 7.85 (d, *J* = 8.2 Hz, 1H), 7.81 (d, *J* = 8.2 Hz, 1H), 7.66 (s, 1H), 7.48 (s, 2H), 4.44 (s, 2H+2H, two signals overlapped), 2.54 (s, 3H); ^{13}C{^{1}H} NMR ($CDCl_3$, 100 MHz) 169.6 (1C), 147.0 (1C), 144.0 (1C), 143.6 (1C), 143.5 (1C), 143.2 (1C), 140.7 (1C), 140.5 (1C), 140.3 (1C), 140.0 (1C), 130.5 (1C), 126.3 (1C), 125.5 (1C), 124.3 (1C), 124.1 (1C), 124.0 (1C), 123.9 (1C), 123.8 (1C+1C, two signals overlapped), 118.8 (1C), 117.6 (1C), 41.9 (1C), 41.8 (1C), 21.1 (1C); IR (diamond, cm^{-1}): 3166, 3066, 2852, 1466, 1390, 1260, 1022, 968, 785; HRMS (FAB$^+$) *m*/*z* [M]$^+$ Calcd for $C_{24}H_{14}O_2^+$ 334.0994, found 334.0990.

General synthetic procedure for azaacenohomosumanene (22a–22c)

To a mixture of **16** (10.0 mg, 32.7 μmol, 100 mol%), diamine (35.9 μmol, 110 mol%), and Na_2SO_4 (13.9 mg, 98.1 μmol, 300 mol%) was added $CHCl_3$/AcOH, (1:1 (v/v), 2 mL) at room temperature, and the mixture was stirred at 90 °C for 16 h. After cooling to room temperature, the mixture was carefully poured into saturated aqueous $NaHCO_3$ solution (ca. 20 mL), and extracted with $CHCl_3$ (ca. 10 mL × 3). The combined organic extract was washed with brine (ca. 10 mL), dried over Na_2SO_4. After filtration, the filtrate was concentrated under reduced pressure. The residue was purified by silica-gel column chromatography to give corresponding azaacenohomosumanenes **22**.

***Azaacenohomosumanene* 22a**. Following the general procedure, the crude was purified by silica-gel column chromatography (CH_2Cl_2) to give **22a** as a yellow solid (17.4 mg, 18.5 μmol, 56.7%); R_f = 0.50 (CH_2Cl_2); Melting point: 303 °C (dec.); ^{1}H NMR ($CDCl_3$, 45 °C, 400 MHz) δ (ppm) 8.93 (d, *J* = 7.8 Hz, 2H), 8.37–8.34 (m, 2H), 8.00 (d, *J* = 7.8 Hz, 2H), 7.88–7.86 (m, 2H), 7.58 (s, 2H), 4.49 (s, 4H); ^{13}C{^{1}H} NMR ($CDCl_3$, 45 °C, 100 MHz) 147.3 (2C), 145.7 (2C), 143.1 (1C), 141.5 (2C), 140.0 (2C), 129.6 (2C), 129.5 (2C), 129.4 (2C), 126.6 (2C), 124.5 (2C), 124.1 (2C), 124.0 (2C), 41.9 (4C); IR (diamond, cm^{-1}): 2918, 2849, 1715, 1395, 1260, 801, 743; HRMS (EI$^+$) *m*/*z* [M]$^+$ Calcd for $C_{28}H_{14}N_2^+$ 378.1157, found 378.1153; Elemental Analysis: C, 88.61; H, 3.63. N, 7.22. Calcd for $C_{28}H_{14}N_2$: C, 88.87; H, 3.73. N, 7.40.

***Azaacenohomosumanene* 22b**. Following the general procedure, the crude was purified by silica-gel column chromatography (*n*-hexane/$CHCl_3$ = 1:1) to give **22b** as a violet solid (6.6 mg, 8.2 μmol, 25%); R_f = 0.29 (*n*-hexane/CH_2Cl_2 = 2:1); Melting point: 341 °C (dec.); ^{1}H NMR ($CDCl_3$/CS_2, 600 MHz) δ (ppm) 8.91 (d, *J* = 7.8 Hz, 2H), 7.91 (d, *J* = 7.8 Hz, 2H), 7.50 (s, 2H), 4.50 (s, 4H), 1.39 (s, 36H+16H, two signals overlapped); ^{13}C{^{1}H} NMR ($CDCl_3$/CS_2, 151 MHz) 154.3 (2C), 148.6 (2C), 147.5 (2C), 142.5 (2C), 141.1 (2C), 140.0 (2C), 139.6 (2C), 128.8 (2C), 126.9 (2C), 125.5 (2C), 124.8 (2C), 123.9 (2C), 114.6 (2C), 109.4 (2C), 101.8 (2C), 41.9 (2C), 18.9 (12C), 11.7 (6C); IR (diamond, cm^{-1}): 2923, 2852, 1725, 1259, 1076, 1015, 796, 677, 461; HRMS (EI$^+$) *m*/*z* [M]$^+$ Calcd for $C_{58}H_{58}N_2Si_2^+$ 796.3451, found 796.3466.

***Azaacenohomosumanene* 22c**. Following the general procedure, the crude was purified by silica-gel chromatography (*n*-hexane/$CHCl_3$ = 2:1) to give **22c** as a violet solid (15.5 mg, 18.5 µmol, 56%); R_f = 0.51 (*n*-hexane/CH_2Cl_2 = 1:1); Melting point: 288 °C (dec.); ^{1}H NMR ($CDCl_3$/CS_2, 400 MHz) δ (ppm) 9.46 (s, 2H), 8.80 (d, *J* = 7.7 Hz, 2H), 8.10–8.08 (m, 2H), 7.80 (d, *J* = 7.7 Hz, 2H), 7.55–7.52 (m, 2H), 7.19 (s, 2H), 4.39 (s, 4H), 1.49 (s, 36H+16H, two signals overlapped); ^{13}C{^{1}H} NMR ($CDCl_3$/CS_2, 100 MHz) 147.7 (2C), 146.6 (2C), 142.1 (2C), 139.6 (2C), 139.1 (2C), 139.0 (2C), 132.4 (2C), 131.8 (2C), 128.8 (2C), 128.5 (2C), 126.7 (2C), 126.4 (2C+2C, two signals overlapped), 125.0 (2C), 124.1 (2C), 123.8 (2C), 120.2 (2C), 107.2 (2C), 103.8 (2C), 41.7 (2C), 19.1 (12 C), 11.9 (6C); IR (diamond, cm^{-1}): 2922, 2853, 1723, 1259, 1014, 796, 675, 498, 414; HRMS (EI$^+$) *m*/*z* [M]$^+$ Calcd for $C_{58}H_{58}N_2Si_2^+$ 838.41385, found 838.4144.

***Azaacenohomousmanene* 22d**. To a solution of **16** (10.0 mg, 32.7 µmol, 100 mol%) in $CHCl_3$/AcOH (2 mL, 1:1 (v/v)) were added the diamine (20.6 mg, 35.9 µmol, 110 mol%) and Na_2SO_4 (13.9 mg, 98.1 µmol, 300 mol%) at room temperature, and the mixture was stirred at 90 °C for 16 h. After cooling to room temperature, the mixture was carefully poured into saturated aqueous $NaHCO_3$ solution (ca. 20 mL), and extracted with $CHCl_3$ (ca. 10 mL × 3). The combined organic extract was washed with brine (ca. 10 mL), dried over Na_2SO_4. After filtration, the filtrate was concentrated under reduced pressure. The residue was dissolved in CH_2Cl_2 (15 mL), and to this was added MnO_2 (500 mg, 7.05 mmol, 2156 mol%) at room temperature. After stirring for 30 min at the same temperature, the reaction mixture was filtered through a short pad of Celite®, and eluted with $CHCl_3$ (ca. 100 mL). The filtrate was concentrated under reduced pressure. The residue was purified by silica-gel column chromatography (*n*-hexane/CH_2Cl_2 = 1:1 to 1:2) to give **22d** (14.3 mg, 17.0 µmol, 52%) as a violet solid; R_f = 0.45 (*n*-hexane/CH_2Cl_2 = 1:1); Melting point: 322 °C (dec.); ^{1}H NMR ($CDCl_3$/CS_2, 600 MHz) δ (ppm) 8.95 (d, *J* = 7.8 Hz, 2H), 8.29–8.27 (m, 2H), 7.91 (d, *J* = 7.8 Hz, 2H), 7.89–7.87 (m, 2H), 7.46 (s, 2H), 4.51 (s, 4H), 1.45 (s, 36H+16H, two signals overlapped); ^{13}C{^{1}H} NMR ($CDCl_3$/CS_2, 151 MHz) 148.7 (2C), 147.8 (2C), 144.6 (2C), 142.8 (2C), 142.6 (2C), 141.4 (2C), 140.1 (2C), 139.6 (2C), 131.3 (2C), 130.4 (2C), 128.9 (2C), 127.1 (2C), 125.7 (2C), 124.6 (2C), 124.2 (2C), 122.2 (2C), 110.1 (2C), 103.0 (2C), 41.9 (2C), 19.0 (12 C), 11.9 (6C); IR (diamond, cm^{-1}): 2921, 2853, 1731, 1260, 1013, 800, 669, 466, 408; HRMS (MALDI) *m*/*z* [M]$^+$ Calcd for $C_{58}H_{56}N_4Si_2^+$ 840.40435, found 840.40380.

Single Crystal X-ray Diffraction Analysis.

The diffraction data for **16**, **22b**, and **22c** were recorded on a DICTRIS PILATUS3 X CdTM 1M Detector System (λ = 0.43158 Å) at 100 K at SPring-8 BL02B1. The diffraction images were processed by using RIGAKU RAPID AUTO.[35]

The diffraction data for **22a** was recorded on a XtaLAB Synergy with a Cu-target (λ = 1.54184 Å) equipped with a Rigaku HyPix-6000HE as the detector at 123 K in house. The diffraction images were processed by using CrysAlisPro.[36]

All the structures were solved by dual-space argorithm using SHELXT program[37] and refined by full-matrix least squares calculations on F^2 (SHELXL-2018/3)[38] using the Olex2 [39] program package.

16: Crystallization was conducted by vapor diffusion method. In a small test tube, a solution of **16** in chlorobenzene (5.4 mmol/L, 0.3 mL) was added. The test tube was put into a vial containing *n*-hexane, and this was stored at 5 °C. After 7 days, orange block crystals suitable for single crystal X-ray diffraction analysis were obtained.

$C_{22}H_{10}O_2(C_6H_5Cl)_{0.44}(H_2O)_{0.56}$, orthorhombic, space group $P2_12_12_1$ (No. 19), a = 7.1572(14) Å, b = 13.718(3) Å, c = 16.267(3) Å, V = 1597.1(5) Å^3, ρ_{calcd} = 1.520 g/cm^3, Z = 4, 3214 unique reflections out of 3658 with I>2$\sigma(I)$, 278 parameters, 1.172° < θ < 16.169°, R_1 = 0.0761, wR_2 = 0.2214, GOF = 1.080.

22a: Crystallization was conducted by vapor diffusion method. In a small test tube, a solution of **22a** in $CHCl_3$ (4.4 mmol/L, 0.3 mL) was added. The test tube was put into a vial containing *n*-hexane, and this was stored at 5 °C. After 3 days, yellow needle crystals suitable for single crystal X-ray diffraction analysis were obtained.

$2(C_{28}H_{14}N_2)$, monoclinic, space group $P2_1$/n (No. 14), a = 7.29420(10) Å, b = 30.2650(4) Å, c = 16.2367(3) Å, β = 101.881(2)°, V = 3507.61(10) Å^3, ρ_{calcd} = 1.433 g/cm^3, Z = 4, 5961 unique reflections out of 7198 with I>2$\sigma(I)$, 541 parameters, 4.034° < θ < 76.124°, R_1 = 0.0746, wR_2 = 0.1614, GOF = 1.064.

22b: Crystallization was conducted by vapor diffusion method. In a small test tube, a solution of **22b** in $CHCl_3$ (2.1 mmol/L, 0.3 mL) was added. The test tube was put into a vial containing *n*-hexane, and this was stored at 5 °C. After 5 days, violet needle crystals suitable for single crystal X-ray diffraction analysis were obtained.

$C_{50}H_{54}N_4SSi_2$, triclinic, space group P-1 (No. 2), a = 7.3061(15) Å, b = 16.327(3) Å, c = 17.514(4) Å, α = 83.24(3)°, β = 89.99(3)°, γ = 86.49(3)°, V = 2070.7(7) Å^3, ρ_{calcd} = 1.282 g/cm^3, Z = 2, 7022 unique reflections out of 9526 with I>2$\sigma(I)$, 526 parameters, 0.678° < θ < 15.509°, R_1 = 0.0475, wR_2 = 0.1111, GOF = 1.012.

22c: Crystallization was conducted by vapor diffusion method. In a small test tube, a solution of **22c** in

$CHCl_3$ (2.0 mmol/L, 0.3 mL) was added. The test tube was put into a vial containing *n*-hexane, and this was stored at 5 °C. After 5 days, red violet needle crystals suitable for single crystal X-ray diffraction analysis were obtained.

$2(C_{58}H_{58}N_2Si_2)$, monoclinic, space group $P2_1/c$ (No. 14), a = 20.617(4) Å, b = 33.099(7) Å, c = 13.997(3) Å, β = 101.28(3)°, V = 9367(3) Å^3, ρ_{calcd} = 1.190 g/cm^3, Z = 4, 15991 unique reflections out of 21441 with $I > 2\sigma(I)$, 1141 parameters, $0.925° < \theta < 15.580°$, R_1 = 0.0567, wR_2 = 0.1274, GOF = 1.016.

CCDC 2192125 (**16**), 2192123 (**22a**), 2192124 (**22b**), and 2192122 (**22c**) contain the crystallographic data for this paper. These data can be obtained free of charge from The Cambridge Crystallographic Data Centre (https://www.ccdc.cam.ac.uk/).

Keto/Enol Tautomerization of 3’ and ^{1}H-NMR assignments.

In a glovebox filled with nitrogen gas, to a test tube containing a stir bar, **18** (8.6 mg, 26 μmol, 100 mol%), and K_2CO_3 (7.1 mg, 51 μmol, 200 mol%) was added degassed THF/MeOH (2 mL, 1:1 (v/v)) at room temperature, and the mixture was stirred at the same temperature under shading conditions. After stirring for 1 h, to this was added silica-gel (ca. 1.0 g, Silica Gel 60 N (spherical, neutral), Kanto Chemical Co., Inc.), and the suspension was filtered and washed with CH_2Cl_2 (ca. 50 mL). The filtrate was concentrated under reduced pressure. To the residue was added CD_2Cl_2 (ca. 1 mL) and the solution was transferred to an NMR tube. Then, the NMR tube was taken out from the glove box, and ^{1}H and ^{13}C{^{1}H} NMR measurements were performed. The keto/enol ratio was estimated to be 10:3 from the comparison of the integral values of the proton signal at *a* (8.06 ppm) and *k* (7.96 ppm); ^{1}H NMR (CD_2Cl_2, 400 MHz) δ (ppm) 8.06 (d, J = 7.8 Hz, 1H, *a*), 7.96 (d, J = 7.8 Hz, 1H, *k*), 7.92 (d, J = 7.8 Hz, 1H, *b*), 7.83 (d, J = 7.8 Hz, 1H, *h*), 7.68 (d, J = 7.8 Hz, 1H, *g*), 7.67 (d, J = 7.8 Hz, 1H, *l*), 7.56 (d, J = 7.3 Hz, 1H, *r*), 7.68 (d, J = 7.8 Hz, 1H, *g*), 7.53 (d, J = 7.3 Hz, 1H, *d*), 7.51 (d, J = 7.3 Hz, 1H, *e*), 7.50 (d, J = 7.3 Hz, 1H, *n*), 7.48 (d, J = 7.3 Hz, 1H, *o*), 7.26 (d, J = 7.3 Hz, 1H, *q*), 7.15 (s, 1H, *i*), 5.95 (s, 1H, *j*), 4.41 (s, 2H, *c*), 4.37 (s, 2H, *f*), 4.31 (s, 2H, *m*), 4.27 (s, 2H, *p*), 4.17 (s, 2H, *s*); ^{13}C{^{1}H} NMR (CD_2Cl_2, 100 MHz) 197.1 (1C), 152.6 (1C), 152.5 (1C), 144.6 (1C), 144.3 (1C), 144.2 (1C), 143.9 (1C), 143.3 (1C), 142.6 (1C), 141.3 (1C), 141.2 (1C), 140.9 (1C), 140.8 (1C), 140.43 (1C), 140.36 (1C), 139.7 (1C), 139.5 (1C), 133.6 (1C), 132.3 (1C), 127.5 (1C), 126.6 (1C), 125.5 (1C), 125.0 (1C), 124.8 (1C), 124.7 (1C), 124.7 (1C), 124.6 (1C), 124.5 (1C), 124.4 (1C), 124.3 (1C), 124.2 (1C), 124.10 (1C), 124.07 (1C), 122.4 (1C), 122.3 (1C), 119.3 (1C), 105.8 (1C), 44.0 (1C), 42.3 (1C), 42.03 (1C), 41.99 (1C), 41.3 (1C).

Screening of Reaction Conditions on the Oxidation of 3'.

To a test tube containing a stir bar, **18** (8.6 mg, 26 μmol, 100 mol%), and K_2CO_3 (7.1 mg, 51 μmol, 200 mol%) was added THF/MeOH (2 mL, 1:1 (v/v)) at room temperature. The mixture was irradiated with an ultrasonic wave for 1 min, and then stirred at room temperature under shading conditions. After stirring for 15 min, to this was added silica-gel (ca. 1.0 g, Silica Gel 60 N (spherical, neutral), Kanto Chemical Co., Inc.), and the suspension was filtered and the silica-gel was washed with CH_2Cl_2 (ca. 50 mL). The filtrate was concentrated under reduced pressure. The residue containing **3'** was used without further purification.

Entries 1 and 2: The residue was charged on a PTLC plate, and the PTLC plate was irradiated with UV light (λ = 254 nm for entry 1, λ = 365 nm for entry 2) under air. Then, the PTLC plate was soaked in $CHCl_3$ for separation.

Entry 3: In a glovebox filled with nitrogen gas, to a mixture of **18** (8.6 mg, 26 μmol, 100 mol%) and K_2CO_3 (7.1 mg, 51 μmol, 200 mol%) was added degassed THF/MeOH (2 mL, 1:1 (v/v)) at room temperature, and the mixture was stirred for 15 min at room temperature under shading conditions. To the reaction mixture was added silica-gel (ca. 1.0 g, Silica gel: Kanto Chemical Co., Inc. Silica Gel 60 N (spherical, neutral)), then the mixture was filtered and eluted with CH_2Cl_2 (ca. 50 mL). The filtrate was concentrated under reduced pressure. The residue was directly charged on a PTLC plate, and this was irradiatated with UV light (λ = 254 nm) for 1 h under nitrogen atmosphere. Then, the silica-gel was washed with CH_2Cl_2 and the filtrate was concentrated under reduced pressure. The crude mixture was dissolved in CD_2Cl_2 and to this was added 1,1,2,2-tetrachloroethane in CD_2Cl_2 (0.257 mol/L, 100 μL, 25.7 μmol) as an internal standard. ^{1}H NMR measurement was performed to determine the yield of **3**.

Entry 4: The residue was charged on a PTLC plate, and stands for 1 h under shading conditions and air atmosphere. Then, the mixture was washed with CH_2Cl_2 and the filtrate was concentrated under reduced pressure. The crude mixture was dissolved in $CDCl_3$ and to this was added 1,1,2,2-tetrachloroethane in $CDCl_3$ (0.257 mol/L, 100 μL, 25.7 μmol) as an internal standard. ^{1}H NMR measurement was performed to determine the yield of **16**.

Entry 5: The residue was dissolved in $CHCl_3$ (2.0 mL) and to this was added silica-gel (100 mg, Wakogel B-5F, FUJIFILM Wako Pure Chemical Corporation) at room temperature under air atmosphere. After stirring for 1 h under the irradiation of UV light (λ = 254 nm), the reaction mixture was filtered, and the filtrate was concentrated under reduced pressure. The crude mixture was dissolved in $CDCl_3$ and to this was added

1,1,2,2-tetrachloroethane in $CDCl_3$ (0.257 mol/L, 100 μL, 25.7 μmol) as an internal standard. ^{1}H NMR measurement was performed to determine the yield of **16**.

Entry 6: The residue was dissolved in $CHCl_3$ (2.0 mL) and to this was added silica-gel (100 mg, Wakogel B-5F) and Rose Bengal (2.6 mg, 10 mol%, 2.6 μmol) at room temperature in air atmosphere. After stirring for 1 h under the irradiation of UV light (λ = 254 nm), the reaction mixture was filtered, and the filtrate was concentrated under reduced pressure. The crude mixture was dissolved in $CDCl_3$ and to this was added 1,1,2,2-tetrachloroethane in $CDCl_3$ (0.257 mol/L, 100 μL, 25.7 μmol) as an internal standard. ^{1}H NMR measurement was performed to determine the yield of **16**.

Entry 7: The residue was dissolved in $CHCl_3$ (2.0 mL) at room temperature under air atmosphere. After stirring for 1 h under the irradiation of UV light (λ = 254 nm), the mixture was filtered, and the filtrate was concentrated under reduced pressure. The crude mixture was dissolved in $CDCl_3$ and to this was added 1,1,2,2-tetrachloroethane in $CDCl_3$ (0.257 mol/L, 100 μL, 25.7 μmol) as an internal standard. ^{1}H NMR measurement was performed to determine the yield of **16**.

Time-course Plots of Oxidation of 3’ and 19.

Oxidation on silica-gel of 3’

To a mixture of **18** (60.2 mg, 180 μmol, 100 mol%) and K_2CO_3 (50.0 mg, 360 μmol, 200 mol%) was added THF/MeOH (6 mL, 1:1 (v/v)) at room temperature, and the mixture was irradiated with an ultrasonic wave for 1 min, and then stirred for 15 min at room temperature under shading conditions. To this was added silica-gel (ca. 3.0 g, Silica Gel 60 N (spherical, neutral), Kanto Chemical Co., Inc.). Then, the mixture was filtered and eluted with CH_2Cl_2 (ca. 150 mL). The filtrate was concentrated under reduced pressure to give **3’**.

3’ was dissolved in $CHCl_3$ (3.0 mL), and 0.5 mL of the solution (25.7 μmol of **3’**) was charged on a PTLC plate. Then, the PTLC plate was irradiated with UV light (λ = 254 nm) under air for specified time shown in Table S2. The adsorbed organic compounds were eluted with $CHCl_3$ (ca. 30 mL) immidiately and concentrated under reduced pressure. The residue was dissolved in $CDCl_3$ and to this was added 1,1,2,2-tetrachloroethane in $CDCl_3$ (0.257 mol/L, 100 μL, 25.7 μmol) as an internal standard. ^{1}H NMR measurements were performed and the yield of **16** was calculated by comparing the integral values.

This experiment was conducted three times and the yields in main script were expressed as mean values with standard deviations.

Oxidation on silica-gel of 19

Phenanthrenol **19** (30.0 mg, 0.154 mmol, 100 mol%) was dissolved in $CHCl_3$ (3.0 mL), and 0.5 mL of the solution (25.7 μmol of **19**) was charged on a PTLC plate. Then, the PTLC plate was irradiated with UV light (λ = 254 nm) under air for specified time shown in Table S3. The adsorbed organic compounds were eluted with $CHCl_3$ (ca. 30 mL) immidiately and concentrated under reduced pressure. The residue was dissolved in $CDCl_3$, and to this was added 1,1,2,2-tetrachloroethane in $CDCl_3$ (0.257 mol/L, 100 μL, 25.7 μmol) as an internal standard. ^{1}H NMR measurements were performed and the yield of **7** was calculated by comparing the integral values.

This experiment was conducted three times and the yields in main script were expressed as mean values with standard deviations.

20: ^{1}H NMR ($CDCl_3$, 400 MHz) δ (ppm) 8.18 (d, J = 7.8 Hz, 2H), 8.00 (d, J = 7.8 Hz, 2H), 7.71 (dd, J = 7.8 Hz, J = 7.8 Hz, 2H), 7.46 (dd, J = 7.8 Hz, J = 7.8 Hz, 2H);

The chemical shift of **20** was consistent with its reported in the literature.[40]

Sample Preparation of UV-vis Absorption and Emission Spectroscopies.

To a 5 mL volumetric flask were added a sample (10 μmol) and degassed CH_2Cl_2 (5.0 mL) to give a sample solution (2.0×10^{-3} mol/L). The solution was diluted at 1.0×10^{-5} mol/L with the same solvent and transferred to a quartz cell (optical path length; 10 mm). UV-vis absorption and emission spectroscopy measurements were performed at room temperature.

Electrochemical Analysis.

[^{n}Bu$_4$N][ClO$_4$] was recrystallized from ethyl acetate prior to the CV measurements.

Azaacenohomosumanenes (2.0 μmol) and [^{n}Bu$_4$N][ClO$_4$] (68.4 mg, 0.200 mmol) were dissolved in degassed THF (2.0 mL) to prepared a solution (1.0×10^{-3} mol/L). The cyclic voltammetry was performed using a standard three-hole electrochemical cell with a glassy-carbon working electrode (3.0 mm diameter), a reference electrode (Ag/AgNO$_3$), and a counter electrode (Pt wire). The scan rate was set to 100 mV s^{-1}. The CV sweep was repeated for three consecutive cycles in the negative voltage region.

FP-TRMC Measurement.

Flash-photolysis time-resolved microwave conductivity (FP-TRMC) measurement was performed by setting a film on a quartz substrate in a resonant cavity and probing via continuous microwaves at ~9.1 GHz. The third harmonic generation (THG; 355 nm) of a Nd:YAG laser (Continuum Inc., Surelite II, 5–8 ns pulse duration, 10 Hz) was used as an excitation source (incident photon density, I_0 = 9.1 × 10^{15} photons cm^{-2} pulse^{-1}). The photoconductivity transient ($\Delta\sigma$) was converted to the product of the quantum yield (φ) and the sum of the charge carrier mobilities, $\Sigma\mu$ (= $\mu_h + \mu_e$) by $\varphi\Sigma\mu = \Delta\sigma\ (e\ I_0\ F_{\mathrm{light}})^{-1}$, where e and F_{light} are the unit charge of a single electron and the correction (or filling) factor, respectively.

A powder sample was applied to a double-sided conductive carbon tapes (ca. 8 mm×8 mm) attached to a quartz substrate. The substrate was set in a resonant cavity, and TRMC measurement was performed at room temperature.

Chemical reduction of 22d.

In the nitrogen-filled glove box, to a solution of **22d** (7.4 mg, 100 mol%, 8.8 μmol) in degassed CH_2Cl_2 (2.0 mL) were added cobaltcene (1.6 mg, 100 mol%, 8.8 μmol) at room temperature, and the mixture was stirred at the same temperature for 30 minutes. After stirring, the mixture was concentrated under the reduced pressure. The residue, a violet solid, was used for UV-vis absorption and ESR measurements without further purifications.

Computational study

Otherwise noted, all theoretical calculations using density functional theory (DFT) were performed using Gaussian 09 suite of programs (revision E.01).[41]

Keto-enol tautomerization of 3'$_{\mathrm{enol}}$, 3'$_{\mathrm{keto}}$, 19$_{\mathrm{enol}}$, 19$_{\mathrm{keto}}$, 21$_{\mathrm{enol}}$, and 21$_{\mathrm{keto}}$ (Figure 34)

Geometry optimization calculations were performed by DFT method at ωB97X-D[42] level of theory with Def2-SVP[43] as a basis set for all atoms in the gas phase. Harmonic frequency calculations were conducted at the same level of theory on the optimized geometries to check all the stationary points as minima points. The vibrational frequency calculation (298.15 K, 1 atm) on the optimized geometries were calculated at ωB97X-D level of theory in gas phase with Def2-TZVP as a basis set for all atoms.

The NICS calculations for the optimized coordinates were conducted at B3LYP[44] level of theory in gas phase with 6-311+G(d)[45,46] as a basis set for all atoms.

Elimination of H_2O (Figure 36)

Geometry optimization and transition state (TS) calculations were performed by DFT method at ωB97X-D level of theory with cc-pVDZ[47] as a basis set for all atoms in the gas phase. Harmonic frequency calculations were conducted at the same level of theory on the optimized geometries to check all the stationary points as minima points. Intrinsic reaction coordinate (IRC) calculations[48] were carried out to confirm the transition states connecting the correct reactants and products on the potential energy surface. The vibrational frequency calculation (298.15 K, 1 atm) on the optimized geometries were calculated at ωB97X-D level of theory in gas phase with cc-pVTZ as a basis set for all atoms.

Energy calculation and UV-vis simulation of azaacenes (22a, 22b, 22c, and 22d) (Figures 39 and 43)

Geometry optimizations were performed at ωB97X-D level of theory in gas phase with Def2-SVP as a basis set. The simulation of UV-Vis absorption spectra on the optimized ground state geometries were performed using TD-DFT (time-dependent density functional theory) method at B3LYP level of theory in gas phase with 6-31G(d)[49] as a basis set. The SCF energies (298.15 K, 1 atm) on the optimized geometries were calculated at ωB97X-D level of theory with in THF using IEF-PCM solvation model[50] with 6-311G(d)[45,49d,51] as a basis set for all atoms.

^{1}H NMR (400 MHz) and ^{13}C{^{1}H} NMR (100 MHz) spectra of **16** ($CDCl_3$, 25 °C).

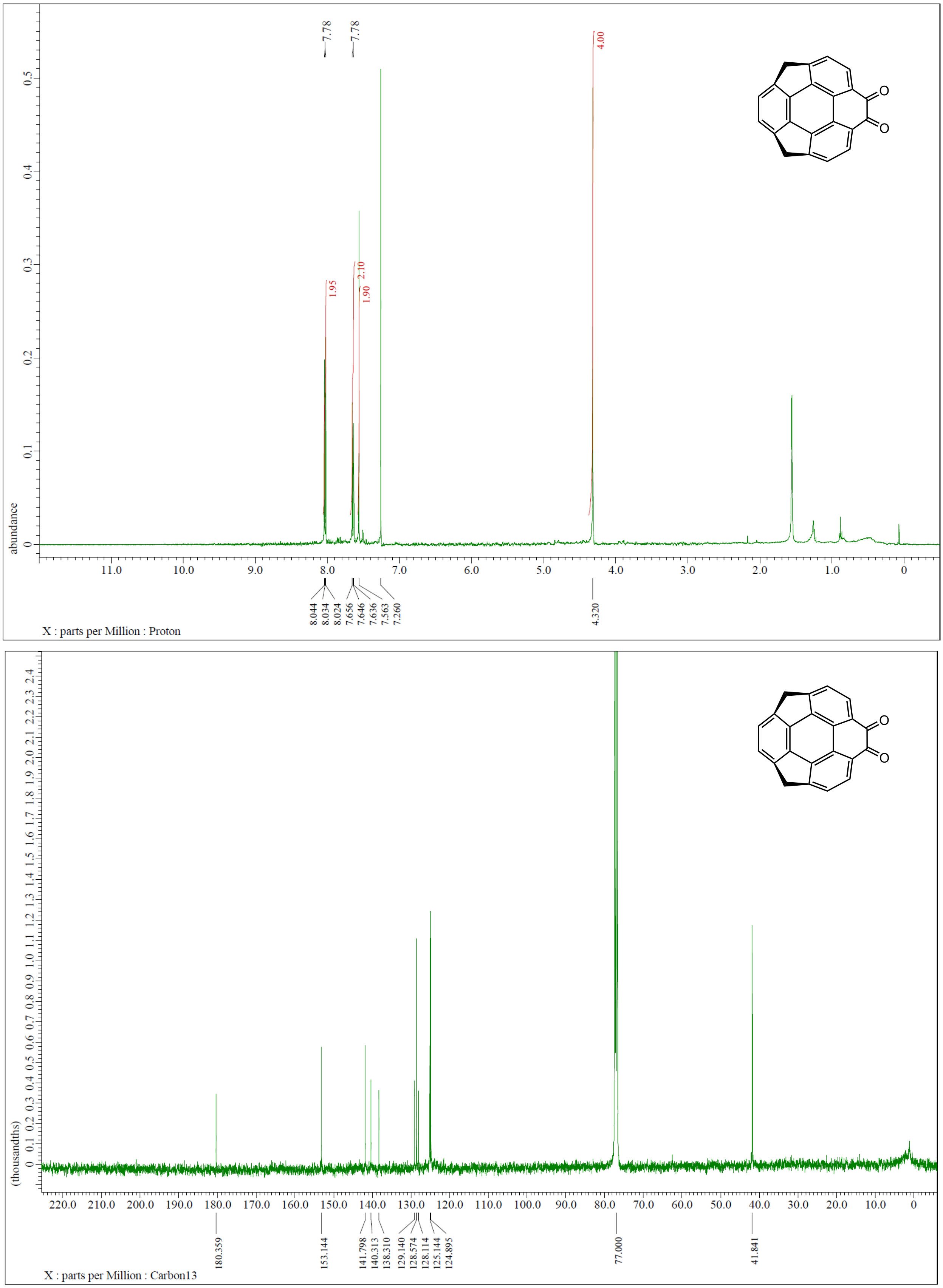

^{1}H NMR (400 MHz) and ^{13}C{^{1}H} NMR (100 MHz) spectra of **17** ($CDCl_3$, 25 °C).

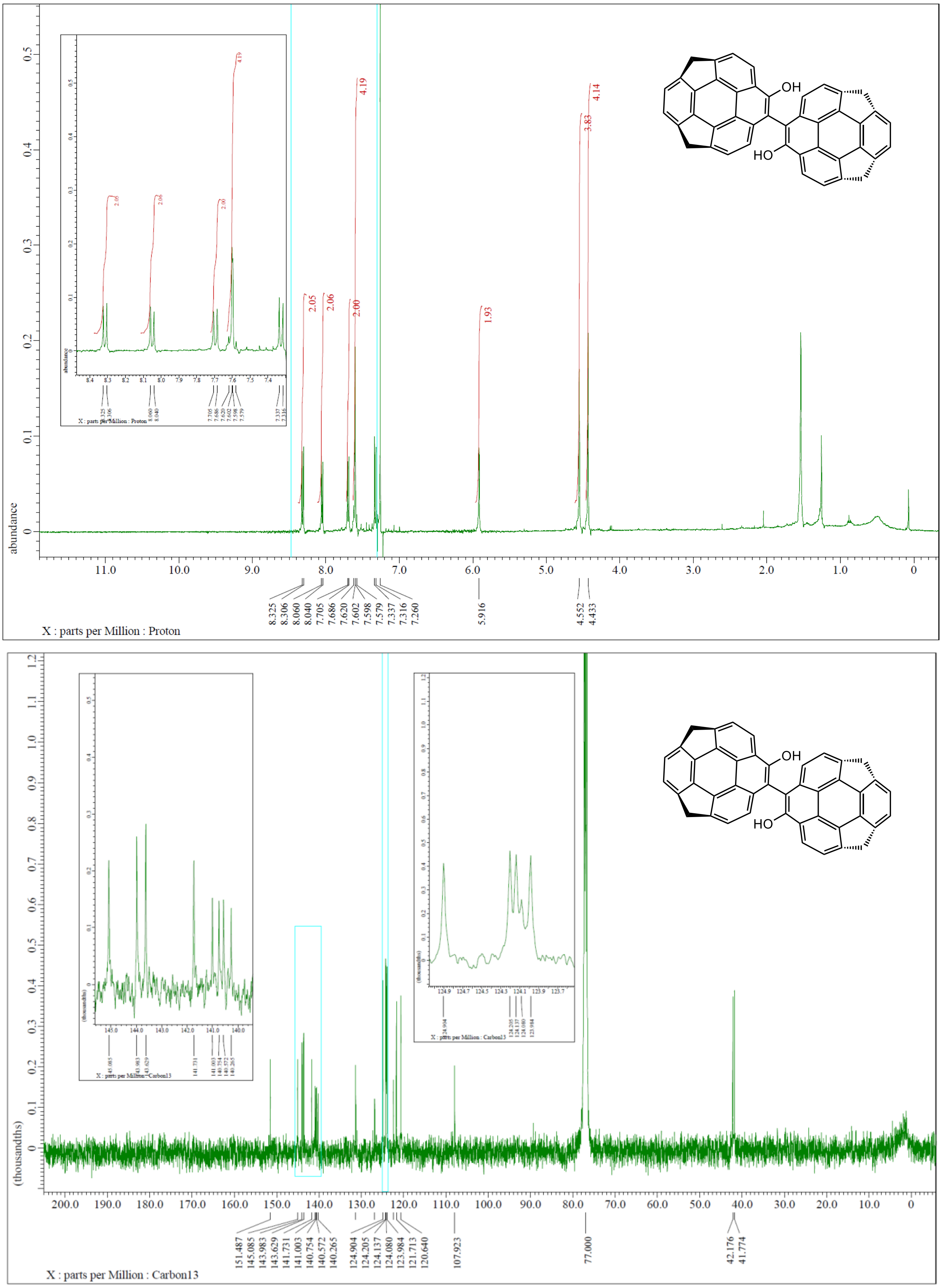

^{1}H NMR (400 MHz) and ^{13}C{^{1}H} NMR (100 MHz) spectra of **18** ($CDCl_3$, 25 °C).

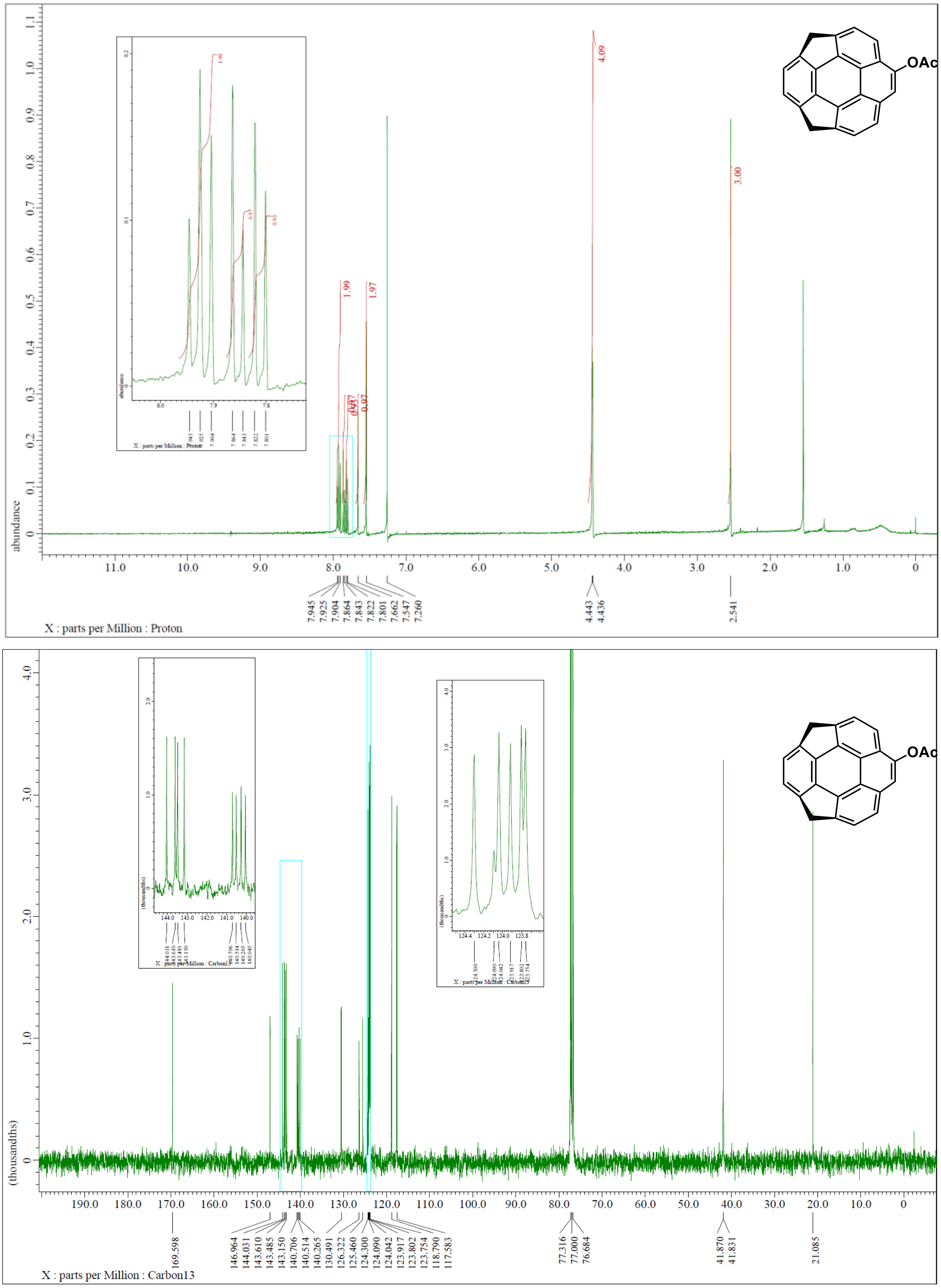

^{1}H NMR (400 MHz) and $^{13}C\{^{1}H\}$ NMR (100 MHz) spectra of **22a** ($CDCl_3$, 45 °C).

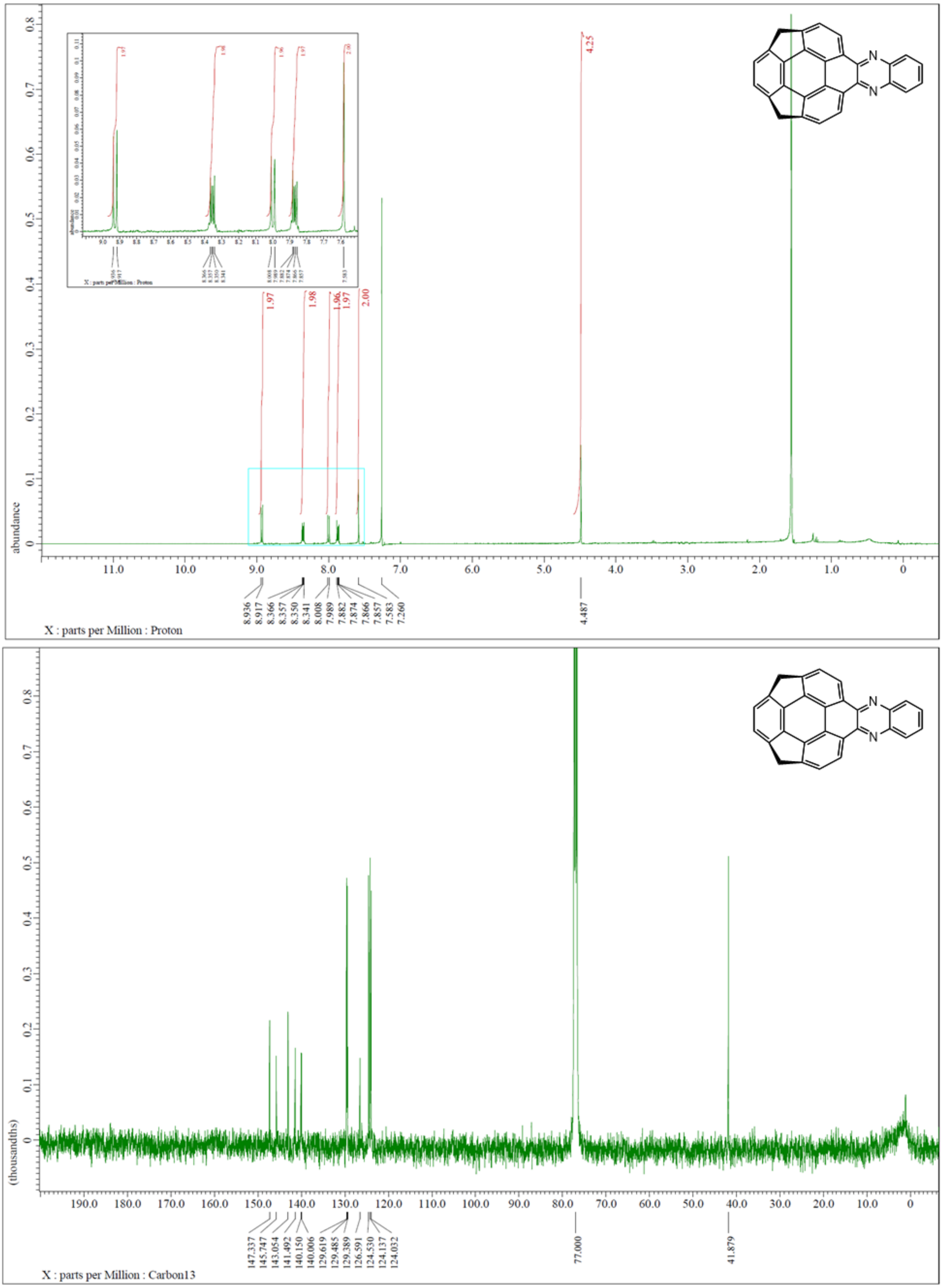

^{1}H NMR (600 MHz) and ^{13}C{^{1}H} NMR (150 MHz) spectra of **22b** ($CDCl_3$/CS_2, 25 °C).

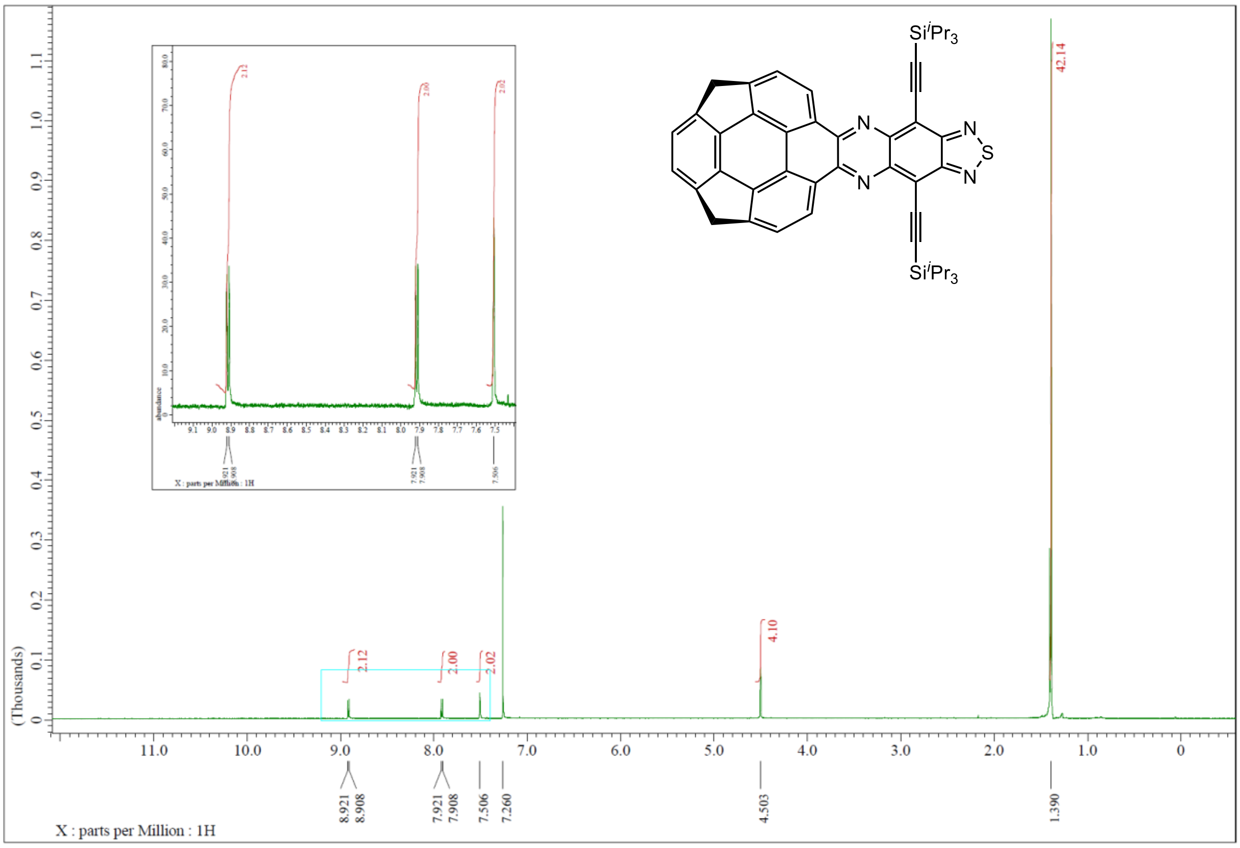

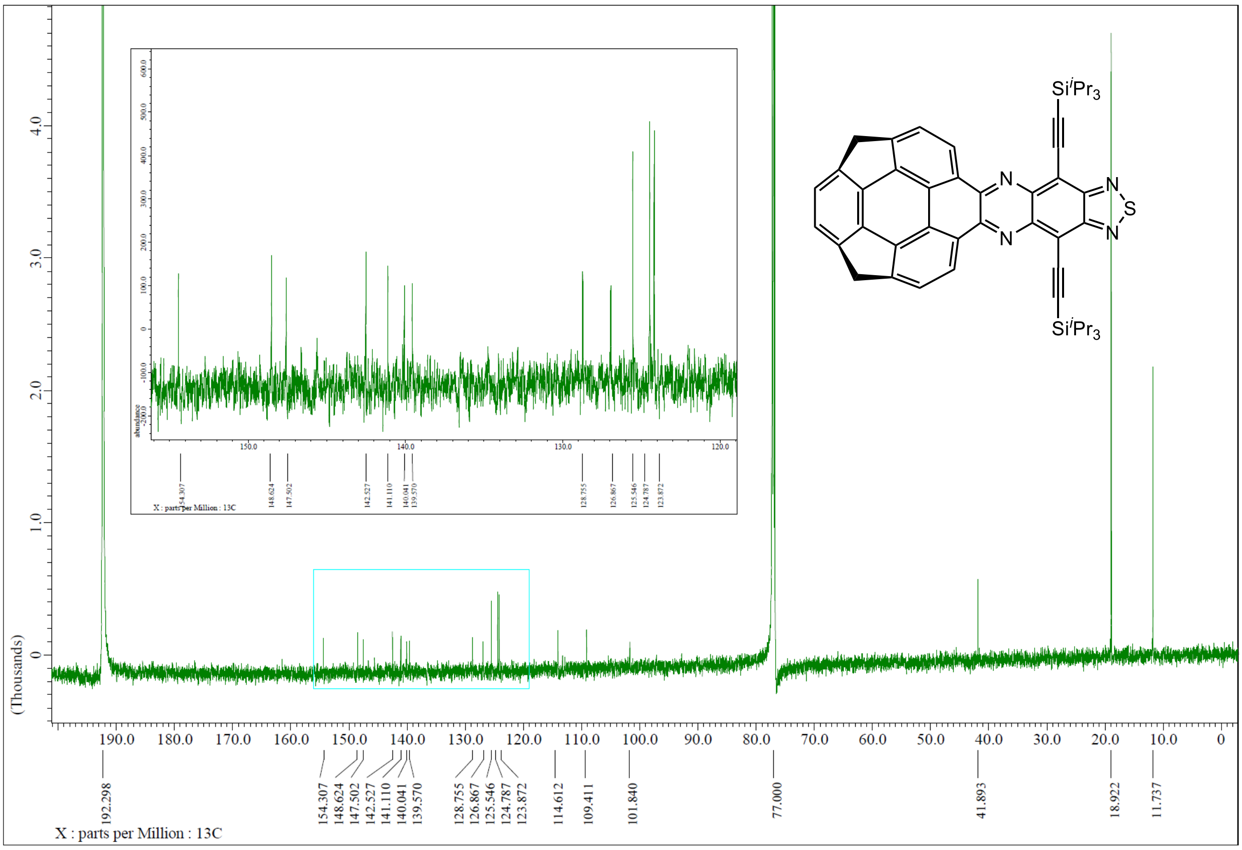

^{1}H NMR (400 MHz) and ^{13}C{^{1}H} NMR (100 MHz) of **22c** ($CDCl_3$/CS_2, 25 °C).

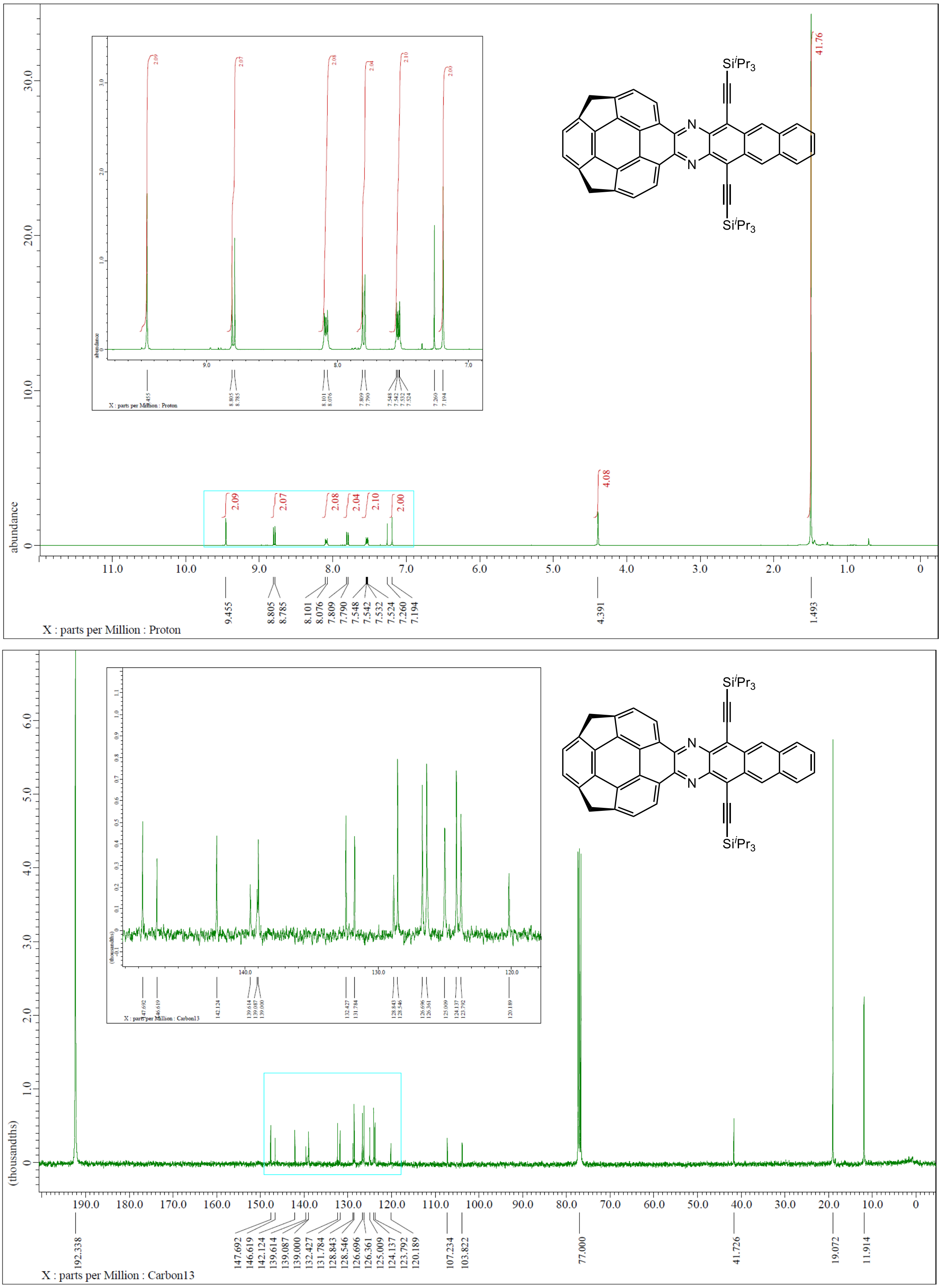

^{1}H NMR (600 MHz) and ^{13}C{^{1}H} NMR (150 MHz) spectra of **22d** (CDCl$_3$/CS$_2$, 25 °C).

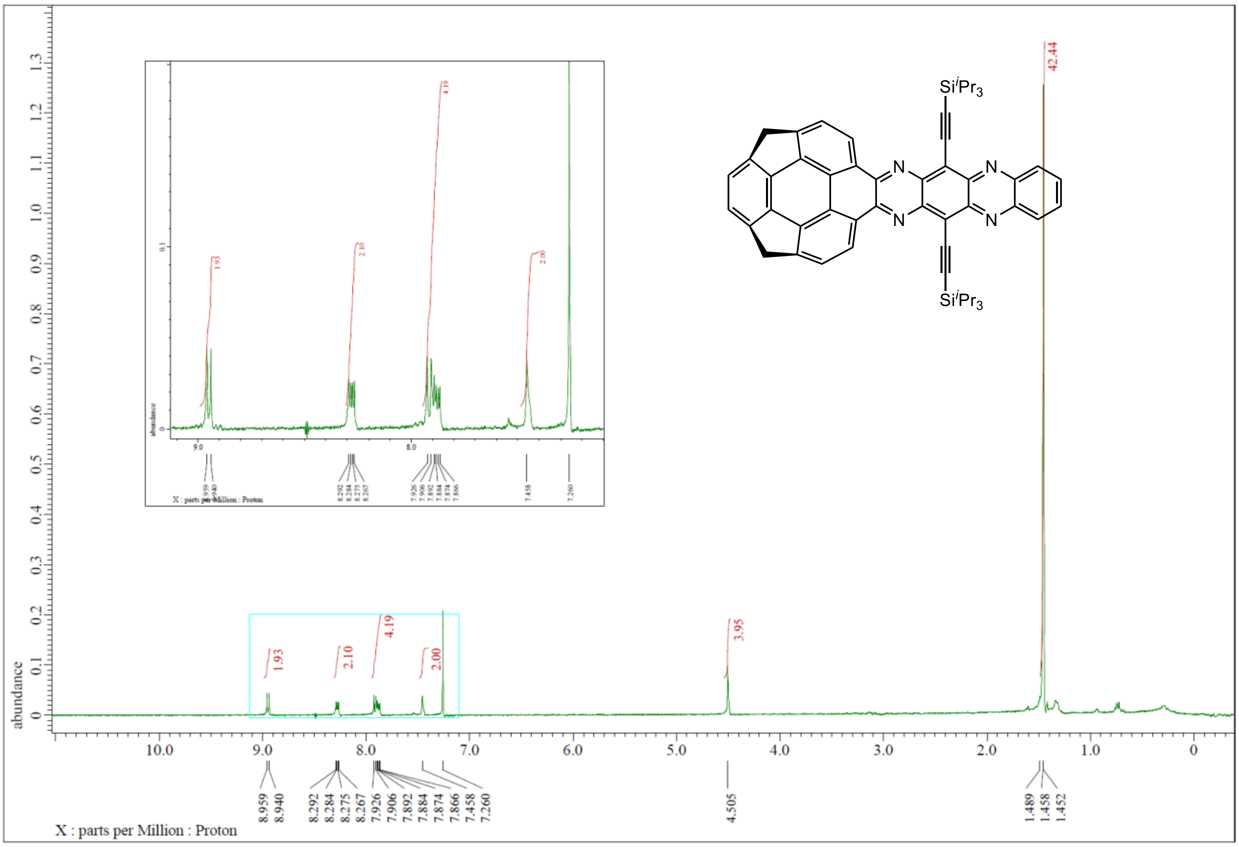

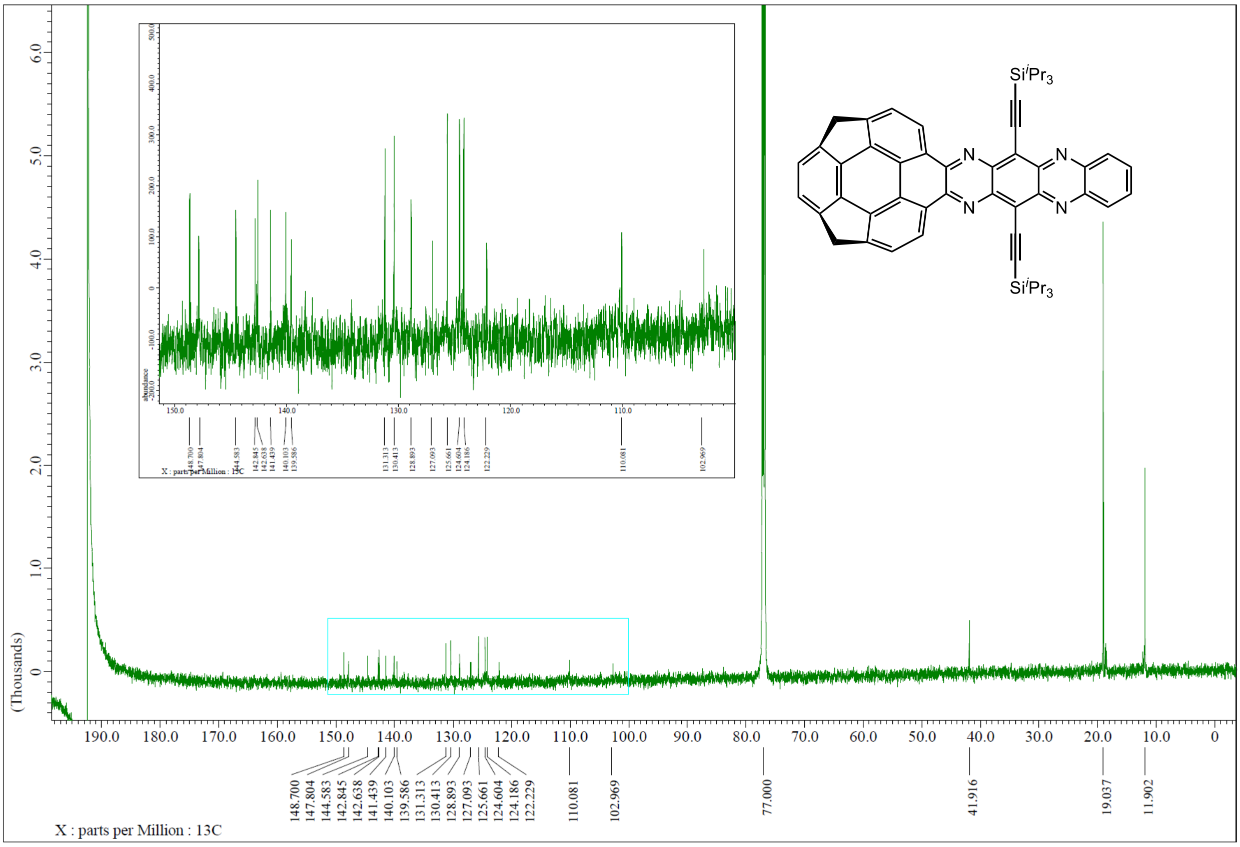

References

1. a) H. W. Kroto, J. R. Heath, S. C. O’Brien, R. F. Curl, R. D. Smalley, *Nature* **1985**, *318*, 162−163 b) R. C. Haddon, *Science* **1993**, *261*, 1545−1550.
2. a) G. Povie, Y. Segawa, T. Nishihara, Y. Miyauchi, K. Itami, *Science* **2017**, *356*, 172−175. b) G. Povie, Y. Segawa, T. Nishihara, Y. Miyauchi, K. Itami, *J. Am. Chem. Soc.* **2018**, *140*, 10054−10059. c) K. Y. Cheung, S. Gui, C. Deng, H. Liang, Z. Xia, Z. Liu, L. Chi, Q. Miao, *Chem.* **2019**, *5*, 838−847. d) Y. Li, Y. Segawa, A. Yagi, K. Itami, *J. Am. Chem. Soc.* **2020**, *142*, 12850−12856. e) K. Y. Cheung, K. Watanabe, Y. Segawa, K. Itami, *Nat. Chem.* **2021**, *13*, 255−259.
3. a) Y.-T. Wu, J. S. Siegel, *Chem. Rev.* **2006**, *106*, 4843−4867. b) V. M. Tsefrikas, L. T. Scott, *Chem. Rev.* **2006**, *106*, 4868−4884. c) M. Saito, H. Shinokubo, H. Sakurai, *Mater. Chem. Front.* **2018**, *2*, 635−661.
4. P. v. R. Schleyer, C. Maerker, A. Dransfeld, H. Jiao, Nicolaas J. R. van Eikema Hommes, *J. Am. Chem. Soc.* **1996**, *118*, 6317−6318.
5. A) Hirsch, A. *Synthesis* **1995**, *8*, 895−913. b) M. Plato, *J. Mater. Chem.* **1997**, *7*, 1097–1109. c) F. Diederich, C. Thilgen, *Science* **1997**, *271*, 317−324. d) Y. Matsuo, E. Nakamura, *Chem. Rev.* **2008**, *108*, 3016−3028.
6. H. Shudo, M. Kuwayama, Y. Segawa, K. Itami, *Chem. Sci.* **2020**, *11*, 6775−6779.
7. X. Zhang, M. R. Mackinnon, G. J. Bodwell, S. Ito, *Angew. Chem. Int. Ed.* **2022**, *61*, e202116585.
8. a) D. V. Preda, L. T. Scott, *Tetrahedron Lett*. **2000**, *41*, 9633−9637. b) A. V. Zabula, S. N. Spisak, A. S. Filatov, A. Y. Rogachev, M. A. Petrukhina, *Angew. Chem. Int. Ed.* **2011**, *50*, 2971−2974. c) M. Yanney, F. R. Fronczek, A. Sygula, *Org. Lett.* **2012**, *14*, 4942−4945. d) C. Dubceac, A. V. Zabula, A. S. Filatov, F. Rossi, P. Zanello, M. A. Petrukhina, *J. Phys. Org. Chem.* **2012**, *25*, 553−558. e) C. Dubceac, A. S. Filatov, A. V. Zabula, M. A. Petrukhina, *Cryst. Growth Des.* **2015**, *15*, 778−785.
9. H. E. Bronstein, L. T. Scott, *J. Org. Chem.* **2008**, *73*, 88−93.
10. a) J. A. Steckel, K. D. Jordan, *J. Phys. Chem. A.* **2002**, *106*, 2572–2579. b) H. Y. Cho, R. B. M. Ansems, L. T. Scott, *Beilstein J. Org. Chem.* **2014**, *10*, 956−968.
11. N. Ikuma, Y. Yoshida, Y. Yakiyama, N. Ngamsomprasert, H. Sakurai, *Chem. Lett.* **2018**, *47*, 736−739.
12. G. M. Strunz, C.-M. Yu, A. Salonius, *Phytochemistry* **1989**, *28*, 2861−2863.
13. E. V. Anslyn, D. A. Doughery, *Modern Physical Organic Chemistry*, University Science Books, Sausalito, CA, **2004**.
14. A. David Rae, A. C. Willis, *Z. Kristallogr. Cryst. Mater.* **2003**, *218*, 221–230.
15. Z. Wang, V. Enkelmann, F. Negri, K. Müllen, *Angew. Chem. Int. Ed.* **2004**, *43*, 1972–1975.
16. A. Ueda, K. Ogasawara, S. Nishida, T. Ise, T. Yoshino, S. Nakazawa, K. Sato, T. Takui, K. Nakasuji, Y. Morita, *Angew. Chem. Int. Ed.* **2010**, *49*, 6333–6337.
17. M. Jakubec, S. Hansen-Troøyen, I. Císařová, J. Sýkora, J. Storch, *Org. Lett.* **2020**, *22*, 3905−3910.

18. D. Wang, Z. Shi, X. Zhang, Z. Cui, Q. Wang, *Org. Chem. Front.* **2021**, *8*, 266−272.

19. U. H. F. Bunz, J. U. Engelhart, B. D. Lindner, M. Schaffroth, *Angew. Chem. Int. Ed*. **2013**, *52*, 3810−3821.

20. a) T. Amaya, S. Seki, T. Moriuchi, K. Nakamoto, T. Nakata, H. Sakane, A. Saeki, S. Tagawa, T. Hirao, *J. Am. Chem. Soc.* **2009**, *131*, 408−409. b) K. Okada, M. Nakano, H. Miyamoto, H. Nakazawa, Y. Uetake, H. Sakurai, *J. Phys. Chem. C.* **2020**, *124*, 19499–19507.

21. a) B. D. Lindner, F. Paulus, A. L. Appleton, M. Schaffroth, J. U. Engelhart, K. M. Schelkle, O. Tverskoy, F. Rominger, M. Hamburger, U. H. F. Bunz, *J. Mater. Chem. C*. **2014**, *2*, 9609−9612. b) A. L. Appleton, S. M. Brombosz, S. Barlow, J. S. Sears, J.-L. Bredas, S. R. Marder, U. H. F. Bunz, *Nat. Commun.* **2010**, *91*, 1−6. c) B. D. Lindner, B. A. Coombs, M. Schaffroth, J. U. Engelhart, O. Tverskoy, F. Rominger, M. Hamburger, U. H. F. Bunz, *Org. Lett.* **2013**, *15*, 666−669. d) B. D. Lindner, J. U. Engelhart, O. Tverskoy, A. L. Appleton, F. Rominger, A. Peters, H. J. Himmel, U. H. F. Bunz, *Angew. Chem. Int. Ed.* **2011**, *50*, 8588−8591.

22. U. H. F. Bunz, J. Freudenberg, *Acc. Chem. Res.* **2019**, *52*, 1575−1587.

23. Q. Xie, E. Perez-Cordero, L. Echegoyen, *J. Am. Chem. Soc.* **1992**, *114*, 3978−3980.

24. H. Qian, F. Negri, C. Wang, Z. Wang, *J. Am. Chem. Soc.* **2008**, *130*, 17970−17976.

25. S. Miao, A. L. Appleton, N. Berger, S. Barlow, S. R. Marder, K. I. Hardcastle, U. H. F. Bunz, *Chem. Eur. J.* **2009**, *15*, 4990−4993.

26. C. M. Cardona, W. Li, A. E. Kaifer, D. Stockdale, G. C. Bazan, *Adv. Mater.* **2011**, *23*, 2367−2371.

27. A. Saeki, S. Yoshikawa, M. Tsuji, Y. Koizumi, M. Ide, C. Vijayakumar, S. Seki, *J. Am. Chem. Soc.* **2012**, *134*, 19035−19042.

28. J. I. Martínez, J. P. Mora-Fuentes, M. Carini, A. Saeki, M. Melle-Franco, A. Mateo-Alonso, *Org. Lett.* **2020**, *22*, 4737−4741.

29. a) D. Cortizo-Lacalle, J. P. Mora-Fuentes, K. Strutyński, A. Saeki, M. Melle-Franco, A. Mateo-Alonso, *Angew. Chem. Int. Ed.* **2018**, *57*, 703−708. b) D. Cortizo-Lacalle, C. Gozalvez, M. Melle-Franco, A. Mateo- Alonso, *Nanoscale* **2018**, *10*, 11297−11301. c) J. P. Mora-Fuentes, A. Riaño, D. Cortizo-Lacalle, A. Saeki, M. Melle-Franco, A. Mateo-Alonso, *Angew. Chem. Int. Ed.* **2019**, *58*, 552−556.

30. a) R. S. Potember, T. O. Poehler, *Appl. Phys. Lett.* **1979**, *34*, 405–407. b) S. Seifert, D. Schmidt, F. Wgrthner, *Chem. Sci.* **2015**, *6*, 1663–1667. c) L. Ji, A. Friedrich, I. Krummenacher, A. Eichhorn, H. Braunschweig, M. Moos, S. Hahn, F. L. Geyer, O. Tverskoy, J. Han, C. Lambert, A. Dreuw, T. B. Marder, U. H. F. Bunz, *J. Am. Chem. Soc.* **2017**, *139*, 15968–15976. d) Y. Kumar, S. Kumar, K. Mandal, P. Mukhopadhyay, *Angew. Chem. Int. Ed.* **2018**, *57*, 16318–16322. e) D.-H. Tuo, C. Chen, H. Ruan, Q.-Q. Wang, Y.-F. Ao, X. Wang, D.-X. Wang, *Angew. Chem. Int. Ed.* **2020**, *59*, 14040–14043.

31. J. S. Miller, A. J. Epstein, W. M. Reiff, *Science* **1988**, *240*, 40–47.

32. Ghosh, T. Ghosh, J. I. Bardagi, B. Kçnig, *Science* **2014**, *346*, 725–728.

33. L. Ji, M. Haehnel, I. Krummenacher, P. Biegger, F. L. Geyer, O. Tverskoy, M. Schaffroth, J. Han, A. Dreuw, T. B. Marder, U. H. F. Bunz, *Angew. Chem. Int. Ed.* **2016**, *55*, 10498−14501.

34. R. Wu, L. Silks, M. Olivault-Shiflett, R. F. Williams, E. G. Ortiz, P. Stotter, D. B. Kimball, R. A. Martinez, *J. Label Compd. Radiopharm.* **2013**, *56*, 581–586.

35. *RAPID-AUTO*. Rigaku Corporation, Tokyo, Japan (**2001**).

36. *CrysAlis PRO*. Rigaku Oxford Diffraction, Yarnton, England (**2015**).

37. G. M. Sheldrick, *Acta Cryst. A* **2015**, *71*, 3–8.

38. G. M. Sheldrick, *Acta Cryst. C* **2015**, *71*, 3–8.

39. *Olex2: a complete structure solution, refinement and analysis program*; O. V. Dolomanov, L. J. Bourhis, R. J. Gildea, J. A. K. Howard, H. Puschmann, *J. Appl. Cryst.* **2009**, *42*, 339–341.

40. J. Sim, H. Jo, M. Viji, M. Choi, J.-A. Jung, H. Lee, J.-K. Jung, *Adv. Synth. Catal.* **2018**, *360*, 852–858.

41. Gaussian 09, Revision E.01, M. J. Frisch, G. W. Trucks, H. B. Schlegel, G. E. Scuseria, M. A. Robb, J. R. Cheeseman, G. Scalmani, V. Barone, B. Mennucci, G. A. Petersson, H. Nakatsuji, M. Caricato, X. Li, H. P. Hratchian, A. F. Izmaylov, J. Bloino, G. Zheng, J. L. Sonnenberg, M. Hada, M. Ehara, K. Toyota, R. Fukuda, J. Hasegawa, M. Ishida, T. Nakajima, Y. Honda, O. Kitao, H. Nakai, T. Vreven, J. A. Montgomery, Jr., J. E. Peralta, F. Ogliaro, M. Bearpark, J. J. Heyd, E. Brothers, K. N. Kudin, V. N. Staroverov, R. Kobayashi, J. Normand, K. Raghavachari, A. Rendell, J. C. Burant, S. S. Iyengar, J. Tomasi, M. Cossi, N. Rega, J. M. Millam, M. Klene, J. E. Knox, J. B. Cross, V. Bakken, C. Adamo, J. Jaramillo, R. Gomperts, R. E. Stratmann, O. Yazyev, A. J. Austin, R. Cammi, C. Pomelli, J. W. Ochterski, R. L. Martin, K. Morokuma, V. G. Zakrzewski, G. A. Voth, P. Salvador, J. J. Dannenberg, S. Dapprich, A. D. Daniels, Ö. Farkas, J. B. Foresman, J. V. Ortiz, J. Cioslowski, and D. J. Fox, Gaussian, Inc., Wallingford CT, 2009.

42. J.-D. Chai, M. Head-Gordon, *Phys. Chem. Chem. Phys.* **2008**, *10*, 6615–6620.

43. F. Weigend, R. Ahlrichs, *Phys. Chem. Chem. Phys.* **2005**, *7*, 3297–3305.

44. P. J. Stephens, F. J. Devlin, C. F. Chabalowski, M. J. Frisch, *J. Phys. Chem.* **1994**, *98*, 11623–11627.

45. R. Krishnan, J. S. Binkley, R. Seeger, J. A. People, *J. Chem. Phys.* **1980**, *72*, 650–654.

46. T. Clark, J. Chandrasekhar, G. W. Spitznagel, P. v. R. Schleyer, *J. Comput. Chem.* **1983**, *4*, 294–301.

47. T. H. Dunning. Jr., *J. Chem. Phys.* **1989**, *90*, 1007–1023.

48. K. Fukui, *Acc. Chem. Res.* **1981**, *14*, 363–368.

49. a) R. Ditchfield, W. J. Hehre, J. A. Pople, *J. Chem. Phys.* **1971**, *54*, 724–728. b) W. J. Hehre, R. Ditchfield, J. A. Pople, *J. Chem. Phys.* **1972**, *56*, 2257–2261. c) P. C. Hariharan, J. A. Pople, *Theor. Chim. Acta.* **1973**, *28*, 213–222. d) M. M. Francl, W. J. Pietro, W. J. Hehre, J. S. Binkley, M. S. Gordon, D. J. DeFrees, J. A. Pople, *J. Chem. Phys.* **1982**, *77*, 3654–3665. e) M. S. Gordon, J. S. Binkley, J. A. Pople, W.

J. Pietro, W. J. Hehre, *J. Am. Chem. Soc.* **1982**, *104*, 2797–2803.

50. G. Scalmani, M. J. Frisch, *J. Chem. Phys.* **2010**, *132*, 114110.
51. A. D. McLean, G. S. Chandler, *J. Chem. Phys.* **1980**, *72*, 5639–5648.

Summary

In this doctoral dissertation, the author developed a method for the synthesis of C70 fragment buckybowls, homosumanene, and their derivatives via various ring expansion reactions from the sumanene derivatives, and in the process revealed unique properties and reactivity derived from the bowl structure.

In Chapter 2, the synthesis and properties of homosumanenes, lactones, lactams, and azahomosumanenes via ring expansion reactions from sumanenone were described. They form a columnar stacking structure in the crystal even though they have a shallow bowl structure. They also undergo bowl inversion very rapidly in solution because of very small bowl inversion energy. Nitrogen-doped analogue of homosumanene, azahomosumanene was also synthesized and utilized as a buckybowls ligand.

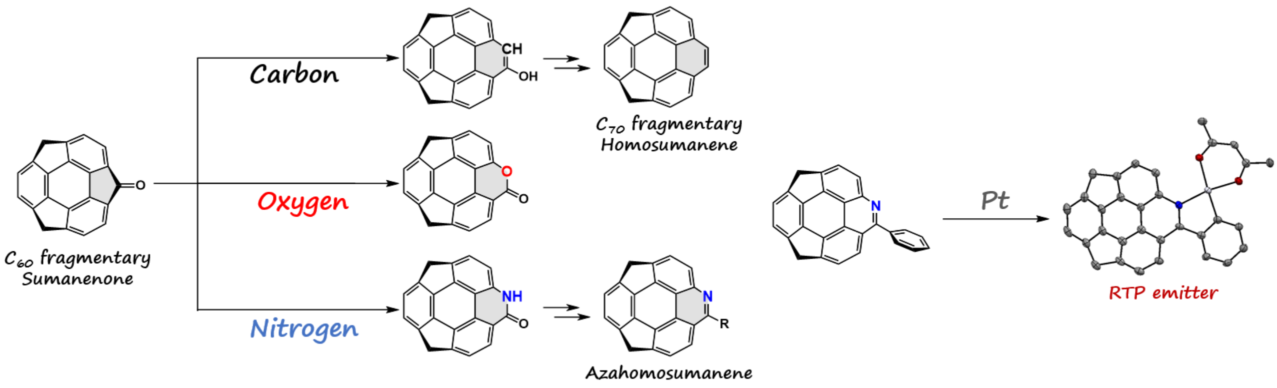

In Chapter 3, a ring-opening reaction of sumanenone involving C-C bond cleavage driven by the release of bowl strain was described. This reaction did not proceed in similar planar molecules, suggesting that the bowl structure significantly affects the reactivity.

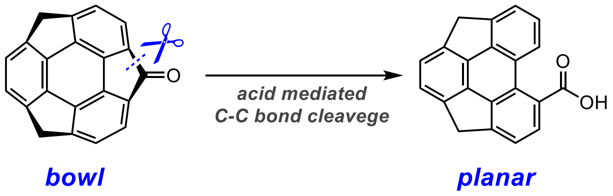

In Chapter 4, the dissymmetrization of the azabuckybowl's concave and convex faces by complexation with platinum was described. The obtained platinum complex was observed as a mixture of two isomers depending on the direction of the bowl, and the isomeric ratio in solution was highly biased due to the difference in thermodynamic stability. The concave/convex faces of the bowls were differentiated through complexation with a square-planar coordination center bearing different ligands.

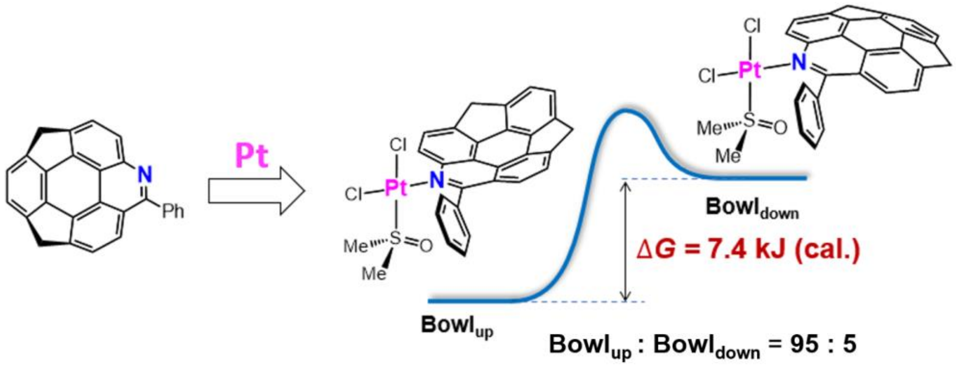

In Chapter 5, the bowl structure of hydroxyhomosumanene affected the keto/enol tautomerism and showed higher reactivity than planar molecules for aerobic oxidation reactions to afford homosumanene *ortho*-quinone. Azaacene-fused homosumanenes were also synthesized from obtained *ortho*-quinone, demonstrating its synthetic utility as a precursor toward further π-extensions. Azaacene-fused homosumanenes showed the bowl-derived stacking structure and the excellent electron affinity derived from azaacene structure.

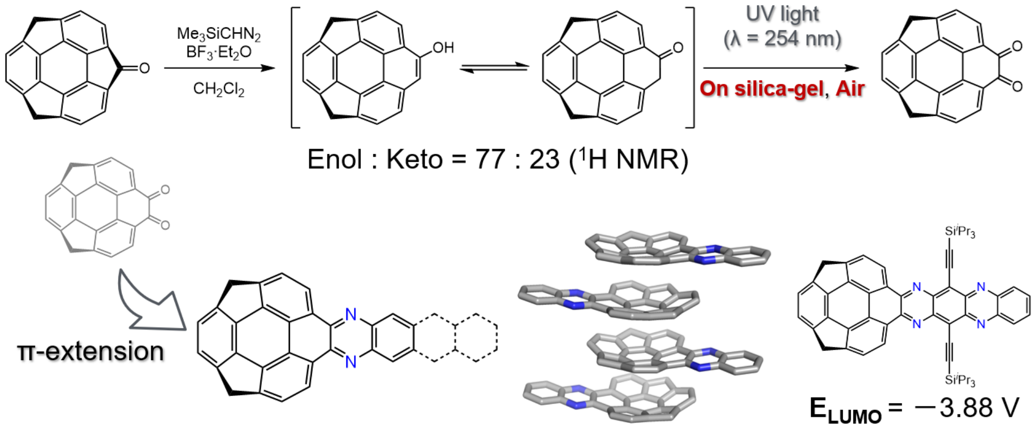

As described above, in this study, new C70 fragment buckybowls, homosumanene, azahomosumanene, and their analogues were synthesized from the ring expansion reaction of sumanene derivatives. The influence of the bowl structure on their reactivity and crystal structure was also clarified. The knowledge obtained in this study about the physical properties derived from the concave/convex faces and the unique reactivity in the curved-π system is expected to lead to the development of the field of precise synthesis of novel curved nanocarbons as well as buckybowls.

List of publications

The content of this thesis has been published in the following papers.

1) Synthesis of the C70 Fragment Buckybowl, Homosumanene, and Heterahomosumanenes via Ring-Expansion Reactions from Sumanenone

   M. Nishimoto, Y. Uetake, Y. Yakiyama, F. Ishiwari, A. Saeki, H. Sakurai, *J. Org. Chem.* **2022**, *87*, 2508−2519.

2) Thermodynamic Differentiation of the Two Sides of Azabuckybowl through Complexation with Square Planar Platinum(II)

   M. Nishimoto, Y. Uetake, Y. Yakiyama, H. Sakurai, *Chem. Asian. J.* **2022**, e202201103.

3) Acceleration Effect of Bowl-shaped Structure in Aerobic Oxidation Reaction: Synthesis of Homosumanene *ortho*-Quinone and Azaacene-Fused Homosumanenes

   M. Nishimoto, Y. Uetake, Y. Yakiyama, A. Saeki, J. Freudenberg, U. H. F. Bunz, H. Sakurai, *Chem. Eur. J.* **2022**, e202203461.

Copyright

The author has obtained the permissions to reuse contents. The author wishes to express his thanks to Copyright Clearance Center, Creative Commons, American Chemical Society, and Wiley-VCH Verlag GmbH, Weinheim.

Credits

Reprinted with permission from M. Nishimoto, Y. Uetake, Y. Yakiyama, F. Ishiwari, A. Saeki, H. Sakurai, *J. Org. Chem.* **2022**, *87*, 2508−2519. Copyright 2022 American Chemical Society.

Reprinted with permission from M. Nishimoto, Y. Uetake, Y. Yakiyama, H. Sakurai *Chem. Asian J.* **2022**, e202201103. Copyright 2022 Wiley-VCH Verlag GmbH, Weinheim.

Reprinted with permission from M. Nishimoto, Y. Uetake, Y. Yakiyama, A. Saeki, J. Freudenberg, U. H. F. Bunz, H. Sakurai, *Chem. Eur. J.* **2022**, e202203461. Copyright 2022 Wiley-VCH Verlag GmbH, Weinheim.

Acknowledgements

I would like to express my sincere gratitude to Professor Hidehiro Sakurai for providing me with a complete research environment, much guidance, and encouragement during the course of this doctoral dissertation research. I am deeply grateful to Associate Professor Yumi Yakiyama for her careful guidance, help with X-ray crystallographic analysis, and knowledge. I am deeply grateful to Assistant Professor Yuta Uetake for giving me precise advice during my research and teaching me various knowledge and skills through daily discussions, as well as how to write a thesis.

I would like to express my sincere gratitude to Professor Takashi Hayashi and Professor Akinori Saeki for reviewing my doctoral dissertation and for their suggestions and advice.

I would like to thank Professor Akinori Saeki (Osaka University), Associate Professor Yohei Takeda (Osaka University), and Lecturer Fumitaka Ishiwari (Osaka University) for their cooperation in photophysical property measurements. We thank Prof. Masaki Kawano (Tokyo Institute of Technology), Assistant Prof. Hiroyoshi Otsu (Tokyo Institute of Technology), and Prof. Mao Minoura (Rikkyo University) for their cooperation in single crystal X-ray structure analysis. We thank Dr. Kyoko Inoue (Analysis Center, Osaka University) for her cooperation in two-dimensional NMR measurements. I appreciate the great help from Prof. Uwe H. F. Bunz (Heidelberg University), Dr. Jan Freudenberg (Heidelberg University), and Mr. Soh Kushida (Strasbourg University) with the synthesis of azaacene-fused homosumanenes.

I would like to thank Dr. Yuki Yoshida for providing me with many skills and knowledge on how to carry out my research. I would like to thank Dr. Hironobu Nakazawa, with whom I had a friendly competition in the same year and who helped me in every aspect of my research and personal life. I would like to thank Ms. Michiko Ebukuro, Ms. Yuki Matsuo, Ms. Karin Fujino, and Ms. Marika Moriyasu for their support in various administrative tasks and research activities. I would like to thank all the students in Sakurai Laboratory with whom I have shared many hardships and joys, both in research and outside of research.

X-ray crystallography was performed at SPring-8 BL40XU (Proposal No. 2018A1405, 2018B1275, 2018B1419, 2019B1654, 2021B1591) and Pohang Accelerator Laboratory (PAL) 2D beamline (Proposal No. 2017-second-2D-031). Quantum chemical calculations were performed at the Institute for Molecular Science, Center for Computational Science (Project: 22-IMS-C068). This work was supported by JST SPRING, Grant Number JPMJSP2138. I would like to express our sincere appreciation for this support.

Finally, I would like to express my deepest gratitude to my father, Satoshi Nishimoto, my mother, Kaoru Nishimoto, my wife, Ruriko Nishimoto, and all those who have supported me in every aspect of my university life.

March 2023

Mikey Nishimoto